MINIATURE, SUBMERSIBLE ELECTROMAGNETIC PUMPS OF MOLTEN LEAD AND SODIUM TEST LOOPS FOR GEN-IV NUCLEAR REACTORS DEVELOPMENT

Ragai M. Altamimi and Mohamed S. El-Genk

Institute for Space and Nuclear Power Studies and Nuclear Engineering Department

The University of New Mexico, Albuquerque, NM, USA

The Institute for Space Nuclear Power Studies Technical Report

No. UNM-ISNPS-1-2023.

June 2023

PAGE LEFT INTENTIONALLY BLANK

ACKNOWLEDGMENTS

This research is partially funded by the University of New Mexico's Institute for Space and Nuclear Power Studies (ISNPS) and by the Battelle Energy Alliance, LLC under Award No. DE-AC07-051D14517 to the University of New Mexico's Institute for Space and Nuclear Power Studies. This research made use of the high-performance computing capabilities of the UNM Center for Advanced Research Computing, supported in part by the National Science Foundation.

Executive Summary

Heavy metals and alkali Liquid Metals are suitable coolants for Generation IV terrestrial nuclear reactors for operating at elevated temperatures for achieving plant thermal efficiency more than 40% and the thermochemical generation of hydrogen fuel. In addition, the low vapor pressure of these liquids eliminates the need for a pressure vessel and instead operates slightly below ambient pressure. A primary issue with the uses of these coolants is their compatibility with nuclear fuel, cladding and core structure materials at elevated temperatures more than 500^{o}C. Therefore, in pile and out-of-pile test loops have been constructed or being considered for quantifying the effect of the operating temperature flow velocity on the compatibility of versus fuel and structural materials with heavy liquid metals of lead (Pb) and lead Bismuth Eutectic (LBE) and alkali liquid metals of sodium for fast spectrum nuclear reactors. Recently, two in-pile test loops are thought for supporting the developments of molten lead and liquid sodium-cooled advanced reactors in the US and investigating the compatibility of several structure and cladding materials with these liquid metals at different temperatures and flow rates in a prototypical irradiation environment. These test loops were to be placed at designated locations within the core of the sodium-cooled, fast neutron spectrum 300 MW_{th} Versatile Test Reactor (VTR). In these in-pile loops. It is desirable to employ miniature submersible electromagnetic pumps (EMPS) with no moving parts for reliable operation. which is the focus of the present research. These pumps need to fit within the 2.5-inch diameter standard tube for the test loop riser downstream of the test article of one or more nuclear fuel rodlets, and with compatible components with molten lead and liquid sodium initially at temperatures up to 500^{o}C. At these temperatures, 316SS cladding and structure materials is suitable choice, but not at higher temperature for which nickel free materials are being investigated.

The objective of this research is therefore to develop designs and conduct performance analyses of miniature, submersible EMP for operating at temperatures $\leq$ 500^{o}C in in-pile and out-of-pile test loops for supporting the current development of Gen-IV molten Pb and liquid Na fast neutron spectrum terrestrial nuclear reactors. The two miniature submersible designs investigated are of a Direct Current-ElectroMagnetic pump (DC-EMP) and an

Alternating Linear Induction Pump (ALIP). In the DC-EMP), in which DC electric current from Cu electrodes flows through the working fluid flowing in a narrow rectangular duct in the perpendicular direction to those of the flow and the generating magnetic flux density using permanent magnet(s). The produced Lorentz force in the pump duct drives the fluid flow. The ALIP's linearly traveling magnetic fields produced by 3-Phase alternative currents in winding coils surrounding the annular flow duct generate electrical current in the perpendicular directions of the generated electric current and magnetic field. The generated Lorentz force drives the flow in a narrow annular flow duct. The two submersible EMPs have an outer diameter of 66.8 mm outer diameters, which fit in a 2.5-inch standard tube with an inner diameter of 68.8 mm, and 1.00 mm clearance to the wall's inner surface.

The developed DC-EMP employs Alnico-5 permanent magnets with Hiperco-50 pole pieces for focusing the magnetic field lines in the 316SS rectangular flow duct and operating at temperatures up to 500^{o}C. The novel 66.8mm pump design has dual pumping stages for enhance performance, enabled using a pair of Alnico-5 permanent magnets mounted along the rectangular flow duct and with opposite magnetizing directions in the two pumping regions of the flow duct. The electrical currents through the flow duct in the two pumping regions are supplied in opposite directions perpendicular to those of the flow and the magnetic field flux density, so that the generated Lorentz forces in the two pumping stages act in the same flow direction. The developed ALIP design employs high-temperature, ceramic insulated Copper wires for winding coils, and Hiperco-50 center core and stators.

The performance analyses for the two pump designs are conducted using the lumped, electrical Equivalent Circuit Model (ECM). For the present DC-EMP the ECM on MATLAB platform is linked to the FEMM software, for calculating the effective electrical currents and magnetic field distribution in the pump duct at zero flow. The fast-running ECM includes a few simplifying assumptions, nonetheless it has been shown by other investigators and in this work to overpredict the pump characteristics by 10- 25%. The implements ECM for the present ALIP design is improved compared to the widely used and originally proposed model by Baker and Tessier. The accuracy of the improved ECM for the present ALIP design is confirmed by comparing predictions to the reported experimental data by others for low-flow sodium, small ALIP. The ECM predictions of the pump characteristics are <6% higher than reported experimental measurements.

The performed parametric analyses of the present 66.8 mm diameter DC-EMP design investigated the effects of varying the dimensions of the flow duct width and height, the length of the current electrodes the thickness of the ALNICO-5 permanent magnets, and the separation distance of the two pumping regions on the pump performance parameters. These include the pump characteristics and the cumulative pumping power, pump efficiency and the dissipated thermal power as functions of flow rate of molten lead and liquid sodium. The parametric analyses of the ALIP investigated the effects on the pump performance parameters of varying the dimensions, the winding wire diameter, the width of the annular flow duct, the length of center core, the terminal voltage and current frequency.

The present miniature, submersible DC-EMP for circulating molten lead at inlet temperature of 500°C, has a maximum efficiency of 11.3% at a flow rate of 5.75 m^3/h (16.2 kg/s) and pumping pressure of 282 kPa, with a dissipated thermal power of 3.2 kW. For liquid sodium at the same temperature, the maximum pump efficiency is much higher; 36.5% at a flow rate of 3.95 m^3/h (0.9 kg/s) and pumping pressure of 379 kPa and dissipated thermal power of 4.1 kW. The predicted efficiency of the miniature, submersible ALIP design for molten lead at inlet temperature of 500°C is lower than for the Dc-EMP. The ALIP maximum efficiency of 6.7% occurs at a flow rate of 3.37 m^3/h (9.5 kg/s) and pumping pressure of 263 kPa, with a dissipated thermal power of 3.2 kW. For liquid sodium at the same temperature, pump efficiency increases to 26.3% and occurs at a flow rate of 9.66 m^3/h (2.2 kg/s), pumping pressure of 364 kPa, and dissipated thermal power of 2.7 kW.

To gain insight into the pump operation parameters and quantify the effect of the simplifying assumption in the ECM, this work conducted 3-D MagnetoHydroDynamic (MHD) numerical analyses of the present design of the 66.8 mm diameter dual-stage DC-EMP using Star-CCM+. The results of these analyses are not easily attainable otherwise, even experimentally. The MHD analyses solve the coupled electromagnetism, and the momentum and energy balance equations in the pump flow duct to obtain detailed spatial distributions of the coupled electrical, magnetic, thermal, and fluid flow parameters, and calculate the pump characteristics. The adequacy of the numerical mesh refinements for results conversion is confirmed using the Grid Convergence Index (GCI) criterion.

The 3-D MHD numerical analyses results show strong dependence of the spatial distribution of the magnetic field on the value and the distribution of the electric current in the flow duct and confirm a negligible effect of joule heating on fluid temperature and pump characteristics. The MHD results of the pump characteristics are lower but in general agreement with the ECM predictions, with the difference increasing with increased flow rate and input electrodes electric current up to 12% and 14% for molten lead and liquid sodium, respectively.

TABLE OF CONTENTS

LIST OF FIGURES

LIST OF TABLES

NOMENCLATURE

A	Cross-section area of flow annulus (m^2)
$\vec{A}$	Magnetic vector potential
a	Width of flow duct (m), Ratio of inner to outer annular flow channel diameters
A_c	Cross-section area of winding conductor (m)
ALIP	Annular Linear Induction Pump
AUV	Autonomous Underwater Vehicle
B	Magnetic flux density in (T)
B_i	Induced magnetic field flux density (T)
B_o	Magnetic field flux density at zero flow (T)
$\bar{B}_o$	Effective magnetic flux density at zero flow (T)
B_r	Radial magnetic field flux density (T)
B_{sat}	Saturation magnetic field flux density (T)
b	Height of flow duct (m)
c	Length of current electrode (m), Length of pump section (m)
C_p	Specific heat (J/kg.K)
CFD	Computational Fluid Dynamics
D	Pump outer diameter (m)
$\bar{D}_a$	Mean diameter of flow annulus (m)
D_e	Flow duct equivalent hydraulic diameter (m)
D_h	Equivalent hydraulic diameter (m)
D_{iw}	Inner diameter of inner duct wall (m), center core diameter (m)
D_o	ALIP outer diameter (m)
D_{ow}	Inner diameter of outer duct wall (m)
D_s	Stator inner diameter (m)
DC-EMP	Direct Current Electromagnetic Pump
E	Pump terminal voltage (VDC)
$\vec{E}$	Electric field in (V/m)
E_A	Air gap induced voltage (V)

E_B	Pump terminal voltage (V)
E_i	Induced emf (VDC)
ECM	Equivalent Circuit Model
ELTA-CL	Extended Length Test Article – Cartridge Lead
emf	Electromotive force (V)
EMP	Electromagnetic pump
F	Force (N)
F_L	Lorentz force (N)
f	Electrical current frequency (Hz), friction factor
FBR	Fast Breeder Reactor
FEMM	Finite Element Method Magnetics
FSP	Fission Surface Power
GCI	Grid Convergence Index
GEN-IV	Generation four reactors
GFR	Gas-cooled Fast Reactors
GIF	Generation four International Forum
H	Magnetizing force (Oe)
HTGR	High-Temperature Gas-cooled Reactors
I	Electrical current (A)
I_e	Pump effective current (A)
I_{eo}	Pump effective current at zero flow (A)
I_{FEMM}	FEMM input current (A)
I_f	Fringe current (A)
I_{fo}	Fringe current at zero flow (A)
I_i	Induced electric current (A)
I_{in}	Electrode input current (A)
I_{le}	Leakage current (A)
I_m	Induced electric current in the non-magnetic gap (A)
I_p	Phase electrical current (A)
I_w	Duct wall current (A)

ISNPS	Institute for Space and Nuclear Power Studies
J	Electrical current density in (A/m^2)
k	Thermal conductivity (W/m.K)
k_1	Fringe correction factor
k_d	Winding distribution factor
k_{nm}	Multiplier factor for non-magnetic gap width
k_p	Pitch factor
L	Total pump length (m), Magnetic field's characteristic length (m), Inductance (H)
l	Length (m)
l_{ex}	Extension length of ALIP center core (m)
l_{ext}	Extension length of pump duct (m)
l_p	Length of pump duct (m)
l_{sep}	Separation distance (m)
LFS	Lead-cooled Fast Reactor
l_{t}	Average length of coil turns (m)
$\dot{m}$	Mass flow rate of working fluid (kg/s)
M	Magnetizing direction
MHD	MagnetoHydroDynamic
MSR	Molten Salt Reactor
N	North pole
$\vec{n}$	Normal vector to the boundary surface
$N_{c,ph}$	Number of coils per phase in stator
N_p	Number of poles
$N_{\mathrm{t,c}}$	Number of windings turns per coil
$N_{t,ph}$	Number of windings turns per phase
$N_{w,p}$	Number of winding wires connected in parallel per phase
P	Power (W)
ΔP	Net pumping pressure (Pa)
ΔP_{loss}	Friction pressure losses (Pa)
ΔP_o	Pump static pressure (Pa)

ΔP_p	Developed pumping pressure from Lorentz force (Pa)
P_c	Permeance coefficient
P_f	Power factor
PD	Dissipated thermal power (W)
PE	Electrical input power (W)
PGSFR	Prototype Gen IV Sodium cooled Fast Reactor
PP	Pumping power (W)
PP_{peak}	Peak pumping power (W)
Q	Flow rate (m^3/h)
Q_{ro}	Run-out flow rate (m^3/s)
Q_{syn}	Synchronous working fluid flow rate (m^3/s)
Re	Reynolds number ($\dot{m}\, D_h / A\, \mu$)
Re_m	Magnetic Reynolds number
R_c	Electrical resistance of coils conductor per phase (Ω)
R_e	Working fluid electrical resistance in pump region (Ω)
R_{fo}	Fringe electrical resistance (Ω)
R_{iw}	Electrical resistance of flow duct inner wall (Ω)
R_{ow}	Electrical resistance of flow duct outer wall (Ω)
R_{stat}	Static electrical resistance (Ω)
R_{wf}	Electrical resistance of working fluid (Ω)
S	South pole, Reluctance (1/H)
s	Slip ratio
SCWR	Supercritical Water-cooled Reactors
SFR	Sodium-cooled Fast Reactor
SRPS	Space Reactor Power System
T	Temperature (^oC or K)
U	Mean velocity of the working fluid in (m/s)
$\vec{u}$	velocity in (m/s)
u_d	Developed velocity profile (m/s)
$\vec{u}^T$	Turbulence velocity (m/s)

UNM	University of New Mexico
VHTR	Very High-Temperature gas Reactor
VTR	Versatile Test Reactor
W_s	Stator slot width (m)
W_t	Stator tooth width (m)
X_l	Leakage reactance (Ω)
X_m	Magnetizing reactance (Ω)

Subscripts

cu	Cumulative
e	Effective
ex	Extension
f	Fringe
g	Gap
ins	Insulation
m	Magnet
p	Pump
$peak$	Peak value
w	Pump duct wall
wf	Working fluid

Greeks

δ	Thickness (m)
δ_a	Annular flow channel width (m)
δ_c	Coil height (m)
δ_{cl}	Slot clearance height (m)
δ_{ins}	Electrical insulation thickness (m)
δ_{iw}	Thickness of annular duct inner wall (m)
δ_m	Magnet thickness (m)
δ_{nm}	Total non-magnetic gap width (m)
δ_{ow}	Thickness of annular duct outer wall (m)
δ_{sb}	Stator back depth (m)

δ_w	Duct wall thickness (m)
ε_o	permittivity in (F/m)
η	Dynamic viscosity (Pa.s), Efficiency (%)
η_{peak}	Peak efficiency (%)
η_T	Turbulence viscosity (Pa.s)
μ	Magnetic permeability in (H/m), Dynamic Viscosity (Pa.s)
μ_o	Permeability of free space (1.2567×10^{-6} H/m)
ρ	Electric charge density in (C/m^3), Density (kg/m^3)
ρ_c	Electrical resistivity of winding conductor (Ω.m)
ρ_e	Electrical resistivity (Ω.m)
ρ_w	Electrical resistivity of annular duct walls (Ω.m)
ρ_{wf}	Electrical resistivity of working fluid (Ω.m)
σ	Electric conductivity in (S/m)
τ	Pole pitch (m)
ϕ	Magnetic field (Wb)

1 INTRODUCTION

Increasing interest in clean and sustainable energy has gained significant importance in the contemporary world. In our pursuit to mitigate the environmental impact of energy production and reduce greenhouse gas emissions, existing and advanced nuclear reactor technologies could play a key role in a balanced energy policy aiming to improve the environment and effectively reduce greenhouse gas emissions. Among these technologies, generation -III and Generation IV (GEN-IV) reactors with advanced passive operation and safety features stand out for their potential to revolutionize the field of nuclear power (Pioro, 2022). In addition, the development of the deployment of small modular and microreactors in remote communities and island nations can replace the dependence on burning coal and wood for energy.

Gen-IV reactors being developed for potential deployment in 2020, would operate at high temperatures of 1,000-1,300 K for the generation of electricity at high thermal efficiency approaching 40%-50%, the production of green hydrogen using thermochemical processes, and many industrial applications. They offer enhanced safety features, ensuring robust and fail-safe operation (Buckthorpe, 2017). These reactors incorporate passive safety systems that rely on natural convection, reducing the reliance on active mechanical systems and minimizing the risk of accidents (Abram and Ion, 2008). Additionally, the high thermal efficiency of Gen-IV reactors contributes to their economic viability for meeting the rising energy demands of the future (Abram and Ion, 2008; Buckthorpe, 2017). Furthermore, Gen-IV reactors would minimize the production of long-lived radioactive actinides by having fast neutron energy spectra.

The Gen-IV reactor designs incorporate different technologies and employ various coolants, including heavy and alkali liquid metals, gases, and molten salts, each offering unique advantages and complexities. Two notable concepts are Lead-cooled Fast Reactors (LFRs) and Sodium-cooled Fast Reactors (SFRs) (Locatelli, 2013).

LFRs employ liquid lead as the primary coolant, taking advantage of its attractive thermal properties of vapor pressure or high boiling temperature and high thermal conductivity and thermal energy storage capacity (Alemberti, 2014). The low vapor pressure enables high-temperature operation at or near atmospheric pressure, thus eliminating the need for a heavy reactor pressure vessel. Additionally, lead serves as an effective radiation shield, minimizing the risk of radiation leakage, and chemically exhibits non-reactivity with air and water in the event of system leakage.

SFRs share many of the attributes of the LERs but utilize the alkali liquid metal of sodium as the primary coolant. This coolant exhibits exceptional heat transfer properties and low pumping power requirements, facilitating efficient heat removal from the reactor core and improving thermal efficiency and fuel utilization (Ohshima and Kubo, 2016). Sodium also possesses a low neutron absorption cross-section, allowing for higher neutron flux and increased fuel burnup in the core, thereby enhancing overall reactor performance (Wydler, 2005; Heinzel et al., 2017; Sabharwall et al., 2013). The liquid sodium low vapor pressure eliminates the need for a pressure vessel for reactor operation slightly below atmospheric pressure. Moreover, the fast spectrum within the reactor core enhances the conversion of fertile materials such as uranium-238 or thorium-232 into fissile of plutonium-239 or uranium-233, significantly enhancing nuclear fuel utilization efficiency by up to 50 times (Locatelli, 2013). This is in addition to burning generated actinides in the nuclear fuel during reactor operation by fast neutron fission, thus simplifying spent fuel storage requirements.

The development and deployment of lead and sodium-cooled fast reactors, however, encounters several challenges, particularly in the areas of fuel and structural materials, and their compatibility with the coolant at high temperatures > 500^{o}C (Allen and Crawford, 2007; Murty and Charit, 2008). The structural materials employed in LFRs and SFRs must withstand significantly higher temperatures, radiation doses, and corrosive environments. Therefore, comprehensive studies are being performed worldwide to evaluate the compatibility of candidate fuel and structural materials with sodium and lead coolants in Gen-IV reactors. These studies involve testing candidate materials under various operational conditions using self-contained in-pile and out-of-pile test loops (Takahashi et al., 2002; Crawfort et al., 2007).

In-pile test loops are specifically designed to simulate the extreme conditions encountered within a nuclear reactor (Van Tichelen et al., 2020) for testing candidate materials under a typical thermal and radiation environment by incorporating the test loop into the core of a nuclear test reactor. In-pile tests yield valuable insights into the behavior of various material and alloys in radiation environment, including corrosion, mechanical integrity, and resistance to radiation damage (Van Tichelen et al., 2020). Out-of-pile test loops for testing the materials compatibility at typical thermal, but not radiation, conditions They provide simplicity and low operation cost testing at controlled conditions to evaluate candidate materials under specific conditions such as varying temperatures, flow rates, and chemical compositions (Spencer et al., 1987). Out-of-pile tests are instrumental in investigating material compatibility and performance across a wide range of operating parameters. They also facilitate long-term testing to assess material degradation and aging effects (Spencer et al., 1987). The data obtained from in-pile and out-of-pile testing help identity the effect of irradiation of the materials and fuel compatibility with sodium and led coolants play a crucial role in determining the materials that exhibit suitable compatibility and performance characteristics for future licensing of lead and sodium cooled reactors and ensures long-term reliability, safety, and efficient operation of Gen-IV LFRs and SFRs (IAEA, 2012; Gougar et al., 2015; McDuffee et al., 2019; Quan et al., 2020; El-Genk et al., 2020).

1.1 Research Needs

Recently, two in-pile test loops are thought to supporting the developments of molten lead and liquid sodium-cooled advanced reactors in the US and investigating their compatibility with various materials and alloys for the reactor containment and structure and cladding of fuel elements with these liquid metals at different temperatures and flow rates in a prototypical irradiation environment (Fig. 1-1) (Quan et al., 2020; Kim et al., 2022, El-Genk et. al, 2023). These test loops were to be placed at designated locations within the core of the sodium-cooled 300 MW_{th} Versatile Test Reactor (VTR) (McDuffee et al., 2019). The VTR is a one-of-a-kind facility designed for performing fast-spectrum neutron irradiation tests at elevated temperatures using self-contained test cartridges for Gen-IV nuclear reactors cooled with molten lead, liquid sodium, helium gas and molten salt (El-Genk et al. 2020; Choi et al., 2021; Roglans-Ribas et al., 2022; Farmer et al., 2022; McDuffee et al., 2022). Fig 1-1 presents a cross-sectional view of the lead loop test cartridge for investigating materials and nuclear fuel compatibility at typical temperature and irradiation condition in the VTR (Kim et al. 2022; El-Genk et al. 2020, 2023).

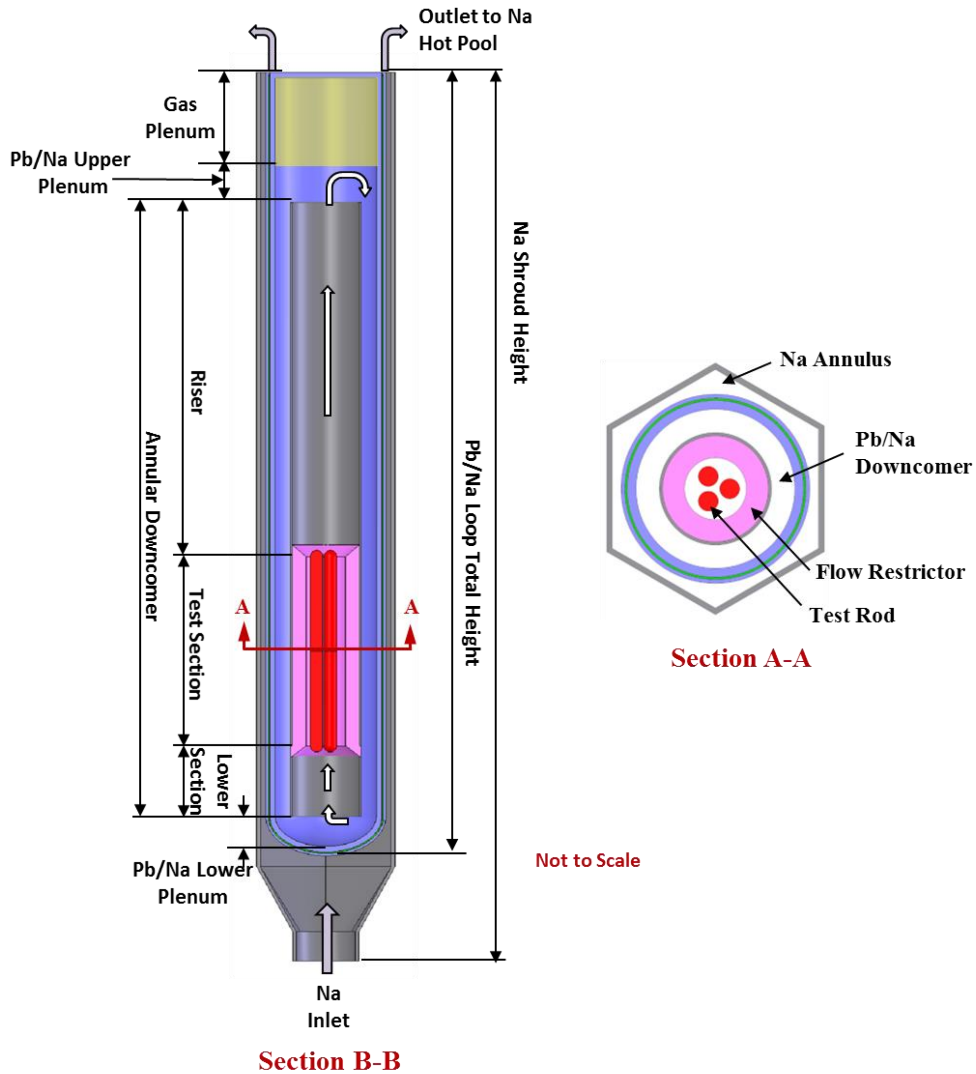

Figure 1-1: Sectional views of the VTR Extended Length Test Assembly-Cartridge Lead (ELTA-CL) (El-Genk et al., 2020, 2023).

Key requirements for the molten lead and liquid sodium test loops are the selection of methods for circulating these coolants through the nuclear fuel test article or test section and rejecting fission heat (e.g., Fig. 1-1). The circulated liquid metals in the loops remove the heat generated in the test article, preventing localized hotspots, and maintaining thermal stability. An attractive option for circulating molten lead and liquid sodium within the VTR in-pile test loops is to employ miniature submersible electromagnetic pumps (EMPs). They offer the advantages of passive operation, sealed structure, absence of moving parts, low maintenance, and high operational reliability. However, these pumps need to fit within the riser tube of the test loop of a few inches in diameter, either upstream or downstream of the test article of one or more nuclear fuel rodlets. Only a limited number of submersible EMPs have been designed for circulating liquid metals at high operating temperatures, however, they are large to be used in self-enclosed in-pile and out-of-pile test loops (Johnson, 1973; Ota et al., 2004; Polzin and Godfroy, 2008; Polzin et al., 2010; Nashine et al., 2020). Therefore, there is a need to develop miniature submersible EMPs for in-pile and out-of-pile test loops investigating nuclear fuel and structure materials compatibility with molten lead and sodium under prototypical temperatures and radiation environments.

1.2 Research Objectives

The objectives of the research performed in this dissertation are develop miniature submersible EMP designs for circulating molten lead and liquid sodium in out-pile and in-pile test loops at $\leq 500^{o}$C. At this temperature, 316SS cladding and structure is suitable choice, but not at higher temperatures. The three-fold objectives are to:

1. Develop designs of miniature, submerged, dual-stages DC-EM pumps, with appropriate selections of materials, for circulating molten lead and liquid sodium at $\leq 500^{o}$C in test loops to support of materials and fuel developments for Gen-IV sodium and molten lead fast nuclear reactor. The developed pumps are 57 mm, 66.8 mm, 95.4 mm, and 133.5 mm to fit into 2-inch, 2.5-inch, 3.5-inch, and 5-inch standard tube diameters for the test loops. The developed DC-EMP designs employ two Alnico 5 permanent magnets with Hiperco-50 pole pieces for focusing magnetic field in flow duct. The performance of these pumps is calculated using the Equivalent Circuit Model (ECM) (Altamimi and El-Genk, 2023) linked to the Finite Element Method Magnetics (FEMM) software in MATLAB platform. Calculated results for molten lead and liquid sodium include the pump characteristics, cumulative pumping power and efficiency as functions of flow rate and at different temperatures.
2. Perform 3-D, Magnetohydrodynamic (MHD) numerical analyses of the developed 66.8 mm diameter submersible dual-stages DC-EMP for circulating molten Pb and liquid Na at 500^{o}C. The coupled electromagnetism, and momentum and energy balance equations are solved using the capabilities of Star-CMM+ commercial software (Siemens, P.L.M., 2018) to calculate the pump characteristics and 3-D distributions of the flow, electric current and magnetic field flux density, and the Lorentz force density in flow duct. The Grid Convergence Index (GCI) criterion is

used to confirm the adequacy of numerical mesh refinement employed in the MHD analyses and confirm the results conversion. and

3. Develop a 66.0 mm diameter submersible Annular Linear Induction Pump (ALIP) design, with appropriate selections of materials, for circulating molten lead and alkali metals of sodium and sodium-potassium-78 (NaK-78) alloy at temperatures up to 500^{o}C. This is in addition to developing to developing an improved Equivalent Circuit Model for investigating the ALIP performance and validating the model predictions using reported experimental measurements by other investigators for sodium ALIP at 200^{o}C and 330^{o}C. The improved ECM is used to investigate the effects of varying terminal voltage, current frequency, winding wire diameter, center core length, the width of liquid flow annulus, and working fluid type and temperature on performance of the developed miniature ALIP design.

The next Chapter provides a background on the various technologies under consideration for Gen-IV nuclear reactors, with a particular focus on sodium and lead cooled reactors. Challenges associated with the development and licensing of these reactors and the use of test loops for addressing these challenges are also provided in this chapter. Furthermore, the next Chapter provides a comprehensive discussion of the electromagnetic pumps, including their categorization and operational principles, with specific attention given to DC-EMPs and ALIPs, and a literature review of designed and developed electromagnetic pumps for circulating liquid metals in various applications.

Chapter 3 introduces the analysis approach used the ECM for investigating the performance characteristics of DC-EMPs. An assessment of the accuracy in the ECM is also presented in this chapter.

Chapter 4 presents and discusses the design development and performance analyses of the miniature, submersible dual-stage DC-EMPs of different diameters. The results of the parametric analyses of the dimensional and electrical parameters are also presented in this chapter. The impacts of working fluid type and operating temperature on pump performance are also investigated in this chapter.

Chapter 5 details the performed 3-D MHD numerical analyses of the 66.8 mm diameter submersible dual-stage DC-EMP performance. The mathematical model, numerical modeling approach, mesh sensitivity analyses, and the verification of the model predictions are presented. The impacts of electric input current, flow rate, temperature rise in the pump duct on pump performance are investigated.

The improved ECM used for analyzing the performance characteristics of ALIP is described and validated in Chapter 6. Chapter 7 presents and discusses the design development and performance analyses of the 66.8 mm diameter submersible ALIP. The results of the parametric analyses of the effects of the dimensional and electrical parameters are also presented in this chapter. Summaries and conclusions based on the obtained research results are provided in Chapter 8, and Chapter 9 gives suggested recommendations for future work.

2. BACKGROUND

This chapter presents an overview of the various technologies under consideration for Gen-IV nuclear reactors, with a particular focus on liquid metal-cooled reactors such as LFRs and SFRs. It explores the challenges associated with the development and licensing of liquid metal nuclear reactors, highlighting the necessity of in-pile and out-of-pile test loops for material testing. The chapter describes the in-pile and out-of-pile test loops design and their utilizations in nuclear power applications. Furthermore, it provides a comprehensive discussion of the electromagnetic pumps, including their categorization and operational principles, with specific attention given to DC-EMPs and ALIPs. Lastly, the chapter includes a literature review of designed and developed electromagnetic pumps for circulating liquid metals in various applications.

2.1 Gen-IV nuclear technologies

In the contemporary world, there is a growing interest in clean and sustainable energy as we strive to mitigate the environmental impact of energy production and reduce greenhouse gas emissions. Nuclear reactor technologies, both existing and advanced, have the potential to play a pivotal role in achieving a balanced energy policy that improves the environment and effectively reduces greenhouse gas emissions. Among these technologies, Generation IV (Gen-IV) reactors with their advanced passive operation and safety features stand out as game-changers in the field of nuclear power (Locatelli et al., 2013). In the late 1990s, international collaborations were formed among countries, research institutions, and industry experts, aiming to explore and develop advanced nuclear technologies. The Generation 4 International Forum (GIF), established in 2001 by the US Department of Energy, played a crucial role in coordinating these efforts. GIF, representing governments of 13 countries where nuclear energy is a major player in the energy sector, aimed to design reactors that prioritize passive operation, safety, reliability, efficiency, waste reduction, and proliferation resistance while expanding the applications of nuclear energy beyond electricity generation (Kelly, 2014).

Various reactor concepts were considered and investigated initially by the GIF, among which, six most promising technologies have been selected as the Gen-IV nuclear reactors for focused research and development efforts (Kelly, 2014). These six advanced reactor concepts are the Sodium-cooled Fast Reactors (SFR), Lead-cooled Fast Reactors (LFR), Molten Salt Reactors (MSR), Gas-cooled Fast Reactors (GFR), Supercritical Water-cooled Reactors (SCWR), and High-Temperature Gas-cooled Reactors (HTGR) (Abram and Ion, 2008). Currently, these reactor concepts are at the forefront of research and development efforts worldwide. Depending on their respective degrees of technical maturity, Gen-IV reactors are expected to become available for commercial introduction in the period around 2030 or beyond (Kamide et al., 2021). The path from current nuclear systems to Gen-IV systems is described in a 2002 roadmap report by GIF entitled "A Technology Roadmap for Generation IV nuclear energy systems", which was later updated in 2013 to account for the progress done during the first decade after introducing the Gen-IV reactors concept (Kelly, 2014).

Table 2-1: Main characteristics of Gen-IV nuclear reactors (Kelly, 2014).

Reactor type	**Neutron spectrum**	**Coolant**	**Core Outlet Temp. (^oC)**	**Fuel cycle**	**Power (Mw_e)**
VHTR	Thermal	He	900-1000	Open	250-300
GFR	Fast	He	850	Closed	1200
SCWR	Thermal/ fast	H_2O	510-625	Open/ closed	300-1500
MSR	Thermal/ fast	F/Cl salts	700-800	Closed	250-1000
SFR	Fast	Na	500-550	Closed	30-2000
LFR	Fast	Pb	480-570	Closed	20-1000

* Fl: Fluoride, Cl: Chloride

The selected Gen-IV reactor concepts rely on a variety of reactor systems, energy conversion, and fuel cycle technologies. Their designs feature thermal and fast neutron spectra, closed and open fuel cycles as well as a wide range of reactor sizes from very small to very large. Compared to previous reactors generations, Gen-IV reactors are designed to operate at higher systems temperatures (Locatelli et al., 2013). This allows for enhancing the plant efficiency and for possible plant utilization for hydrogen production. The adoption of closed fuel cycle technologies by reprocessing and recycling radioactive materials of plutonium, uranium, and minor actinides enhances the sustainability of nuclear reactors and significantly minimizes waste generation (Driscoll, 2005). Table 2-1 below summarizes the six Gen-IV reactors' main characteristics, and the remainder of this section provides a brief description of each reactor type (Kelly, 2014).

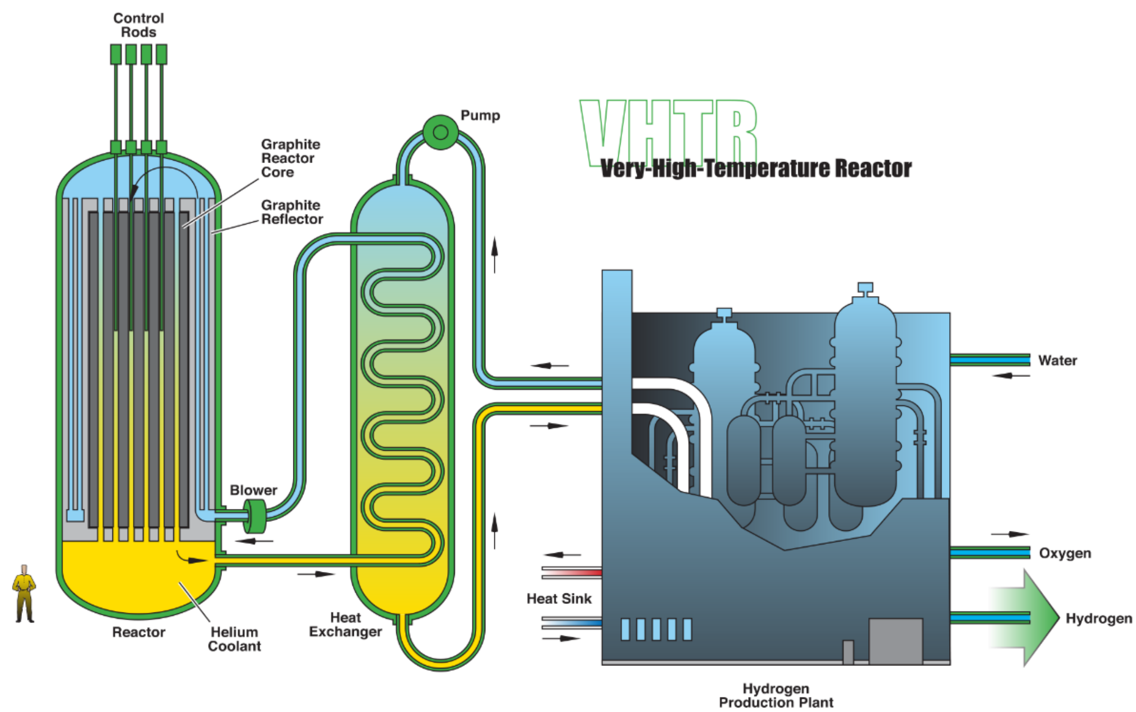

Figure 2-1: Conceptual illustration of Very High Temperature Gas Reactor (VHTR) (Kelly, 2014).

2.1.1. *Very High-Temperature gas Reactor (VHTR)*

The VHTR (Fig. 2-1) is a helium-gas-cooled, graphite-moderated, thermal neutron spectrum reactor with a core outlet temperature between 900 to 1,000^{o}C, sufficient to support high-temperature processes such as the production of hydrogen by thermochemical processes (Kadak, 2016; Zhang et al., 2019). The reference thermal power of the reactor is set at a level that allows passive decay heat removal, currently estimated to be about 600 MW_{th} (Kadak, 2016). At first, a once-through LEU (<20% 235U) fuel cycle will be adopted, but a closed fuel cycle will be assessed, as well as potential symbiotic fuel cycles with other types of reactors (especially light-water reactors) for waste reduction purposes (Kelly, 2014). Among the six Gen-IV nuclear reactors, the VHTR is primarily dedicated to the cogeneration of electricity and hydrogen, the latter being extracted from water by using thermo-chemical, electro-chemical, or hybrid processes with reduced emission of CO_2 gases. Its high outlet temperature makes it attractive also for the chemical, oil, and iron industries (Kadak, 2016).

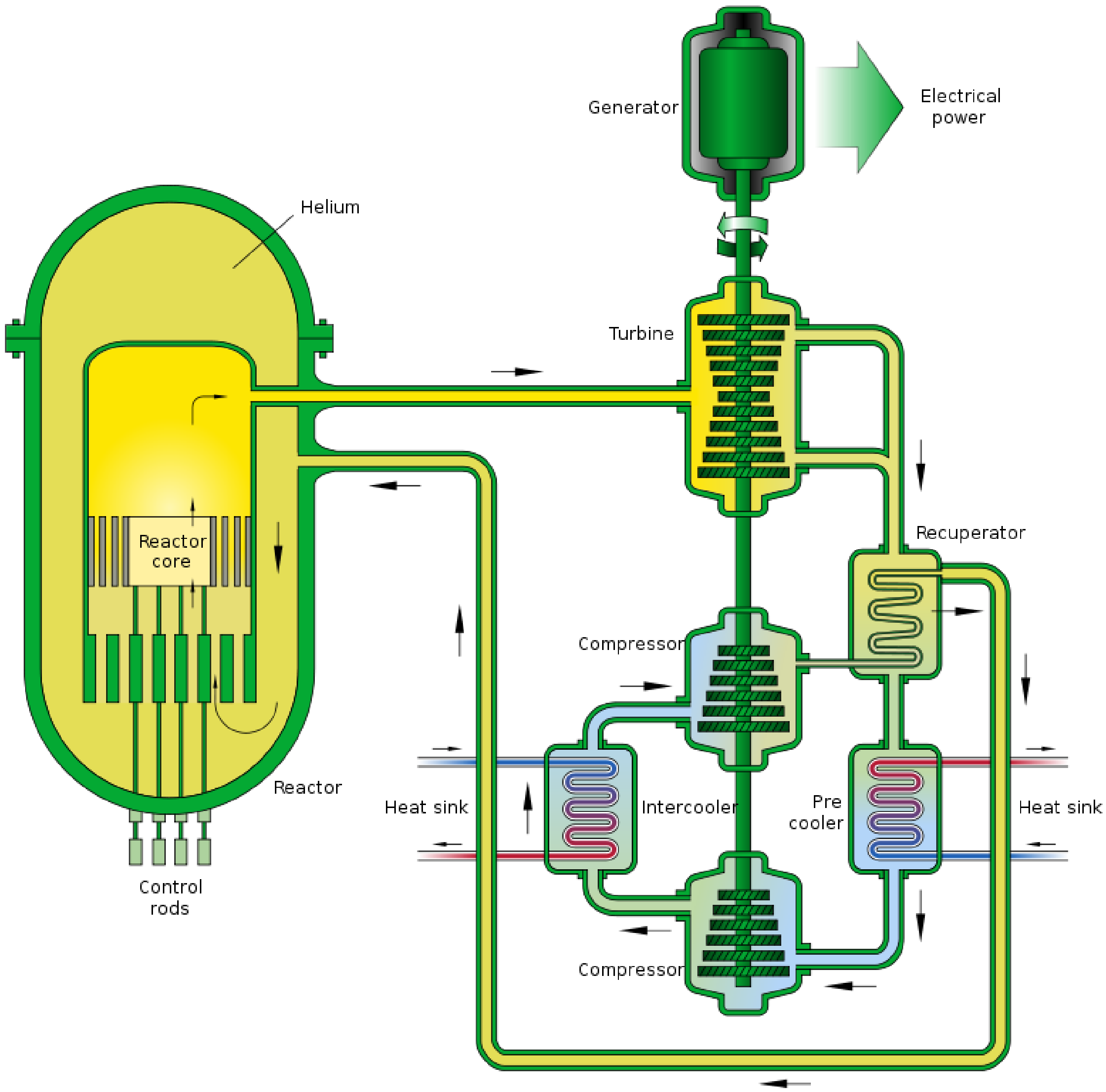

Figure 2-2: Conceptual illustration of Gas-cooled Fast Reactor (GFR) (Kelly, 2014).

2.1.2. Gas-cooled Fast Reactor (GFR)

The GFR (Fig. 2-2) is a high-temperature helium-cooled fast-spectrum reactor with a core outlet temperature in the order of 850°C. The reference design for GFR is based around a 2,400 MW_{th} reactor core contained within a steel pressure vessel (Hejzlar, 2005; Kelly, 2014). The core consists of an assembly of hexagonal fuel elements, each consisting of ceramic-clad, mixed-carbide-fueled pins contained within a ceramic hex-tube. A heat exchanger transfers the heat from the primary helium coolant to a secondary gas cycle containing a helium-nitrogen mixture which, in turn, drives a closed-cycle gas turbine. The heat from the gas turbine exhaust is used to raise steam in a steam generator which is then used to drive a steam turbine. Such a combined cycle is common practice in natural gas-fired power plants so represents an established technology, with the only difference in the GFR case being the use of a closed-cycle gas turbine (Stainsby et al., 2011).

The GFR uses a closed fuel cycle like that of the SFR and a reactor systems technology similar in the VHTR. Therefore, its development approach is to rely, in so far as feasible, on technologies developed for the VHTR for structures, materials, components and power conversion system, and the SFR on fuel reprocessing cycle. Nevertheless, it calls for specific R&D beyond the current and foreseen work on the VHTR and SFR systems, mainly on core design and safety approach (Kelly, 2014).

2.1.3. Super-Critical Water-cooled Reactor (SCWR)

The SCWR (Fig. 2-3) is a high-temperature, high-pressure water-cooled reactor operating with a direct energy conversion cycle and above the thermodynamic critical point of water at 374°C and 22.1 MPa (Rahman, 2020). The higher thermodynamic efficiency and plant simplification opportunities afforded by the high-temperature single-phase coolant translate into improved plant economics. A wide variety of reactor options are currently being considered, including those with thermal and fast neutron spectra and with either pressure vessel or pressure tubes configurations (Schulenberg, 2014).

Unlike current water-cooled reactors, the coolant in the SCWR will experience a significantly higher enthalpy rise in the core, which reduces the core mass flow for a given thermal power and increases the core outlet enthalpy to superheated conditions (Schulenberg, 2014). For both pressure vessel and pressure-tube configurations, a once-through steam cycle has been investigated. As in a Boiling Water Reactor (BWR), the superheated steam will be supplied directly to the high-pressure steam turbine and the feed water from the steam cycle will be supplied back to the core. Thus, the SCWR concepts combine the design and operation experiences gained from hundreds of water-cooled reactors with those experiences from hundreds of fossil-fired power plants operated with supercritical water (SCW). In contrast to some of the other Gen-IV nuclear systems, the

SCWR can be developed incrementally step-by-step from current water-cooled reactors (Kelly, 2014).

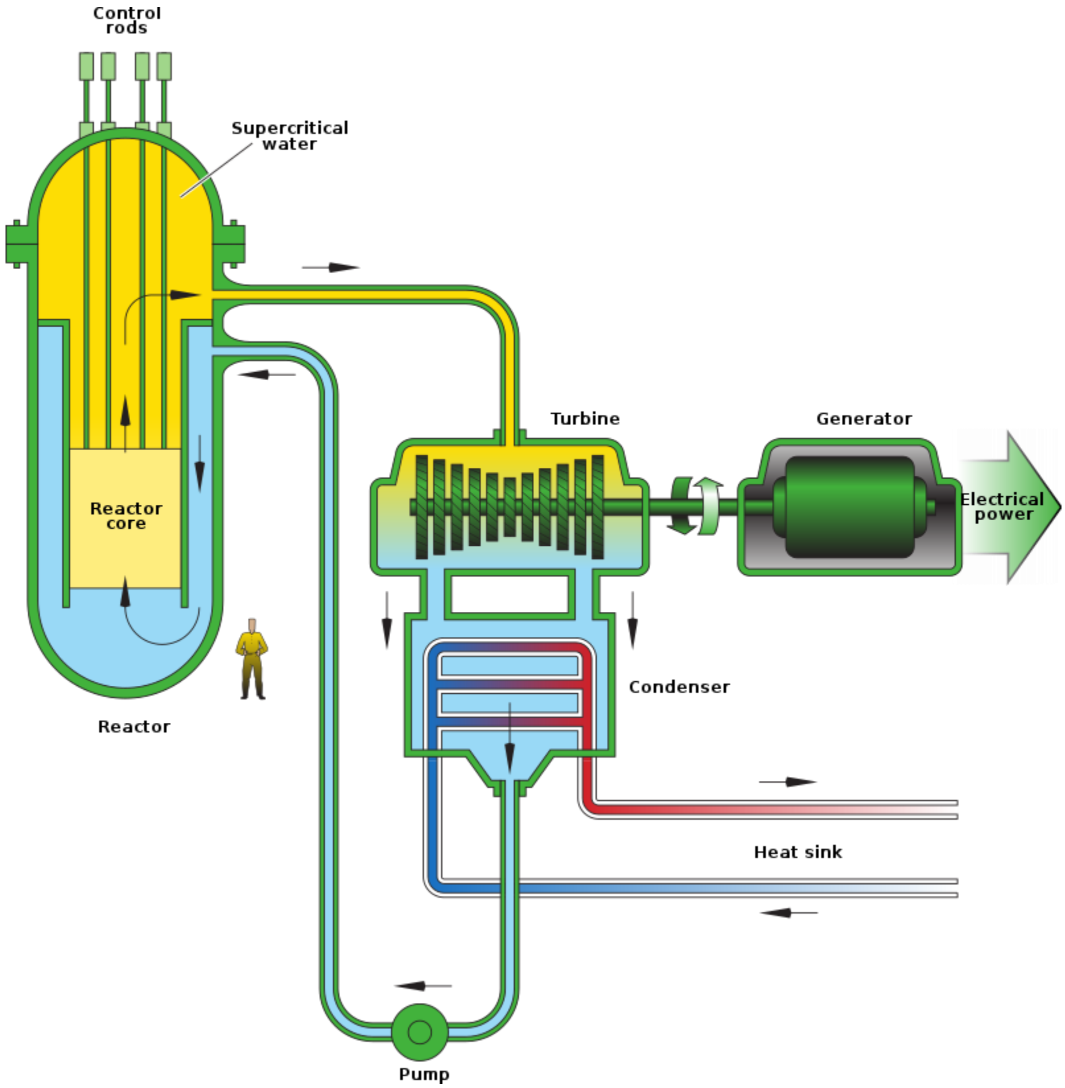

Figure 2-3: Conceptual illustration of SuperCritical Water-cooled Reactor (SCWR) (Kelly, 2014).

2.1.4. Molten Salt Reactor (MSR)

MSRs (Fig. 2-4) are an advanced type of nuclear reactor that utilizes a liquid fuel mixture of fluoride or chloride salts. These reactors offer unique advantages and capabilities compared to traditional solid-fuel reactors. In an MSR, the fuel is dissolved directly in the molten salt coolant, eliminating the need for solid fuel elements (Serp et al., 2014). This allows for continuous fuel reprocessing, improved resource utilization, and the ability to operate at high temperatures in the order of 700-800°C (Kelly, 2014; Serp et al., 2014). MSRs have inherent safety features, including passive cooling and negative temperature feedback, which contribute to their high level of inherent safety. The use of liquid fuel also enables efficient actinide burning and waste reduction, as well as the potential for a thorium-based fuel cycle. MSRs have gained significant attention due to their potential for improved safety, enhanced fuel utilization, reduced waste production, and the ability to generate both electricity and other valuable products, such as hydrogen (Renault, 2009).

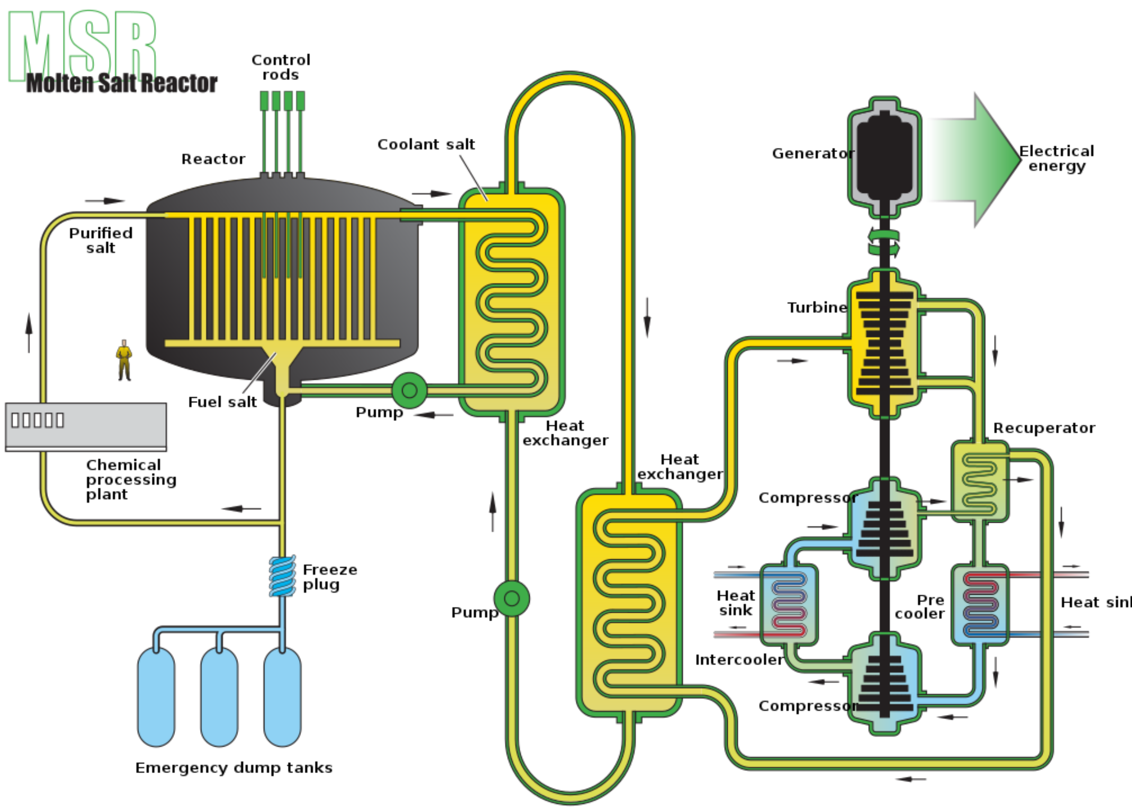

Figure 2-4: Conceptual illustration of Molten Salt Reactor (MSR) (Kelly, 2014).

Research and development efforts on MSRs have been ongoing for several decades (Renault, 2009). Building on earlier work conducted in the 1950s and 1960s, modern research has focused on developing fast-spectrum MSR concepts, such as the Molten Salt Fast Reactor (MSFR). The MSFR combines the benefits of fast neutron reactors with the advantages of molten salt fluorides as a fluid fuel and coolant. Efforts are aimed at resolving feasibility issues, such as developing effective corrosion control measures and advancing fuel reprocessing technologies. The potential of MSRs extends beyond electricity generation, as their use as burners for transuranic waste from light-water reactors and their applicability in other industrial processes, such as high-temperature applications, demonstrate their versatility (Kelly, 2014).

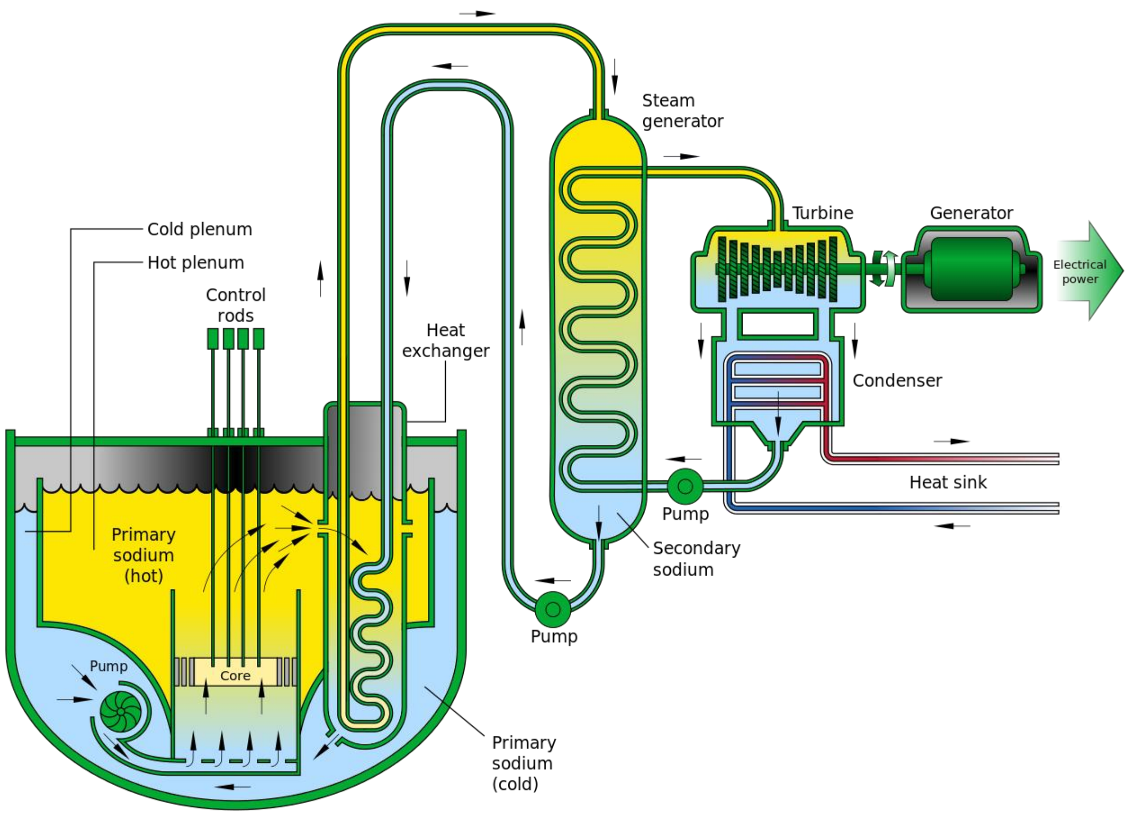

Figure 2-5: Conceptual illustration of Sodium-cooled fast reactor (SFR) (Kelly, 2014).

2.1.5. Sodium-cooled Fast Reactor (SFR)

The SFR (Fig. 2-5) is a high-temperature fast-spectrum reactor utilizing liquid sodium as a core coolant with an outlet temperature in the order of 500-550°C (Abram and Ion, 2008). These reactors operate at higher temperatures compared to conventional water-cooled reactors, allowing for improved thermal efficiency and enhanced energy production. The utilization of fast neutrons spectra enables efficient utilization of fuel and the ability to burn long-lived radioactive isotopes, including transuranic elements. By utilizing liquid sodium, SFRs offer excellent heat transfer properties, allowing for the efficient removal of heat from the reactor core to improve the thermal efficiency of the plant and fuel utilization (Ohshima and Kubo, 2016). This, in turn, facilitates the design of compact and high-power density reactor systems. In addition, sodium possesses a low neutron absorption cross-section, which allows for higher neutron flux and fuel burnup in the core and enhances the overall performance of the reactor (Wydler, 2005; Heinzel et al., 2017). SFR features a closed fuel cycle for fuel breeding and/or actinide management. The reactor may be arranged in a pool layout or a compact loop layout. The reactor-size options which are under consideration range from small (5 to 150 MW_e) modular reactors to larger reactors (300 to 1,500 MW_e). A variety of fuel options are being considered for the SFR, with mixed oxide preferred for advanced aqueous recycling and mixed metal alloy preferred for pyrometallurgical processing (Kelly, 2014).

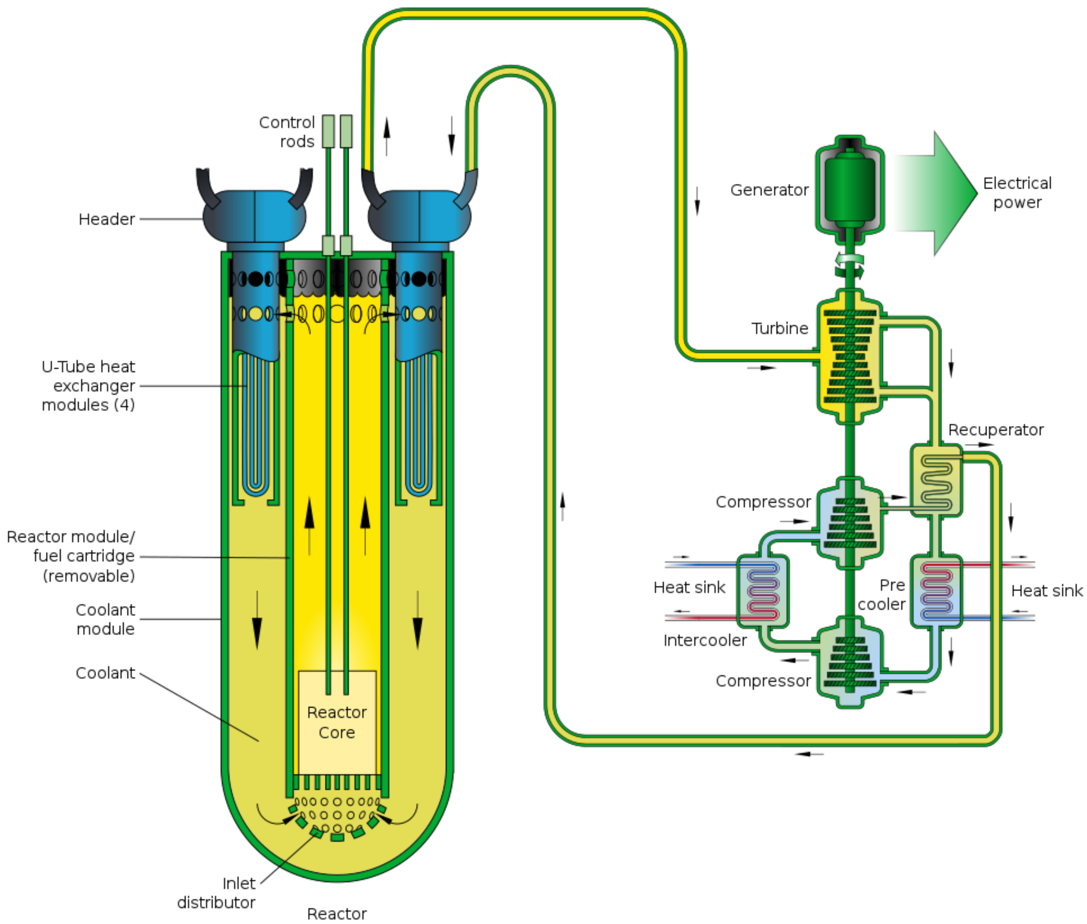

Figure 2-6: Conceptual illustration of Lead-cooled Fast Reactor (LFR) (Kelly, 2014).

2.1.6. Lead-cooled Fast Reactor (LFR)

The LFR (Fig. 2-6) is characterized by a fast-neutron spectrum and a closed fuel cycle with full actinide recycling, possibly in central or regional fuel cycle facilities. The coolant may be either lead (preferred option) or lead/bismuth eutectic. Lead has attractive thermal properties of high boiling temperature and thermal conductivity (Alemberti, 2014). This enables operation at high temperatures and enhances the heat transfer from the reactor core to improve plant thermal efficiency. In addition, lead acts as a superior radiation shield, reducing the potential for radiation leakage. Furthermore, Lead does not react with air and water in case of systems leakage. The LFR may be operated as a breeder, a burner of actinides from spent fuel, using inert matrix fuel, or a burner/breeder using thorium matrices. Two reactor size options are currently under consideration: a small 50-150 MWe transportable system with a very long core life, and a medium 300-600 MWe system. In the long term, a large system of 1,200 MWe may be envisaged (Kelly, 2014).

2.2. Recent advancements and challenges of LFRs and SFRs development

The development process of LFRs and SFRs involves a systematic approach that includes several key steps (Abram and Ion, 2008). It begins with extensive research and conceptual design studies, where various reactor configurations, core designs, and fuel options are evaluated. Following this, experimental and prototype reactors are constructed to validate the proposed designs and gather operational data (Roelofs, 2019). These reactors undergo rigorous testing and analysis to assess their performance, safety features, and fuel cycle characteristics (Wydler, 2005). Additionally, research and development efforts focus on addressing specific challenges associated with these technologies, such as corrosion issues, materials compatibility, and thermal-hydraulic behavior by performing extensive experimental testing under representative environments using self-enclosed in-pile and out-of-pile test loops. Through collaborations between industry, research institutions, and regulatory bodies, the development process emphasizes continual improvement and refinement of reactor designs, fuel cycles, and operational strategies (Abram and Ion, 2008; Roelofs, 2019).

LFRs have achieved notable progress in terms of technological development and research, positioning them as a viable option for advanced nuclear energy systems (Orlov and Gabaraev, 2023). One notable LFR design is the BREST-OD-300 reactor being pursued in Russia (Shadrin et al., 2016). BREST-OD-300 is an innovative lead-cooled fast neutron reactor that operates on a closed fuel cycle, incorporating both uranium and plutonium fuels. Extensive research has been conducted to optimize the reactor's core design, thermal-hydraulic characteristics, and safety features. The ongoing BREST-OD-300 project aims to validate the feasibility of LFR technology for large-scale deployment by demonstrating its enhanced fuel utilization, waste reduction, and safety performance (Shadrin et al., 2016).

Another significant development in LFR technology is the MYRRHA (Multi-purpose hYbrid Research Reactor for High-tech Applications) project, based in Belgium. MYRRHA seeks to establish the technical viability and versatility of LFRs through the construction of a flexible and innovative research reactor (Abderrahim, 2012). The project focuses on utilizing lead-bismuth eutectic (LBE) as a coolant and aims to serve as a platform for research in materials science, enabling the study of irradiation effects on structural materials and the development of advanced materials for high-temperature applications. It also supports the production of medical isotopes, contributing to the advancement of nuclear medicine and cancer treatment (Engelen, 2015). Extensive research efforts have been dedicated to optimizing the reactor's thermal-hydraulic behavior, addressing material corrosion and compatibility issues, and ensuring efficient and reliable heat transfer characteristics (Abderrahim, 2012; Engelen, 2015).

In Sweden, the SEALER (Swedish Advanced Lead Reactor) design is one of the innovative concepts being developed in the field of LFRs (Roelofs, 2021). The core of the SEALER reactor consists of hexagonal fuel assemblies utilizing mixed oxide (MOX) fuel containing transuranic elements, which enables efficient transmutation of long-lived radioactive waste (Wallenius, 2017). The SEALER design incorporates advanced passive safety systems to ensure inherent safety during normal and abnormal operating conditions. These safety features include natural circulation of the coolant, which eliminates the need for active pumps, as well as a negative temperature coefficient of reactivity, which causes the reactor power to decrease automatically in response to temperature increases. Ongoing research and development efforts in the SEALER project are focused on optimizing the design, improving safety aspects, and assessing the economic viability of the reactor design (Wallenius and Bortot, 2014).

In the US, the PLFR reactor, also known as the WLFR (Westinghouse Lead Fast Reactor), is an innovative lead-cooled fast reactor design that has gained significant attention in recent years (Ferroni, 2019; Liao, 2021). Developed by Westinghouse, this reactor with an electric power of 300 MW is planned to be used for several years to demonstrate and improve the LFRs technology (Ferroni, 2019; Liao, 2021).

The SFRs technology, on the other hand, has been more extensively researched and developed over the years, with a greater number of operational and experimental reactors built and tested worldwide (Aoto, 2014; Ho, 2019). This accumulated knowledge and experience have led to a better understanding of the technology and its associated challenges, paving the way for significant advancements in the fields of reactor design and safety, and materials compatibility (Aoto, 2014).

The Indira Gandhi Centre for Atomic Research (IGCAR) in India has made notable progress with the domestically designed 500 MW_e Prototype Fast Breeder Reactor (PFBR) (Kale, 2020). PFBR represents a significant advancement in SFR technology, aiming to validate the technical viability of SFRs in India. By employing liquid sodium as a coolant, the reactor demonstrates the country's commitment to achieving a closed fuel cycle while utilizing thorium resources as part of its long-term energy strategy (Kale, 2020; Rajan, 2021). Extensive research has focused on core design optimization, coolant system performance, and the development of advanced safety features to ensure the successful operation of the reactor.

Toshiba has also contributed to SFR technology with its 4S (Super-Safe, Small, and Simple) reactor design (Nobuyuki, 2005). The 4S reactor is a compact and inherently safe sodium-cooled fast reactor intended for small-scale applications, such as remote power generation or deployment in regions with limited infrastructure. Research endeavors have focused on enhancing the reactor's passive safety features, fuel performance, and compact design characteristics to ensure efficient operation and cost-effectiveness (Nobuyuki, 2005).

In Russia, OKBM Afrikantov has made significant progress with the BN-1200 reactor, a sodium-cooled fast neutron reactor based on the successful BN series (Ashurko, 2019). The BN-1200 aims to demonstrate the technical feasibility, safety, and economic viability of large-scale SFRs. Research activities have focused on optimizing core performance, addressing safety concerns, and ensuring reliable and efficient heat removal through the sodium coolant system.

China National Nuclear Corporation (CNNC) is also actively involved in SFR research and development with its CFR-600 design (Ji et al., 2021). CFR-600 is a medium-sized SFR that incorporates advanced safety features and closed fuel cycle capabilities.

Extensive efforts have been made to optimize core design, enhance fuel performance, and develop advanced control and safety systems to ensure the reliable operation of the reactor.

One prominent development of SFRs is the Natrium reactor being pursued by TerraPower in collaboration with GE Hitachi Nuclear Energy (Casella, 2022). The Natrium system is an advanced SFR that integrates a fast reactor with a molten salt energy storage system. This innovative design aims to provide flexible and dispatchable power generation while enabling the storage and utilization of excess electricity. Extensive research and development efforts have focused on optimizing the reactor's core design, fuel performance, and sodium coolant system to enhance its safety, reliability, and efficiency (Bragg-Sitton, 2022).

The collective progress made in these LFRs and SFRs designs, and research projects highlight the significant advancements and potential of these reactors. However, the utilization of lead and sodium in LFRs and SFRs designs concepts introduces material compatibility challenges that necessitate thorough testing and evaluation of candidate fuel and structure materials (Murty and Charit, 2008; Yvon and Carre, 2009). The structural materials employed in LFRs and SFRs must withstand significantly higher temperatures and radiation doses. Furthermore, liquid metals of sodium, lead, and their alloys, have unique chemical properties that can interact with fuel cladding and structural materials, potentially causing corrosion, embrittlement, and other forms of degradation (Allen et al., 2010). To address these challenges, a rigorous testing process is employed, which involves testing the candidate fuel and structure materials at different operational environments of high temperature, radiation flux, and flow rates in self-enclosed in-pile and out-of-pile test loops (Takahashi et al., 2002; Crawfort et al., 2007).

2.3. In-pile and out-of-pile liquid metal test loops

In-pile test loops are designed to simulate the extreme conditions experienced within a nuclear reactor (Van Tichelen et al., 2020). By placing candidate materials near a neutron source within the core of a nuclear research reactor, these test loops assess how the materials perform under irradiation. The materials are subjected to high temperatures, neutron flux, and the corrosive environment of the liquid metal coolant. In-pile tests provide valuable insights into the material's behavior, including corrosion resistance, mechanical integrity, and resistance to radiation damage.

On the other hand, out-of-pile test loops are installed outside the reactor environment. These tests allow for a more controlled assessment of candidate materials under specific conditions, such as varying temperatures, flow rates, and chemical compositions (Spencer et al., 1987). Out-of-pile tests are valuable for investigating material compatibility and performance over a wide range of operating parameters. They can also facilitate long-term testing to evaluate material degradation and aging effects (Spencer et al., 1987).

Both in-pile and out-of-pile test loops involve monitoring key material parameters, such as corrosion rates, mechanical properties, and changes in microstructure (Takahashi et al., 2002). The data obtained from in-pile and out-of-pile testing is critical for identifying and licensing materials that exhibit suitable compatibility and performance characteristics for liquid metal environments in nuclear power applications. This information supports the long-term reliability, safety, and efficient operation of advanced nuclear reactor designs (IAEA, 2012; Gougar et al., 2015; McDuffee et al., 2019; Quan et al., 2020; El-Genk et al., 2020).

A critical component of these test loops is the circulation pumps, which drive the flow of liquid metals within the loops. These pumps play a key role in removing heat from the test article, preventing localized hotspots, and maintaining thermal stability. They also ensure consistent and representative flow conditions for the tested materials, ensuring exposure to realistic operating environments (El-Genk et al., 2023). Electromagnetic pumps are a promising option for circulating these liquid metals due to their passive operation, sealed structure, absence of moving parts, low maintenance requirements, and high operational reliability (Altamimi and El-Genk, 2023). It is important for these pumps to have a compact design to fit within the limited space of the test loop and to utilize compatible components that can withstand the desired operating temperatures.

2.4. Electromagnetic Pumps

Electromagnetic pumps utilize the fundamental principles of electromagnetism to passively circulate liquid metals (Barnes, 1953). These pumps harness the interaction between electric currents and magnetic fields, to produce Lorentz force to propel the fluid of choice in the perpendicular direction to that of both the electric current and the magnetic field flux density in the pump duct (Fig. 2-7). Unlike mechanical pumps, electromagnetic pumps do not have moving parts, making them more reliable with much less maintenance requirements. These pumps are also hermetically sealed. Their applications span a wide range of applications, including but not limited to nuclear reactors and test loops, metals mining and industrial processes, and solar energy (Baker and Tessier, 1987). These pumps offer enhanced control over fluid flow, precise manipulation of flow rates, and improved safety measures. Consequently, electromagnetic pumps demonstrate promising potential as a solution for diverse pumping requirements.

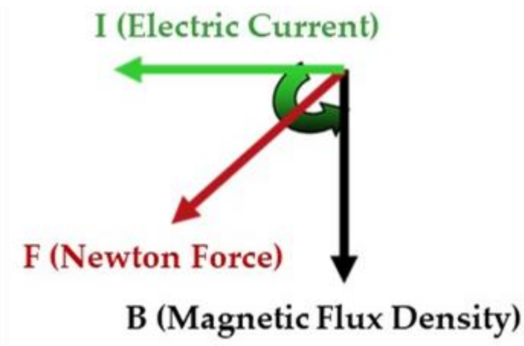

Figure 2-7: Relation of Electromagnetic pump's electric, magnetic, and Lorentz force vectors (Altamimi and El-Genk, 2023).

2.4.1. Classification of electromagnetic pumps

The electromagnetic pump encompasses various types, each distinguished by unique characteristics that should be carefully considered for use in different applications. These characteristics include the source of electric current in the working fluid (conducted through an electrode or induced by traveling magnetic fields), the type of pump's input current (AC or DC), the shape of the flow path (flat, annular, etc..), and the method of magnetic field generation (permanent magnet or electromagnet) (Baker and Tessier, 1987). The size and output capacity of electromagnetic pumps can range from small laboratory pumps to large pumps employed in heavy metals and liquid metals cooled fast reactor nuclear reactors (Al-Habahbe et al., 2016).

Electromagnetic pumps are classified into two primary categories (Fig. 2-8): conduction pumps and induction pumps. Conduction pumps directly supply current to the liquid metal from the power source through current electrodes, while induction pumps induce a current in the liquid metal through transformer action using a traveling magnetic field. Conduction electromagnetic pumps can be further categorized as DC and AC types based on the input current type and their structural design. DC conduction pumps can be either electromagnet based, or permanent magnet based, depending on the approach employed to generate the magnetic field (Baker and Tessier, 1987).

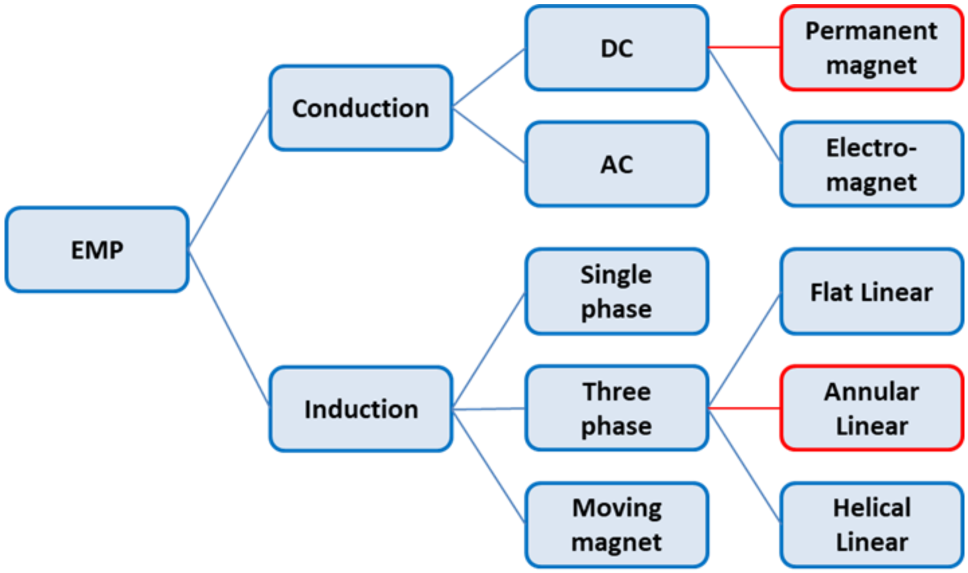

Figure 2-8: Classification of electromagnetic pumps (Baker and Tessier, 1987).

In contrast, induction electromagnetic pumps differ in the method used to generate the magnetic field (Fig. 2-8). Moving magnet induction pumps employ a moving permanent magnet to create a progressing magnetic field, while stationary magnet induction pumps utilize a fixed electromagnet of coils and stators. Stationary magnetic induction pumps can be classified as three-phase or single-phase, depending on the number of phases of the input current. Three-phase pumps can be further divided into FLIP and ALIP, distinguished by the type of duct that covers the flow path. Additionally, a helical linear induction electromagnetic pump exists, which forms a spiral flow path (Blake, 1957).

This study concentrates on permanent magnet DC-Electromagnetic Pumps (DC-EMP) and Annular Linear Induction Pumps (ALIP) as the primary focus. These pump types are specifically suitable to be designed and developed for the installation and use in in-pile test loops, where pump size plays a crucial role. Furthermore, these pump types offer the advantage of employing diverse component materials that are well-suited for operating at elevated temperatures of 500°C and are compatible with liquid metals of lead and sodium. The next sections will describe the operation principles of DC-EMP and ALIP and provide a literature review of their design and utilization for circulating liquid metals in nuclear power-related applications.

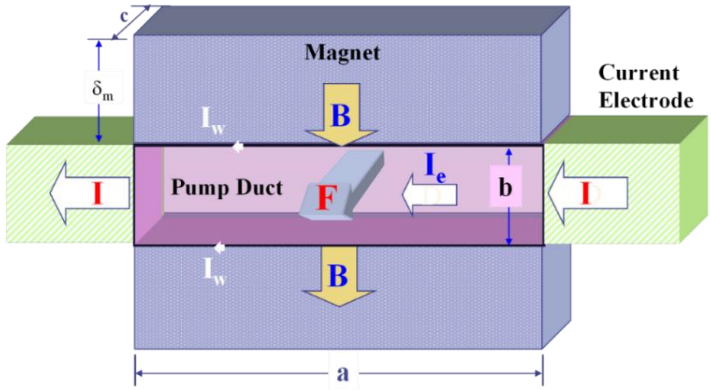

Figure 2-9: A schematic of the operation principle of a DC- EMP (Altamimi and El-Genk, 2023).

2.4.2. Operation Principle of DC Conduction EM Pumps

A DC-EMP propels the flow of an electrically conductive liquid through a rectangular duct by utilizing the generated Lorentz force (F_L) perpendicular to both the magnetic field flux density (B) and the DC electrical current (I) within the flow duct (Fig. 2-9), with a magnitude of F_L= $I_e x B$ (Barnes, 1953). The magnetic field flux density (B) is produced by a pair of rectangular permanent magnets oriented in a similar magnetizing direction (Fig. 2-10a), or alternatively, a horseshoe-type magnet (Fig. 2-10b) positioned on the wide sides of the flow duct (ac), while the electrical current is supplied by two electrodes located on the narrow sides of the duct (bc) (Fig. 2-9). The resulting pumping pressure (ΔP_P) across the flow duct is equivalent to the generated Lorentz force (F_L) divided by the area of the pump duct flow (a x b), ΔP_P= F_L/(a b) = $I_e x B$/b (El-Genk and Paramonov, 1994).

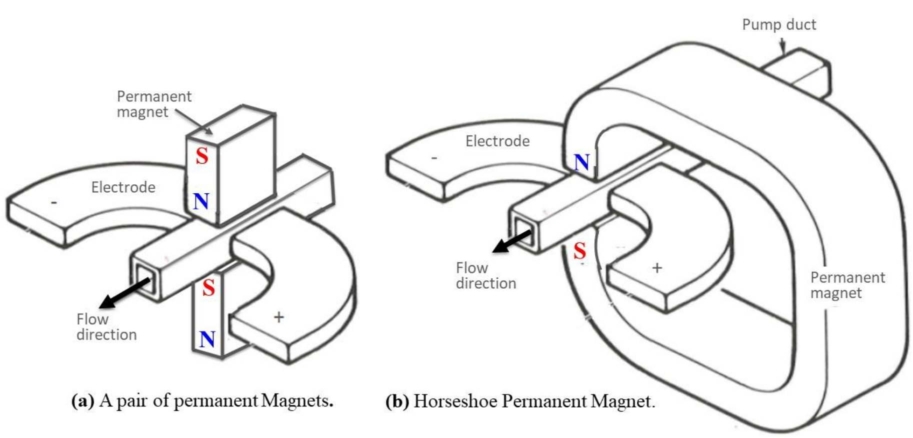

Figure 2-10: Shapes of Permanent magnets for DC-EMPs (Kim et al., 2014).

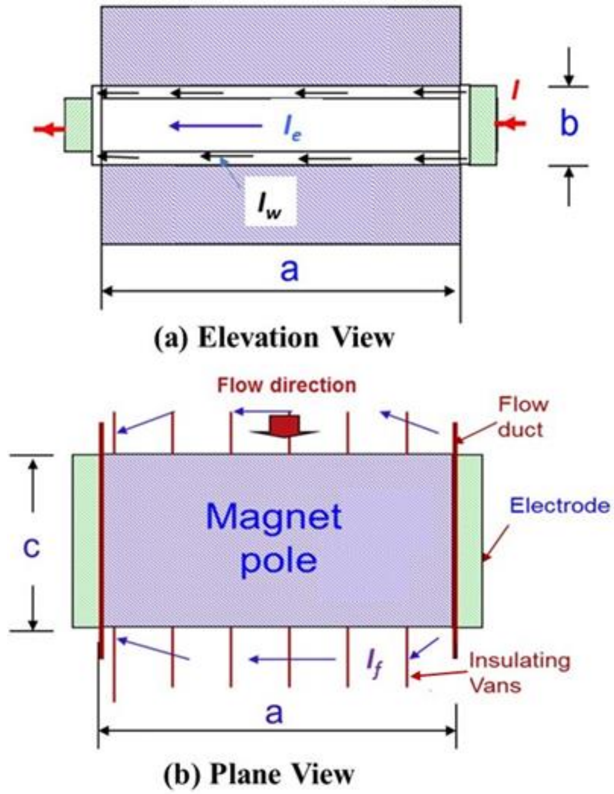

Figure 2-11: Cross-sectional views of a DC-EMP and an illustration of the electrical current components in the pump (Altamimi and El-Genk, 2023).

In an ideal DC-EMP, the supplied current (I) flows uniformly through the working fluid within the flow duct, as does the magnetic flux density. However, this is not the case. The electric current (I) supplied by the electrodes consists of three components: (a) the effective current (I_e), which interacts with the magnetic flux (B) to generate the Lorentz force in the flow duct, (b) the current that passes through the duct walls, I_w, (Fig. 2-11a), and (c) the fringe currents, I_f, flowing upstream and downstream of the duct region (Fig. 2-11b) (El-Genk and Paramonov, 1994). The wall and fringe currents (I_w and I_f) do not contribute to the generation of the Lorentz force for propelling the liquid metal flow through the pump duct. Similarly, only a fraction of the magnetic field flux density contributes to the Lorentz force generated within the pump's flow duct.

The movement of the liquid in the duct, perpendicular to the applied magnetic field, induces an opposing electromotive force, emf (E_i), which diminishes the effective current within the pump duct (I_e) and increases the wall and fringe currents (Fig. 2-11). The magnitude of the induced emf, E_i, depends on the flow rate, magnetic flux density, and pump duct height (Baker and Tessier, 1987). The induced emf is considered a source of performance reduction of DC-EMP. Another source of performance reduction in the DC-EMP is caused by the armature effect, which arises from the induced magnetic field when the conductive fluid carries the current (Baker and Tessier, 1987). This induced magnetic field leads to an increase in the magnetic flux density at the upstream end of the pump and a decrease at the downstream end, directly proportional to the pump current. This non-uniform magnetic field distribution results in an uneven allocation of the Lorentz force and pumping pressure throughout the pump duct. Consequently, the efficiency of the electromagnetic pump is significantly diminished (Altamimi and El-Genk, 2023).

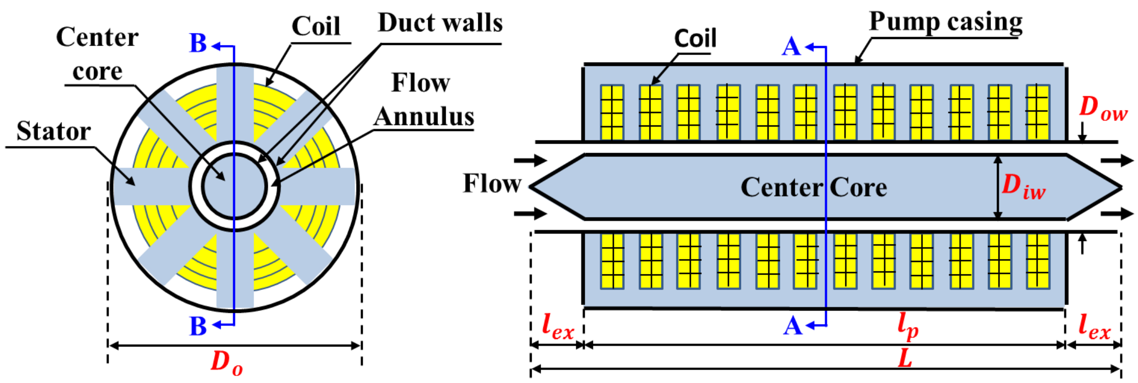

(a) ALIP radial cross-section view A-A (b) ALIP axial cross-section view B-B

Figure 2-12: Radial and Axial cross-section views of Annular Linear Induction Pump showing main pump components (El-Genk et al., 2020).

2.4.3. Operation Principle of Annular Linear Induction Pumps

An ALIP consists of two major parts, an electromagnetic and an annular duct for the flow of an electrically conductive fluid (Fig. 2-12). The electromagnetic part consists of a laminated center core, stators, and winding coils of 3-phase alternating current conductors with electrical insulation (Fig. 2-12) (Nashine and Rao, 2014). The stator is made using laminated E-shaped metal sheets possessing high magnetic permeability, curie temperature, and saturation magnetic field flux density (Baker and Tessier, 1987). These sheets are stacked together with insulation in between. The cylindrical center core of the electromagnetic part is also made of laminated metal sheets stacked radially, with cone-shaped extensions for guiding the working fluid into and out of the annular flow region. The winding coils, made of highly conductive materials, such as copper, are electrically insulated using ceramic materials to withstand high temperatures (Baker and Tessier, 1987).

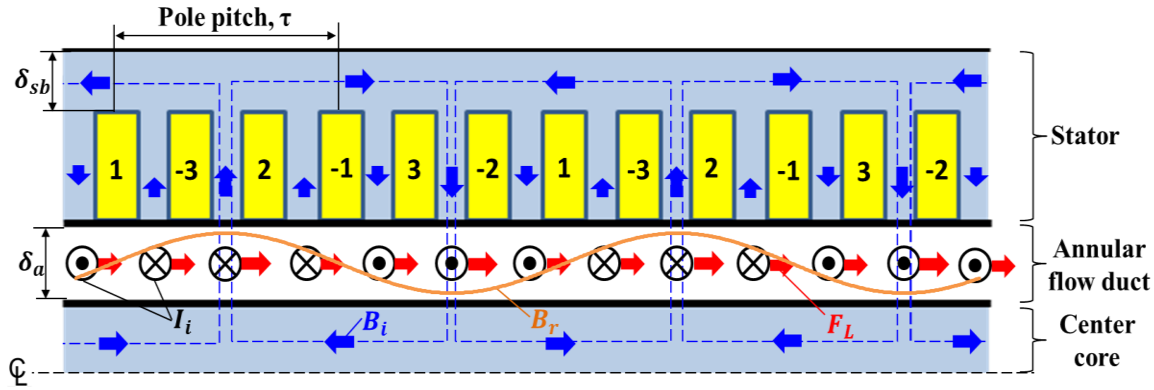

Figure 2-13: Schematic cross-section view illustrating the operation principle of an ALIP (Baker and Tessier, 1987).

An ALIP is powered by the symmetric 3-phase alternating currents, with a 120° phase shift, through the winding coils with a 60° shift between neighboring coils (Fig. 2-13 and 2-14). The current flow in each of the winding coils produces a magnetic field, B_i, which surrounds the coils and travels radially through both the stator tooth and annular flow duct, and axially through the stator back and the center core, which serves as a return path of the magnetic field (Momozaki. 2016).

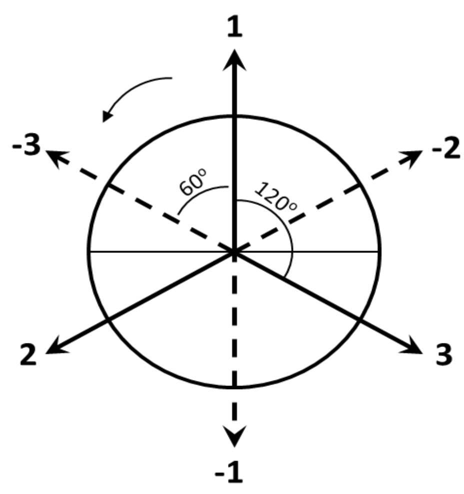

Figure 2-14: Phase relationship of the coil connection with 3-phase power (Baker and Tessier, 1987).

The produced sinusoidal magnetic fields by the winding coils, B_r, in the annular flow duct (Fig. 2-13) travels axially along the flow duct with time commensurate with the frequency of the supplied alternating current in the winding coils. According to Faraday's law of electromagnetic induction, the traveling magnetic fields produce eddy currents, I_i, in the walls of the flow annulus and the fluid in it (Baker and Tessier, 1987). These traveling currents in the circumferential directions create secondary magnetic fields that oppose the main traveling magnetic field in the flow duct (Fig. 2-13). The interaction of the circumferentially traveling induced currents and the radially traveling magnetic fields in the flow duct generates Lorentz forces, F_L, in the perpendicular direction, driving the working fluid in the annular flow duct (Fig. 2-13).

In the ALIP, the magnetic poles, which have the same length (τ), are defined based on the direction of the radially traveling magnetic fields through the flow duct. The magnetic field produced by one pole travels from the center core toward the stator, while the field produced by the other pole travels in the opposite direction, from the stator toward the center core (Fig. 2-13). These pole pairs are periodically repeated along the axial direction of the flow, with each repetition occurring after a 360° shift in the winding coils (Fig. 2-13). The induced electrical currents within the flow duct caused by the first pole type travel in a counterclockwise direction, while those induced by the other pole type travel in a clockwise direction (Momozaki. 2016). Despite the opposite directions of the magnetic fields and induced electrical currents for the two pole types, the resulting Lorentz forces, following Fleming's right-hand rule, are in the same direction as the fluid flow (Fig. 2-15). The sum of the Lorentz forces in all pump poles generates the pumping pressure required to move the working fluid within the annular duct of the ALIP (Baker and Tessier, 1987).

Pole 1: *B* travels radially towards the stator and *I* travels circumferentially in counter-clockwise direction

Pole 2: *B* travels radially towards the center core and *I* travels circumferentially in clockwise direction

Figure 2-15: Directions of generated Lorentz force in the flow annulus for the two ALIP magnetic pole types following Fleming’s right-hand rule (Baker and Tessier, 1987).

Varying the terminal voltage and the electrical current frequency changes the magnitude of the generated Lorentz force and hence, the pumping pressure, which both are directly proportional to the applied terminal voltage and inversely proportional to the frequency of the supplied electrical current. A desirable ALIP feature is that flowing liquid metal does not directly contact any parts of the pump, except the walls of the annular flow duct. Furthermore, the absence of moving parts increases the reliability and robustness, and with a hermetical seal, improves the operation safety of the ALIP. The next section will provide a literature review of designed and developed electromagnetic pumps of DC-EMP and ALIP types for circulating liquid metals in various applications.

2.4.4. A review of EM pumps uses.

Small size DC-EMPs with either permanent magnets or self-induced electromagnets have and are being considered for space reactor power systems and in-pile and ex-pile liquid metals test loops for investigating material compatibility (Watt et al., 1958; Johnson, 1973; El-Genk, 2009; IAEA, 2013). Large DC-EMPs, with electromagnets, have been used to circulate alkali and heavy liquid metal coolants in nuclear reactors and various industrial applications (Daoud and Kandev, 2008; IAEA, 2008; Deng et al., 2013; IAEA, 2020). Small DC-EMPs with thermoelectric energy conversion elements for DC power generation had been used for circulating liquid NaK-78 at 543 ^{o}C in the primary loop of the SNAP-10A space nuclear reactor power system launched by the United States in 1965 (Perlow, 1964; Davis, 1966) and for circulating molten lithium in the US SP-100 nuclear reactor power system (Wright, 1985; El-Genk and Rider, 1990; Mondt et al., 1994).

The DC-EM for the SNAP-10A power system had two Alnico 5 horseshoe magnets with iron pole pieces that generated a magnetic field flux density of 0.24 T (Davis, 1966). The magnet's temperature was maintained below 298^{o}C using radiative cooling into space. A radiator with aluminum fins also rejected the waste heat from the thermoelectric elements for the pump into space. The NaK-78 flow duct of the SNAP-10 A pump was 25.4 mm wide, 87.6 mm long, and 10.16 mm high. This pump produced a pumping pressure of 7.58 kPa at a flow rate of 3 m^3/h and electrode current provided by thermoelectric elements was 534 A at a terminal voltage of 0.32 VDC.

Johnson (1973) has designed and measured the performance of a double-throat DC-EMP for circulating liquid NaK-78 in space nuclear reactor power systems at 316^{o}C. The pump's Alnico 5 magnets with hiperco-50 pole pieces and an iron yoke provided a magnetic field flux density in the pump duct of 0.235T. The pump duct was 12.7 mm high, 24.9 mm wide, and 58.4 mm long. At an electrode current of 1,570A, the pumping pressure at a volumetric flow rate of 6.3 m^3/h was 14.5kPa. Polzin and Godfroy (2008) have designed and evaluated the performance of a DC-EMP for circulating NaK-78 at temperatures up to 607^{o}C in a test loop in support of NASA's effort to develop affordable Fission Surface Power (FSP) systems to use on the lunar surface. The selected high strength Neodymium magnets for this pump have a low curie point of 80 - 100^{o}C. The pump flow duct was 1.59 mm high, and 95 mm wide and long. The FluxTrol pole pieces of the magnet helped focus the magnetic field flux density in the flow duct and minimize losses to the surroundings. They used a water-cooled copper block to maintain the magnet's temperature below its curie point. At an electrode current of 110A and terminal voltage of 0.02 VDC, the performed analysis of the pump showed a uniform magnetic field flux density of 1.05 T in the flow duct and predicted a pumping pressure of 34.5 kPa at a Nak-78 volumetric flow rate of 0.114 m^3/h.

Kim et al. (2014) have designed a DC-EMP for circulating liquid sodium to remove the decay heat from a Prototype Gen. IV Sodium-cooled Fast Reactor (PGSFR). The pump is to operate at 195^{o}C and employs a samarium-cobalt permanent magnet with a soft iron yoke to generate a magnetic field flux density of 0.134T in the flow duct, 150 mm wide, 74.8 mm long, and 20.8 mm high. At an electrode current of 5,671A and a terminal voltage of 0.106 VDC, they predicted a pump efficiency of 8.31%, and gross and net pumping pressures of 14.34 KPa and 10.0 kPa, respectively, at a sodium flow rate of 18 m^3/h.

Lee and Kim (2017) have designed and fabricated a much smaller DC-EMP with a samarium-cobalt permanent magnet for circulating liquid sodium in an experimental test loop at 300^{o}C. The pump flow duct was 38.4 mm wide, 1.8 mm high, and 90 mm long. At electrode currents of 116 A, they predicted a net pumping pressure of 5 kPa at a sodium flow rate of 0.18 m^3/h and a pump efficiency of 27.2%. Most recently, Lee and Kim (2018) developed a small DC-EMP for circulating liquid lithium in a heavy-ion accelerator at 200^{o}C and a flow rate of 6 cm^3/s. The pump flow duct was 1.0 mm high, 22 mm wide, and 216 mm long. At an electrode current of 3,740 A, the pump provided a net pumping pressure of 1.5 MPa at a rate of 6 cm^3/s.

Table 2-2 lists different developed permanent magnets DC-EMP designs for circulating liquid metals. In summary, reported permanent magnet DC-EMPs have been designed and employed for circulating alkali liquid metals of sodium, NaK-78, and lithium at temperatures ranging from 196 to 607°C. External cooling by radiation into space or forced convection has been employed to maintain the magnet temperature below a set point lower than their curie points. Radiatively cooled DC-EMPs have been used and considered in space nuclear reactor power systems. The reported pump designs for circulating liquid metals for decay heat removal systems, heavy-ion accelerators, and out-pile test loops, are actively cooled by forced and natural convection of either air or water.

ALIPs have long history of development and use in circulating liquid metals for nuclear power applications, including Space Reactor Powers Systems (SRPS) (Polzin, 2010; Geng and Reid, 2016), nuclear power plants (Ota et al., 2004; Aizawa et al., 2011; IAEA, 2018; Nashine et al., 2020), and LM experimental facilities used to support compatibility investigations of candidate high-temperature materials for advanced reactors concepts (Baker et al., 1983; IAEA, 2013; Locatelli, 2013; Nashine and Rao, 2014; Kim, 2014; Kwak and Kim, 2019; Mignot et al., 2019).

Nashine and Rao (2014) have designed and tested an ALIP for circulating liquid sodium at 350°C in a Steam Generator Test Facility (SGTF) used for supporting the development of the Indian prototype Fast Breeder Reactor (FBR). The ALIP was designed using the equivalent circuit approach and adopted reflux-type EMP where the sodium inlet and outlet are both located on one side. The designed pump used forced air cooling to maintain its coil temperature between 100 to 120°C and has an outer diameter of 59cm, a total length of 93cm, and an annulus flow channel width of 1.05 cm. The pump was tested at a 360V line voltage and a current frequency of 50Hz to provide a net pressure head of 394 kPa at a flow rate of 125 m^3/h and an efficiency of 18%. The comparison between the experimentally obtained net pressure head and the theoretical predictions using the equivalent circuit approach showed the latter overestimates reported measurements by about 25%.

Kwak and Kim (2019) have designed and fabricated an ALIP for circulating liquid sodium in Prototype Generation-IV Sodium-cooled Fast Reactor (PGSFR) with an electric power of 150 MWe currently under development in Korea. The pump was designed using the equivalent circuit approach and its performance evaluation was conducted in a thermal-hydraulics test loop for circulating sodium at 340°C the pump operated using 5 pole pairs and had an outer diameter of 46cm, a center core length of 120cm, and an annulus flow channel width of 1.22cm. A net pumping pressure of 400 kPa at a sodium flow rate of 85 m^3/h and efficiency of 25% was obtained when supplying 391 VAC at a frequency of 60Hz. The comparison between the experimentally obtained net pumping pressure and the theoretical predictions using the equivalent circuit approach showed that the latter consistently overestimates the pump performance by up to 16%.

For space nuclear reactor power applications, Polzin et al., (2010) have designed and tested an ALIP for circulating liquid Nak-78 in the Affordable Fission Surface Power (AFSP) system developed by NASA for potential deployment on the lunar surface. The designed pump has an outer diameter of ~22cm, and a total length of ~55cm and has applied forced cooling of helium gas to mitigate the occurrence of short electrical circuits between coils conductors at high operating temperatures. The performance of the pump was tested in the Early Flight Fission-Test Facility (EFF-TF) at Marshall Space Flight Centre (MSFC), over a range of operating conditions, including NaK-78 temperatures ranging from 125 to 525 ^{o}C, input power frequencies between 33 and 60 Hz, and pump line voltages from 5 to 120 V. The maximum efficiency measured during testing was around 6% when the pump operated at 120 V and 125^{o}C. The net developed pressure measured during the test varied between < 1 to 90 kPa with flow rates of up to 20.5m^3/h.

Work was also done on designing and constructing ALIPs for operating submerged in working fluid at high temperatures without active (external) cooling. Ota et al., (2004) have designed and tested a large capacity submersible, self-cooled ALIP for circulating liquid sodium in a 600MWe Japanese Fast Breeder Reactor (FBR) with the potential of improving plant reliability and economic performance. The submersible ALIP was designed to be self-cooled by immersing into sodium and applying high-temperature electrical insulation to transfer power losses to the pumped and surrounding sodium. The outer diameter of the developed pump was 190cm and its length was 440cm, with a large annulus flow channel width of 7.7cm, allowing for a large pumping flow rate. The pump was tested in an experimental test facility for 2,550 h while operating at 452^{o}C sodium temperature, 1,350 VAC and current frequency of 20Hz. The designed pump could provide a net pumping pressure of 250 kPa at a flow rate of 9,600 m^3/h and pump efficiency of 40%. Recently, Nashine et al., (2020) have developed a submersible ALIP for draining sodium from the main vessel of Indian fast reactors if the situation warrants. The submersible pump was designed to be self-cooled by immersing into sodium and applying high-temperature inorganic mineral electrical insulation of magnesium oxide (MgO) to transfer power losses to both pumped and surrounding sodium. The designed pump had an outer diameter of 40 cm, total length of 74.4 cm, an annular flow channel that is 0.126 cm wide, and insulated coil wires 0.6 cm in diameter. The performance of the pump was measured in two arrangements; in an out-of-pile sodium test loop at 200^{o}C, and while submerged in a sodium pool at temperatures up to 550^{o}C. The designed pump provided a net pumping pressure of 400 kPa at a flow rate of 2 m^3/h with line voltage of 150V and current frequency of 50 Hz.

Table 2-3 lists different developed and constructed ALIP designs for circulating liquid metals in nuclear power-related applications. In summary, reported ALIPs have been designed and employed for circulating alkali liquid metals of sodium, NaK-78, and lithium at temperatures ranging from 125 to 550^{o}C. External cooling by gas or liquid was used for maintaining the coil's temperature below the maximum operating temperature of the conductor's insulation. External cooling is not applicable for submersible ALIPs; therefore, they require the use of high-temperature electrical insulations for coil conductors to allow self-cooling in the working fluid. Reported submersible ALIPs in the literature are relatively large in diameter with values between 40 to 190cm.

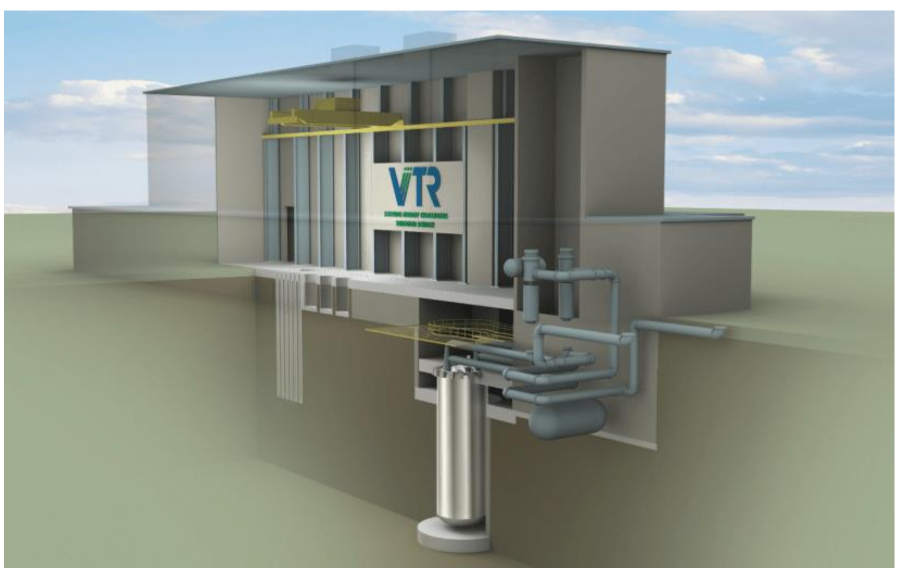

Figure 2-16: VTR facility (Roglans-Ribas et al., 2022).

2.5. US Versatile Test Reactor

In February 2017, the DOE Office of Nuclear Energy's (NE's) Nuclear Energy Advisory Committee (NEAC) released a final report evaluating the needs and requirements for a new U.S. test reactor. The key recommendation of this report, the "Assessment of Missions and Requirements for a New U.S. Test Reactor," was for the DOE to proceed immediately with pre-conceptual design planning activities to support a new test reactor (Roglans-Ribas et al., 2022). To fulfil the NEAC recommendations and to meet the direction provided in the NEICA, the DOE established the Versatile Test Reactor (VTR) program in 2017.

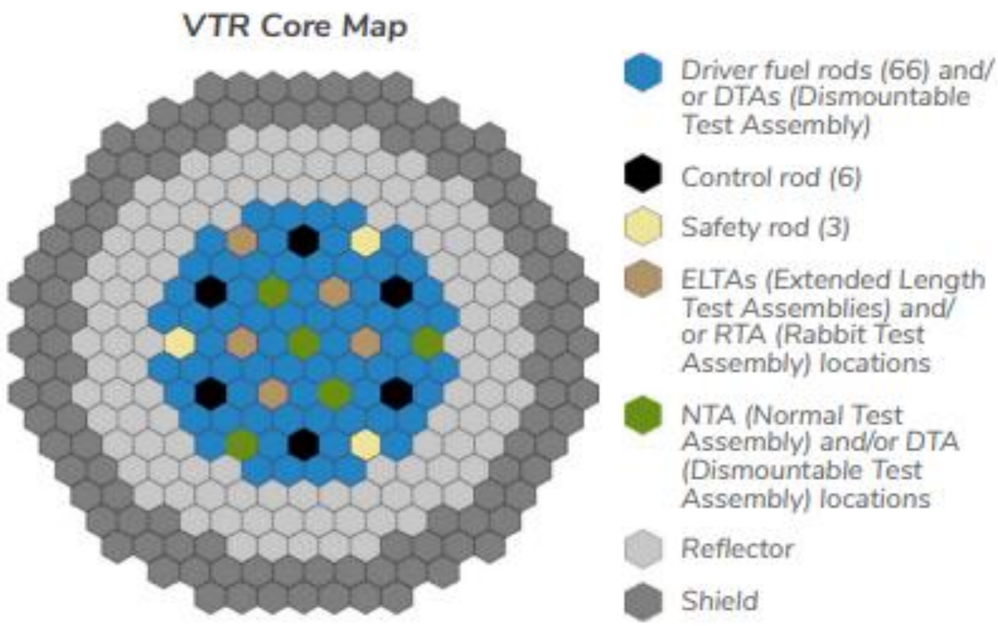

Figure 2-17: VTR conceptual design core map (Heidet and Roglans-Ribas, 2022).

The VTR is a fast flux test reactor designed to perform irradiations on nuclear fuels, materials, and components (Fig. 2-16). Even though its mission is focused on irradiation tests on prototypical fuels and materials, it is anticipated that this experimental facility will have a multipurpose mission for its expected operational lifetime. The main requirements and preliminary assumptions for the reactor include (Balderrama et al., 2018):

- Achieve fast flux of approximately $4x10^{15}$ n/cm^{2}sec in its core (Fig 2-17)
- Reach a thermal power of 300 MW_{th}
- Effective testing height ≤ 1 m

- Provide flexibility for novel experimental techniques.
- Being capable of running loops representative of typical fast reactors (potential coolants: Sodium, Lead, Lead Bismuth Eutectic, Helium and Molten Salt)
- Being capable of performing many experiments simultaneously.

The reactor's control systems and safety features ensure stable and reliable operation, while allowing for precise control of reactor parameters and experimental conditions. Additionally, the VTR offers flexible irradiation positions and methods, enabling researchers to study materials under various neutron spectra and fluence levels (Pasamehmetoglu, 2019). The VTR serves as a vital tool for advancing nuclear science and technology across various domains. Its primary applications include (Roglans-Ribas et al., 2022):

1. Nuclear Fuel Development: The VTR facilitates the testing and qualification of advanced nuclear fuels, including those designed for enhanced safety, higher efficiency, and reduced waste production. Researchers can investigate fuel behavior under realistic operating conditions, assess fuel performance, and explore novel fuel cycle options.
2. Materials Testing: The VTR provides a controlled environment to study the behavior and durability of materials exposed to high neutron fluxes, elevated temperatures, and corrosive conditions. This aids in the development of robust materials for reactor components, such as cladding, structural materials, and coolant systems.
3. Neutron Irradiation Experiments: The VTR enables researchers to conduct neutron irradiation experiments for various purposes, including the production of medical isotopes, testing of radiation-resistant materials, and fundamental nuclear physics research.
4. Advanced Reactor Concepts: The VTR supports the development and validation of advanced reactor designs, such as LFRs, SFRs, MSRs, and GFRs. By simulating the operating conditions and performance of these innovative concepts, the VTR contributes to their commercial viability and enhanced safety.

By supporting applications such as nuclear fuel development, materials testing, neutron irradiation experiments, and advanced reactor concepts, the VTR contributes significantly to the progress of nuclear research and innovation, paving the way for a sustainable and secure future in the field of nuclear technology (Roglans-Ribas et al., 2022).

The next section describes the analysis methodology used in the present work for evaluating the performance of the developed miniature, submersible DC-EMPs for circulating heavy and alkali metals in both in-pile and out of pile test loops in support of the developments of molten lead and sodium cooled Gen-IV nuclear reactors (Fig. 1-1).

Table 2-2: A review of permanent magnets DC-EMP designs for circulating liquid metals.

Author, year	**Application**	**fluid**	**Temp. (^oC)**	**Cooling**	**Operating point**	**Magnet**
Davis, K. A.,1966	SNAP-10A Space reactor power system	NaK-78	542	Radiator	7.58 kPa @ 3.0 m^3/h	ALNICO 5
Johnson, 1973	NASA Space reactor power system	NaK-78	316	NC of air	14.5 kPa @ 6.3 m^3/h	ALNICO 5 with pole pieces
Polzin and Godfroy, 2008	NASA's affordable Fission Surface Power (FSP) test loop	NaK-78	607	Water-cooled copper block	34.5 kPa @ 0.114 m^3/h	Neodymium
Kim et al., 2014	Decay heat removal system of Prototype FBR	Na	195	NC of air	10 kPa @ 1.0 m^3/h	samarium cobalt
Lee and Kim, 2017	Small sodium test loop	Na	300	NC of air	5 kPa @ 0.18 m^3/h	samarium cobalt
Lee and Kim, 2018	Heavy ion accelerator for stripping uranium ions	Li	200	NC of air	1.5 MPa @ 0.0216 m^3/h	samarium cobalt

Table 2-3: A review of developed and constructed ALIP designs for circulating liquid metals.

Author, year	**Application**	**fluid**	**Temp.(°C)**	**Diameter**	**Cooling**	**Operating point**	**Winding Insulation**
Ota et al, 2004	Japan Fast Breeder Reactor (FBR)	Na	335	1.9 m	Immersed in Na	250 kPa @ 9600 m^3/h	High-Temp. insulation
Polzin et al, 2010	NASA Lunar surface Power reactor	NaK-78	125-525	46 cm	Helium	90 kPa @ 4.5 m^3/h	Not reported
Nashine and Rao, 2014	Sodium test loops for FBR	Na	350	59 cm	Forced air	320 kPa @ 110 m^3/h	Not reported
Kwak and Kim, 2019	Sodium thermal hydraulics test loop	Na	340	46 cm	NC of air	400 kPa @ 85 m^3/h	Asbestos
Nashine et al, 2020	India FBR prototype	Na	550	40 cm	Immersed in Na	400 kPa @ 2 m^3/h	Mineral insulator

3. ANALYSES METHODOLOGY OF DC-EMPS' PERFORMANCE

3.1 Introduction

The performance characteristics of DC-EMPs depend on the liquid properties and temperature, the dimensions and wall materials of the flow duct, the magnet material and the value of the magnetic flux density, and the values of the input electric current and fringe resistance (El-Genk et al., 2020; Lee and Kim, 2017; Zhang et al., 2020). These design and performance parameters are typically based on direct experimental measurements. However, for new pump designs with desired specific operation and performance requirements direct measurements are not possible a priori. Instead, the electrical Equivalent Circuit Method (ECM) can help develop a preliminary pump design and predict the performance characteristics. The wide use of the ECM is because of its simplicity despite incorporating simplifying assumptions that result in over predicting the pump performance (Baker and Tessier, 1987; Nashine et al., 2007). These include assuming constant fringe resistance, constant and uniform magnetic field flux, and electrical current densities, neglecting the electrical contact resistance of the duct wall, and neglecting the dependences of the fringe resistance and magnetic flux density on the flow rate of the pumped liquid metals and input electrical current. The used values of the fringe resistance and the magnetic flux density in the ECM were either arbitrarily assumed or estimated using unvalidated empirical relations (Baker and Tessier, 1987; Nashine et al., 2007; Zhang et al., 2020).

Johnson (1973) has designed and measured the performance of a DC-EMP for circulating liquid NaK-78 working fluid and coolant for SRPSs. With limited direct measurements, he conducted performance analysis using the ECM. The analysis used the measured magnetic flux density in the pump duct at zero flow and an assumed fringe resistance based on previous experimental studies of DC-EMP of different geometries. which are both assumed constant and independent of the input electrical current and liquid flow rate. For operating at 316 ^{o}C and input current of 1,570 A, the ECM overestimated the static pressure at zero flow by ~ 15% and underestimated it by ~ 20% at a flow rate of ~ 2 kg/s, compared to the experimental measurements. The differences are due to uncertainties in the dimensions of the manufactured pump duct and an inaccurate estimate of the fringe resistance.

Nashine et al. (2007) used the ECM to investigate the performance of a DC-EMP design for circulating Sodium at 560 ^{o}C in fast reactors auxiliary systems. The constructed and tested pump provided a pumping pressure of 176 kPa at an input electrical current of 2,000. Nashine et al. (2007) used an empirical correlation proposed by Baker and Tessier (1987) for calculating the fringe resistance in the performed analysis with the ECM. The ECM predictions of the pump characteristics were > 40% higher than those measured. Post experiment analysis indicated that the suggested expression by Baker and Tessier overestimates the value of the fringe resistance by ~25%, contributing to overestimating the pump characteristics by > 40%.

Umans et al. (2013) have used the ECM to help design and analyze the performance of a DC-EMP with u-shaped current electrodes for circulating Gallium in a power system for Autonomous Underwater Vehicles (AUVs). Their analysis neglected the fringe resistance and used a constant magnetic flux density value. The ECM predictions of the static pressure were ~ 2.6 times those measured. This difference is explained to be due to the shapes of the magnet and current electrode, which caused large nonuniformities in the actual magnetic flux and the electric current densities in the tests. Measurements showed low current density exists in the regions of high magnetic flux density and vice versa.

Recently, Lee and Kim (2017) designed a DC-EMP for circulating liquid sodium at 300 ^{o}C in an experimental test loop. They used the ECM to perform parametric analyses of the pump dimensions to provide a pumping pressure of 5 kPa at sodium flow rate of 0.18 m3/h. Lee and Kim (2017)used empirical correlation proposed by Baker and Tessier (1987) to estimate the fringe resistance in the ECM analysis. They also performed 3D numerical analysis using ANSYS code to perform Magnetohydrodynamics (MHD) analysis of the pump characteristics. Results showed that calculated pumping pressure using MHD analyses at sodium flow rate 0.18 m^3/h of 4.3 kPa is ~ 52.4% of the predicted value using ECM (8.2 kPa). These results confirmed that contribution of the assumed values of the fringe resistance and the magnetic flux density in the ECM to overpredicting the characteristics of the sodium DC-EMP. The reported experimental measurements in the literature for the performance of DC-EMPs are either limited or incomplete for validating the ECM predictions (Johnson, 1973; Lee and Kim, 2017). Reported results showed the ECM overpredicts the performance characteristics of DC-EMPs by up to 40% (Nashine et al., 2007).

In summary, due to its simplicity the ECM is widely used to evaluate the performance and predict the characteristics of DC-EMPs. However, due to the incorporated assumptions and arbitrary input values of the fringe resistance and the magnetic field flus density, the ECM overestimates the pump performance. These assumptions include neglecting the duct wall electrical contact resistance and using arbitrary constant input values of the fringe resistance and effective magnetic flux density and neglecting the effects of the input electrical current and the liquid flow rate. Therefore, it is desirable to quantify the effects of these assumptions on the predictions of the performance and characteristics of DC-EMPs, which requires experimental measurements or performing MHD analysis of the DC-EMP design of interest. Such an analysis is computationally intensive compared to using the ECM. The ECM can help in the development of a preliminary design or conduct approximate performance analysis of DC-EMPs using constant values of the fringe resistance and the magnetic field flux density that equal those at zero flow. This requires confirming a reliable approach for calculating these values, which is a focus of this work.

The objectives of this chapter are to: (a) analyze the reported experimental measurements for a mercury DC-EMP (Watt et al., 1957) to determine the values of the fringe resistance and the magnetic flux density and their dependences on the liquid flow rate and the input electrical current; (b) examine the accuracy of the 2D Finite Element Method Magnetics (FEMM) software of calculating the fringe resistance and the magnetic field flux density at zero flow for use in ECM; (c) compare reported measurements of the mercury DC-EMP (Watt et al., 1957) characteristic to the predictions of the ECM to quantify the effects of the various assumptions.

3.2. Equivalent Circuit Model (ECM) of DC-EMP

Barnes (1953) was the first to apply the Equivalent Circuit Model (ECM) for predicting the performance of DC-EMPs for circulating liquid sodium for cooling fast spectrum nuclear reactors. The ECM represents an equivalent circuit diagram for the pump (Fig. 3-1). It includes the electrical resistances of the flow duct wall, Rw, the fringe current flow, If, upstream and downstream of the pump duct, Rf, and of the coolant flowing through the pump duct, Re. The ECM also includes the induced opposing voltage, Ei, by the liquid metal flow in the pump duct. A current source provides the total current, I, to the pump electrodes at a terminal voltage, E. Eq. 3-1 below, expresses the developed pumping pressure for driving the liquid metal flow through the pump duct, Δ P, in terms of the applied magnetic field flux density, various resistances, the total electrical current, the height of the flow duct, b, and liquid metal volumetric flow rate, Q, as:

$$\Delta P_p = \left[\frac{B(Q,I)}{10^4\, b(R_w R_f + R_e R_w + R_f R_e)}\right]\left[R_w\, R_f\, I - \left(\frac{B\,(R_w + R_f)}{10^4\, b}\right) Q\right] \qquad (3\text{-}1)$$

In this expression, ΔP_p, is the developed pumping pressure across the flow duct in Pa, $B\ (Q, I)$ is the effective magnetic flux density in the pump duct in Gauss, I is the total electrical current supplied to the pump in amperes (A), b is the height of the pump duct in meters, and Q is the volumetric flow rate of the liquid metal flow through the duct in m3/s. All electrical resistances (R_w, R_f and R_e) in Eq. 3-1 are in Ohm (Ω).

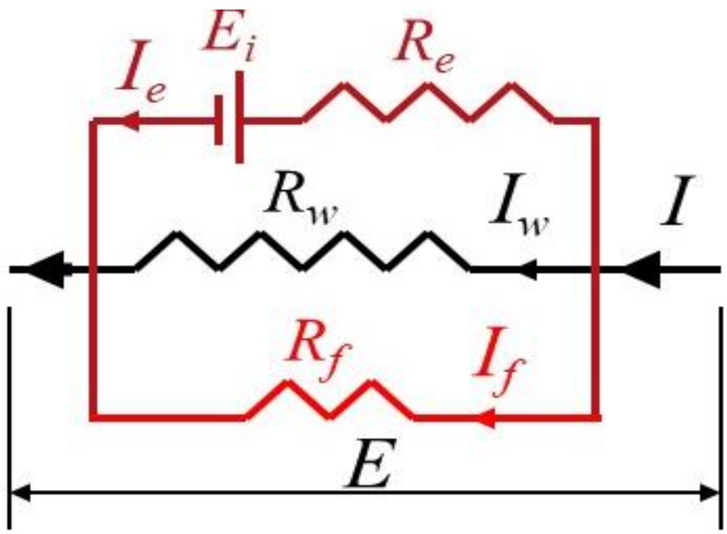

Figure 3-1: DC-EMP equivalent electric circuit.

The net pumping pressure developing across the flow duct, ΔP, after accounting for the friction pressure losses, ΔP_{loss}, of the flowing liquid metal through the pump duct, is given as:

$$\Delta P = \Delta P_p - \Delta P_{loss} \qquad (3\text{-}2)$$

In the present analysis, the following expression (Haskins and El-Genk, 2017) calculates the friction pressure losses, ΔP_{loss} for the liquid flow in the pump duct, as:

$$\Delta P_{loss} = \frac{a}{2}\left(\frac{c}{D_e^{1+b}\ A^{2-b}}\right)(\mu^b \rho^{1-b})\ Q^{2-b} \tag{3-3}$$

In this expression, D_e is the flow duct equivalent hydraulic diameter in meters, A is the duct cross-sectional flow area in m2, c is the duct length in meters, ρ is the density of the liquid in kg/m3, μ is the dynamic viscosity of the liquid in Pa.s. For laminar flow, the coefficient "a" and the exponent "b" equal 64 and 1.0, respectively, while for turbulent flow "a" and "b" are 0.184 and 0.2, respectively (McAdams, 1954). The pump efficiency equals the net pumping power divided by the input electrical power, as:

$$\eta_p(\%) = \frac{Pumping\ power}{Electrical\ \ power} \text{ x } 100 = \frac{\Delta P_p\ .\ Q}{I\ E} \tag{3-4}$$

Eqs. 3-1 to 3-3 calculate the pump characteristics (ΔP versus Q) at different values of the magnetic flux density and the electrical current input, and in terms of the electrical properties of the duct wall and the flowing liquid. The electrical resistances of the duct wall and the liquid in terms of their electrical properties at the specified liquid temperature, and the values of B and Rf, which are functions of the liquid flow rate, Q, and the input current, I, need to be known a prior. Therefore, using ECM with simplifying assumptions, although easy and straightforward, overpredicts the pump characteristics and performance parameters. These assumptions include constant and uniform distributions of I and B and neglecting the dependence of both B and Rf on the liquid flow rate, Q, and the supplied electrical current, I, as well as neglecting the contact electrical resistance of the duct wall. To quantify the effect of these assumptions, the present work compared the predicted pump characteristics using the ECM to the reported measurements for a mercury DC-EMP (Watt et al. 1957).

The next section describes the mercury DC-EMP designed and evaluated by Watt et al. (1957). It also presents and analyzes the reported experimental measurements and pump characteristics used to determine the values and the dependences of the magnetic flux density, B, and the Fringe resistance, Rf, on the liquid mercury flow rate, Q, and the input electrical current, I. It is worth noting that the values of the magnetic flux density and the fringe resistance at zero flow, B_o and R_{fo}, are independent of the input electrical current, I.

3.3. Assessment of ECM-FEMM for DC-EMP performance analyses

Watt et al. (1957) designed and constructed a DC-EMP for circulating liquid mercury in a test loop at room temperature. The pump had stainless steel duct and copper current electrodes. Electromagnets generate magnetic flux density in the pump duct. Laminated blocks extended the poles of the electromagnets beyond current electrodes to obtain a uniform distribution of the magnetic flux density in the liquid flow duct (Fig. 3-2). This duct was 355 mm long, 152 mm wide, and 15.1 mm high and the duct wall was 0.6 mm thick. The supplied DC to the Cu electrodes varied from 1,980 to 10,400 A. Performed measurements included the electrodes' terminal voltages, the magnetic flux density in the pump duct at zero flow, B_o, and the pumping pressure, DP, up to 300 kPa for circulating the liquid mercury in the test loop with 101.6 mm diameter piping at a volumetric flow rate, Q, up to ~ 26 m^3/h.

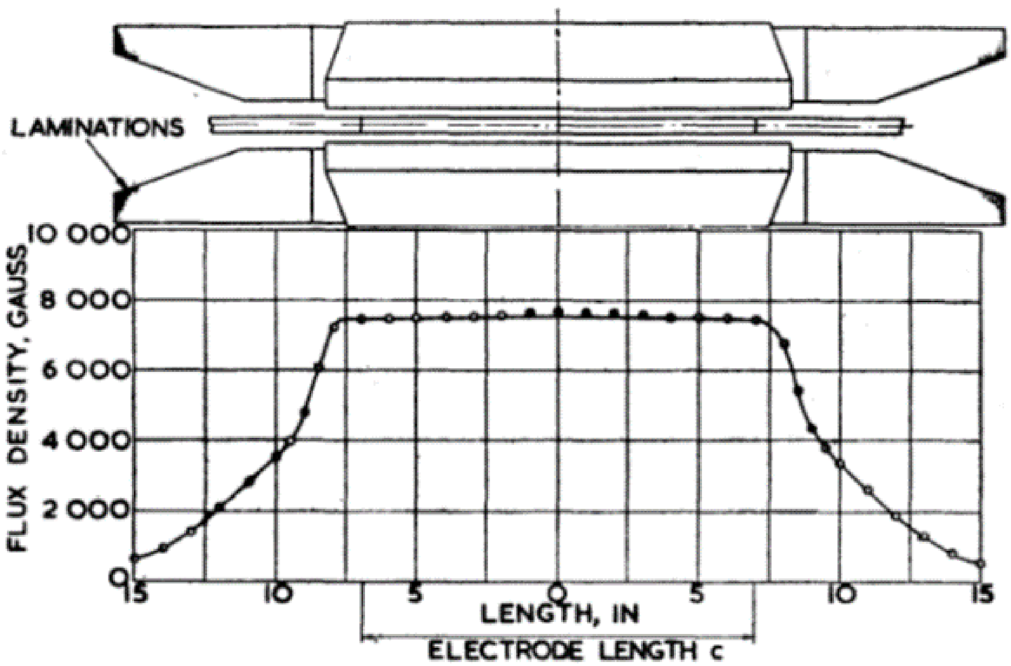

Fig. 3-2: Extended electromagnet poles and the measured magnetic flux density along the effective duct length of the mercury DC-EMP (Watt et al. 1957).

3.3.1. Reported Experimental Measurements

Watt et al. (1957) measured the voltage difference across the pump duct at different electrodes currents and mercury circulation rates (Fig. 3-3). The total static electrical resistance of the pump duct, R_{stat}, is determined from the measured terminal voltages at electrode currents ranging from 2,000 – 6,000 A, at zero flow, is ~19.6 μΩ. The static electrical resistance across the pump duct includes those of the duct wall, Rw, the fringe current, Rf, and the liquid mercury residing in the pump duct, Re (Fig. 3-2). After draining liquid mercury from the pump duct the measured duct wall resistance was 230 μΩ. The reported experimental data displayed in Fig. 3-3 shows the terminal voltage increases with increased electrode current and linearly at the same slope of ~ 0.01056 with an increased circulation rate of liquid mercury in the test loop. The reported measurements of the terminal voltage, E, in Fig. 3-3 are correlated in the present work in terms of the measured values of static electrical resistance of the pump duct, R_{stat}, the input electrode current, I, and the flow rates of liquid mercury, Q, as:

$$E(\mathrm{Q, I}) = R_{stat}\, I + 0.01056\, Q = 19.6\ 10^{-6}\, I + 0.01056\, Q \qquad (3\text{-}5)$$

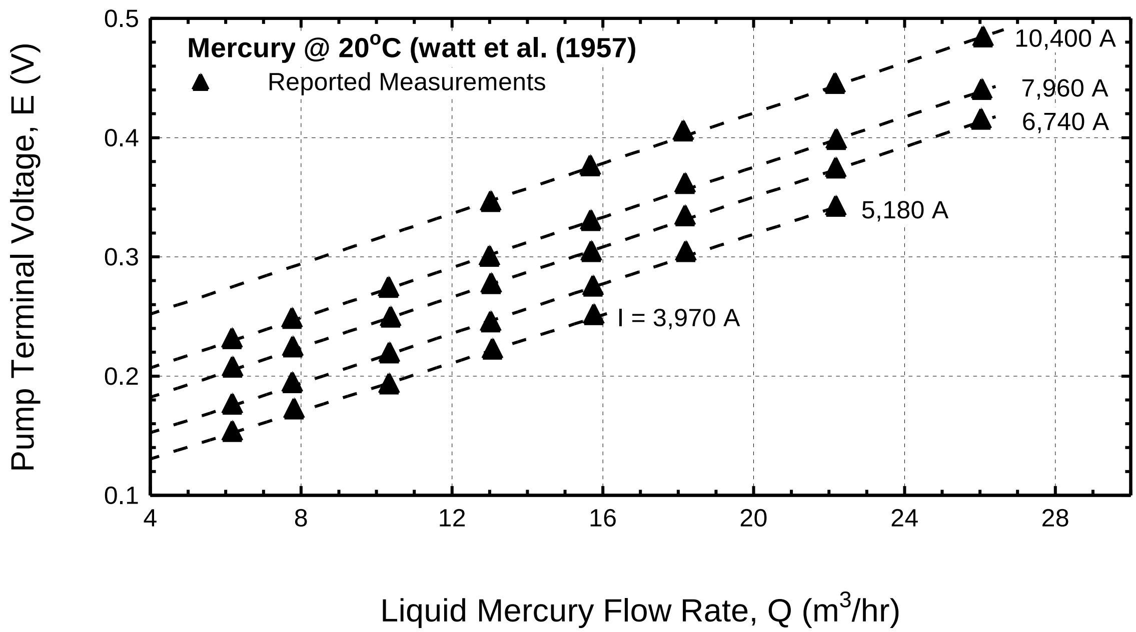

Fig. 3-3: Reported measurements of the terminal voltage at different electrode currents and circulation rate of liquid mercury (Watt et al. 1957).

3.3.2. Fringe resistance

Based on the pump equivalent circuit diagram in Fig. 3-1, the following expression calculates the total fringe resistance for the mercury pump, as:

$$R_f(Q,I) = E(Q,I) \,/\, \left[I - \frac{\left(E(Q,I) - E_i(Q,I)\right)}{R_e} - \frac{E(Q,I)}{R_w} \right] \qquad (3\text{-}6)$$

In Eq. 3-6, Ei (Q, I) is the induced opposing voltage in the pump duct due to the flow of liquid mercury in the applied magnetic field. The following expression calculates the induced voltage, Ei. It is zero when the liquid metal in the pump duct is stationary, Q = 0, in terms of the magnetic flux density in the pump duct, B, and the duct height, b, as:

$$E_i = B\, Q / b \qquad (3\text{-}7)$$

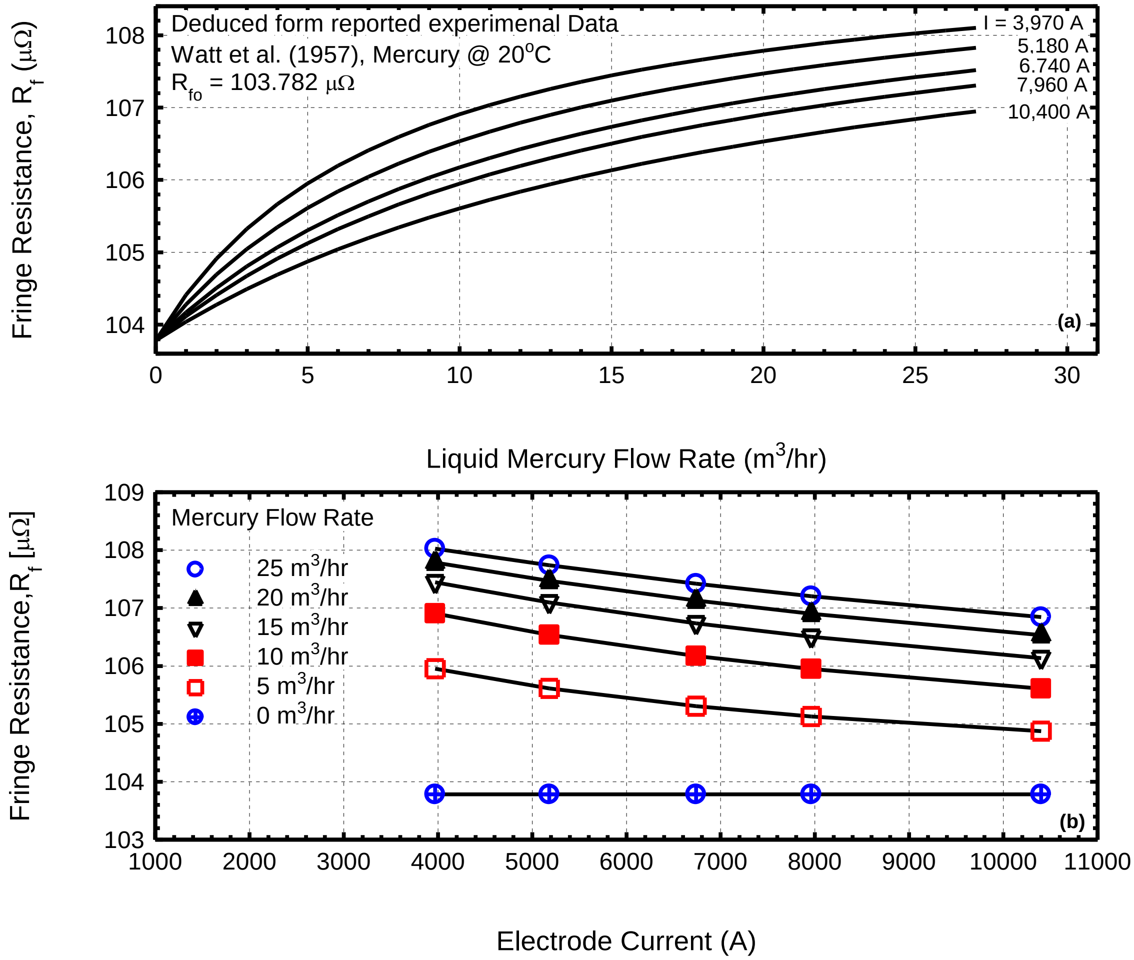

Fig. 3-4: Dependences the obtained values of the total fringe resistance from the reported electrical measurements of the input electrical current and mercury flow rate (Watt et al. 1957).

The obtained value of the total fringe resistance for the mercury DC-EMP design (Watt et al. 1957) from the reported measurements at zero flow is 103.782 $\mu\Omega$ (Fig. 3-4a). This value is independent of the supplied electrical current to the electrodes (Fig. 3-4). The results presented in this figure show that the values of the total fringe resistance for the mercury DC-EMP increase almost logarithmically with increased mercury flow rate (Fig. 3-4(a)) and decrease almost linearly with increased electrical current supplied to the pump's electrodes (Fig. 3-4b). The largest value of the fringe resistance, Rf, for I = 3970 A is only 4.3% higher than at value at zero flow, R_{fo} (Fig. 3-4). Therefore, using the fringe resistance in the ECM equals that at zero flow (i.e., $R_f = R_{fo}$), and neglecting the changes with the mercury flow rate and the electrodes current (Fig. 3-4) cause the ECM to underpredict the pumping pressure by a few percentages.

3.3.3. Pump characteristics

In the performed tests of the mercury DC-EMP in Fig. 3-2, Watt et al (1957) measured the pressure rise between upstream and downstream points of the pump duct, ΔP_o, using a bourdon tube pressure gauge at different flow rates and electrodes current. The net pumping pressure, Δ P, is determined by subtracting the measured pressure losses, ΔP_{loss}, at zero electrode current from the calculating pumping pressure (Eq. 3-2). Fig. 3 5a plots the reported values of the net pumping pressure versus the mercury flow rate at different electrode currents. The characteristics in this figure show the net pumping pressure decreases linearly with increased flow rate of mercury through the pump duct and increases with increased electrode current.

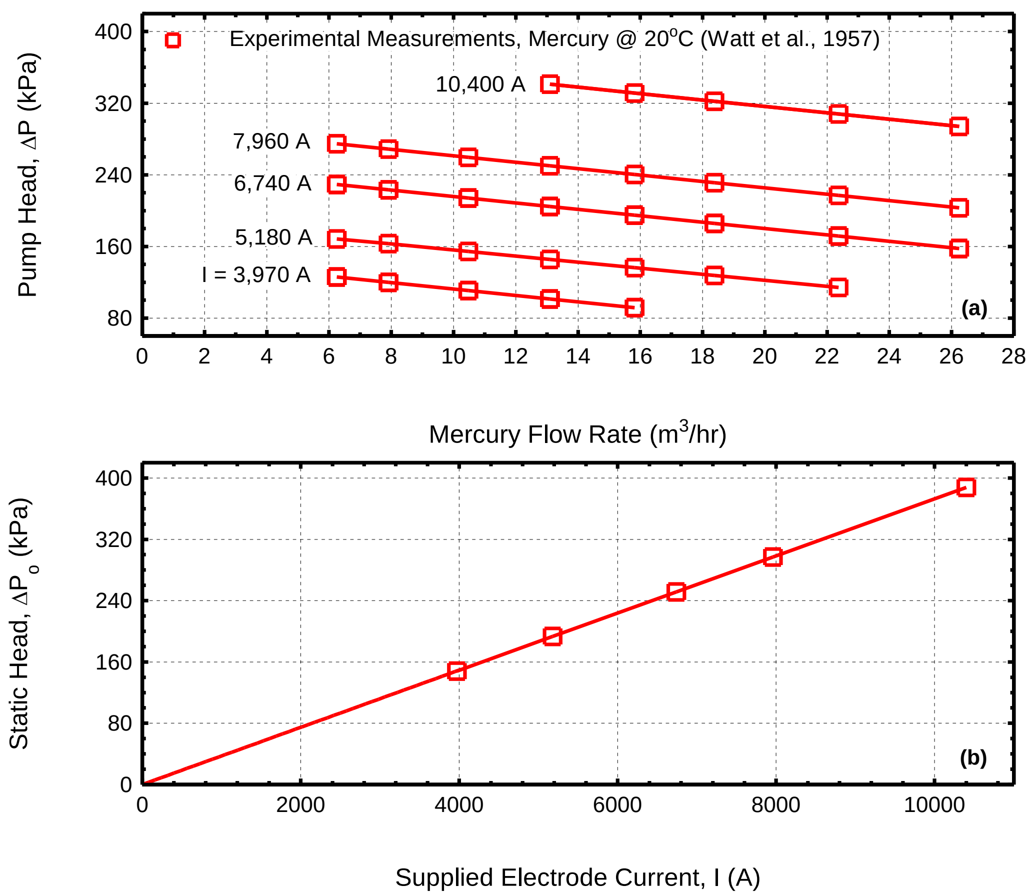

Fig. 3-5: Measured static pressure and characteristics of the mercury DC-EMP (Watt et al. 1957).

The extrapolated value of the pumping pressure to zero flow rate is the static pressure, Δ Po, which increases linearly with increased electrode currents, I (Fig. 3-5b). These results are consistent with Eq. 3-1 from which the static pumping, Δ Po, is expressed as:

$$\Delta P_o = \left[\frac{B_o\, R_w\, R_f}{10^4\, b\left(R_w R_f + R_e R_w + R_f R_e\right)}\right] I \tag{3-8}$$

In Eq. 3-8 since the temperature of the liquid mercury in the performed tests was constant (20 ^oC), the electrical resistances are also constant and so is the magnetic flux density at zero flow, B_o. Based on the results presented in Fig. 3-5(b), the determined magnetic flux density in the pump duct (Fig. 3-2) at zero flow of liquid mercury is independent of the values of the electrodes' electrical current and equals 7,750 Gauss.

3.3.4. Wall electrical contact resistance

As indicated in Eq. 3-1 and 3-8, the dynamic and the static pressure for a DC-EMP depend on the electrical resistance of the flowing liquid, R_e, the total fringe resistance for the current flows upstream and downstream of the pump duct, R_f, and the electrical resistance of the duct walls, R_w. The calculated values of R_e and R_w are functions of the duct and wall dimensions and the electrical resistivities of the liquid and the duct wall materials at 20 ^oC. For mercury DC-EMP of Watt et al. (1957), the measured wall resistance, R_w, was 230 μΩ. However, the value determined based on the wall dimensions and electrical resistivity is 217 μΩ. The difference between the measured and calculated wall resistances of 13 μΩ, or 5.65% of the measured value, is because the calculated wall resistance neglects the of wall contact resistance due to brazing or welding. In the absence of the actual measurements, the wall contact resistance is not be possible to quantify.

Fig. 3-6 presents the ECM predictions of the characteristics for mercury DC-EMP (Watt et al. 1957) using the measured wall resistance and the calculated values of wall resistance that neglects the contact resistance. Results show when neglecting wall contact resistance, the ECM with input electrical current of 6,740A overestimates the pumping pressure for the mercury DC-EMP by 0.64 to 2.346 kPa (0.2 to 1.4%), depending on the mercury flow rate. In these predictions, the ECM used the determined values of the fringe resistance and the magnetic field flux density from the reported measurements at zero flow (Watt et al. 1957).

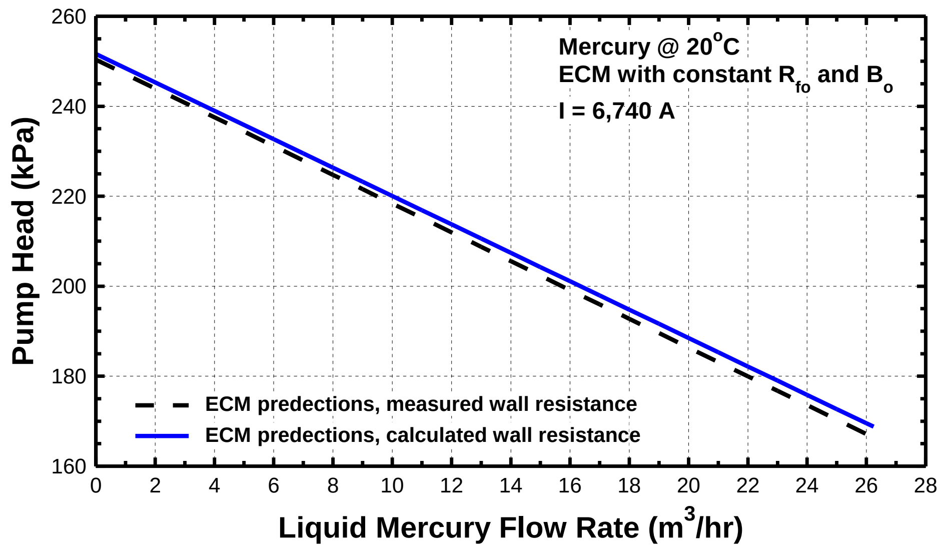

Fig. 3-6: Comparison of ECM predictions of the mercury pump characteristics using measured and calculated wall resistance.

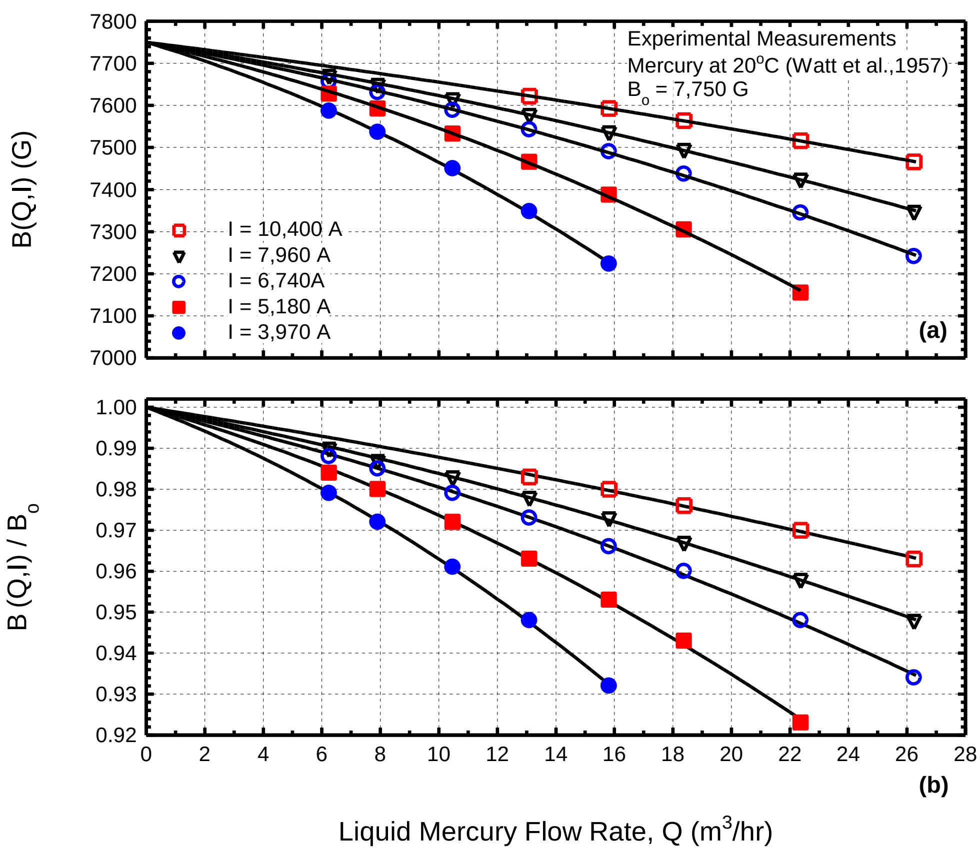

Figure 3-7: Reported measurements of the magnetic flux density in the pump duct at zero flow and as a function of mercury flow and the input electrical current (Watt et al. 1957).

3.3.5. Magnetic flux density

The reported experimental characteristics of the mercury DC-EMP (Watt et al. 1957) in Fig. 3-5 are used to determine the dependences of the magnetic flux density, B, on the flow rate of the liquid mercury in the pump duct and input electrical current, I. The values of the magnetic flux density, B, obtained using Eq. 3-1 from the reported measurements of the net pumping pressure, ΔP, electrodes electrical current, I, and the mercury flow rate, Q, are presented in Fig. 3-7. Fig. 3-7a confirms that the magnetic flux density at zero flow rate, B_o, is independent of the electrodes' current. However, the values of the magnetic flux density, B, decrease with the increased flow rate of liquid mercury and/or the electrical current to the electrodes. The results in Fig. 3-7 show that at mercury flow rate of 15.82 m^3/h, the decrease in B relative to its value at zero-flow value, B_o, varies from 2% to 6.8% with increased electrical current to the electrodes from 10,400A to 3,970 A, respectively (Fig. 3-7b). At an electrical current of 6,740 A, the values of B at mercury flow rates of 15.82 to 26.24 m^3/h are 3.4% and 6.6%lower than B_o. The results in Fig. 3-7b also show that the largest decrease in the magnetic flux density of 7.7% is for electrodes' current of 5,180 A and mercury flow rate of 22.37 m3/h. The decreases in the effective magnetic flux density, B, with increased liquid flow rate are due to the corresponding increases of the induced opposing voltage, Ei, due to the flow of the electrically conductive liquid in the applied magnetic field in the pump duct. This induced voltage increases with increased mercury flow (Eq. 3-7). Therefore, neglecting the effect of the liquid flow rate on the magnetic flux density in the pump duct may result in a few percentages difference between the measured values of the pumping pressures and those predicted using the ECM. The ECM predictions are based on assuming constant values of the magnetic flux density and fringe resistance that equal those for zero flow (i.e., $B = B_o$, and $R_f = R_{fo}$).

In summary, the presented results in this section for the mercury DC-EMP designed, constructed, and evaluated by Watt et al. (1957) demonstrate the importance of the reported experimental measurements that included the total electrical resistance and the magnetic flux density at zero flow, the pump static pressure and operation characteristics at different values of the electrical current to the electrodes. These measurements helped determine the values of the total fringe resistance and the effective magnetic flux density with increased electrodes electrical current and flow rate of liquid mercury. Results show the total fringe resistance for the mercury DC-EMP increased with increased mercury flow rate and/or decreased electrodes' current. The determined total fringe resistance at zero flow = 103.782 μΩ and is independent of the input current, while the pump static pressure increases linearly with increased electrical current. For electrical currents from 3,970 A to 10,400 A, the obtained values of the total fringe resistance and the effective magnetic flux density for the mercury pump (Watt et al., 1957) are 4.3% higher and 7.7% lower, respectively, than their values at zero flow.

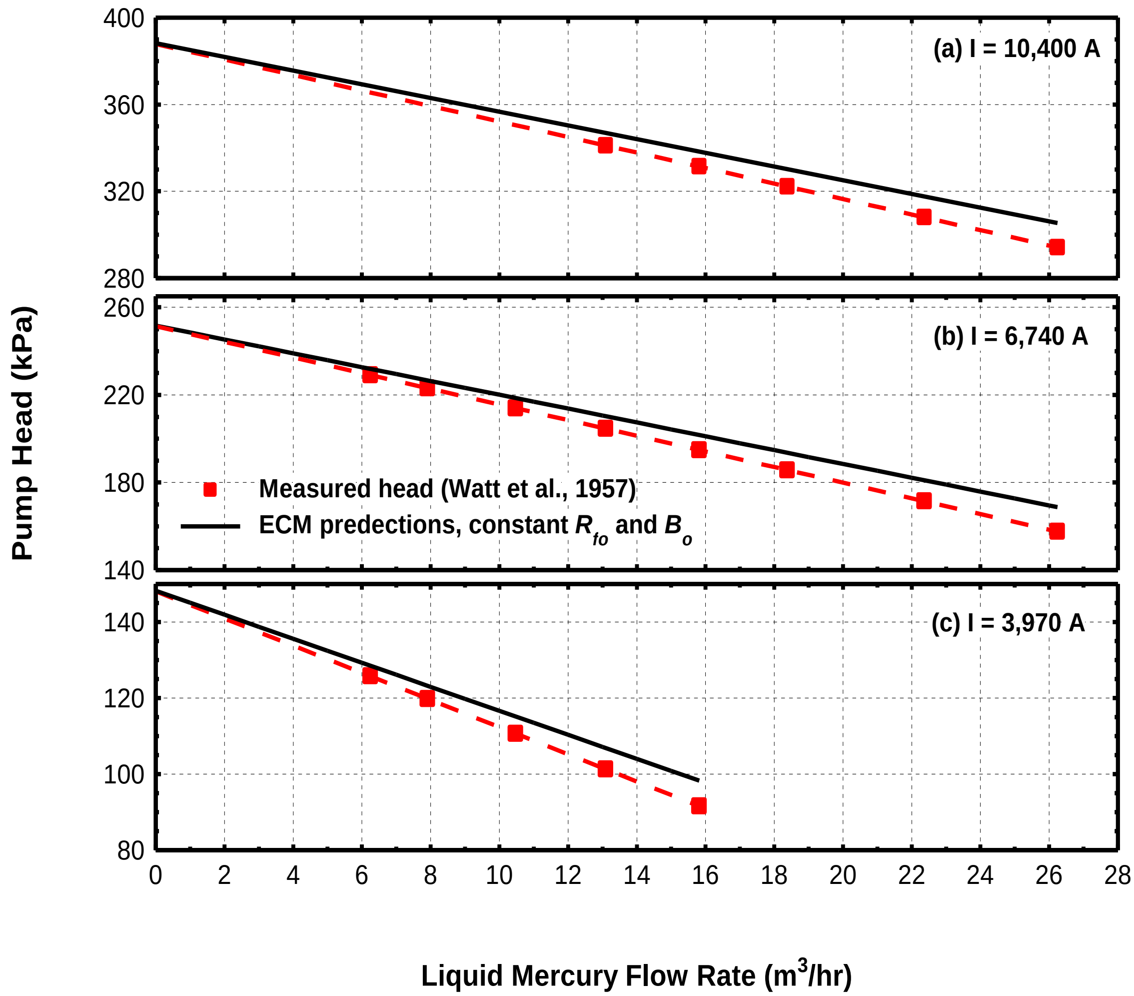

Figure 3-8: Comparison of ECM predictions of the mercury pump characteristics with reported measurements (Watt et al. 1957).

Direct measurements of the values and the dependences of the fringe resistance and the magnetic flux density on the liquid flow rate are challenging to perform in practice with acceptable uncertainties. However, the static measurements of the total electrical resistance and the magnetic flux density are much easier to conduct. In the absence of direct experimental measurements for an actual DC-EMP design, it is almost impossible to predict the pump performance a prior with confidence. However, the ECM could calculate the pump performance characteristics subject to the assumptions of constant values of the total fringe resistance and the magnetic flux density, regardless of the liquid flow rate, and neglecting the wall contact resistance. Thus, the ECM analysis needs applicable values of the magnetic flux density and fringe resistance for the pump design concept of interest.

3.4. ECM Predictions of the Mercury DC-EMP Characteristics

This section uses the ECM to predict the performance characteristics of the mercury DC-EMP (Watt et al. 1957) and compares them to the reported measurements to quantify the effects of the various assumptions on the ECM predictions. Fig. 3-8 compares the ECM predictions of the mercury pump characteristics to the reported experimental measurements for three values of the electrical current values of 3,970A, 6,740A, and 10,400A. The presented predictions are for constant fringe resistance and magnetic flux density values equal to those measured and determined from the reported experimental measurements at zero flow (R_{fo} and B_o). The predictions of the static pressure at different electrical currents agree with the extension of the reported measurements values. However, the ECM predictions overestimate the measured characteristics of the mercury DC-EMP (Watt et al. 1957). With increased liquid flow rate with the difference increasing with increased liquid flow rate and decreased electrodes current to as much as ~ 6.8% (Fig. 3-9). As the results in this figure show, the magnitude of overestimating the pump characteristics using the ECM predictions depends on the values of both the electrical current and the liquid mercury flow rate.

As shown in Figs 3-8 and 3-9, assuming constant R_{fo} and B_o and neglecting their dependences on the input electrical current and the mercury flow rate, and neglecting the pump duct wall contact resistance and the effect of Joule heating on raising the temperatures of the flowing liquid and the pump structure the ECM overpredicts the performance characteristics of the mercury DC-EMP. For the same mercury flow rate, the magnitude of overestimating the pumping pressure increases with decreasing the electrical current. For the same electrical current, the magnitude of overestimating the pumping pressure using the ECM also increases with the increasing flow rate of liquid mercury. For example, at a mercury flow rate of 15.82 m^3/h and input currents of 3,970A, 6.740A, and 10,400 the ECM overestimates the pumping pressure by 6.85%, 3.38%, and 2.1%, respectively. Similarly, at a mercury flow rate of 26.24 m3/h. and input currents of 6,740A and 10,400A, the ECM overestimates pumping pressure by 6.62% and 3.7%, respectively (Fig. 3-9).

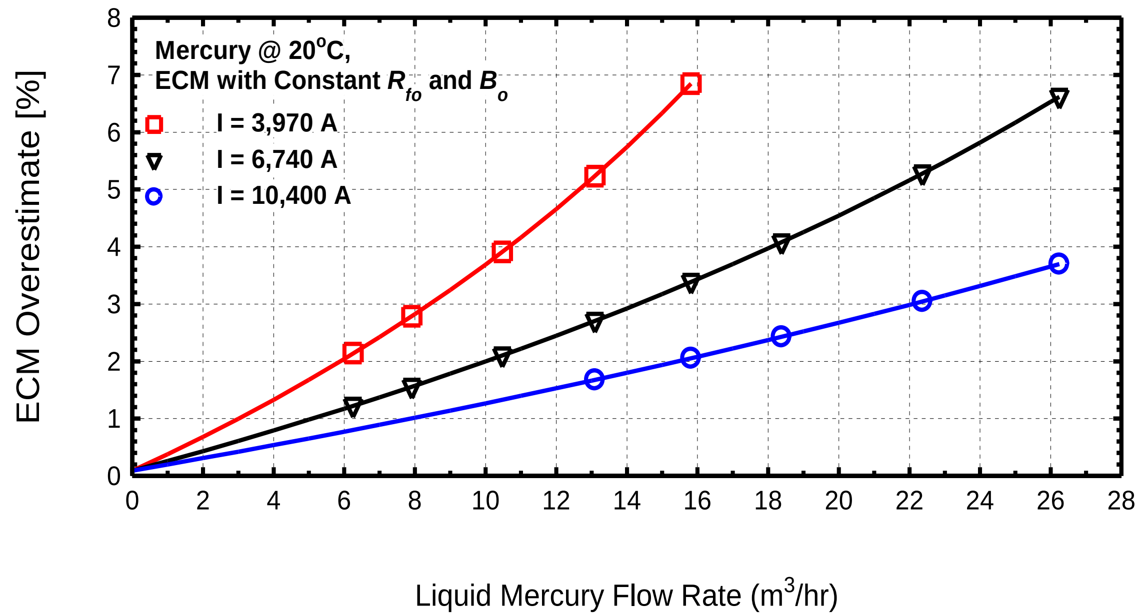

Fig. 3-9: The ECM predictions magnitude of overestimating the measured characteristics of the mercury DC-EMP (Watt et al. 1957).

These overestimates are due to the combined effect of the inherent assumptions in the ECM. The actual values of the fringe resistance and the effective magnetic flux density in the pump duct are higher and lower, respectively, than their values at zero flow, which are independent of the input current value. The fringe resistance, however, increases with decreased electrical current and/or increased mercury flow rate. On the other hand, the effective magnetic flux density in the pump duct decreases with decreased electrical current and / increased mercury flow rate. Neglecting the duct wall electrical contact resistance decreases the total electrical resistance of the pump duct. The Joule heating would increase the temperatures of the flowing liquid mercury and duct wall and hence their electrical resistance as well as total duct resistance. Suggested empirical expressions the literature used by investigators to estimate the fringe resistance in the ECM analysis. Watt (1959) proposed the following expression for calculating fringe resistance in terms of the electrical resistance of the liquid in the pump duct, Re, multiplied by a correction factor, k1, as:

$$R_f = k_1 R_e \qquad (3\text{-}9)$$

The correction factor, k_1, in terms of the ratio of the pump duct width and length (a/c), is:

$$k_1 = 1.78\, e^{-0.245\,(\frac{a}{c})} + 15.1\, e^{-3.81\,(\frac{a}{c})} \qquad (3\text{-}10)$$

Baker and Tessier (1987) had proposed calculating the fringe resistance from multiplying the effective liquid resistance, Re, with the ratio of pump duct length and width (c/a) and a constant correction factor 2.5, as:

$$R_f = 2.5\, R_e \left(\frac{c}{a}\right) \qquad (3\text{-}11)$$

Table 3-1: Experimental and calculated values of R_{fo} for mercury Pump

Method	**R_f (μΩ)**	**difference (%)**
R_{fo} obtained from reported measurements, Fig. 3-4a	103.8	---
R_f calculated using Eq. 3-9	121.5	+17.05
R_f calculated using Eq. 3-11	158	+ 52.2

Unlike the results presented in Fig. 3-4 for the mercury pump of Watt et al. (1957), the calculated values of Rf using Eq. 3-9 and 3-11 are independent of both the liquid flow rate and the input electrical current. The calculated fringe resistances for the mercury DC-EMP using these expressions are compared in Table 3-1 to that determined from the reported experimental measurements by Watt et al. (1957) at zero flow rate, R_{fo} = 103.782 μΩ (Fig. 3-4 and Table 3-1).

The calculated R_f values using the Watt (1959) expression in Eq. 3-9 = 121.5 μΩ, is 17.05% higher than the experimental value. The estimate of Rf using the expression by Baker and Tessier (1987) in Eq. 3-11 is 52.2% higher than the experimental value for zero flow in Fig. 3-4 and Table 3-1. The values of R_{fo} in Table 3-1 are used in the ECM to calculate the characteristics of the mercury pump at an input electrical current of 6,740 A and the measured magnetic flux density at zero flow, B_o = 7,750 G Fig. 3-9a. Fig. 3-10 compares the calculated to the experimental characteristics. The high estimates of fringe resistance values using the recommended empirical expressions by Watt (1959) and Baker and Tessier (1987) increased the ECM predictions of the pumping pressure compared to the reported measurements, which decreased slower with liquid mercury flow rate (Fig. 3-10).

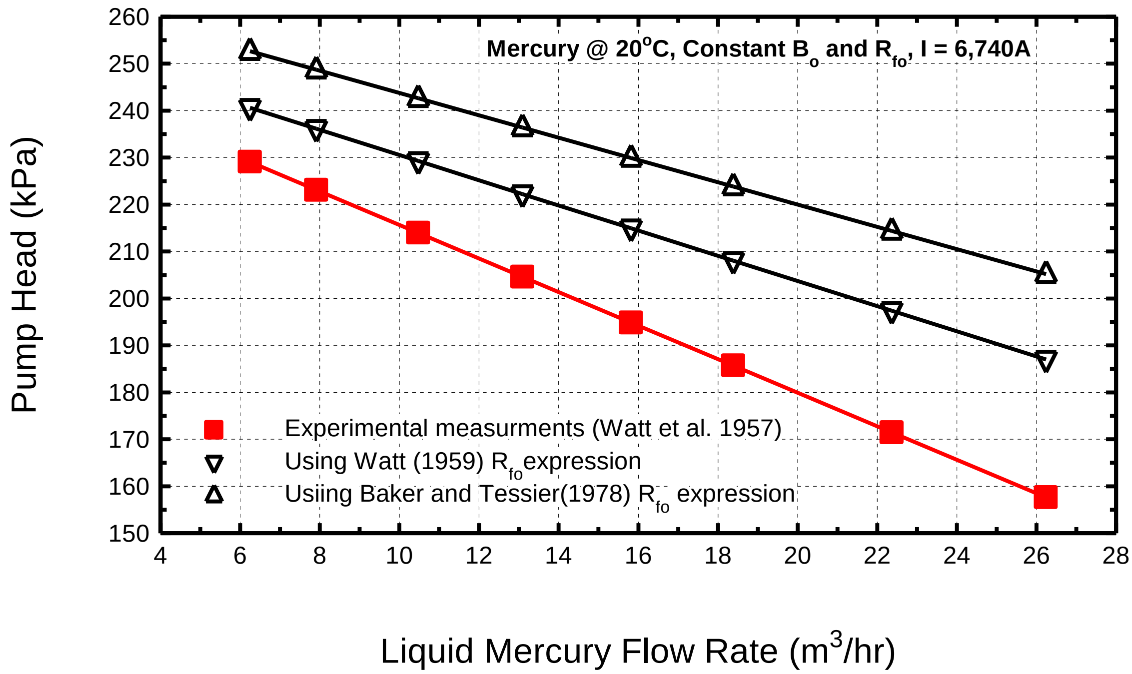

Fig. 3-10: Comparison of the experimental characteristics of the mercury Pump to those calculated using ECM with different values of R_{fo} and input electrical current of 6740A.

The ECM predictions of the mercury pumping pressure using Watt's (1957) and Baker and Tessier's (1987) expression for the fringe resistance are as much as 23.2%, and 15.7% higher than reported measurements (Watt et al. 1957). Based on these results, overestimating the fringe resistance and, to a lesser extent, neglecting its dependence on the liquid flow rate (Fig. 3-4a) in ECM results in overestimating the characteristics of the mercury DC-EMP. Instead, with the determined value of the fringe resistance at zero flow, R_{fo}, from the reported experimental measurements of the pump characteristics and the magnetic flux density at zero flow rate, the ECM overestimated the experimental pump characteristics at electrodes current of 6,740 by only < 6.6% (Fig. 3-9). As indicated earlier, this difference could be attributed to not accounting for the dependence of the fringe resistance and the magnetic flux density on the electrodes current and the liquid flow rate (Fig. 3-4), and neglecting the wall contact resistance in the ECM predictions.

Actual experimental measurements for an existing pump design (e.g., Watt et al. (1957)), could quantify the effects of the assumptions in the ECM on the predictions of the pump performance. In the absence of such measurements using the ECM to estimate the performance of a DC-EMP for meeting certain performance requirements is easy, but predictions of the pump characteristics will be higher than actual. The present results have shown that such overprediction is due to the inherent assumptions in the ECM such as using constant values of the fringe resistance and the magnetic flux density that equal those at zero flow, R_{fo} and B_o, respectively. Nonetheless, the ECM results would be useful for optimizing the design prior to the fabrication of the pump. Therefore, for given magnet and pump designs and working fluid, there is a need to accurately calculate the values R_{fo} and B_o to incorporate in the ECM for calculating the pump characteristics and performing parametric analysis to optimize the pump design, which is a focus of the present work described in the following section.

3.5. Finite Element Magnet Methods (FEMM)

This section is to demonstrate the effectiveness and accuracy of the FEMM software for calculating the fringe resistance and the magnetic flux density at zero flow, R_{fo}, and B_o, respectively. To estimate B_o, however, the FEMM software requires the actual magnet dimensions. However, Watt et al. (1957) did not provide these dimensions for the mercury pump. The accuracy of FEMM software for calculating B_o is determined by comparing its predictions to reported measurements for different magnet designs with stagnant liquids. The FEMM is open-source software for solving magnetostatic problems, magnet time-harmonic, electrostatic, electric current flow, and steady-state heat flow in two-dimensional planar and axisymmetric domains (Baltzis, 2008). The input CAD-geometry of the magnet and computational domain are discretized into a triangular first-order grid of finite mesh elements. The software includes traditional variation formulation for solving relevant partial differential equations and built-in libraries of physical thermal, electrical and magnetic properties of varied materials. Users may predefine the largest mesh element sizes in the numerical grid in the different regions of the computation domain or use the built-in mesh auto-generator. The software allows inspecting the fields' solutions at arbitrary points or contours of the geometry for exporting or plotting various parameters of interest (Meeker, 2015).

Linking the FEMM inter-process communications to MATLAB (Meeker, 2015) significantly reduces the processing time and that for extracting and graphically displaying and plotting the results. This linking is quite effective for performing a DC-EMP design optimization that requires a substantial number of FEMM simulations to calculate the values of the fringe resistance and magnetic flux density at zero flow, R_{fo}, and B_o, respectively. These values are used in the ECM to calculate the performance of different pump designs. The entire process is fast and effective for down selecting a pump design before the actual fabrication and assembly of the pump components. As shown in Fig. 3-4, the values of R_{fo} for the mercury pump are independent of the input electrical current. The specified effective electrical current in the FEMM analysis, IFEMM, equals the input current, I, minus the wall current, I_w, thus IFEMM = I – I_w. In addition, the user specifies the materials of choice for the pump duct wall, current electrodes, the working fluid, and the total input electrical current to the electrode for a zero-voltage at the surface of the exit current electrode. The FEMM software then calculates the current density distribution including the total fringe current, Ifo, flowing through the liquid upstream and downstream of the pump duct. The calculated Ifo value when subtracted from the input electrical current to the FEMM software, IFEMM, gives the effect current across the static liquid in the pump duct, Ieo, as:

$$I_{eo} = I_{FEMM} - I_{fo} = I - I_w - I_{fo} \tag{3-12}$$

The present work calculated the fringe resistance in terms of the effective electrical current, Ieo, and the electrical resistance of the static liquid in the duct, Re, as:

$$R_{fo} = \frac{I_{e0}\, R_e}{I_{fo}} \tag{3-13}$$

The calculated value of Re in Eq. 3-13 is based on the dimensions of the pump duct and the electric resistivity of the working fluid, ρ_{wf}, at the liquid temperature, as

$$R_e = \frac{a\, \rho_{wf}}{b\, c}. \tag{3-14}$$

The FEMM calculates the magnetic flux density at zero flow using the Magnetics package, which simulates both permeant and induced magnets. It solves Maxwell’s equations of Gauss's law for magnetism and Ampere’s law (Meeker, 2015) for the planner distribution of the magnetic flux density, $B_o(\mathrm{y, z})$, in the pump duct at zero flow (Fig. 3-4). In these calculations, the FEMM material libraries provide the magnetic permeability, B-H curves, and magnetization directions of permanent magnets. The following equation calculated the effective magnetic flux density in the pump duct at zero liquid flow, B_o, (Meeker, 2015), as:

$$B_o = \frac{\left(\int_{-0.5c}^{+0.5C} \int_{-0.5b}^{+0.5b} B_o(y,z)\, dy\, dz\right)}{b\, c} \tag{3-15}$$

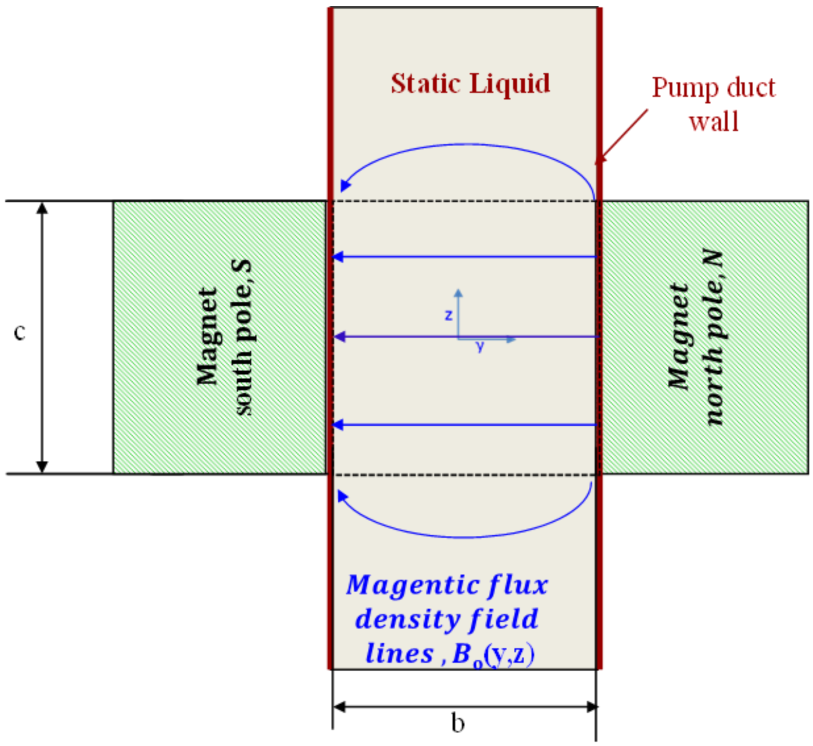

Figure 3-11: Calculated 2-D magnetic flux density field, B_o (y, z) by FEMM software.

3.5.1. Validation of FEMM Analyses

In this section, analysis of the current flow field in the mercury DC-EMP (Watt et al. 1957) is conducted to calculate the fringe resistance at zero flow rate, R_{fo}, using the FEMM software and compare it to that obtained from the reported electrical measurement. Because the magnet dimensions were not reported for the mercury DC-EMP by Watt et al. (1957), it was not possible to conduct FEMM analysis to determine the value of the magnetic flux density at zero flow, B_o, and compare it to the values obtained from the reported experimental measurements. Therefore, to validate the FEMM capability of calculating B_o, this work conducted field analysis of the seawater thruster reported by Li et al. (2021) using the FEMM software and the calculated values of the magnetic flux density at zero flow, B_o, are compared to reported measurements (Li et al., 2021). The results presented in Fig. 3-4 and 3-10 for the mercury DC-EMP show that R_{fo} and B_o are independent of the value of the current electrode. The following subsections detail the performed FEMM analysis for calculating both R_{fo} and B_o.

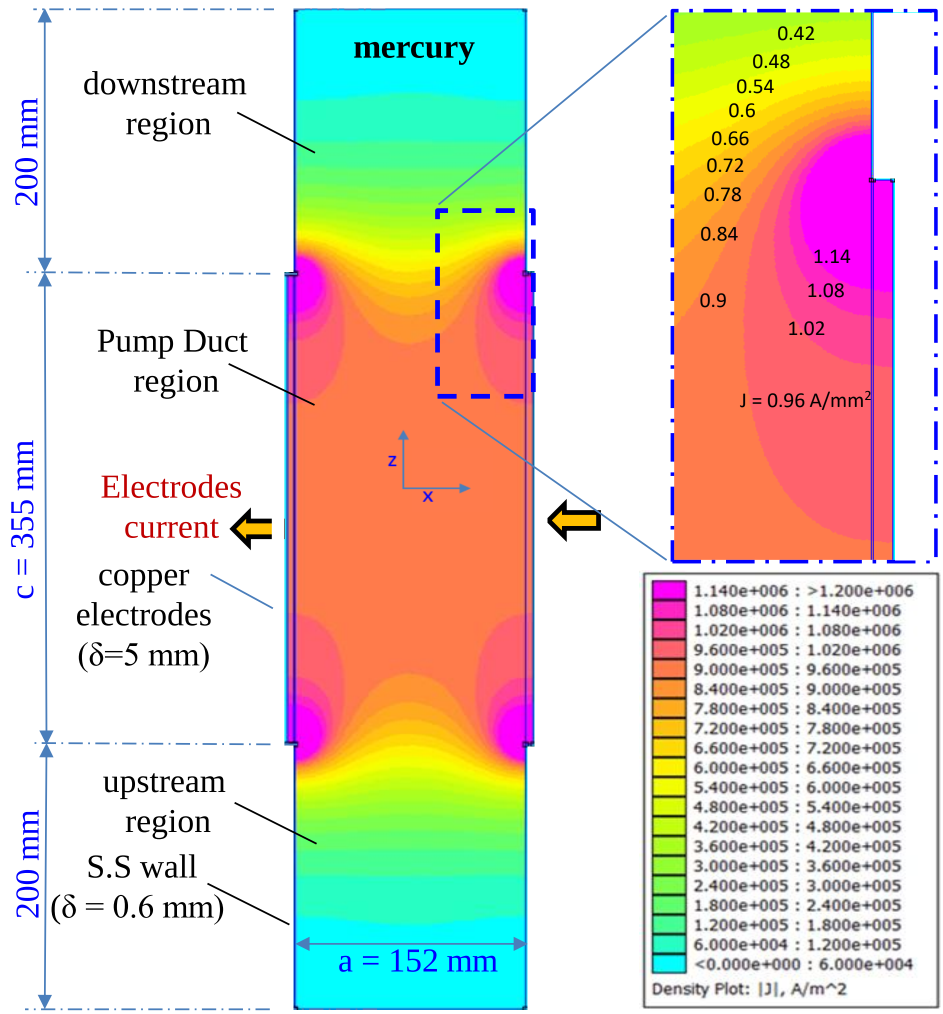

Figure 3-12: The calculated electrical current flow field in the duct and the upstream and downstream sections of the mercury DC-EMP at zero flow using the FEMM software.

3.5.1.1. Fringe resistance at zero flow

The input to the performed FEMM analyses to calculate the fringe resistance at zero flow of mercury, R_{fo}, for the mercury DC-EMP of Watt et al. (1957), includes the pump duct dimensions and materials. To provide details of the fringe current density field lines, the used lengths of the downstream and upstream sections of the pump duct in the FEMM calculations are longer than half the pump duct length, c. The FEMM built-in auto mesh generator produced the numerical meshing of the computation domain. The used electrode electrical current in the performed analysis, IFEMM = 6,155 A.

Fig. 3-12 presents the calculated current density, J, field distribution in the pump duct. The current density distributions are symmetric in the left and right halves and in the top and bottom halves of the pump duct. At the mid-plane of the pump duct, the current density is ~ 0.9 A/mm^2, which is less than the input current density of 1.12 A/mm2. Four regions in the pump duct near the edges of the current electrodes indicate large current densities ~ 1.4 A/mm2. This edge effect is caused by the movement of electrons toward regions of high geometric gradients. The results also show a gradual decrease in current density with increased distance along the z-axis until eventually reaching zero. The computation domain extending from the input and the exit of the pump duct shows the fringe currents (Fig. 3-13) flow paths in the top half of the pump duct and the downstream section of the duct. The flow lines of the electrical current across the pump duct are mostly uniform but experience a curvature when exiting the pump duct into the upstream and downstream regions Fig. 3-13.

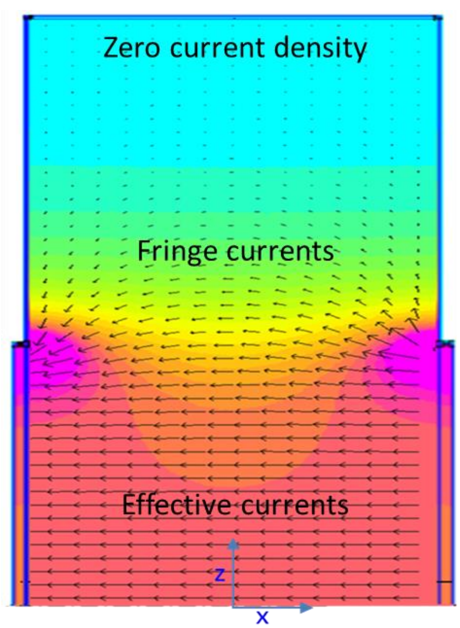

Figure 3-13: The calculated electrical current flow field in the duct of the mercury DC-EMP (Watt et al. 1957).

Integrating the calculated current flow fields in the pump duct and both upstream and downstream of the duct determines the effective current flow across the duct, I_{eo}, and the total fringe current, Ifo, respectively. The solutions of Eqs. 3-13 and 3-14 determine the total fringe resistance, R_{fo}, using the calculated fringe current and the current flow in the duct. The calculated total fringe resistance for the mercury DC-EMP using a largest numerical mesh element size of 0.2 mm in the FEMM analysis (Table 3-2) is 104.59 μΩ, which is only ~ 0.8% higher than the value of 103.78 μΩ obtained from the reported experimental measurement (Fig. 3-4a). This excellent agreement demonstrates the effectiveness and accuracy of the FEMM analysis for calculating the fringe resistance in DC-EMPs at zero flow. The next subsection presents the results of investigating the effect of changing the numerical mesh element size in the computation domain in the FEMM analyses on the calculated values of the total fringe resistance, R_{fo}, for the mercury DC-EMP (Watt et al. 1957).

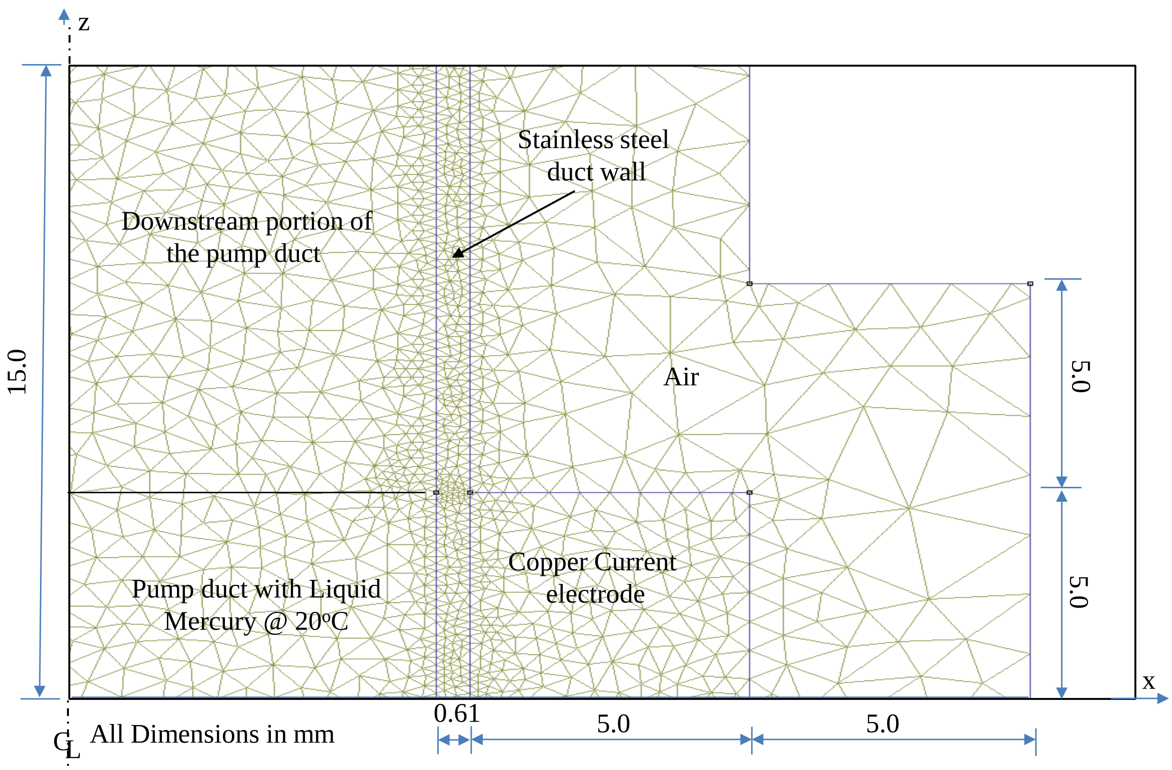

Fig. 3-14: Applied numerical mesh grid with largest mesh element size of ~ 2.0 mm in the FEMM software to calculate R_{fo} for the mercury DC-EMP with (Table 3-2).

3.5.1.2.Sensitivity analysis

Fig. 3-14 presents examples of the applied numerical mesh grid within the computation domain in portions of the pump duct and the upstream section of the duct. The size of the numerical mesh elements in the liquid region is largest at the center of the duct and decreases gradually with decreasing distance from the interface between the liquid and the inner surface of the duct wall. Near this interface, the size of the numerical mesh elements in the liquid is the smallest. Similarly, the size of the numerical grid mesh elements in the current electrode and the surrounding air within the computation domain is smallest near the interface with the outer surface of the duct wall. The mesh auto-generator in the FEMM software generated the numerical mesh grid within the computation domain (Fig. 3-14) with the largest mesh element size of ~2.0 mm in the ambient air region. Additional analyses are performed with finer numerical mesh grids with smaller sizes of 0.25 and 0.5 mm of the largest mesh elements to quantify the effect of numerical mesh refinements on the calculated values of R_{fo} for the mercury DC-EMP (Watt et al. 1957).

Table 3-2: Sensitivity of calculated values of R_{fo} for the mercury DC-EMP (Watt et al. 1957) using FEMM analysis to the largest mesh element size in the computational domain.

Parameter	**Largest mesh element size (mm)**		
	~ 2.0*	0.5	0.25
Calculated fringe resistance, R_{fo} (μΩ)	104.58	104.50	104.48
Total number of mesh elements Normalized value	46,650 1.0	538,861 11.55	2,108,441 45.2
Computation real time (s)** Normalized value	4.5 1.0	47.75 10.6	187.25 41.6

* Mesh auto-generator; **Using Intel octa-core i7-8665U CPU @ 2.1 GHz.

Table 3-2 compares the results of the performed analysis of calculating R_{fo} for the mercury DC-EMP, using the FEMM software with coarse and fine numerical mesh grids. Results show that increasing the refinement of the applied numerical mesh grid negligibly changes the calculated value of R_{fo} < 0.1% but significantly increases the total number of the numerical mesh elements in the computation domain and the computation time using the same hardware. The numerical mesh refinement with the computation domain decreases the size of the largest mesh element in the applied numerical grid in the FEMM analysis from ~2 mm to 0.5 and 0.25 mm. Therefore, a numerical mesh grid produced by the FEMM mesh auto-generator with the largest mesh element size of ~ 2 mm is a practical choice considering the large savings in the computation time (Table 3-2) without impacting the results.

It is worth noting that the calculated value of R_{fo} using the present FEMM analysis of 104.48 μΩ (Table 3-2) is only 0.56% higher than that obtained from the report experimental measurements (103.8 μΩ) for the mercury DC-EMP by Watt et al. (1957). In comparison, the suggested correlations of Watt (1959), Eqs. 3-9 and 3-10, and Baker and Tessier (1987), Eq. 3-11, overpredict the value of R_{fo} by 17% and 52%, respectively (Table 3-1). Consequently, the calculated characteristics of the mercury DC-EMP (Watt et al. 1957) using the ECM with the R_{fo} values based on the proposed expressions by Watt's (1959) and Baker and Tessier's (1987) are as much as 23.2% and 15.7% higher, respectively, than the reported measurements (Fig. 3-10).

The next subsection examines the accuracy of the FEMM software analysis for predicting the magnetic flux density at zero flow, B_o. It was not possible to calculate B_o for the mercury DC-EMP because Watt et al. (1957) did not report the needed magnet dimensions in the input to the FEMM analyses. Instead, the present work compared the calculated B_o value using FEMM analysis for a permanent magnet in an MHD thruster for seawater propulsion to the reported experimental value (Li et al., 2021).

3.5.1.3. Magnetic flux density at zero flow

The operation principle of an MHD thruster is like that of a DC-EMP. In the latter, the induced Lorenz force drives the liquid in the pump duct, while in the former this force moves the thruster relative to the liquid. The MHD thruster reported by Li et al. (2021) employs NdFeB (N35) permanent magnets, Aluminum electrodes, plastic electrical insulation, metal housing, and saltwater working fluid Fig. 3-15. The total length of the thruster is 100 mm, the square liquid flow region is 50 mm on the side, and the magnet is 10 mm thick. Li et al. (2021) measured the magnetic flux density along the y-axis at the mid-plane of the thruster liquid region (x = 0, z = 0) with the metal shell removed. Fig. 3-16 presents the reported measurements of the magnetic flux density along the y-axis. They are highest in the middle of the duct (y= +20 mm) and decrease rapidly with increased distance toward the two ends of the thruster. The measured values of the magnetic flux density are symmetric except near the ends of the thruster. The slight asymmetry may be due to imperfections in the manufacturing of the magnets.

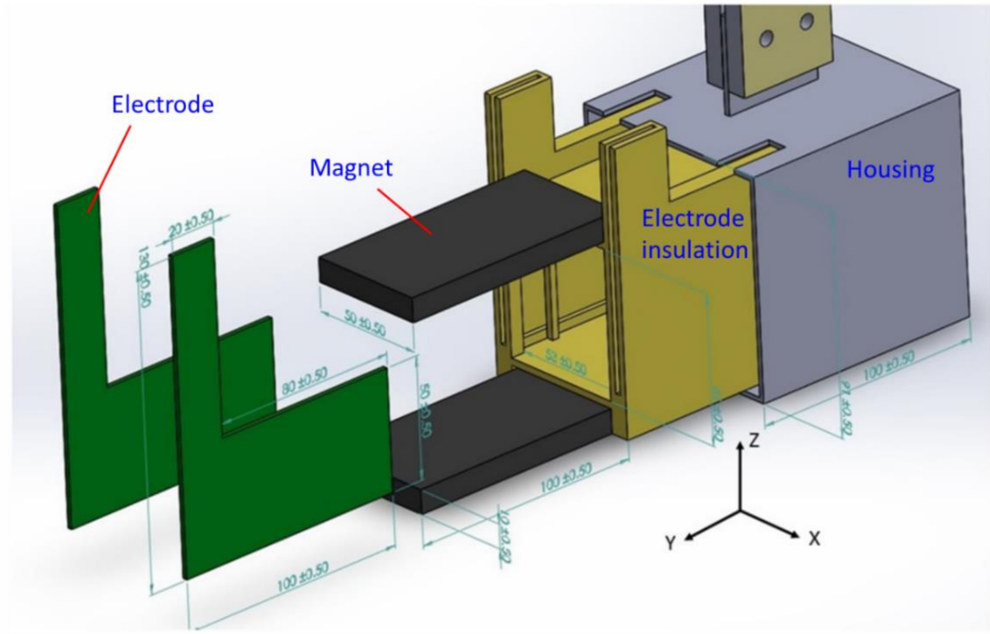

Figure 3-15: Isometric view of the MHD thruster of Li et al. (2021).

The present analysis compared the calculated values of the magnetic flux density along the y-axis of the thruster duct using the FEMM software to the reported measurements (Li et al., 2021) in Fig. 3-16. There is excellent agreement between the calculated and measured values of the magnetic flux density, across the thruster duct, except near the ends of the magnet where the calculated values are slightly lower than the reported measurements by Li et al. (2021), These differences, however, insignificantly affect the value of the average magnetic flux density, $\bar{B}_o$, based on the calculated lateral distribution of the local values in the thruster duct region. The determined value of $\bar{B}_o$, based on the reported measurements of the axial distribution of the magnetic flux density in Fig. 3-16 is ~ 9.955x10-2 T, compared to 9.962x10-2 T for the calculated value based on the FEMM analysis results, a difference of less than 0.1%. These results confirm the accuracy of the FEMM analysis for calculating the magnetic flux density for permanent magnets at zero flow.

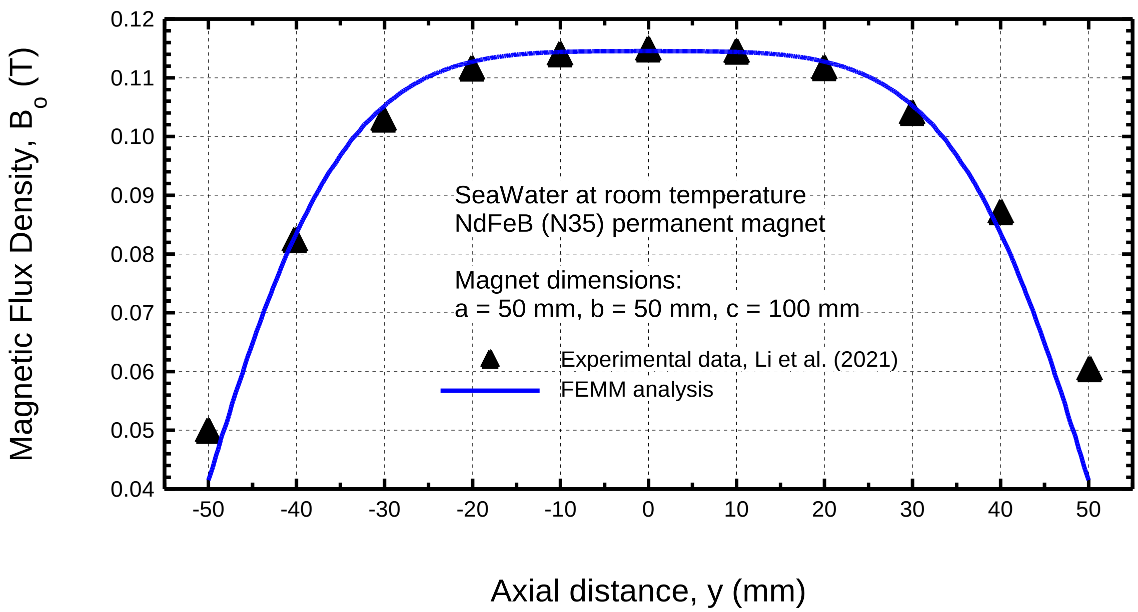

Figure 3-16: Comparison of the axial distribution of the measured values of the magnetic flux density for an MHD thruster (Li et al., 2021) at zero flow to that calculated using FEMM analysis.

3.6.Summary and Conclusions

The analysis of the reported experimental measurements for the mercury DC-EMP by Watt et al. (1957) determined the values of the total fringe resistance, Rf, and the magnetic flux density, B, in the pump duct and their dependence on the electrodes' electrical current and the flow rate of mercury at 20 ^{o}C. Results show that Rf increases with decreased electrical current and increased flow rate of liquid mercury, while the magnetic flux density decreases with increased flow rate and decreased electrical current. Results also show that the pumping pressure decreases with increased flow rate of mercury and/or decreased electrical current. The pump static pressure at zero flow increases linearly with increased electrical current While the values of the fringe resistance and the magnetic flux density at zero flow, R_{fo}, and B_o, respectively, are independent of the value of the electrical current. The present ECM analysis uses these values and that of the measured wall contact resistance to predict the pump characteristics and compare them to the reported measurements.

The present work investigated using the current flow package of the 2-D FEMM software for calculating R_{fo} for the Mercury DC-EMP. The calculated value is in excellent agreement with that from the reported measurement to within 0.8%. The present analysis used the FEMM magnetic package to calculate B_o, of NdFeB (N35) permanent magnet for an MHD thruster of Li et al. (2021). The average value of 9.962x10-2 T calculated using the FEMM software is within only 0.1% of that measured, ~ 9.955x10-2 T. These results confirm the accuracy of the FEMM software for calculating R_{fo} and B_o for DC-EMPs. Incorporating the values for the mercury DC-EMP (Watt et al. 1957) into the ECM analysis, the predicted characteristics at different electrical current values are consistently higher than the reported measurements by < 10%, depending on the value of the electrical current. These ECM results show that neglecting the measure wall electrical contact resistance of 13 μΩ decreases the ECM predictions of the pump characteristics by ~ 0.2% - 1.4%, depending on the liquid mercury flow rate.

Therefore, the ECM may be used to perform parametric analysis and predict the performance of DC-EMP designs prior to construction using the calculated values of R_{fo} and B_o by the FEMM software, based on the selected dimensions of the liquid flow duct, electrical current electrodes, and the magnet. However, although are consistent with those of the actual pumps after construction, the ECM predictions can overestimate the pump characteristics but by ~ <10%. This is due to neglecting the effects of the liquid flow and the electrical current on the fringe resistance and the magnetic flux density in the pump duct, and the electrical contact resistance of the duct wall.

4. DESIGN AND PERFORMANCE ANALYSES OF MINIATURE, DUAL-STAGE DC-EMP

4.1 Introduction

Alkali metals of sodium and sodium-potassium alloys and heavy metals of molten lead and Lead Bismuth Eutectic (LBE) coolants have been employed as coolants in nuclear reactors for terrestrial and space power generation (IAEA, 2008; El-Genk, 2009, Al-Habahbeh et al., 2016). In addition to their low vapor pressures at elevated temperatures, these liquids offer attractive features of increasing the rate of heat removal from the nuclear fuel rods and operating nuclear reactors at high power densities and plant thermal efficiency for electricity generation (Locatelli, 2013). Among pumping options for circulating alkali and heavy metals in nuclear power applications, Direct Current-Electromagnetic Pumps (DC-EMP) offer design simplicity, passive operation with the absence of moving parts, and high operation reliability. They can also operate immersed in the coolant of choice (Baker and Tessier, 1987; IAEA, 2008).

Small size DC-EMPs with either permanent magnets or self-induced electromagnets have and are being considered for space reactor power systems and in-pile and ex-pile liquid metals test loops or cartridges for investigating material compatibility (Johnson, 1973; El-Genk, 2009; IAEA, 2013). Large DC-EMPs, with electromagnets, have been used to circulate alkali and heavy liquid metal coolants in commercial nuclear reactors and various industrial applications (Daoud and Kandev, 2008; IAEA, 2008; Deng et al., 2013; IAEA, 2020). Small DC-EMPs with thermoelectric energy conversion elements for DC power generation had been used for circulating liquid NaK-78 at 543^{o}C in the primary loop of the SNAP-10A space nuclear reactor power system launched by the United States in 1965 (Perlow, 1964; Davis, 1966) and for circulating molten lithium in the US SP-100 nuclear reactor power system (Wright, 1985; El-Genk and Rider, 1990; Mondt et al., 1994). The DC-EM for the SNAP-10A power system had two Alnico 5 horseshoe magnets with iron pole pieces that generated a magnetic field flux density of 0.24 T. The magnet's temperature was maintained below 298^{o}C using radiative cooling into space. A radiator with aluminum fins also rejected the waste heat from the thermoelectric elements for the pump into space. The NaK-78 flow duct of the SNAP-10 A pump was 25.4 mm wide, 87.6

mm long, and 10.16 mm high. This pump produced a pressure head of 7.58 kPa at a flow rate of 3 m^3/h and current provided by thermoelectric elements was 534 A at a terminal voltage of 0.32 VDC.

Johnson (1973) has designed and measured the performance of a double-throat DC-EMP for circulating liquid NaK-78 in space nuclear reactor power systems at 316°C. The pump's Alnico 5 magnets with hiperco-50 pole pieces and an iron yoke provided a magnetic field flux density in the pump duct of 0.235T. The pump duct was 12.7 mm high, 24.9 mm wide, and 58.4 mm long. At an electrode current of 1,570A, the pumping pressure at a volumetric flow rate of 6.3 m^3/h was 14.5kPa. Polzin and Godfroy (2008) have designed and evaluated the performance of a DC-EMP for circulating NaK-78 at temperatures up to 607°C in a test loop in support of NASA's effort to develop affordable Fission Surface Power (FSP) systems to use on the lunar surface. The selected high strength Neodymium magnets for this pump have a low curie point of 80 - 100°C. The pump flow duct was 1.59 mm high, and 95 mm wide and long. The FluxTrol pole pieces of the magnet helped focus the magnetic field flux density in the flow duct and minimize losses to the surroundings. They used a water-cooled copper block to maintain the magnet's temperature below its curie point Polzin and Godfroy (2008). At an electrode current of 110A and terminal voltage of 0.02 VDC, the performed analysis of the pump showed a uniform magnetic field flux density of 1.05 T in the flow duct and predicted a pumping pressure of 34.5 kPa at a Nak-78 volumetric flow rate of 0.114 m^3/h.

Kim et al. (2014) have designed a DC-EMP for circulating liquid sodium to remove the decay heat from a Prototype Gen. IV Sodium-cooled Fast Reactor (PGSFR). The pump is to operate at 195°C and employs a samarium-cobalt permanent magnet with a soft iron yoke to generate a magnetic field flux density of 0.134T in the flow duct, 150 mm wide, 74.8 mm long, and 20.8 mm high. At an electrode current of 5,671A and a terminal voltage of 0.106 VDC they predicted a pump efficiency of 8.31%, and gross and net pumping pressures of 14.34 KPa and 10.0 KPa, respectively, at a sodium flow rate of 18 m^3/h.

Lee and Kim (2017) have designed and fabricated a much smaller DC-EMP with a samarium-cobalt permanent magnet for circulating liquid sodium in an experimental test loop at 300°C. The pump flow duct was 38.4 mm wide, 1.8 mm high, and 90 mm long. At electrode currents of 116 A, they predicted a net pumping pressure of 5 KPa at a sodium flow rate of 0.18 m^3/h and pump efficiency of 27.2%. Most recently, Lee and Kim (2018) developed a small DC-EMP for circulating liquid lithium in a heavy-ion accelerator at 200^{o}C and flow rate of 6 cm^3/s. The pump flow duct was 1.0 mm high, 22 mm wide, and 216 mm long. At an electrode current of 3,740 A, the pump provides a net pressure head of 1.5 MPa at a rate of 6 cm^3/s.

In summary, reported permanent magnet DC-EMPs have been designed and employed for circulating alkali liquid metals of sodium, NaK-78, and lithium at temperatures ranging from 196 to 607^{o}C. External cooling by radiation into space or forced convection has been employed to maintain the magnet temperature below a set point lower than their curie points. Radiatively cooled DC-EMPs have been used and considered in space nuclear reactor power systems. The reported pump designs for circulating liquid metals for decay heat removal systems, heavy-ion accelerators, and out-pile test loops, are actively cooled by forced and natural convection of either air or water.

Recently, there has been an interest to develop submerged miniature DC-EMPs for circulating liquid sodium and molten lead in both self-enclosed ex-pile and in-pile loops for materials development and compatibility investigation at elevated temperatures ($\geq$ 500^{o}C). This supports the development of Gen-IV (IAEA, 2012; Gougar et al., 2015; McDuffee et al., 2019; Quan et al., 2020; El-Genk et al., 2020) advanced sodium fast reactors (SFRs) and Lead fast Reactors (LFRs). An example is the Extended Length Test Assembly-Cartridge Lead (ELTA-CL) (Fig. 1-1), a molten lead, self-enclosed in-pile test loop for testing the compatibility of nuclear fuel, cladding, and reactor structure materials with circulating molten lead up to 700^{o}C in a prototypical irradiation environment in the Versatile Test Reactor (VTR) (McDuffee et al., 2019; El-Genk et al., 2020; Kim et al., 2022). This in-pile test cartridge, and a VTR in-pile test loop for liquid sodium (Quan et al., 2020), are to be placed at designated locations within the core of the sodium cooled, fast neutron spectrum, 300 MW_{th} VTR (Roglans-Ribas et al., 2022). The VTR provides prototypical high-temperature irradiation environments to qualify and evaluate the compatibility of advanced nuclear fuels and high-temperature reactor structure materials with different coolants, including molten lead, liquid sodium, helium gas, and molten salt (McDuffee et al., 2019; El-Genk et al., 2020; Farmer et al., 2022; Kim et al., 2022; Roglans-Ribas et al., 2022).

Various pumping options investigated for circulating molten lead up to 500°C in the ELTA-CL without active cooling (El-Genk et al., 2020) include submerged miniature DC-EMP, submerged miniature Annular Linear Induction Pump (ALIP), gas lift pumping, and axial-centrifugal flow miniature mechanical pump (El-Genk et al., 2020). These pumps with diameters of 57 and 66.8 mm fit within the riser tube above the text article in the ELTA-CL (Fig. 1-1) of 3 rodlets in a triangular lattice. Therefore, the objective of this chapter is to develop designs and evaluate the performance of submerged, dual-stages, miniature DC-EMPs for circulating molten lead and liquid sodium at ≤500°C without active cooling in the ELTA-CL and similar in-pile and ex-pile test loops.

The developed designs in this work are for pump diameters of 57mm, 66.8mm, 95.4 mm, and 133.5 mm that fit within 2, 2 ½, 3 ½, and 5 inches standard stainless-steel pipes, respectively. Each pump has two Alnico 5 permanent magnets with Hiperco-50 pole pieces for focusing the magnetic field lines in the flow duct and reducing losses to the surrounding. The Equivalent Circuit Model (ECM) and the Finite Element Method Magnetics (FEMM) software are linked in MATLAB platform to calculate the performance characteristics of these pumps for a wide range of parameters and determine the dimensions for the highest cumulative pumping power and peak efficiency. These dimensions are the height and width of the flow duct, the thickness of the magnets, the length of the current electrodes, and the separation distance between the two pumping regions. The FEMM software calculates the magnetic flux and electrical current densities in the flow duct within the two pumping regions, and the fringe resistances at zero flow.

The ECM model for calculating the pump characteristics neglects the wall interfacial resistances, joule heating, and the effect of liquid metal flow on both the magnetic flux density and the fringe resistance in the flow ducts. Instead, it employs the calculated values of the magnetic field flux density and fringe resistance using the FEMM software at zero flow. In Chapter 3 of this Dissertation, it has been shown that the ECM overestimated the experimentally measured characteristics for a mercury DC-EMP by less than 7% attributed to the above-mentioned assumptions (Watt et al., 1957 and Altamimi and El-Genk, 2022). Therefore, the current approach for optimizing the dimensions and the performance of the present miniature DC-EMP designs would be comparatively and preliminary acceptable, subject to future fabrication and experimentally testing of the present miniature DC-EMP designs.

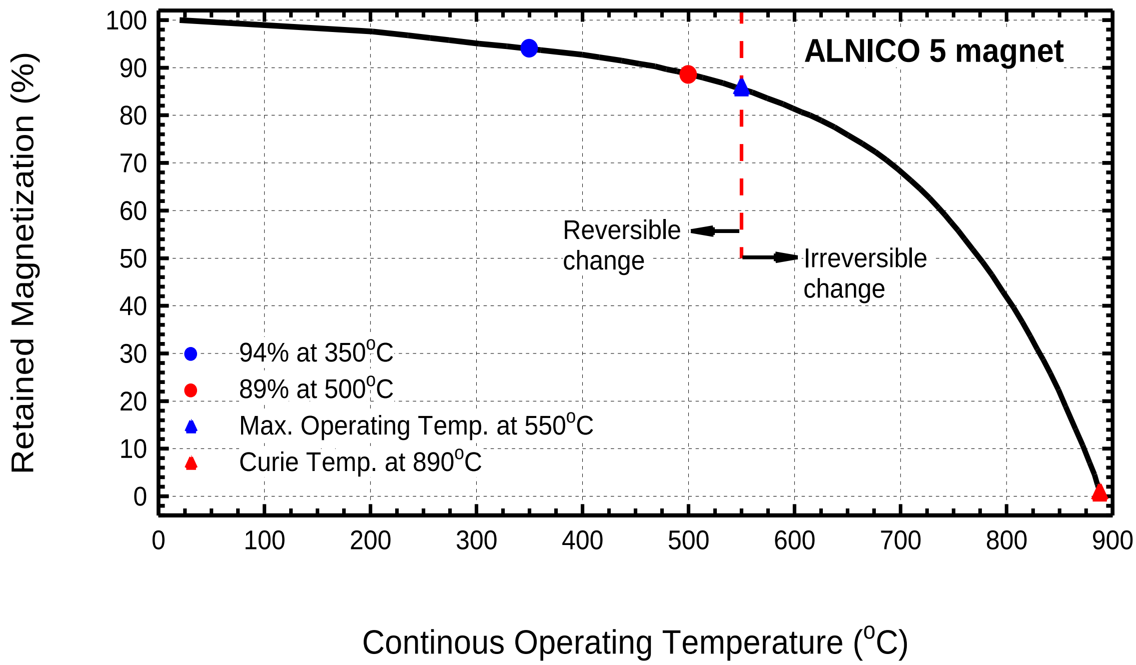

Figure 4-1: Temperature demagnetization of Alnico 5 permanent Magnet (Moskowitz, 1995).

4.2. Design layout and material selection

To develop submerged miniature DC-EMP designs for circulating molten lead and liquid sodium at temperatures of up to 500°C it is important to select suitable materials of the permanent magnet and the test loop structure. Among commercially available materials for permanent magnets, Alnico alloys, with 8–12wt.% aluminum (Al), 15–26wt.% nickel (Ni), 5–24wt.% Cobalt (Co), up to 6wt.% Copper (Cu), up to 1wt% Titanium (Ti), and the rest iron (Fe), have excellent temperature stability and capable of operating at temperatures exceeding 500°C (Moskowitz, 1995; Heck, 2013; Rehman et al., 2018). The Alnico 5 alloy comprised of 8% Al, 14% Ni, 24% Co, 3% Cu copper, and the balance of 51% Fe, is the most widely used due to its high magnetic remanence and energy product $(BH)_{max}$ (Arnold Magnetic Technology, 2003). In addition, at 500°C, Alnico 5 magnets maintain 89% of their residual magnetic field strength at room temperature and experience no permanent reduction of magnetization strength up to 550°C (Fig. 4-1). Further increase in temperature, however, irreversibly decreases the magnetic field strength until reaching the curie point of 890°C at which the magnet becomes paramagnetic (Moskowitz, 1995).

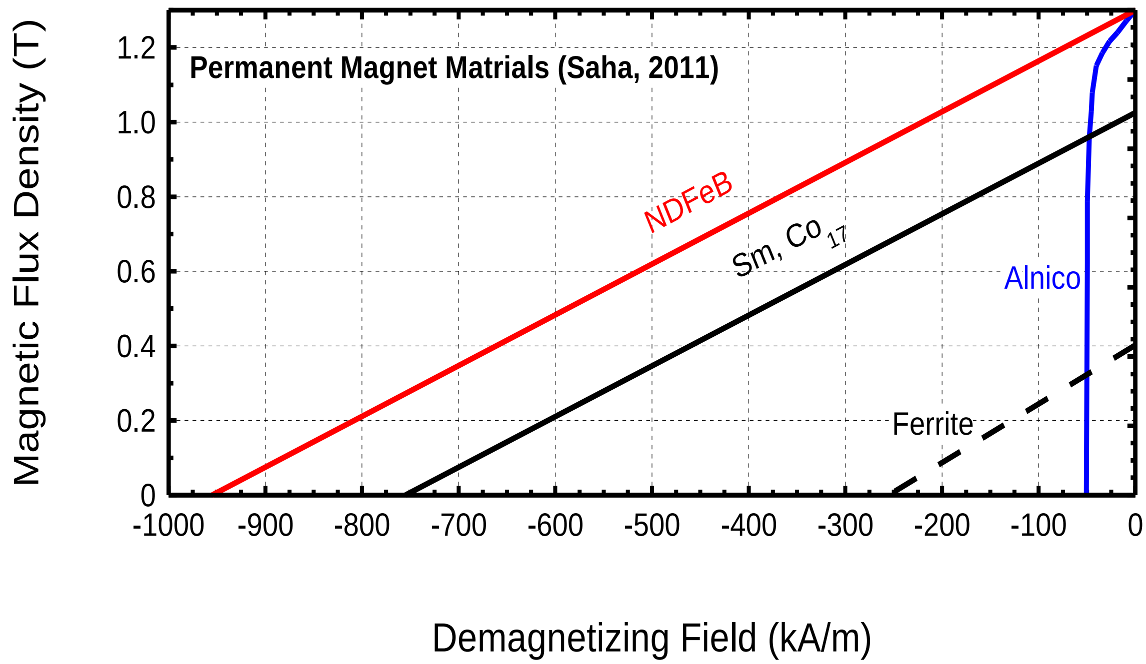

Figure 4-2: Demagnetization curves of permanent magnet materials (Saha, 2011).

Despite their excellent magnetic stability at elevated temperatures and high magnetic field strength, Alnico magnets have a low coercive force compared to other permanent magnets and a sharp decrease in the B-H curve after the knee point (Fig. 4-2) (Saha, 2011). Therefore, to avoid self-demagnetization the magnet's effective length-to-diameter ratio, and consequently, the permeance coefficient (P_c =B/H) need to be large enough to operate above the knee of its demagnetization curve (Maroufian and Pillay, 2019). For best performance, the length of the Alnico 5 magnet is recommended to be 4 to 5 times the pole equivalent diameter (Moskowitz, 1995). Thus, using Alnico 5 permanent magnets in typical DC-EMP designs (Fig. 2-10) will increase the pump diameter, beyond those of the present miniature pumps for circulating molten lead and liquid sodium in-pile test loops in the VTR.

To comply with recommended aspect ratio of the Alnico 5 magnets, the developed designs of the miniature DC-EMP employ two Alnico 5 permanent magnets with opposite magnetizing directions along the length of the rectangular flow duct (Fig. 4-3a). This arrangement satisfies the magnets' effective length to equivalent diameter to minimize self-demagnetization. In addition, the present miniature DC-EMP designs (Fig. 4-3) have small diameters and two successive pumping regions for enhanced performance. For the same flow direction along the pump duct, the magnetic flux density, and the electrode electrical current in the two pumping regions are in opposite directions. The magnetic field lines in the two pumping regions of the developed miniature DC-EMP (Fig. 4-3) extend between the two magnet poles and across the liquid metal flow duct in a perpendicular direction to both those of the electric current and induced liquid flow (Figs. 4-3 and 4-4).

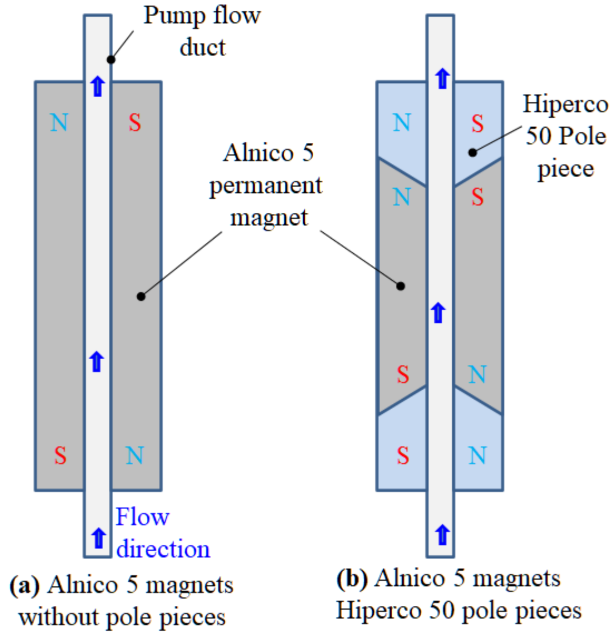

Figure 4-3: Arrangement of the Alnico 5 magnets: (a) without pole pieces, and (b) with Hiperco-50 pole pieces for developed miniature DC-EMP with two pumping regions.

Fig. 4-4a presents the calculated distribution of the generated magnetic flux by the Alnico 5 magnets using the FEMM software for zero molten lead flow at 500°C in 66.8 mm diameter pump of the developed design (Fig. 4-3). The generated magnetic flux densities in the two pumping regions are similar but not uniform with a large part traveling outside the pump duct. This decreases the produced Lorentz force for driving the liquid metal flow in the pump duct. However, attaching pole pieces of high magnetic permeability material at both ends of the Alnico 5 magnets (Fig. 4-3b) redirect and focus the magnetic field lines across the flow duct and reduce losses to the surrounding (Fig. 4-4b). A suitable choice for pole pieces material is Hiperco-50, which has one of the highest magnetic permeabilities of commercially available soft magnets, and a high curie point of ~940°C

(Jayaraman, 2015). With Hiperco pole pieces attached to Alnico 5 magnets, the magnetic field lines travel in straight lines and at uniform flux densities across the flow duct in the two pumping regions, which help improve the pump performance (Figs. 4-4b and 4-5). As indicated in Fig. 4-5, the effective magnetic flux densities are uniform in the two pumping regions using the FEMM software for stagnant molten lead in the pump duct at 500°C. This suggests that the generated Lorentz force in the two pumping regions and the performance of the present pump designs (Fig. 4-3) using Alnico 5 permanent magnets with Hiperco-50 pole pieces would be higher than without pole pieces.

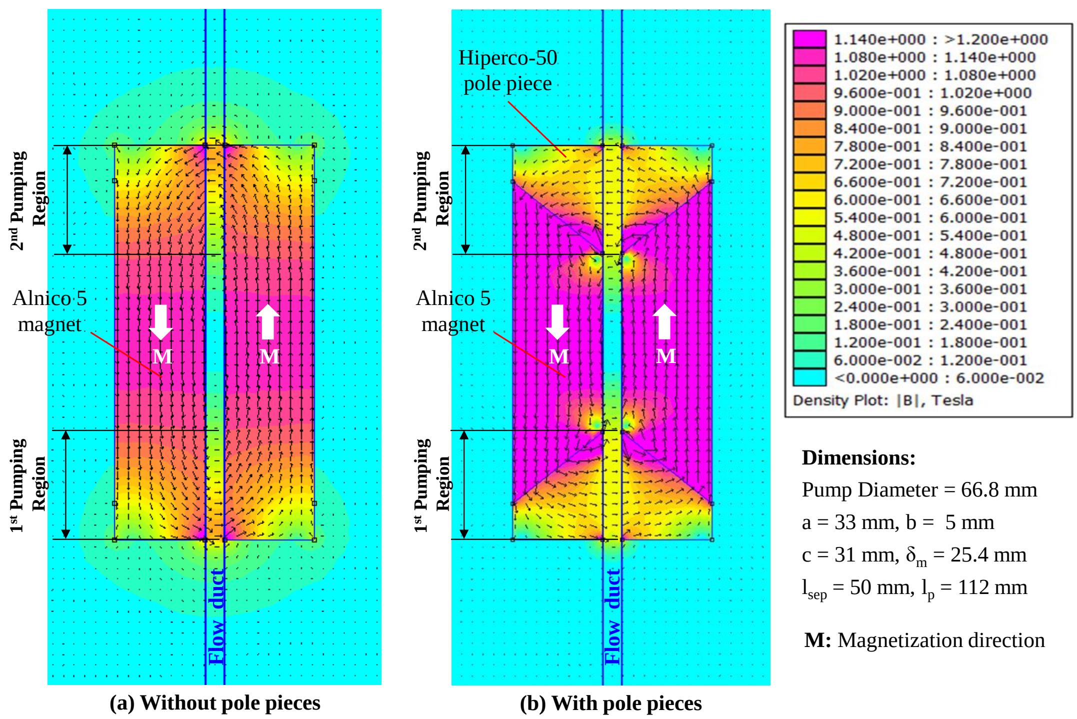

Figure 4-4: Calculated magnetic flux distributions produced by the Alnico 5 magnets: (a) without pole pieces, and (b) with Hiperco-50 pole pieces, at zero flow of molten lead at 500 °C for representative dimensions of the developed miniature DC-EMP design.

The calculated axial distributions of the magnetic flux density using the FEMM software in the flow duct center of the miniature dual-stages DC-EMP (Fig. 4-5) confirm the effectiveness of the Hiperco-50 pole pieces in redirecting and focusing the magnetic field across the duct (Fig. 4-4b and 4-5). These distributions are the same in the two pumping regions, dropping to zero at mid-point of the separation distance between the current electrodes. The effective magnetic flux density contributing to the Lorentz force generation in the pump duct increased by 5.2%, from 0.5165 T to 0.5432 T, when attaching the pole pieces to the Alnico 5 magnets (Fig. 4-4 and 4-5).

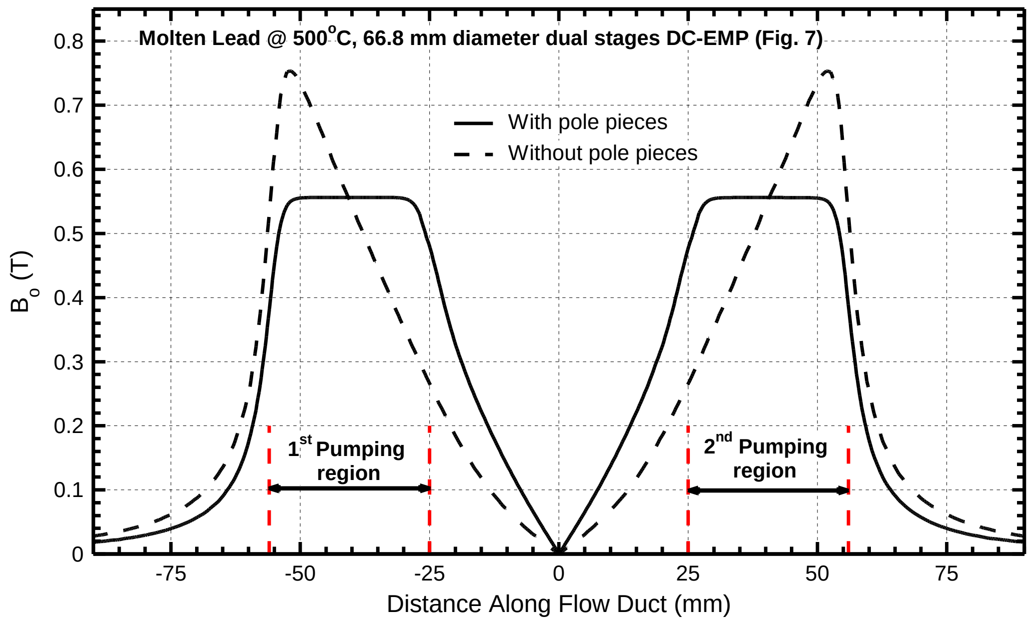

Figure 4-5: Calculated axial distribution of magnetic field flux density at zero flow molten lead at 500 °C in a miniature, dual-stages 66.8 mm diameter DC-EMP of representative dimensions (Table 4-3).

In addition, the pole pieces redirect the magnetic fields lines in the flow duct to produce a uniform Lorentz force in the flow direction. Without the pole pieces, the magnetic field travels across the duct in curvature paths, reducing the Lorentz force in the flow direction and hence, the pumping pressure and the pump efficiency. Noting that the increase in the effective magnetic flux density would vary with the pump design dimensions. The magnetic flux density in the flow duct in the two pumping regions is almost uniform when attaching Hiperco-50 pole pieces but drops rapidly outside these regions. Such drops represent a small loss which does not contribute to the generated Lorentz force in the duct within the two pumping regions (Figs. 4-4b and 4-5). The total pumping pressure is the sum of those produced by the Lorentz force in the two pumping regions.

As delineated in Fig. 4-6, the developed miniature, dual-stages DC-EMP designs (Fig. 4-7) experiences electrical current leakage (I_{le}) or exchange between the electrodes in the two pumping regions. Fig. 4-6 presents the calculated electric current distribution using the FEMM software in the pump duct for zero molten lead flow at 500°C. The leakage current,

I_{le}, from pumping region 2 to the lower pumping region combines with the main current exiting the electrode. Similarly, the leakage current from pumping region 1 flows upward and combines with the current exiting the electrode in pumping region 2 (Fig. 4-6).

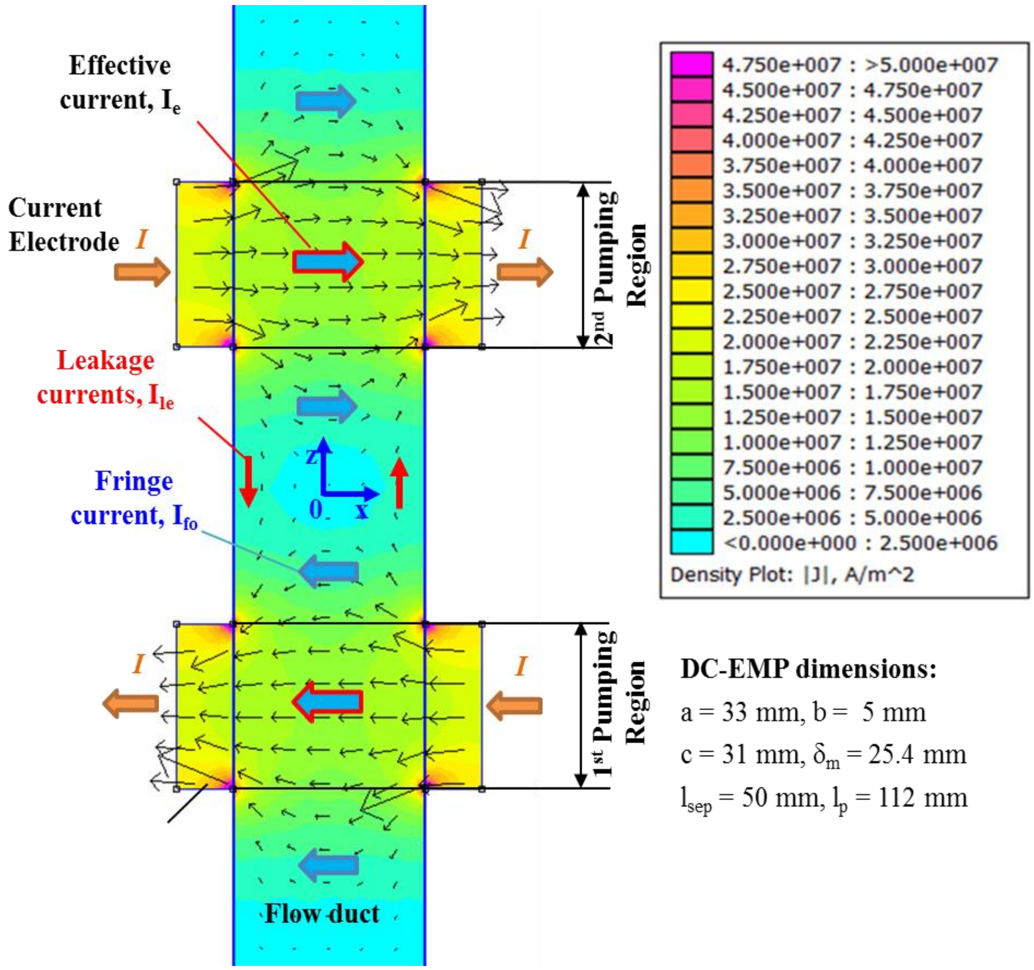

Figure 4-6: Calculated distributions of the electrical current at zero molten lead flow in the miniature dual-stages DC-EMP.

The leakage currents decrease the effective current (I_e) flowing across the flow duct in the two pumping regions and hence the pumping pressure and the performance of the pump. The magnitudes of the leakage currents are inversely proportional to the separation distance (l_{sep}) between the current electrodes in the two pumping regions (Fig. 4-7), which also depends on the total length of the two Alnico 5 magnets. Therefore, the separation distance between the two pumping regions, l_{sep}, in the present design of the miniature DC-EMPs of different diameters needs to be large enough to minimize the leakage currents without excessively increasing the total length of the pump, L (Fig. 4-7).

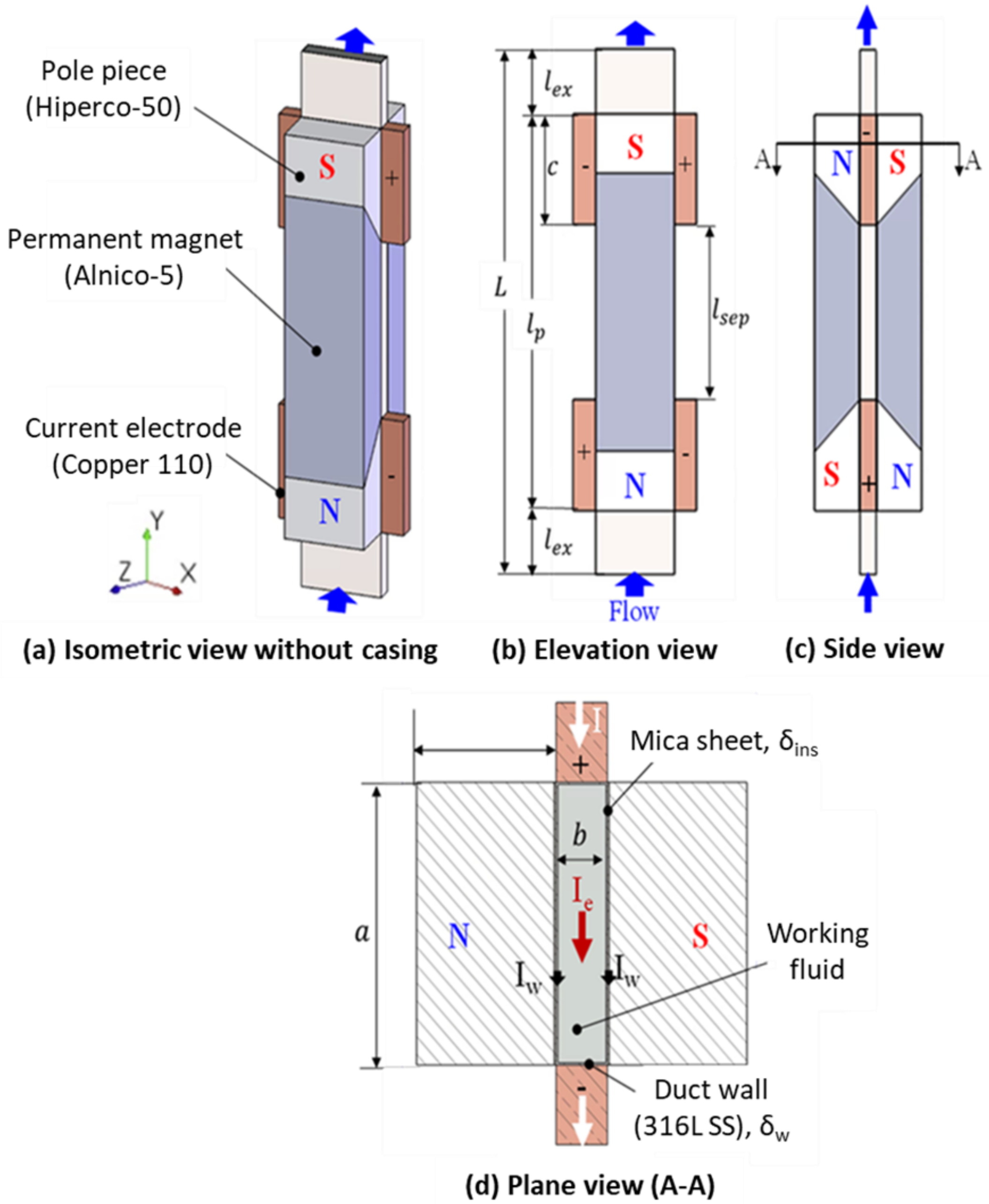

Figure 4-7: Isometric and cross-sectional views of the developed miniature DC-EMP design with two pumping regions of molten lead or sodium at < 500 ^{o}C.

For the 66.8 mm diameter miniature DC-EMP analyzed, the calculated percentage of the leakage currents from input current of 3.5% is considered losses as it does not contribute to the generated Lorentz force in the pump duct (Fig. 4-6). Only 65% of the pump input current travels across the flow duct in the two pumping regions and contributes to the generation of the Lorentz force for driving molten lead flow through the pump duct and hence the generated pumping pressure (Fig. 4-6). In addition, the calculated fringe currents, I_{fo}, upstream and downstream of the two pumping regions, which represent 31.5% of the input electrode currents, are also considered as losses. Their contribution to the generated Lorentz force in the two pumping regions is negligible due to the small magnetic field in the fringe region (Figs. 4-4b and 4-5).

Figure 4-7 presents isometric and cross-sectional views of the developed design of the submerged miniature DC-EMP with two pumping regions for molten lead and liquid sodium at $\leq 500^{o}$C and without active cooling. The length of the two pumping regions equals that of the current electrodes, 2c. The entrance and exit extensions of the rectangular flow duct each is l_{ex} long, help produce a uniform and hydraulically developed liquid flow in the pump duct and minimize the flow entrance and exit effects, and hence, the total pressure losses along the pump duct. In the first and second pumping regions, the magnetic field generated by the Alnico 5 magnets and the supplied electrical currents in perpendicular directions produce the Lorentz force for driving the flow. The length of the flow duct between the two pumping regions equals the separation distance, l_{sep}, between the two current electrodes and affects the magnitudes of the effective currents in the pumping regions, I_e, and the leakage currents, I_{le}, exchanged between the two regions (Figs. 4-6 and 4-7). The contribution to the Lorentz force and the pumping pressure by the interaction of the fringe currents and fringe magnetic fields is negligible.

The magnet structure in the second pumping region has an opposite polarity and magnetic flux direction to those in the first pumping region (Figs. 4-4b and 4-7c). Similarly, the electrical currents in the two regions are supplied in opposite directions so that the generated Lorentz force acts in the flow direction (Figs. 4-6 and 4-7b). The dimensions of the flow duct in the two pumping regions (length (c), width (a), and depth (b)) and the thickness of the duct wall, δ_w, are the same for pump diameters (Fig. 4-7d). The thickness of the electrical insulation (δ_{ins}) between the flow duct and the Hiperco-50 pole pieces and Alnico 5 magnets minimize the distortion and the decrease in the magnetic flux density across the flow duct and the decrease in the effective electric current due to the induced opposing electromagnetic force due to the liquid flow in the generated magnetic field.

In addition to the Alnico 5 permanent magnets that are mechanically attached to the Hiperco-50 pole pieces, other selected materials are 316L stainless steel for the walls of the flow duct and the pump casing and support structure, Copper 101 for the current electrodes, and Mica sheets for electrically insulating the Alnico 5 magnets and Hiperco-50 pole pieces from the duct wall. These materials are compatible with Molten lead and sodium at temperatures of $\leq 500^{o}C$ and have desirable thermophysical properties. The 316L stainless steel has good corrosion resistance and excellent weldability (Zhang, 2009). Copper 101 has one of the highest electrical and thermal conductivities at elevated temperatures of commercially available electrical conductors. It is easy to machine and cold work and suitable for high electric current densities at elevated temperatures (Eldrup and Singh, 1998). The copper electrodes and the 316L stainless steel duct walls are joined by brazing while the Alnico 5 permanent magnets and the Hiperco-50 pole pieces are mechanically fastened to the 316 stainless steel structure. Finally, the Mica sheets have high electrical resistivity and can withstand high currents at elevated temperatures (Zaharescu, 2006).

4.3.Pump dimensions optimization model

The performed analyses to calculate the characteristics of the developed DC-EMP design with two pumping regions for different diameter pumps are conducted using the lumped parameters ECM (Baker and Tessier, 1987; Lee and Kim, 2017). In these analyses, the ECM is linked to the FEMM software for calculating the magnetic field flux density and the fringe and leakage currents for zero flow of molten lead and sodium at $\leq 500^{o}C$. The FEMM numerically calculates the magnetic flux density, B_o, in the two pumping regions, the fringe resistances, $R_{fo,}$ and the leakage currents, I_{le}, at zero flow by solving magnetostatics and electrostatics relations for the pump geometry (Meeker, 2015).

Despite the simplicity and ease of application, the ECM has several assumptions that affect the accuracy of predicting the performance pumping characteristics (Watt et al., 1957; Altamimi and El-Genk, 2023). The values calculated by the FEMM software are used in the ECM performance analyses, neglecting the effect of liquid metal flow on the effective magnetic flux density, fringe resistances, and leakage currents. Other assumptions in the ECM include uniform magnetic flux and electrical current densities in the flow duct in the two pumping regions and neglecting the liquid-wall thermal and electrical contact resistances and the effect of joule heating on the temperature and hence the electrical resistances of flowing liquid and the wall of the pump duct.

According to the results reported in Chapter 3 of this Dissertation for a single pumping region mercury DC-EMP (Altamimi and El-Genk, 2023), the measured magnetic flux density at zero flow and 20°C and the deduced values of the fringe resistance, R_{fo}, from the experimentally reported performance characteristics at different flow rates and electric currents, were used in the ECM to calculate the characteristics of the mercury DC-EMP (Altamimi and El-Genk, 2022). Results showed that the predictions of the ECM of the pumping pressure were < 7% higher than reported measurements of the pump characteristics at different flow rates and electrical currents (Watt et al., 1957). In the same study the estimates of the FEMM software of the values of B_o and R_{fo} used in the ECM performance analyses were within 1% of those deduced from the reported measurements by Watts et al. (1957). Thus, despite the inherent assumptions in the ECM, the obtained results are considered useful for performing parametric analyses of the present design of dual-stages miniature DC-EMPs designs of different dimensions and determining those for achieving highest cumulative pumping power, PP_{cu}, and peak efficiency, η_{peak}.

The parametric analyses link the ECM and the FEMM software to a developed model for screening the generated results for the duct dimensions of the pumps of different diameters for maximizing the cumulative pumping power and the peak efficiency. These dimensions include the flow duct height, b, and width, a, the magnet thickness, δ_m, the length of the current electrodes, c, the separation distance between the pumping regions, l_{sep}, and the pump total length. The next subsections briefly describe the ECM used in the present performance analyses (Baker and Tessier, 1987), the FEMM software, and the pump dimensions selection model.

As indicated earlier, the values of magnetic flux density, fringe resistance, and leakage currents in the ECM performance analyses for molten lead and liquid sodium are calculated using the FEMM software at zero flow and 500°C. The easy to use and fast running FEMM software is an open-source suite of programs for solving 2D and axisymmetric magnetics, electrostatics, and heat and current flow problems (Baltzis, 2008). It discretizes the geometry and computational domain into a triangular first-order grid of finite cell elements. This software applies traditional variation formulation to solve relevant partial differential equations using a user defined or built-in libraries of the physical, thermal, electrical, and magnetic properties of the working fluid and structural materials (Meeker, 2015). The software inspects the solutions fields at arbitrary points, contours, or 2-D distributions of the geometry for exporting or plotting various parameters of interest. The calculated values of the magnetic flux and electrical current densities, fringe resistance, and leakage currents for zero flow at ≤ 500°C are used in the input to the ECM to calculate the performance characteristics of the developed dual-stages, miniature DC-EMP designs in the present work, subject to the inherent ECM assumptions discussed earlier.

In this work, written scripts in MATLAB platform fully control the FEMM software (Meeker, 2015) for implementing and solving the governing equations and extracting the calculated values of electrical and magnetic parameters. These scripts also link the FEMM software to the ECM also written in MATLAB scripts, to conduct performance analyses of the developed miniature DC-EMP designs. This linkage is quite effective in determining the pump dimensions for the highest cumulative pumping power, PP_{cu}, and peak efficiency, η_{peak}. Such linkage saves much computational time as the developed pump performance database involves a considerable number of FEMM-ECM simulations of the present designs (Fig. 4-7) for different diameter pumps.

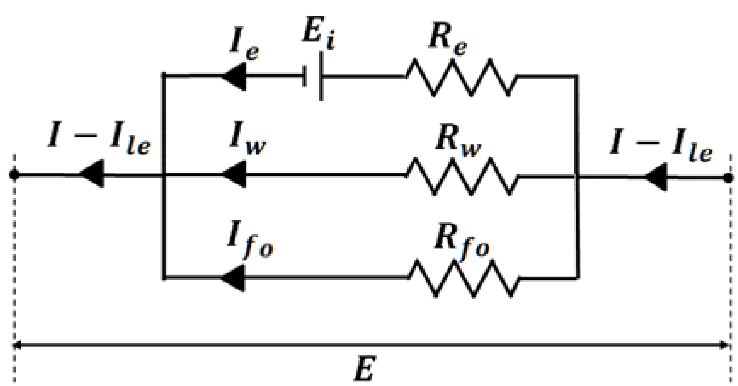

Figure 4-8: Electrical circuit diagram for one of the two pumping regions in the developed miniature DC-EMP designs (Fig. 4-9).

4.3.1. ECM for Dual-stage DC-EMP

The ECM is widely used for analyzing the performance of DC-EMPs, subject to the simplifying assumptions detailed earlier. Because of its simplicity and low computational requirements, ECM is a first order designing tool (O'Grady et al., 2021). It is used in the present work to estimate the performance and conduct parametric analyses of the miniature dual pumping regions DC-EMP designs developed in this work (Fig. 4-8). These are for pump diameters of 57, 66.8, 95.4, and 133.5 mm for molten lead and liquid sodium flows at $\leq 500^{o}$C (Fig. 4-8). Fig. 4-9 presents an electrical circuit diagram for one pumping region of present pump designs (Fig. 4-8).

The supplied electrode electric current, I, at a terminal voltage, E, is the sum of those passing through the flowing liquid in the pump duct, I_e, the duct walls, I_w, the fringe currents, I_{fo}, up and downstream of the pumping region, and the leakage current, I_{le}, to the other pumping region (Fig. 4-6). Only the effective current, I_e, contributes to the generated Lorentz force for driving the liquid flow and the corresponding pumping pressure, ΔP_P. As shown in Fig. 4-8, the ECM accounts for the opposing emf, E_i, induced in the pump duct by the flow of the electrically conductive working fluid in the perpendicular direction to that of the generated magnetic field by the Alnico 5 magnets. The generated pumping pressure, ΔP_p, to drive the liquid flow through the pump duct in one of the pumping regions is expressed as:

$$\Delta P_p = \left[\frac{B_o}{b(R_w R_{fo} + R_e R_w + R_{fo} R_e)}\right]\left[R_w\, R_{fo}\,(I - I_{le}) - \left(\frac{B_o\,(R_w + R_{fo})}{b}\right) Q\right] \qquad (4\text{-}1)$$

At static conditions, i.e., Q = 0, the static pumping pressure, ΔP_o, can be expressed as:

$$\Delta P_o = \frac{B_o I_{e0}}{b} = \left[\frac{B_o}{b(R_w R_{fo} + R_e R_w + R_{fo} R_e)}\right]\left[R_w\, R_{fo}\,(I - I_{le})\right] \qquad (4\text{-}2)$$

The net increase in pressure in the two pumping regions of the developed miniature DC-EM pump designs (Fig. 4-7), ΔP, is given as:

$$\Delta P = 2 * \Delta P_p - \Delta P_{loss} \qquad (4\text{-}3)$$

In this expression, the friction pressure losses, ΔP_{loss}, of the molten lead or sodium flow in the pump duct may be calculated using the Darcy–Weisbach equation and the friction factor correlation given by McAdams (1954). The results are arranged as the product of a geometry term, a liquid properties term, and an operation term (Haskins and El-Genk, 2016), as:

$$\Delta P_{loss} = \left(\frac{a}{2}\right)\left(\frac{L}{D_e^{1+b} A^{2-b}}\right)\left(\frac{\mu^b}{\rho}\right)\dot{m}^{2-b} = \left(\frac{a}{2}\right)\left(\frac{L}{D_e^{1+b} A^{2-b}}\right)\left(\mu^b \rho^{1-b}\right) Q^{2-b} \qquad (4\text{-}4)$$

In this expression, the mass flow rate, $\dot{m}$, is equal to (Q*ρ), the coefficients a and b depend on the flow conditions. For laminar flow at Re $\leq$ 2,300, a = 64 and b =1, and for turbulent flow at Re $\geq$ 4,000, a = 0.184 and b = 0.2. For the transition flow region, 2,300 $\leq$ Re $\leq$ 4,000, the value of the pressure losses is determined by interpolation between the laminar and turbulent flow values determined from Eq. 4-4 for Reynolds number of 2,300 and 4,000, respectively.

The Pumping Power, PP, and the pump efficiency, η, of the developed miniature dual regions DC-EM pump designs, are calculated, respectively, as:

$$PP = \Delta P \, . Q \tag{4-5}$$

$$\eta(\%) = \frac{Pumping\ power}{Electrical\ power} \text{ x } 100 = \frac{\Delta P\ Q}{2\ I\ E}. \tag{4-6}$$

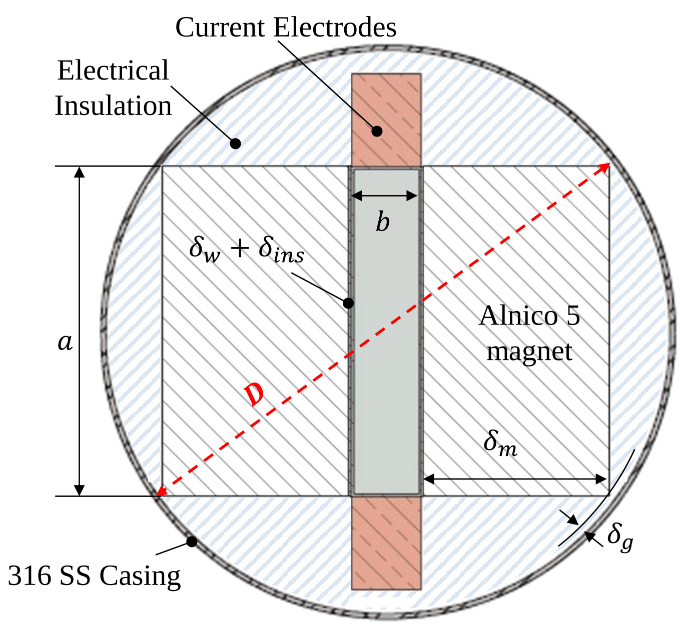

Figure 4-9: Cross-section view of the pumping region of the present miniature DC-EMP Design (Fig. 4-7).

As indicated earlier, the values of magnetic flux density, fringe resistance, and leakage currents in the ECM performance analyses (Eq. 4-1) for molten lead and liquid sodium are calculated using the FEMM software at zero flow and 500°C. In this work, written scripts in MATLAB platform fully control the FEMM software (Meeker, 2015) for implementing and solving the governing equations and extracting the calculated values of electrical and magnetic parameters. These scripts also link the FEMM software to the ECM also written in MATLAB scripts, to conduct performance analyses of the developed miniature DC-EM pump designs. This linkage is quite effective in determining the pump dimensions for the highest cumulative pumping power, PP_{cu}, and peak efficiency, η_{peak}. Such linkage saves much computational time as the developed pump performance database involves a considerable number of FEMM-ECM simulations of the present designs (Fig. 4-7) for different diameter pumps.

4.3.2. Pump dimensions model

The performance of the developed designs of the miniature, two pumping regions DC-EMPs of different diameters (Fig. 4-7) depends on the operating temperature, the type and physical properties of the working fluid, and the dimensions and materials of the different pump components, including the flow duct, the Alnico 5 permanent magnets, the Hiperco-50 pole pieces, and the copper current electrodes (Fig. 4-7). For the present designs of miniature DC-EMPs of different diameters and total lengths for pumping molten lead or liquid sodium at 500^{o}C, a developed model screens the generated performance database using the linked ECM-FEMM for the pumps' dimensions to provide the highest cumulative pumping power, PP_{cu}, and the peak efficiency. The cumulative pumping power, PP_{cu}, is calculated as:

$$PP_{cu} = \int_{o}^{Q_{ro}} \Delta P(Q) dQ \tag{4-7}$$

The screened dimensions are those of the flow duct width (a) and height (b), the length of the current electrodes (c), the thickness of the Alnico 5 permanent magnet (δ_m), and the separation distance between the two pumping regions (l_{sep}).

Table 4-1: Operation parameters and dimensions used in the performance analyses of developed designs of miniature DC-EMPs of different diameters for molten lead and liquid sodium.

Parameter	Value	Parameter	Value
Exit temperature (^{o}C)	500	Insulation thickness, δ_{ins} (mm)	0.25
Electrodes current, I (A)	3,500	Gap thickness, δ_g (mm)	1.0
Duct wall thickness, δ_w(mm)	0.5	Flow-duct Extension, l_{ex} (mm)	25

Table 4-2: Ranges of dimensions investigated for the effects on the performance of the developed miniature DC-EMPs of different diameters for circulating molten lead and liquid sodium.

Parameter	**Pump Diameter (mm)**			
	57	**66.8**	**95.4**	**133.5**
Flow duct height, b (mm)	5 to 15			
Flow duct width, a (mm)	2b to 35	2b to 46	2b to 74	2b to 112
Magnet thickness, δ_m(mm)	10 to 24.6	10 to 29.5	10 to 43.9	10 to 63.0
Separation distance, l_{sep}(mm)	30 to 100			
Electrode length, c (mm)	30 to l_{sep}			

For specified values of b, c, δ_m, l_{sep}, and pump diameter, D, the width of the flow duct, a, is determined (Fig. 4-9), as:

$$a = \sqrt{(D)^2 - \left(b + 2\,[\delta_w + \delta_{ins} + \delta_m + \delta_g]\right)^2} \quad (4\text{-}8)$$

In this expression, the specified values of other dimensions in the input to the present performance analyses are same for all pump diameters (Table 4-1). For the specified ranges of parameters in Table 4-2, the performed parametric analyses not only calculate the values of the magnetic flux density, B_o, the fringe resistance, f_{Ro}, and the effective and leakage electrical currents in the flow duct at zero flow and specified temperatures $\leq 500^oC$, but also the pumping pressure corrected for the friction pressure losses in the flow duct as a function of the flow rate of the working fluid, which is either molten lead or sodium. The pump dimensions for achieving the highest cumulative pumping power and the highest pump efficiency, are determined separately for each two working fluids. The obtained results are presented, compared, and discussed in this subsection (Tables 4-3 and 4-4).

The calculated magnetic field flux density in the pumping regions at zero flow, B_o, using the FEMM software is proportional to the magnet thickness, δ_m and L_{sep}, and inversely proportional to the flow duct height, b, and width, c. On the other hand, the effective electrical current in the flow duct of the two pumping regions, I_e, is proportional to the length of the current electrodes, c, and the separation distance L_{sep}, and inversely proportional to the width of the flow duct, a (Figs. 4-4 and 4-6). Furthermore, the friction pressure losses in the pump duct (Eq. 4-4) are proportional to the values of c and L_{sep}, and inversely proportional to those of a and b. Based on the governing equations in the ECM (Eqs. 4-1 and 4-3), the developed pumping pressure as a function of the volumetric flow rate in the pump duct, $\Delta P(Q)$, is proportional to the values of magnetic flux density, B_o, and the effective electrical current, I_e, decreases as the volumetric flow rate of the working fluid, Q, increases. Increasing this flow rate increases the friction pressure losses (Eq. 4-4) and decreases the net pumping pressure (Eqs. 4-1 and 4-2), which is zero at runout flow rate, Q_{ro}. expressed from Eq. 4-1 as:

$$Q_{ro} = \left(R_w\, R_{fo}\, (I - I_{le})\right) / \left(B_o\, \left(R_w + R_{fo}\right)/\mathrm{b}\right) \tag{4-9}$$

This flow rate depends not only on the temperature, and the physical and electrical properties of the working fluid but also on the pump dimensions including the total length and cross-sectional area of the flow duct.

4.4.Results and discussions

This section presents and discusses the results of the performed parametric analyses to determine the dimensions of the developed miniature, dual-stages DC-EMP designs for achieving the highest cumulative pumping power, PP_{cu} (Eq. 4-7), and the highest peak efficiency, η_{peak} (Eq. 4-6). These analyses for pumps of different diameters are for molten lead and liquid sodium at exit temperature of 500^{o}C. The developed pump designs with outer diameters of 57, 66.8, 95.4, and 133.5 mm fit within standard 2, 2 ½, 3 ½, and 5 inches diameter SS316 pipes. This section also presents the results investigating the effects of the electrode current, I, and working fluid types and temperatures on the performance characteristic of the pumps.

4.4.1. Pumps optimized dimensions.

The linked ECM and the FEMM software in MATLAB platform, for the range of dimensions listed in Table 4-2 and the parameters in Table 4-1, generated a large performance database for molten lead and liquid sodium working fluids and different pump diameters. The separation distance between the current electrodes in the two pumping regions, l_{sep}, varied from 30 to 100 mm, with the latter resulting in a total pump length of 300 mm (Fig. 4-7). The generated database of the pumping pressure, pump efficiency, and pumping power versus the volumetric flow rate of the working fluid for pump diameters of 57, 66.8, 95.4, and 133.5 mm is screened for the pump dimensions to achieve the highest PP_{cu} and η_{peak}. Tables 4-3 and 4-4 list the determined dimensions of the developed designs of the miniature, dual-stages DC-EMPs of different diameters for pumping molten lead and sodium at 500°C and at the highest PP_{cu} and η_{peak}. The miniature DC-EMP with the smallest diameter of 57 mm for pumping molten lead and sodium at 500°C produces peak pumping powers of 368 and 392 W and achieve peak efficiencies of 14.7% and 44.3%, respectively (Tables 4-3, 4-4).

The results highlighted in bold in tables 4-3 and 4-4 and delineated in Fig. 4-10 show that increasing the pump diameter increases the performance for both molten lead and liquid sodium at the same temperature of 500°C, including the peak pumping power, PP_{peak} and the peak efficiency, η_{peak}. Such increases are because both the magnet thickness and flow duct flow area in the larger diameter pumps are larger, which increases the pumping pressure and decreases the frictional pressure losses, respectively. Results listed in tables 4-3 show that for molten lead increasing the pump diameter from 57 mm to 133.5 mm increases PP_{peak}, ~99% from 368 W to 732 W and η_{peak} ~103% from 14.7% to 29.9% (Fig. 4-10). Similar trends but at higher values are listed in Table 4-4 and shown in Fig. 4-10 for liquid sodium at same temperature. The peak pumping power for liquid sodium increases ~96% from 392 W to 767 W and η_{peak} increases ~16% from 44.3% to 51.2% with increased pump diameter from 57 mm to 133.5 mm (Table 4-4). These values are higher than for molten lead (Table 4-3).

Table 4-3: Dimensions of the miniature dual-stages DC-EMPs of different diameters for highest PP_{cu}, and η_{peak} of molten lead at 500°C.

Criterion	**D (mm)**	**Optimized dimensions (mm)**								
		b	$\boldsymbol{\delta_m}$	**a**	$\boldsymbol{c}$	$\boldsymbol{L_{sep}}$	$\boldsymbol{L_p}$	$\boldsymbol{PP_{peak}}$**(W)**	$\boldsymbol{\eta_{peak}}$ **(%)**	$\boldsymbol{Q_{ro}}$**(m³/h)**
Highest PP_{cu}	57	5	20.4	31	30	43	103	**368**	9.6	10.8
	66.8	5	25.4	33	31	50	112	**437**	11.3	11.4
	95.4	5	40.3	38	37	65	139	**604**	15.4	12.2
	133.5	5	59.3	45	50	72	172	**728**	18.3	12.9
Highest η_{peak}	57	8.6	21.8	17.2	73	87	233	145	**14.7**	7.7
	66.8	8.7	26.8	17.3	54	63	171	181	**17.4**	8.0
	95.4	8.9	41.4	17.6	62	79	203	247	**24.6**	8.7
	133.5	9	60.6	18	75	91	241	319	**31.6**	8.9

Table 4-4: Dimensions of miniature, dual-stages DC-EMPs of different diameters for highest PP_{cu}, and η_{peak} of liquid sodium at 500°C.

Criterion	D (mm)	Optimized dimensions (mm)								
		b	δ_m	**a**	c	L_{sep}	L_p	PP_{peak}**(W)**	η_{peak} **(%)**	Q_{ro}**(m³/h)**
Highest PP_{cu}	57	5	23.6	17.1	35	40	110	**392**	34.0	10.7
	66.8	5	28.3	19.1	46	51	143	**456**	36.5	11.4
	95.4	5	42.8	22.4	59	74	192	**643**	39.1	11.9
	133.5	5	61.9	26.2	72	82	226	**767**	40.2	12.6
Highest η_{peak}	57	5.6	24.1	11.1	52	55	159	312	**44.3**	9.0
	66.8	5.7	29.0	11.6	57	61	175	349	**45.9**	9.5
	95.4	6.0	43.3	12.0	65	76	206	446	**48.7**	10.4
	133.5	6.4	62.2	12.8	75	91	241	526	**51.2**	10.8

For the different pump diameters in Tables 4-3 and 4, the values of PP_{peak} for liquid sodium are ~ 5% - 7 % higher and those of η_{peak} are ~ 75% to 200% higher than for molten lead. The significant difference in the pump efficiencies for circulating molten lead and sodium, despite the close pumping power values, is because of the significant difference in the electrical resistances. The electrical resistivity of molten lead is more than three times that of sodium. Hence, for the same electrode current, the terminal voltage for pumping molten lead and the electrical power input to the pump are higher, significantly decreasing the efficiency of the lead pump compared to that for liquid sodium (Eq. 4-6). Furthermore, for the same pump diameter, the flow duct cross-sectional areas for pumping liquid sodium are smaller than for molten lead, including those for achieving the highest PP_{cu} and η_{peak} (Tables 4-3, 4-4). Conversely, for the same diameters, the lengths of the pumps for liquid sodium and the dimensions for the highest PP_{cu} and η_{peak} are larger than for molten lead at 500°C (Tables 4-3, 4-4).

The pump dimensions for achieving the highest PP_{cu} (Tables 4-3, 4-4) produce higher pumping pressures and runout flow rates (Q_{ro}) than those for the highest η_{peak}. The small duct height (b) and large magnet thickness (δ_m) in these pumps increase the magnetic flux density, B_o, and hence the pumping pressure. In addition, the large duct width (a) increases the duct flow area and the runout flow rate (Q_{ro}) (Eq. 4-9). Also, the decreased pressure losses increase the net pumping pressure (Eq. 4-3). Increasing the width of flow duct, a, increases the pump efficiency and decreases the terminal voltage, E, needed to provide the specified electrodes current of 3,500 ADC (Table 4-1). Increasing the length of the current electrodes, c, and the separations distance, L_{sep}, between the two pumping regions increase the effective electrical current in the flow duct by decreasing the fringe and leakage currents outside the pumping regions.

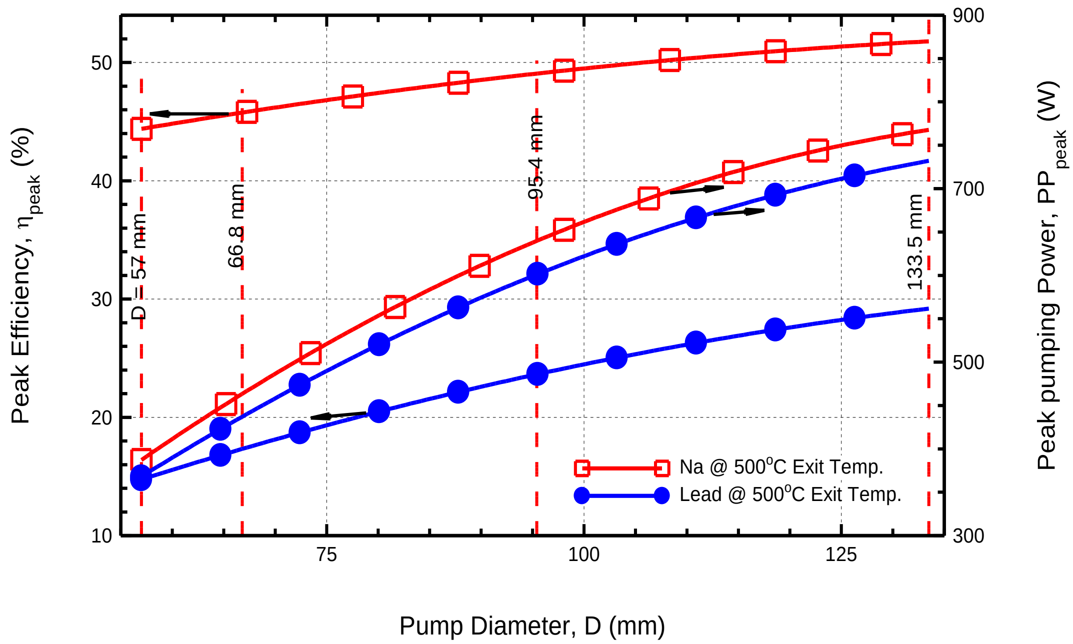

Figure 4-10: Comparisons of achievable PPpeak and η_{peak} by the miniature, dual-stages DC-EMPs of different diameters for molten lead and liquid sodium at 500 °C.

4.4.2. Performance comparison

This subsection presents and compares the results of the calculated performance of the developed designs of the miniature dual-stages DC-EMPs with different diameters of 57.0 to 133.5 mm. The results in Figs. 4-10 and Tables 4-3 and 4-4 for pumping molten lead and liquid sodium at 500°C show that for the different diameter pumps with dimensions for achieving the highest PP_{cu} the values of static pressure, the runout flow rate, and the pumping power are higher than for those with the dimensions for achieving highest η_{peak}.

The performance characteristics in Figs. 4-11 and 4-12 for molten lead and liquid sodium show that the static pressure at zero flow, the pumping power, the pump efficiency, and the runout flow rate increase with increased pump diameter. For the 57 mm diameter pump the static pressure for pumping molten lead is 378 kPa, the runout flow rate is 10.8

m^3/h, and the peak efficiency of 9.6% occurs at a flow rate of 5.5 m^3/h and a pumping pressure of 240 kPa. At a flow rate of 5.9 m^3/h, the pumping pressure at the peak pumping power of 368 W is 224 kPa.

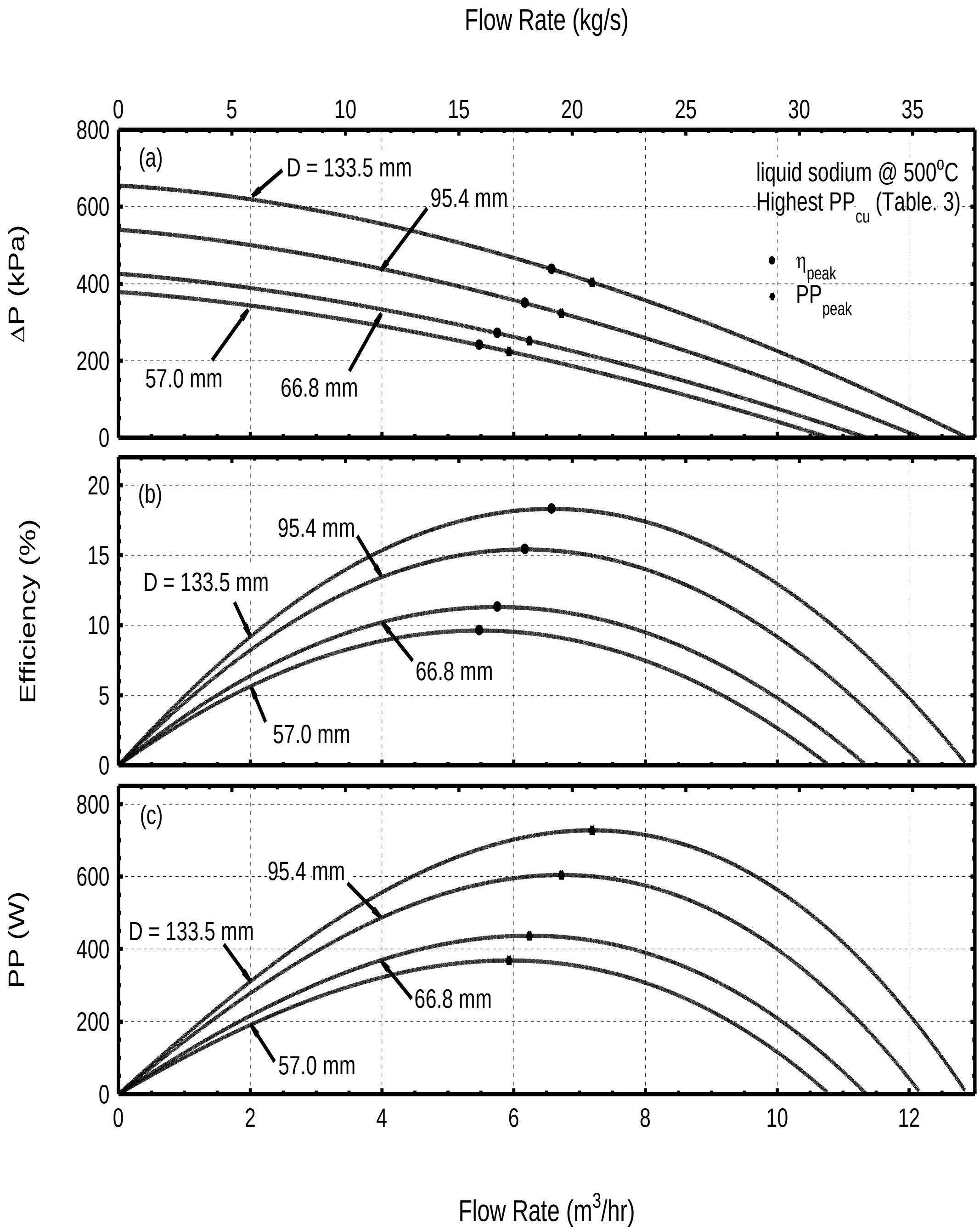

Figure 4-11: Calculated performance of miniature, dual-stages DC-EMPs of different diameters and determined dimensions for achieving the highest PPcu of molten lead at 500 °C (Table 4-3).

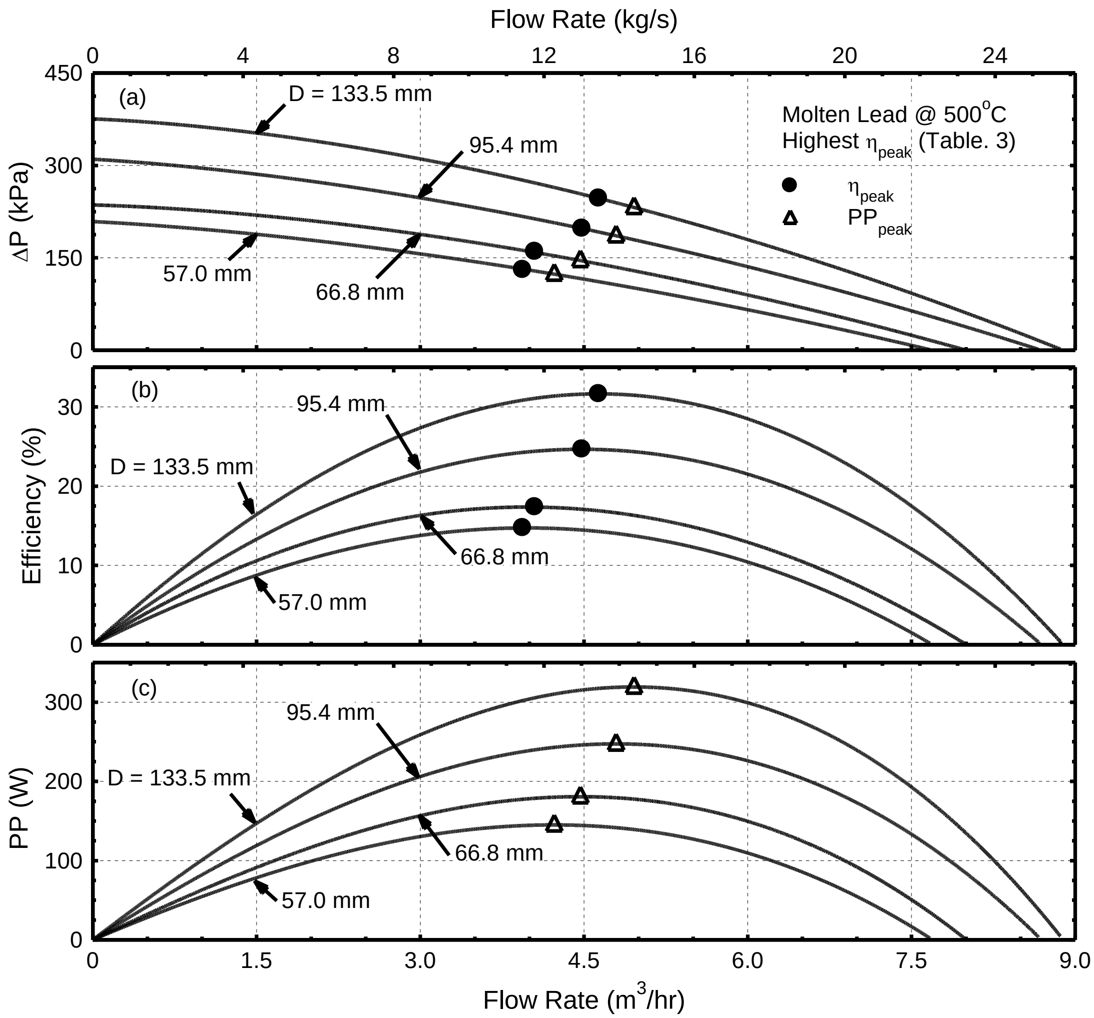

he

Figure 4-12: Calculated performance of miniature, dual-stages DC-EMPs of different diameters and determined dimensions for highest η_{peak} for lead at 500 ^oC (Table 4-3).

Increasing the pump diameter from 57 to 133.5 mm increases the static pressure and the runout flow rate for molten lead to 655 kPa and 12.9 m^3/h, respectively, and the peak efficiency of 18.3% occurred at higher flow rate and pumping pressure of 6.6 m^3/h and 437 kPa, respectively. Similarly, the higher pumping power of 728 W for the 133.5 mm diameter pump occurs at a higher flow rate of 5.9 m^3/h and pumping pressure of 404 kPa (Fig. 4-11a-c).

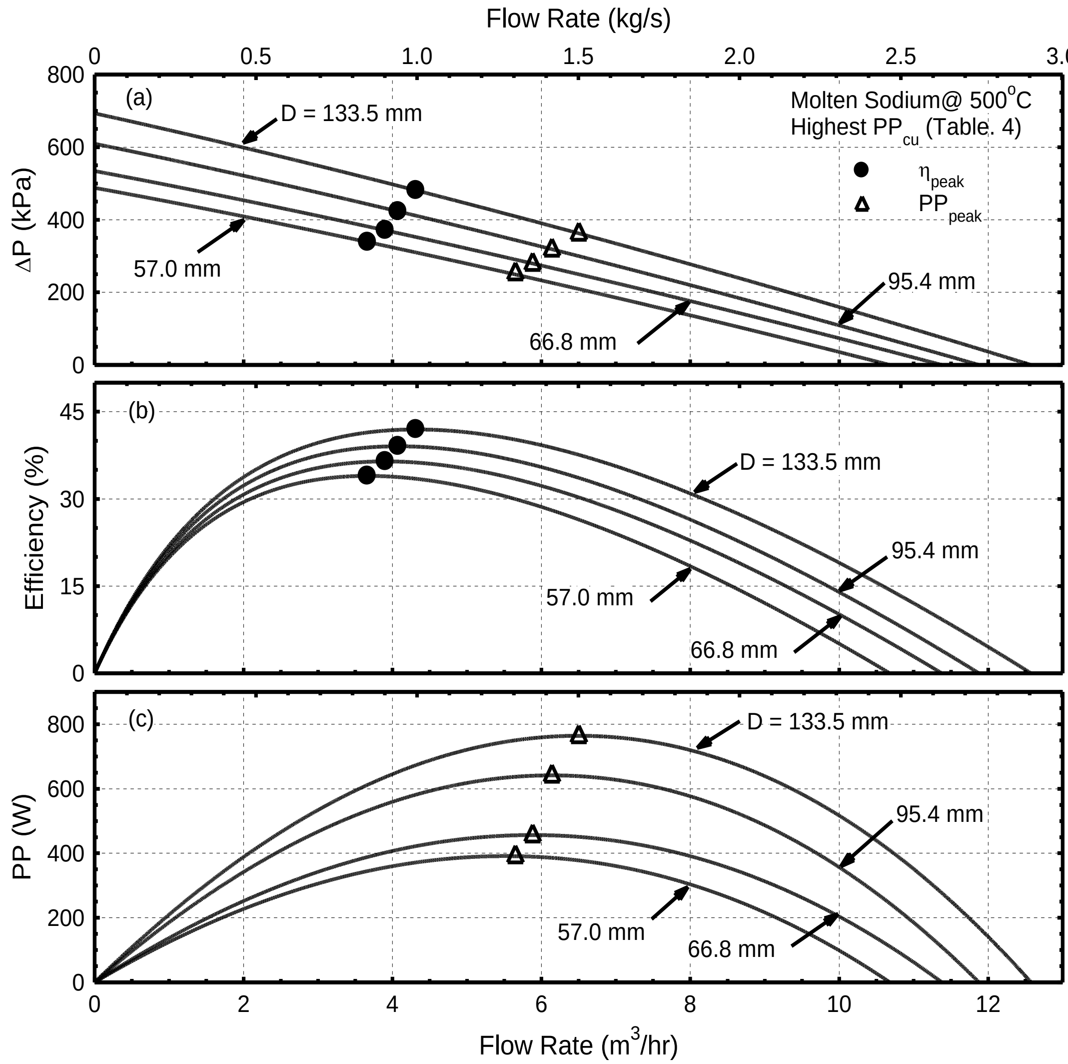

Figure 4-13: Calculated performance of miniature, dual-stages DC-EMPs of different diameters with determined dimensions for achieving highest PPcu and for liquid sodium at 500 °C (Table 4-4).

Similar trends but different values for pumping are found for the different pump diameters with dimensions for the highest peak efficiency (Fig.4-12a-c). Increasing the pump diameter from 57 to 133.5 mm increased the static pressure and the runout flow rate of molten from 209 to 375 kPa and from 7.7 m^3/h to 8.9 m^3/h, respectively (Fig. 4-12a) and the higher peak efficiency of 14.7% at flow rate of 3.9 m^3/h and pumping pressure of 131 kPa increased to 31.6% at flow rate of 4.6 m^3/h and pumping pressure of 247 kPa. Similarly, the pumping power of 145 W at a flow rate of 4.2 m^3/h and pumping pressure of 124 kPa increased to 319 W at molten lead flow rate of 5.0 m^3/h and pumping pressure of 232 kPa (Fig. 4-12)

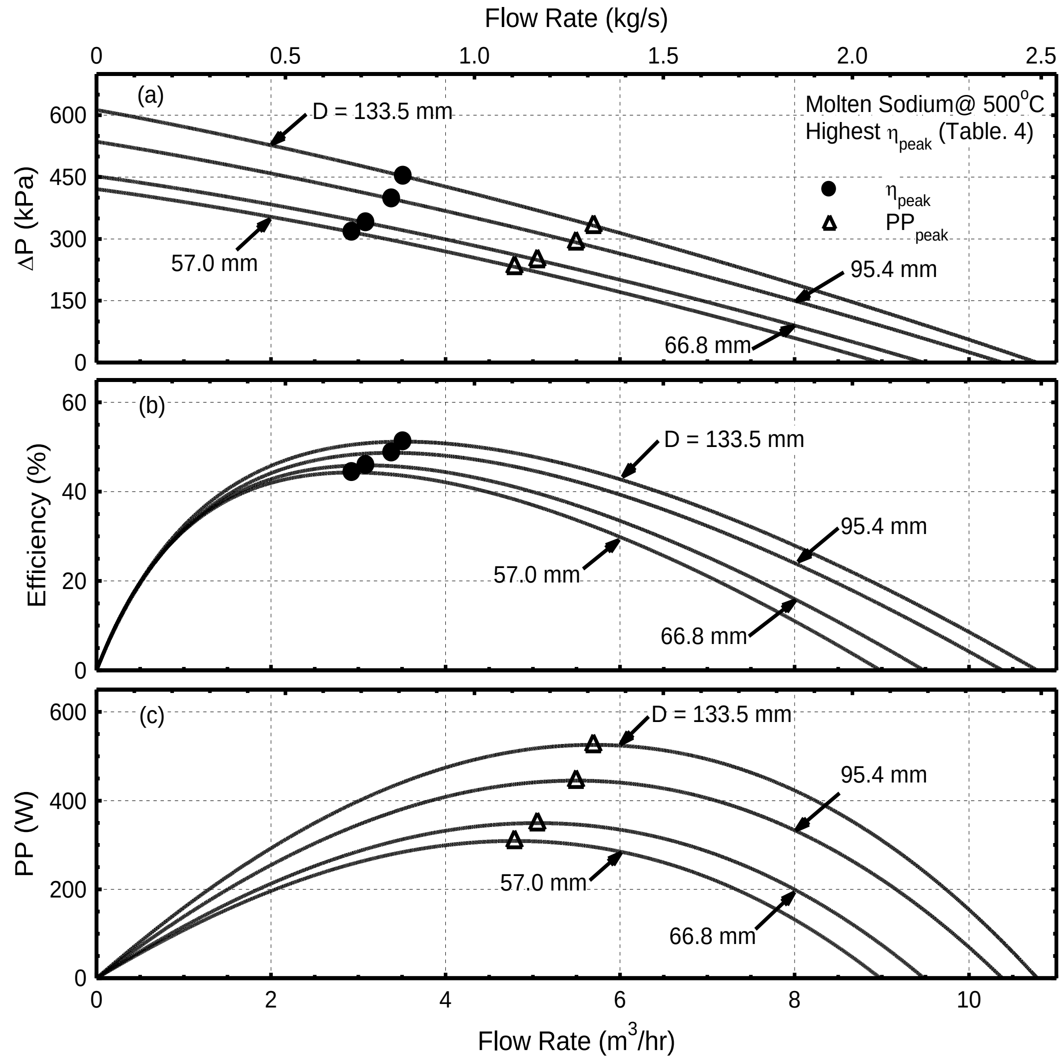

Figure 4-14: Calculated performance of miniature, dual-stages DC-EMPs of different diameters with determined dimensions for the highest η_{peak} of liquid sodium at 500 °C (Table 4-4).

In general, the performance curves of the pumps of different diameters and with dimensions for circulating molten sodium (Figs. 4-13 and 4-14) are higher than those for circulating molten lead (Figs. 4-11 and 4-12), including the static pressure, the peak pumping power, and the peak efficiency. The runout volumetric flow rates are comparable, while the runout mass flow rate for molten lead is significantly higher because lead density is more than an order of magnitude higher than that of liquid sodium at the same temperature of 500^{o}C (Foust, 1978; Sobolev, 2011). The pump diameters (57.0 to 133.5 mm) with dimensions for pumping liquid sodium at the highest PP_{cu} (Table 4-4 and Fig. 4-13) produce static pressures between 488 and 693 kPa, runout flow rates between 10.7 to 12.6 m^{3}/h, peak efficiencies between 34.0 to 42.0% and peak pumping power between 392 to 767 W. The same pump diameters with dimensions for pumping liquid sodium at the highest η_{peak} (Table 4-4 and Fig. 4-14) produce static pressures between 420 and 613 kPa, runout flow rates between 9.0 to 10.8 m^{3}/h, peak efficiencies between 44.3 to 51.2% and peak pumping power between 312 to 526 W.

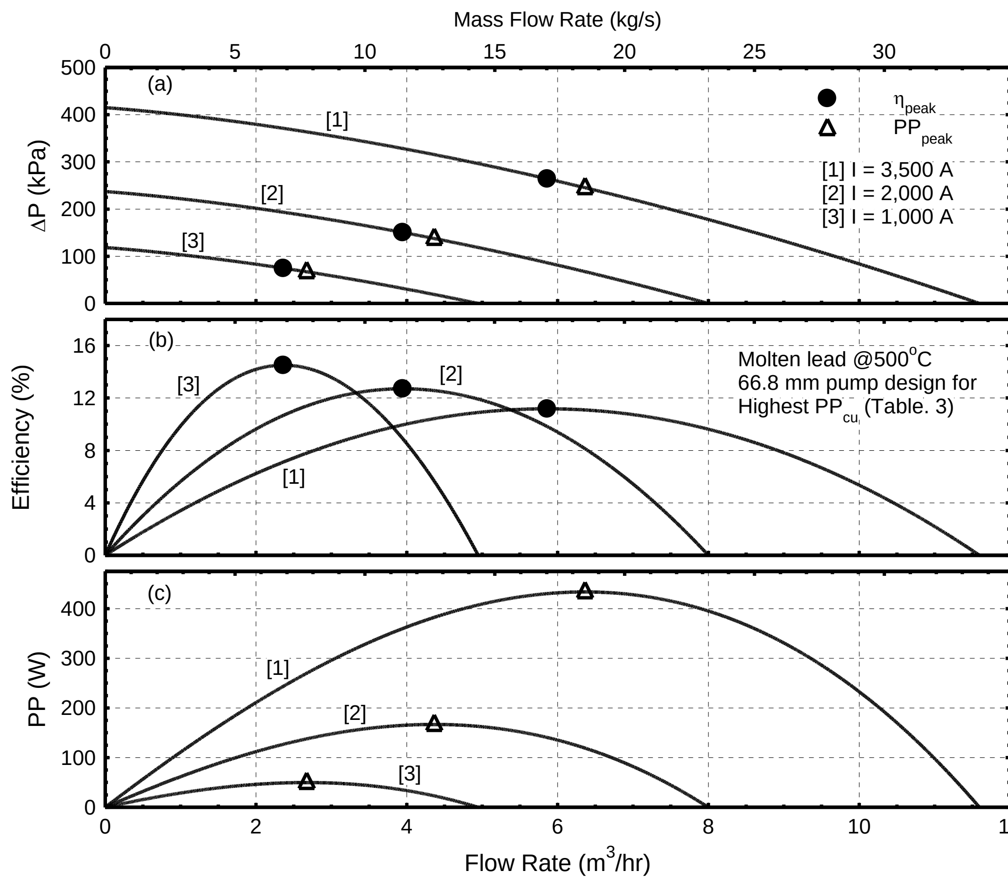

Figure 4-15: Effects of electrical current on the performance of the 66.8 mm diameter, dual-stages DC-EMP with dimensions for achieving the highest PPcu of molten lead at 500 ^{o}C (Table. 4-3).

4.4.3. Effect of input currents on pump performance

This subsection presents the calculated results using the linked ECM and the FEMM software of the effect for varying the electrodes input current, I, in the two pumping regions of the present miniature dual-stages DC-EMP design with different diameters on the performance characteristics. The obtained results are for the 66.8 mm diameter pump with dimensions for achieving the highest PP_{cu} of molten lead at 500°C (Table 4-3). The performed analysis is for input currents, I, of 1,000, 2,000, and 3,500A. As indicated by Eqs. 4-1 and 4-5, the total generated pumping pressure and the pumping power in the two regions of the pump increase proportionally with the input electrical current.

The results presented in Fig. 4-15 show that increasing of the electrical input current from 1,000 A to 3,500A increases the static pressure for molten lead from 119 to 437 kPa, the runout flow rate from 4.9 to 11.4 m^3/h, and the peak pumping power from 50 to 437 W. On the other hand, the pump peak efficiency decreases from 14.5% to 11.3% (Fig. 4-15b). The pump efficiency is proportional to the pumping power, but inversely proportional to the input electrode current (Eq. 4-6). Therefore, depending on the demand curve for potential applications, the pump supply curve could be adjusted to either decrease or increase the working fluid flow rate for steady state operation. This is when the generated pumping pressure equals that at the intersection of the demand and supply curves.

Table 4-5: Physical properties of molten lead and liquid sodium at 350 and 500 °C (Foust, 1978; Sobolev, 2011).

Working fluid	Temperature, T (°C)	Electric resistivity, ρ_e (μΩ.m)	Density, ρ (kg/ m^3)	Viscosity, μ (μ Pa.s)	$\mu^{0.2}/\rho$
Lead (Pb)	500	1.03	10,452	1,814	429
	350	0.96	10,644	2,531	450
Sodium (Na)	500	0.32	832	283	3,717
	350	0.23	868	367	3,753

4.4.4. *Effects of fluid temperature and type on pump performance*

For given pump diameter and dimensions, changing the temperature changes the physical and electrical properties of the working fluid including the electrical resistivity, dynamic viscosity, and density as well as those of the various pump components (Foust, 1978; Sobolev, 2011). The changes in the pump duct wall, equivalent, and fringe resistances affect the performance of DC-EMP. This subsection presents the results of investigating the effects of decreasing the exit temperature of molten lead and liquid sodium from 500°C to 350°C on the performance characteristics of the developed miniature dual-stages DC-EMP. Presented results are of 66.8 mm diameter pump with dimensions for achieving the highest PP_{cu} of molten lead and liquid sodium at 500°C (Tables 4-3, 4-4). Decreasing the exit temperature of the working fluid in the pump flow duct from 500 to 350°C decreases the electrical resistivity of molten lead from 1.03 to 0.96 μΩ.m and from 0.32 to 0.23 μΩ.m for liquid sodium (Table 4-5).

These decreases in the electrical resistivities increase the effective electrical currents in the flow duct of the two pumping regions and the generated pumping pressure. In addition, lowering the temperature of the working fluid from 500°C to 350°C increases the magnetic permeability, and hence the magnetic flux density, B_o, in the flow duct in the two pumping regions from 89% of its saturation value at 20°C to 94%, respectively (Fig. 4-2). This increase in the effective magnetic field flux density contributes to increasing the generated Lorentz force in the flow duct and the pumping pressure. Conversely, the resulting increase in B_o also increases the opposing induced electromotive force in the pump duct (BQ/b), causing the pumping pressure to decrease slightly faster with increased flow rate. Furthermore, decreasing the temperature from 500°C to 350°C increases the densities, ρ, of molten lead and liquid sodium from 10,452 to 10,644 kg/m^3, and from 832 to 868 kg/m^3, respectively. Similarly, the dynamic viscosity, μ, for molten lead and liquid sodium from 1,814 to 2,531 μPa.s and from 283 to 367 μPa.s, respectively (Table 4-5). These increases in the working fluid density and viscosity increase the friction pressure losses of the flow in the pump duct, ΔP_{loss}, which are proportional to (μ^b/ρ) (Eq. 4-4), decreases net pumping pressure, ΔP, which decreases with increased flow rate (Eqs. 4-3, 4-4 and Fig. 4-16).

Fig. 4-16 compares the calculated performance characteristics of the 66.8 mm diameter, dual-stages, DC-EMP for pumping molten lead and liquid sodium at exit temperatures of 350 and 500°C. The pump dimensions (Tables 4-3, 4-4) are those for achieving the highest PP_{cu} with an electrode current of 3,500 A. At low flow rates, the pumping pressures for both working fluids at 350°C are higher than at 500°C. This is because of the increases in the effective electrical currents and the magnetic flux density in the pump duct. At high flow rates, the induced opposing electromotive force due to the flow in the magnetic field and the friction pressure losses increase, causing the net pumping pressure at 350°C to decrease faster with increase flow rate than at 500°C. Decreasing the working fluid temperature from 500 to 350°C also increases the pumping pressure for molten lead at zero flow rate from 426 kPa to 451 kPa and decrease in the runout mass flow rate from 32.2 kg to 33.0 kg/s. For liquid sodium, the corresponding increase in the static pressure is from 448 kPa to 478 kPa, and the corresponding decrease in the runout mass flow rate is from 2.7 to 1.97 kg/s.

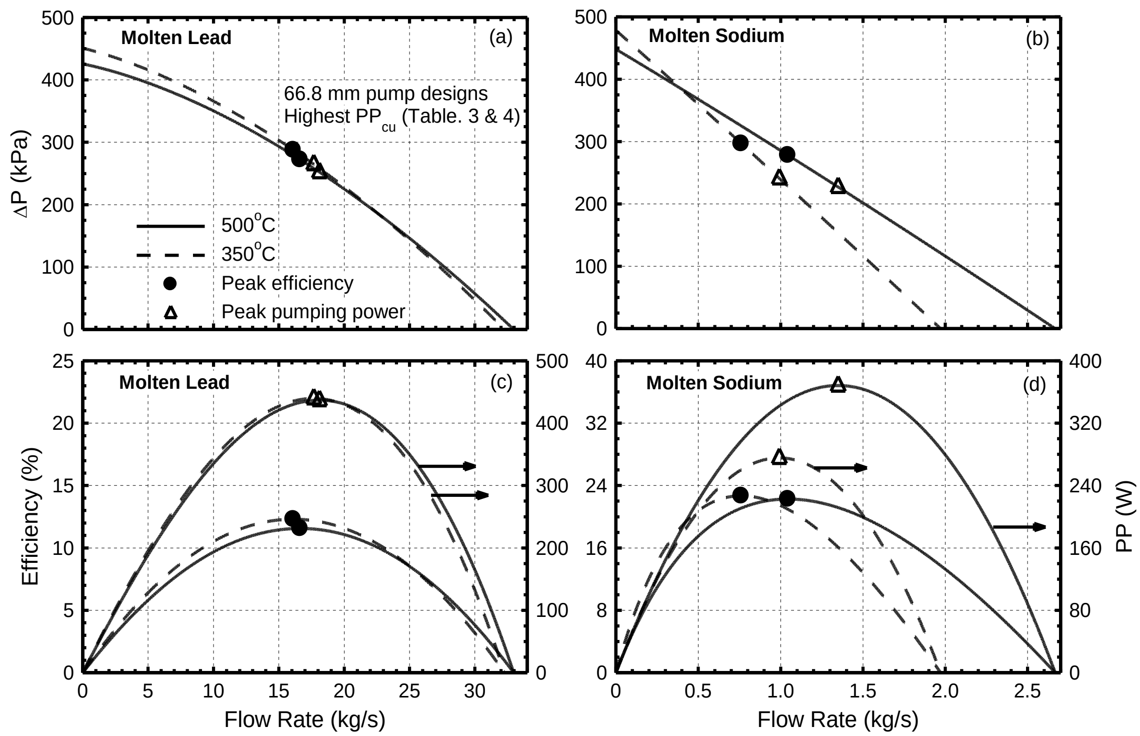

Figure 4-16: Effect of working fluid type and temperature on the performance developed miniature dual-stages DC-EMP design with a 66.8 mm diameter and dimensions for highest PP_{cu} and for electrode current of 3.500 A.

Decreasing the temperature from 500°C to 350°C had a small effect on the pumping power for molten lead (Fig. 4-16c), as the pumping pressures and runout flow rates at the two temperatures are close (Fig. 4-16a). For liquid sodium, the difference between the pumping pressure curves and runout flow rates at 350 and 500°C (Fig. 4-16b), increases the differences in the calculated pumping power curves (Fig. 4-16d). Decreasing the temperature from 500°C to 350°C decreases the peak pumping power for liquid sodium pump from 368 at 1.3 m^3/h to 275 W at 1.0 m^3/h (Fig. 4-16d). According to Table 4-5, decreasing the molten lead temperature from 500 to 350°C decreases the electrical resistivity by less than 7%. This decreases in the voltage across the pump, E, and decreases the supplied electrical power at the electrode current of 3.500 A. With the close pumping power curves, the decreased electrical power with decreased temperature of molten lead from 500 to 350^{o}C increases the pump efficiency (Eq. 4-6) from 11.6 to 12.3% (Fig. 4-16c). For liquid sodium, decreasing the temperature from 500 to 350^{o}C causes ~ 30% decrease in the electrical resistivity. Consequently, the peak pumping power for the molten sodium pump at 500^{o}C is more than 50% larger than that at 350^{o}C (Fig. 4-16d). However, the difference in the peak efficiencies is small, due to the large decrease in the input electrical power.

In summary, decreasing the working fluid exit temperature increases the pumping pressure at low flow rates and decreases it at high flow rates and decreases the runout flow rate. Pump efficiency and pumping power curves for molten lead at 350 and 500^{o}C are close. For pumping liquid sodium, changing the temperature results in larger changes in the pump efficiency and pumping power curves due to changes in sodium properties, particularly electrical resistivity.

4.5. Summary and Conclusions

This work developed designs of submerged, miniature DC-EMPs with two pumping regions and different diameters for circulating molten lead and sodium at temperatures ≤ 500^{o}C without external or active cooling. The developed pumps with outer diameters of 57, 66.8, 95.4, and 133.5 mm fit within 2, 2 ½, 3 ½, and 5 inches standard stainless-steel pipes, respectively. These pumps each have a pair of Alnico 5 permanent magnets, with opposite magnetization directions for driving the liquid flow in the two pumping regions of the pump duct. Increasing the pump diameter increases the thickness of the magnets as well as the cross-section area of the flow duct, which increases the pump performance parameters. These include the static pressure, the pump efficiency, the pumping power, and the runout flow rate. The Hiperco-50 pole pieces of the two Alnico 5 magnetics redirect and concentrate the magnetic flux through the two pumping regions and minimize external losses outside. As a result, the generated magnetic field perpendicular to the flow direction in the two pumping regions is higher and uniform, for improving pumps performance.

The performance characteristics of the different diameter pumps are calculated using the ECM with the calculated values of the magnetic field strength and fringe resistance at zero flow by the Finite Element Method Magnetics (FEMM) software. The generated performance database for a wide range of input and operation parameters using the linked

ECM and FEMM software in MATLAB platform are screened for the dimensions to achieve the highest cumulative pumping power and peak pump efficiency for circulating molten lead and liquid sodium. These dimensions are the flow duct height and width, the magnets thickness, the current electrode length, and the separation distance between the two pumping regions.

Results show that increasing the pump diameter from 57 to 133.5 mm increases the peak values of pumping power, and efficiency by ~100%. For same pump diameter and screened dimensions for achieving the highest cumulative pumping power or peak efficiency, the pumping power, the static pressure, and the efficiency for liquid sodium are higher than for molten lead at the same temperature. For pump diameters of 57 mm to 133.5 mm, the peak pumping power for molten lead increases from 368 to 728W, and the peak efficiencies increases from 14.7% to 31.6%. For liquid sodium, the peak pumping power is higher, ranging from 392 to 767W, and the peak efficiencies are also higher, ranging 44.3 to 51.2%.

Decreasing the electrode current decreases, the pumping pressure, the runout flow rate, and the peak pumping power, but increases the pump peak efficiency. Therefore, when present miniature DC-EMPs are used in applications with known demand curves, the pumps supply curves match the required flow rates and can be adjusted by changing the electrode current. The type and the temperature of the working fluid also affect the pump performance for pumping molten and liquid sodium. Decreasing the working fluid temperature increase the pumping pressure for both liquid sodium and molten lead at low flow rates and decreases it at higher flow rates because of the increased friction pressure losses and the opposing electromotive force generated by the liquid flow in the magnetic field in the two pumping regions. However, both the pump efficiency and the pumping power increase with increased temperature, however, increase are much higher for liquid sodium than molten lead. In summary, the present work provides viable, high-performance designs of miniature, submersed DC-EMP with diameters ranging from 57 mm to 133.5 mm for use in ex-pile or in-pile test loops of liquid sodium and molten lead at temperatures $\leq 500^{o}$C. The determined dimensions for achieving the highest cumulative pumping power and peak efficacy, provide choices to potential users including those in the liquid metals and aluminum mining industries, liquid metals cooled nuclear microreactors for electricity generation and the production of high-temperature process heat.

5. MHD NUMERICAL ANALYSES OF MINIATURE, DUAL-STAGE DC-EMP

5.1. Introduction

A Direct Current-Electromagnetic Pump (DC-EMP) divers the flow of electrically conductive liquids utilizing the generated Lorentz force when a direct electrical current passes through the liquid in a perpendicular direction to that of the applied magnetic field (Baker and Tessier, 1987). The fully passive operation, the absence of moving parts, and sealed structure simplify the pump design and enhance operation reliability when fully submersible in working fluids (Nashine et al., 2007; Lee and Kim, 2018; Altamimi and El-Genk, 2023a). DC-EMPs have been used for circulating heaving and alkali liquid metals in many applications. Examples are space nuclear reactor power systems, terrestrial nuclear reactors, metals processing, electronics cooling, and solar energy (El-Genk et al., 1987; El-Genk, 2009; Kandev, 2012; IAEA, 2013; Zhang et al., 2020; Deng et al., 2021). Furthermore, micro-sized DC-EMPs have also been developed for circulating electrolytes and nanofluids at very low flow rates in chemical and biomedical research and applications (Wang et al., 2004; Abhari et al., 2012; Ito et al., 2014).

For its simplicity, and low computational cost, the Equivalent Circuit Mode (ECM) with several simplifying assumptions, had been used to approximately predict the DC-EMPs characteristics (Baker and Tessier, 1987; El-Genk, 2009). However, the recent advancements in computer capabilities increased the interest in using the MagnetoHydroDynamics (MHD) approach to analyse and predict the performance of DC-EMPs. This 3-D numerical approach solves the coupled electromagnetism, and momentum and energy balance equations, for predicting the characteristics of DC-EMP designs prior to construction and providing detailed images of the flow, electric current and magnetic field strength distributions in the flow duct (Hughes et al., 1995; Kandev, 2012; Aoki et al., 2013; Sun et al., 2021). However, due to the high computational cost of conducting 3-D MHD analyses, the initial parametric analyses of the pump design are usually done using the lumped Equivalent Circuit Model (ECM) (Lee and Kim, 2018; Sun et al., 2021, Altamimi and El-Genk, 2023b). The ECM enables performing large number of optimization and parametric analyses in a relatively short time using modest computer hardware, but includes several simplifying assumptions that contribute to overpredicting the pump characteristics by > 10% (Watt et al, 1957; Altamimi and El-Genk, 2023a; Altamimi and El-Genk, 2023b), and it doesn't provide insight into the coupled physics undergoing in the pump that can be obtained using the 3-D MHD numerical analyses.

Recently, several MHD numerical studies of DC-EMPs have been published, with the majority focusing on micro pumps for chemical and biological applications, of circulating electrolytes and nanofluids at very low flow rates and room temperature utilizing currents in the milliampere range (Wang et al., 2004; Kiyasatfar et al., 2011; Ito et al., 2014; Hasan et al., 2017). Only a handful of reported MHD analyses have been of DC-EMPs for circulating liquid metals at elevated temperatures. Kandev (2012) has conducted MHD simplified numerical analyses of a DC-EMP for circulating molten aluminum at ~700°C, both in the laminar and turbulent flow regimes. The flowing molten aluminum through the pump duct is subjected to a predefined and constant 2-D magnetic field function representing permanent magnets, regardless of the flow rates. This study also neglected the opposing magnetic field produced by the flow in the perpendicular direction to that of the input electric current of ~1800A, and hence its effect on the spatial distributions of the total magnetic field and generated Lorentz force in the pump duct. The reported simulation results showed a formulation of an M shaped velocity profile of molten lead working fluid in flow duct in the two pumping stages.

Lee and Kim (2018) have simulated the performance of DC-EMP for laminar flow of liquid lithium at 200°C in a heavy ion accelerator. They simplified the analyses by only considering the components of the magnetic flux density vector along the duct height and width and of the current density vector along the duct width. As a result, the perpendicular Lorentz force vector had a single component along the duct length, neglecting the generated turbulent Lorentz forces in other directions. The analysis also neglected the effect of the induced magnetic fields in the liquid lithium flow in the perpendicular direction to that of the electric current in the duct, as well as the viscosity term in the Navier-Stokes equation due to the high Hartmann number of the electromagnetic pump. At a flow rate of 6 cm^3/s, the performed MHD calculated a pumping pressure of 1.5 MPa.

Recently, Sun et al. (2021) have designed a small DC-EMP for high-power charging of electric vehicles. They utilized MHD analysis to quantify the effects of changing the values of the input current and magnetic field on the pump performance. The analyses assumed a constant and uniform distribution of the magnetic field across the pump duct for all flow rates and neglected the induced magnetic fields from the electric input current in the pump duct. The MHD analysis predictions of pump characteristics were consistently ~5% higher than the experimentally measured data. This difference may be attributed to the simplifying assumptions in the performed MHD analysis by Sun et al. (2021). Therefore, for accurate prediction of a DC-EMP performance, future MHD analyses need to solve the 3-D coupled electromagnetism, and momentum and energy balance equations to calculates the pump characteristics and provides 3-D images of the flow, electric current and magnetic field strength distributions in the flow duct. In addition, confirm the adequacy of the employed numerical mesh refinement and ascertain the results conversion.

The objective of this chapter is to perform 3-D MHD analyses of a recently developed 66.8 mm diameter, submersible, dual-stage DC-EMP for circulating molten lead and liquid sodium at 500^{o}C in test loops (Altamimi and El-Genk, 2023b). These loops investigate the compatibility of these liquids with nuclear fuel and cladding and structural materials for Gen-IV fast neutron spectrum nuclear reactors (El-Genk et al, 2023). The dual-stage DC-EMP uses a pair of Alnico 5 permanent magnets with Hiperco-50 pole pieces to help focus the magnetic field lines in the pump duct. The predictions of the MHD analyses of the pump performance are compared to those calculated using the lumped approach in the ECM, which has been shown to overpredict the measured performance characteristics DC-EMPs for liquid mercury and alkali metals by > 10% (Watt et al. 1957; Johnson, 1973; Nashine et al, 2006; Zhang, 2020; Altamimi and El-Genk, 2023a). The ECM assumes constant values and uniform electric and magnetic field strength in the pump duct could be calculated using the FEMM model at zero flow (Altamimi and El-Genk, 2023a; Altamimi and El-Genk, 2023b). The ECM also neglects the contribution of the magnetic fields generated in the flow duct by the input electric current and the effects of the flow rate on the values of the effective current and magnetic field strength in the pump duct. These simplifying assumptions effectively decrease the computation time and cost but cause the ECM to overpredict the pump characteristics.

Unlike the ECM, a 3-D MHD analyses of the miniature submersible DC-EMP of Altamimi and El-Genk (2023b) provide insight into the pump operation and the spatial distributions of the fluid flow, and the magnetic field and electric current distributions, and hence the Lorentz force in the pump duct, not even possible experimentally. The MHD analyses solve the coupled electromagnetism, and the momentum and energy balance equations to calculate the pump characteristics and various performance parameters. The adequacy of the numerical mesh refinements and the conversion of the numerical results are confirmed using the Grid Convergence Index (GCI) criterion.

The remainder of this chapter is organized as follows. Section 2 describes the miniature, submersible dual-stage DC-EMP design developed by Altamimi and El-Genk (2023b). Section 3 describes the MHD numerical analyses approach including the governing equations, numerical modelling and meshing, and the mesh grid sensitivity analyses and results conversion. The obtained results of the MHD analyses including the pump characteristics, the effects of the fluid properties and temperature are presented and discussed in section 4. This section also compares the calculated pump characteristics using the present MHD analyses and the ECM for both molten lead and liquid sodium.

5.2. MHD Numerical Analyses Approach

The performed MHD analyses of the present miniature, submersible DC-EMP design used the modelling and simulation capabilities in the Star-CCM+ commercial code (Siemens P.L.M., 2018) to calculate the spatial 3-D distributions of the pump electrical, magnetic flux density and the working fluid flow in the pump duct. The analyses also calculate the special distribution of the generated Lorentz force for driving the fluid flow in the two pumping stages of duct and hence the pumping pressure versus the fluid flow rate. The MHD analyses numerically solve the coupled electromagnetism 3-D equations to those the fluid flow momentum and energy balance equations using the multi-physics CFD software Simcenter STAR-CCM+ (Siemens P.L.M., 2018). The following subsection briefly lists the governing equations and outlines the numerical approach used for solving these equations, including the numerical mesh grid refinements and their effect on the values and the conversion of the calculated parameters.

5.2.1. Governing Equations

The fundamental electromagnetism equations are those of Maxwell and the Ohm's law (Meunier, 2010; Aizawa et al., 2014). These coupled equations define the distributions of the magnetic flux densities, the electric fields, and current densities in the computation domain. Maxwell four equations are those the Faraday's law of induction, the Ampere law, the Gauss law of electricity and the Gauss law of magnetism, given by Eqs. 5-1 to 5-4 for steady-state conditions as (Meunier, 2010; Siemens P.L.M., 2018):

Faraday's law of induction:

$$\nabla \times \vec{E} = 0 \tag{5-1}$$

Ampere's law:

$$\nabla \times \vec{B} = \mu \vec{J} \tag{5-2}$$

Gauss' law of electricity:

$$\nabla . \vec{E} = \frac{\rho}{\varepsilon_o} \tag{5-3}$$

Gauss' law of magnetism:

$$\nabla . \vec{B} = 0 \tag{5-4}$$

The Ohm's law states that the amount of electric current flowing through a conductor is directly proportional to the electric field present in the conductor domain, including the supplied electrical field acting at rest $(\vec{E})$, and the induced electromotive force by the movement of the conductor in the presence of a magnetic field $(\vec{u} \times \vec{B})$. The Ohm's law is then given as:

$$\vec{J} = \sigma \left(\vec{E} + \vec{u} \times \vec{B}\right) \tag{5-5}$$

Substituting Eq. (5-5) and Eq. (5-2) into the Faraday law in Eq. (5-1), gives an expression relating the magnetic flux density, $\vec{B}$, to the flow velocity of the working fluid, $\vec{u}$, as:

$$\nabla \times \left(\frac{\nabla \times \vec{B}}{\sigma\mu} - \vec{u} \times \vec{B}\right) = 0 \tag{5-6}$$

In this equation, the total magnetic flux density, $\vec{B}$, includes: the magnetic fields generated by the permanent magnets, those induced from the supplied electrical current to the pump electrodes, and the from the induced eddy currents in the moving fluid $(\vec{u} \times \vec{B})$. The latter is usually assumed negligible in the literature to reduce the computational time, thus decoupling the magnetic and the fluid flow fields (Kandev, 2012; Hasan et al. 2017; Lee and Kim, 2019). However, this assumption is only valid for fluids flowing at magnetic Reynold numbers, Re_m, much smaller than unity (Davidson, 2002). The magnetic Reynold number is the ratio of the induced magnetic field to the applied magnetic field, and expressed as:

$$Re_m = \mu\, \sigma\, U\, L \tag{5-7}$$

With the calculated values of the current density, $\vec{J}$, and the magnetic flux density, $\vec{B}$, from Eqs. (5-5) and (5-6), the generated Lorentz force for driving the working fluid in the pump duct is calculated as:

$$\vec{F_l} = \vec{J} \times \vec{B} \tag{5-8}$$

The Lorentz force couples the electromagnetic equations to the continuity and momentum balance equations of the fluid flow. At steady-state incompressible turbulent flow, such as those of molten lead and liquid sodium in the dual-stage DC-EMP duct, the continuity and momentum equations are expressed, respectively, as:

$$\rho\, \nabla . \vec{u} = 0 \tag{5-9}$$

$$\rho(\vec{u}.\nabla)\vec{u} = -\nabla P + \nabla.\left((\eta + \eta_T)(\nabla\vec{u} + \nabla\vec{u}^T)\right) + \vec{F_l} \tag{5-10}$$

Eq. (5-10) is the Reynolds-Averaged Navier-Stokes (RANS) form of the Navier-Stokes equation used in present analyses to model the molten lead and liquid sodium flow at Reynold numbers $> 10^4$ (Siemens P.L.M., 2018). Additionally, the energy balance equation for incompressible fluid flow in the presence of applied electrical fields is expressed as:

$$\rho C_p \vec{u}.\nabla T = k\nabla^2 T + \frac{|J|^2}{\sigma} \tag{5-11}$$

The last term of Eq. (5-11) is the Joule (Ohmic) heating generated by the electric current flowing through the working fluid. For liquid metal, DC-EMPs that employ high electric currents, the Joule heating could be large and impact the pump performance by altering the physical and electrical properties of the working fluid due to temperature increases, particularly at low flow rates. In comparison, the Joule heating generated in the 0.5 mm thick 316SS duct walls assumed negligible and the energy balance equation Eq. (5-11) is decoupled from the RANS equation (Eq. 5-10) by assuming that changes in the working fluid temperature across the pump duct will negligibly changes the fluid dynamic viscosity (η). This assumption, which reduces the computational time required for completing the MHD analyses, is investigated and justified in the results section of this study.

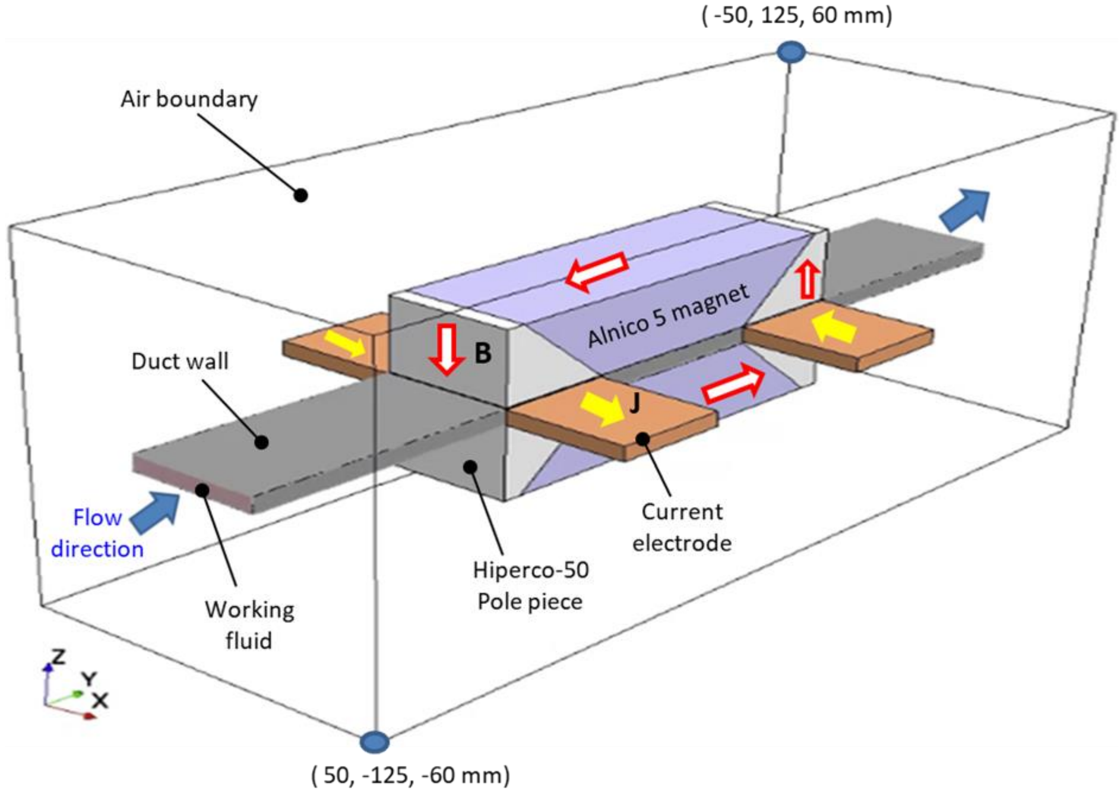

Figure 5-1: Dual-stage DC-EMP and surrounding air domain in STAR-CCM+.

5.2.2. Numerical Modeling

The 3-D MHD equations described in the previous subsection are solved numerically for the calculating the performance parameters and characteristics of dual-stage DC-EMP in Fig. 5-1 using the multi-physics commercial CFD software STAR-CCM+ version 13.06.012 (Siemens P.L.M., 2018). It utilizes the finite element method to discretize the MHD governing equations and employs an iterative approach to couple the electrical, magnetic, fluid flow, and heat transfer physics within the pump duct domain.

The physics models employed in the STAR-CCM+ MHD analyses include those of the electrodynamic potential, the finite element magnetic vector potential, the two-way coupled MHD, the ohmic or joule heating, the segregated fluid temperature, and the k-ε turbulent flow (Siemens P.L.M., 2018). The two-way coupled MHD model in STAR-CCM+ accounts for the induced magnetic fields resulting from the electrical eddy currents induced by the fluid flow in the applied magnetic field, ($\vec{u} \times \vec{B}$) in Eq. (5-5). Thus, it is possible to investigate the effect of varying the fluid flow rate on the magnetic field distribution in the flow duct, and hence the pump performance.

The dual-stage DC-EMP is built into a 3-D domain using the SolidWorks CAD software (SolidWorks Corporation, 2016) which is then imported into STAR-CCM+ for performing the present MHD analyses (Fig. 5-1). A rectangular air boundary surrounding the pump domain encompasses the full distribution of the magnetic fields from the permanent magnets outside the pump. The centered air boundary at the origin is 100 mm wide, 250 mm long and 120 mm high along the x, y, and z coordinates (Fig. 5-1).

The fluid flow at the inlet (y = -125mm) is assumed fully developed with u = (0, u_d, 0) m/s. The developed velocity profile, u_d, is calculated prior to the starting the MHD using fluid flow analyses of the liquid metal entering the pump duct uniformly in the absence of electromagnetic fields. The developed velocity profile for non-slip flow condition at the duct wall is extracted at distance from the entrance of the pump duct = 30 times the duct equivalent hydraulic diameter. The developed velocity profiles obtained for different fluid properties and bulk inlet flow velocities are used in the MHD analyses of the pump. The exit pressure of the fluid flow, at y = 250 mm from the duct entrance, is taken equal to zero Pa and the air boundary is treated as a solid part to eliminate the computational time and cost required for solving the fluid dynamics equations in pump domain. The fluid inlet temperature, at y = -125 mm, is set at 500^{o}C, and the energy balance equation in the fluid region is solved subject at an adiabatic boundary condition at the duct wall.

The outer surfaces of the air boundary for the computational domain (Fig. 5-1) are magnetically and electrically insulated by setting the conditions: $\vec{n} \times \vec{A} = 0$ and $\vec{n} \times \vec{J} = 0$, where $\vec{n}$ is the normal vector to the boundary surface, and $\vec{A}$ is the magnetic vector potential. The interfaces between the air boundary, permanent magnets, pole pieces, electrodes, electrical insulations, duct walls, and the fluid are assumed with an electromagnetic continuity, corresponding to a homogenous Neumann condition (Kandev, 2012; Siemens P.L.M., 2018).

The pair of Electrodes in contact with the duct wall in the first pumping stage has an inlet electrical current at y = -50 mm of $I = I_{in}$, where I_{in} is the electrode input current, and an outlet condition at y = 50 mm of $V = 0$. The same boundary conditions are applied to the pair of electrodes in contact with the duct wall of the second pumping stage, but in the opposite direction. Table. 5-1 lists the physical properties of molten lead used in the performed MHD analyses at a constant temperature of 500°C (Sobolev, 2011). The remanent flux densities and relative magnetic permeabilities of the Alnico5 and Hiperco-50 permanent magnets are calculated using their B-H curves at 500°C. All other pump components are considered to have relative magnetic permeabilities of that of free space (1.257×10^{-6} H/m). The flow of electric currents is only considered in the electrodes, duct walls, and working fluid, with electrical conductivities in the three regions evaluated at 500°C are 20.8, 0.894, and 0.967 10^{6} S/m, respectively (Eldrup and Singh, 1998; Zhang, 2009; Sobolev, 2011). Other pump components and the air boundary are assumed to be electrically non-conductive.

Table 5-1: The physical properties of molten lead at 500°C used in the performed MHD numerical analyses (Sobolev, 2011).

Parameter	**Value**	**Parameter**	**Value**
Electrical conductivity (S/m)	0.967×10^{6}	Dynamic viscosity (Pa.s)	1.81×10^{-3}
Magnetic permeability (H/m)	1.257×10^{-6}	Thermal conductivity (W/m.k)	17.7
Density (kg/m^3)	10,450	Specific heat capacity (J/kg.k)	144

5.2.3. Mesh Refinement Analyses

The implemented mesh grids in the 3-D MHD numerical analyses of the dual-stage DC-EMP in Fig. 5-1 are developed using the tetrahedral Mesher utility with the embedded prism layer Mesher option in STAR-CCM+ (Siemens P.L.M., 2018). The tetrahedral mesh elements are compatible with the finite element discretization in the MHD analyses. To accurately capture the steep change in momentum gradients near the walls, 5 parallel prismatic layers elements are used in a 0.2 mm thick boundary layer. The prism layer's thickness increases by a multiplier of 1.3 with distance from the walls toward the bulk flow in the pump duct.

The MHD analyses implemented four different mesh grids with increased refinements (coarse, intermediate, fine, and finer) to select suitable grid for results conversion in reasonable computational time. The prism layer thickness is kept the same in all four numerical mesh grids with varied sizes of the tetrahedral mesh elements. A representation of the coarse grid used is shown in Fig. 5-2 and the details of the different mesh grid arrangements are listed in Table. 5-2. The coarse mesh grid has approximately 2.77 million mesh elements, ~ 66.7% of them (1.85 million) in the bulk flow of the pump duct. The intermediate grid has about 83.4% more mesh elements than the coarse grid, with a total of 5.08 million elements, including around 71.8% (3.65 million) in the bulk flow. The fine and finer mesh grids have a total of 9.08 and 16.36 million elements, respectively, with 6.81 and 12.7 million elements in the bulk flow region. The average element size in the bulk flow region varied from 0.51 mm in the coarse mesh grid to 0.21 mm in the finer grid.

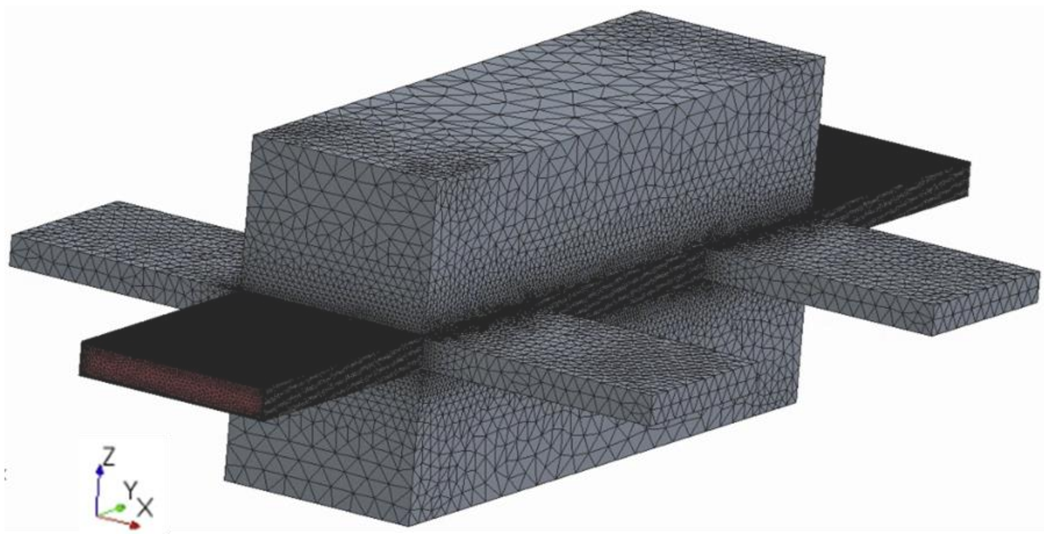

(a) Coarse mesh grid of the dual-stage DC-EMP

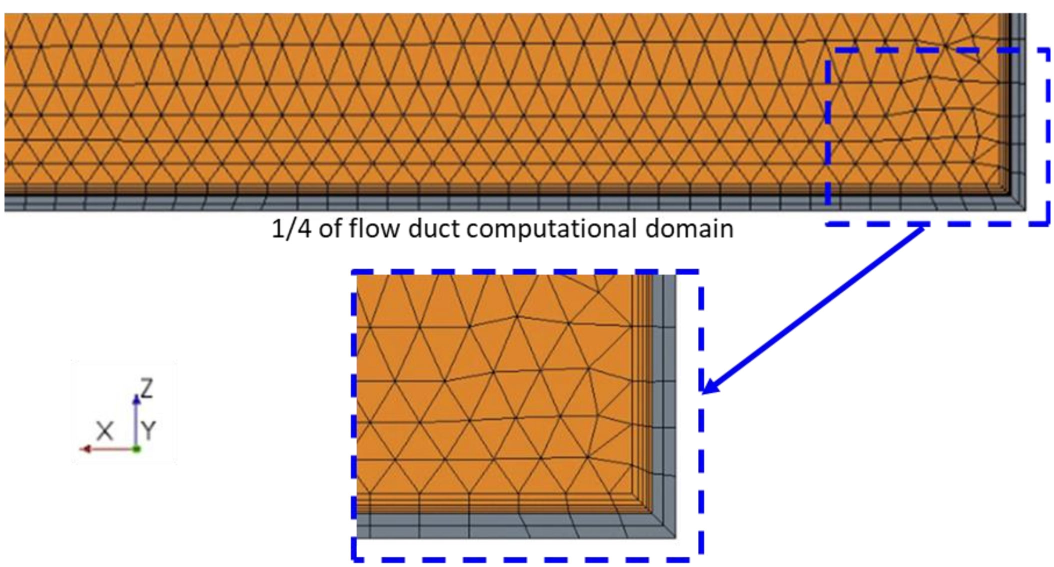

(b) Coarse mesh grid arrangement in the flow duct

Figure 5-2: Representations of the implement course numerical mesh grid with prism layer in the present MHD analyses of the miniature, dual-stage DC-EMP in Fig. 5-1.

Table 5-2: Comparison of four numerical mesh grids implemented in present MHD analyses of miniature, dual-stage DC-EMP in Fig. 5-1.

Pump Region	**Mesh grid elements (Million)**			
	Course	**Intermediate**	**Fine**	**Finer**
Working flow	1.85	3.65	6.81	12.7
Duct wall	0.17	0.28	0.49	0.76
Alnico5	0.25	0.38	0.61	0.98
Pole pieces	0.27	0.41	0.65	1.05
Current electrodes	0.04	0.06	0.09	0.14
Electrical insulation	0.08	0.12	0.19	0.31
Air boundary	0.13	0.18	0.26	0.43
Total	**2.77**	**5.08**	**9.08**	**16.36**

The results obtained using the four different mesh grid arrangements include those of the net pumping pressure versus the fluid flow rate. The pumping pressure is a parameter of interest, influenced by all the physics involved in the MHD analyses, such as electromagnetism, fluid flow, and energy balance. Thus, the convergence of the pumping pressure is considered an indicator for the convergence of other calculated parameters. A convergence is considered when the change in the calculated pumping pressure in 50 sequential iterations is < 0.001%.

The Grid Convergence Index (GCI) method proposed by Roache (1994) is used to determine the sensitivity of the numerical results to changing the refinement of the numerical mesh grid (Table. 5-2). The concept of the GCI is derived from the theory of generalized Richardson extrapolation. It relates the error produced from systematic grid refinements or coarsening to the error produced when doubling or halving the grid size using the second-order method, and is expressed as:

$$GCI_{mn} = F_s \frac{e^{mn}}{r_{mn}^{p}}, \tag{5-12}$$

where n = 1, 2, 3 and m = 2, 3, 4 depending on the refinement stage, F_s is the safet factor equal to 3 when solutions on only two mesh grids are available and is equal to 1.25 when solutions on three mesh grids or more are available (Roache, 1994; Eca and Hoekstra, 2014), e^{mn} is the absolute relative error between solutions of m and n refinement stage, r is the grid refinement factor, and p is the apparent order given for the case of constant grid refinement factor as:

$$p = \left| \frac{\ln\left|\frac{\Phi_1 - \Phi_2}{\Phi_2 - \Phi_3}\right|}{\ln r_{21}} \right|, \tag{5-13}$$

where Φ is the analysis solution using specific mesh grid. The objective of mesh refinement analyses is to decrease the Grid Convergence Index (GCI) to an acceptable level, typically below a predetermined threshold, to establish grid independence. In present analyses, a threshold of 5% is considered sufficient to ensure the solution's accuracy (Almohammadi et al., 2013; Haskins and El-Genk, 2016).

The calculated pumping pressures for circulating molten lead at 3.67 m^3/h, inlet average velocity of 6 m/s and Reynolds number of $3x10^5$, using the different mesh grid arrangements listed in Table. 5-2 are compared in Table. 5-3. This table also compares the changes in the calculated values of the pumping pressure, GCI, and computational time, relative to those determined for the coarse mesh grid. The converged value of the pumping pressure increases, while the corresponding value of the GCI decreases, with increased refinement of the numerical mesh grid in the MHD analyses. Note that the calculated values of the pumping pressure using the fine and finer mesh grids are identical, but the computation time for conversion using the latter is four time larger. The calculated GCI for the intermediate, fine, and finer mesh grids are 14.5%, 1.5%, and 0.6%, respectively. The relative computational time, which represents the time required for the results conversion normalized to that for coarse mesh grid, increases with increased mesh refinement.

Table 5-3: Comparison of the effect of numerical mesh refinement on the calculated values of the pumping pressure and the Grid Convergence Index (GCI) in the present 3-D MHD analyses of the miniature, dual-stage DC-EMP in Fig. 5-1.

Calculated parameter	**Mesh grid elements (Million)**			
	Course	**Intermediate**	**Fine**	**Finer**
Pumping pressure (kPa)	291.21	310.37	316.18	316.33
Relative difference (%)	---	6.58	1.87	0.05
GCI (%)	100	14.5	1.5	0.6
Relative computational time	1	2.7	8.2	32

The results conversion using the course mesh grid took approximately 28 hours to converge on a machine with 32 cores, 3.69 GHz base speed, and 256 GB of RAM. This time increases by ~ 270%, 820% and 3200% with the intermediate, fine, and finer numerical mesh grid, respectively. Based on the results presented in Table. 5-3 the fine mesh grid is considered reasonable compromise for results conversion and computation time considerations, with GCI < 5%. Therefore, the fine mesh grid is implemented in the remainder of the performed MHD analyses, and the obtained results are presented and discussed next.

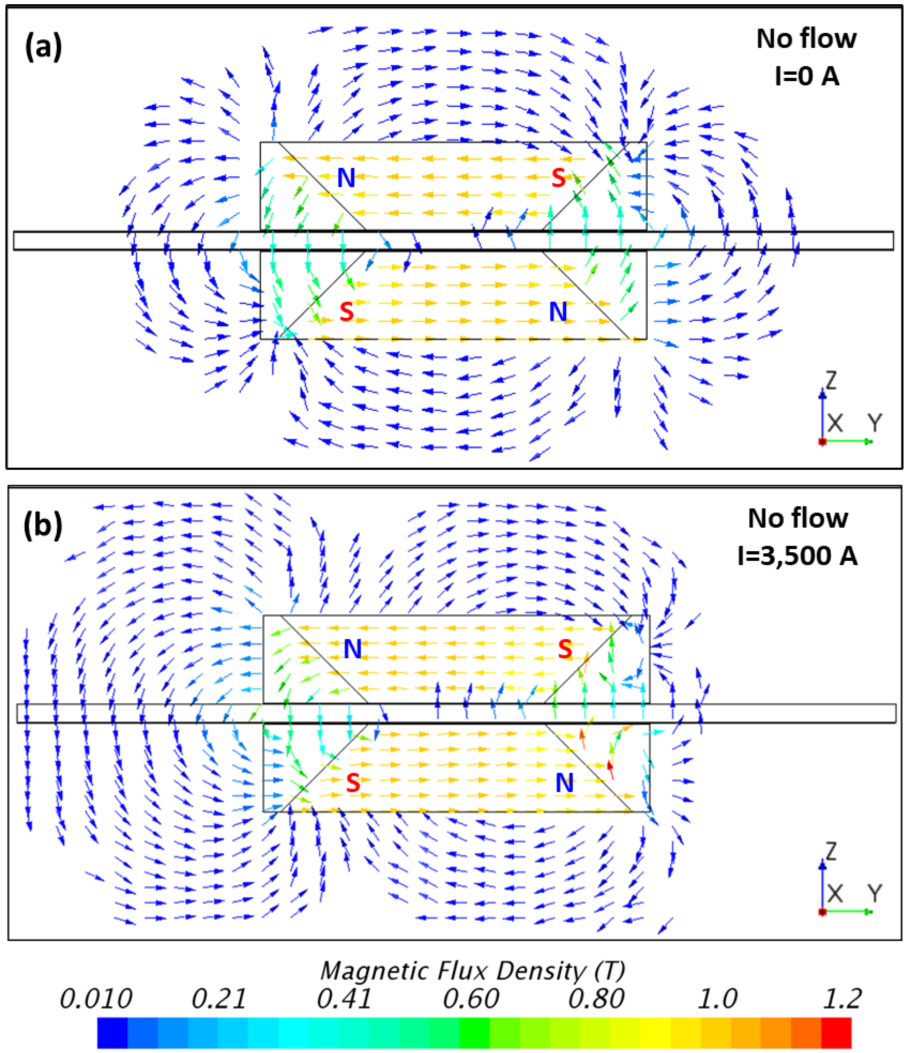

Figure 5-3: Calculated Magnetic field distribution in pump duct and surrounding in present 3-D MHD analyses of the miniature, dual-stage DC-EMP in Fig. 5-1, at zero flow of molten lead at 500^{o}C and (a) zero electric current and (b) electric current, I = 3,500A.

5.3. Results and discussions

This section presents and discusses the obtained results of the 3-D MHD analyses for the miniature dual-stage DC-EMP (Fig. 5-1). First, the magnetic field and electrical current density distributions at zero flow of molten lead at an inlet temperature of 500^{o}C are calculated and used in the MHD analyses performed using the Star-CMM+ commercial code. The MHD results demonstrate the strong coupling of the electrical current and magnetic flux densities in and outside the pump duct as a function of flow rate of molten lead through the pump duct. For molten lead and liquid sodium flows, the obtained performance characteristics of the dual-stage DC-EMP are compared to the predictions of the lumped ECM model.

5.3.1. Magnetic Field Distribution

The magnetic field in the dual-stage DC-EMP comes from three sources, namely: (a) the ALNICO-5 permanent magnets whose flux lines are focused in the pump duct using the Hiperco pole pieces (Fig. 5-1), (b) the electrodes electrical currents passing through the flowing fluid in the pump duct in the perpendicular direction to that of the primary magnetic field in (a) and (c) induced from the generated eddy currents in the flowing fluid in the above sources of the magnetic fields.

The magnetic field distribution in the pump duct, calculated in the 3-D MHD analyses at zero flow of working fluid and zero input current, is that produced by the ALNICO-5 permanent magnets. Obtained results are validated against those of the FEMM analyses used in pump design (Altamimi and El-Genk, 2023b). Fig. 5-3a shows the calculated magnetic flux density distribution in the flow duct of the dual-stage DC-EMP and the surroundings (Fig. 5-1) at zero flow and zero electrical current. Most of the magnetic field lines from the North (N) pole of one magnet travel to the South (S) pole of the other magnet through the Hiperco -50 pole pieces and the pump duct. A small fraction of the magnet field lines travel between the N and S poles of the same magnets outside the pump duct. It is considered a loss since it does not contribute to the generation of the Lorentz force for driving the flow in the pump duct.

The hiperco-50 pole pieces effectively decrease these losses by focusing the magnetic field lines generated by the ALNICO-5 permanent magnets into the pump duct, where the electrical current passes in the perpendicular direction (Fig. 5-1). The pole pieces cause the magnetic field lines to travel in the pump duct in straight lines in the perpendicular direction to those of the electric current and fluid flow, reducing the turbulence in the generated Lorentz force in the pump duct and enhance the pump performance. In the first pumping stage, the input current in Fig. 5-3b that travels across the pump duct in the negative x-direction (towards the reader), generates a magnetic field in the counter-clockwise direction. In the second pumping stage, however, the input electric current travels across the pump duct (Fig. 5-3b) in the positive x-direction (far from the reader) and induces a magnetic field in the clockwise direction. The induced magnetic fields in the two pumping stages travel in similar directions to that of the external magnetic field produced from the permanent magnets across the pump duct (Fig. 5-3a) and upstream.

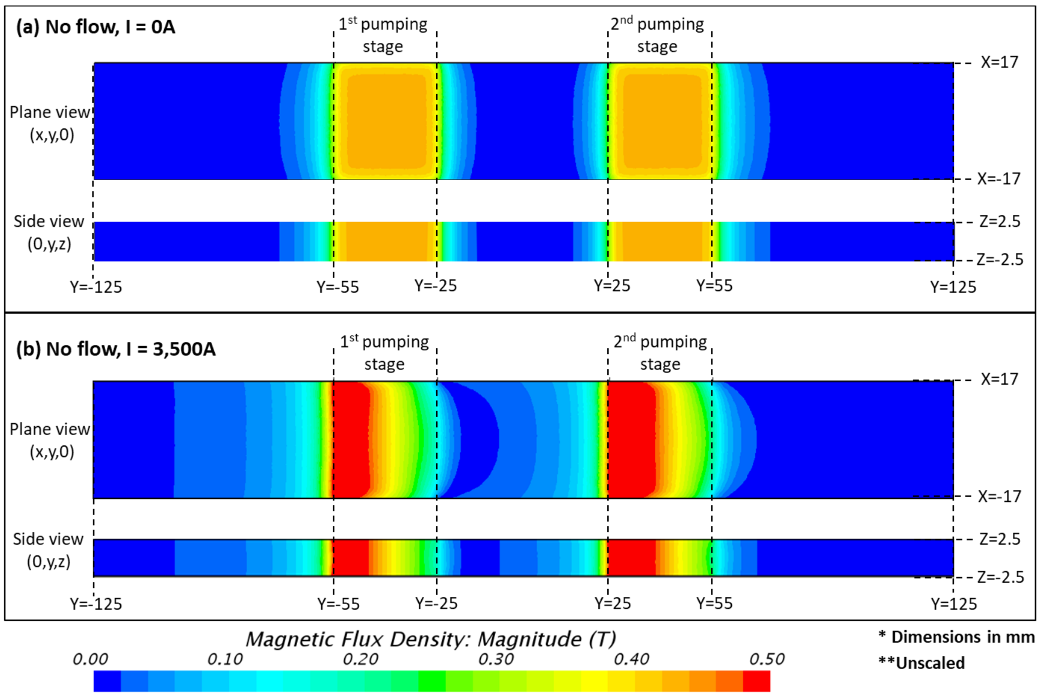

Figure 5-4: Magnetic flux density distribution in flow duct at planes (x,y,0) and (0,y,z) in present 3-D MHD analyses of the miniature, dual-stage DC-EMP (Fig. 5-1), at zero flow of molten lead at 500°C and (a) zero electric current and (b) electric current, I = 3,500A.

The generated magnetic field in the opposing direction downstream of the pumping staged shift in the total magnetic field distribution toward the pump inlet (Fig. 5-3a and Fig. 5-4). The magnetic flux density in the two pumping stages becomes non-uniform with increasing magnitude at inlet and decreasing magnitude at exit of the two pumping stages (Fig. 5-4). Results also show that the input electric current also affects the magnetic field distribution in the pump duct by increasing and decreasing the fringe flux density upstream and downstream of the pumping stages. Fig. 5-4 presents the calculated magnetic field distributions in the pump duct at the mid plans (X-Y) and (Z-Y) and at zero flow rate of molten lead and (a) zero input current and (b) I = 3, 500A. At zero electrical current, the magnetic field distribution in the two pumping stages is symmetric, uniform in the mid of the flow duct in the pumping stages and decreases when distance closer to the duct walls in contact with the current electrodes or upstream and downstream of the pumping stages. A small amount of the magnetic field is fringing outside the pump duct in the two pumping stages (Fig. 5-4a). with an electric current of 3,500 A (Fig. 5-4b) the magnetic field density is highest in the pump duct at the entrance to the two pumping stages and decreasing rapidly with distance from the entrances. Note also that the extents of the fringe magnetic field lines in the pump duct upstream of the pumping stages are limited compared to those downstream of the pumping stage (Fig. 5-4b). The nonuniformity of the magnetic field distribution in the pump duct results in the generation of the highest Lorentz force at the entrance to the two pumping stages (Figs. 5-5 and 5-6).

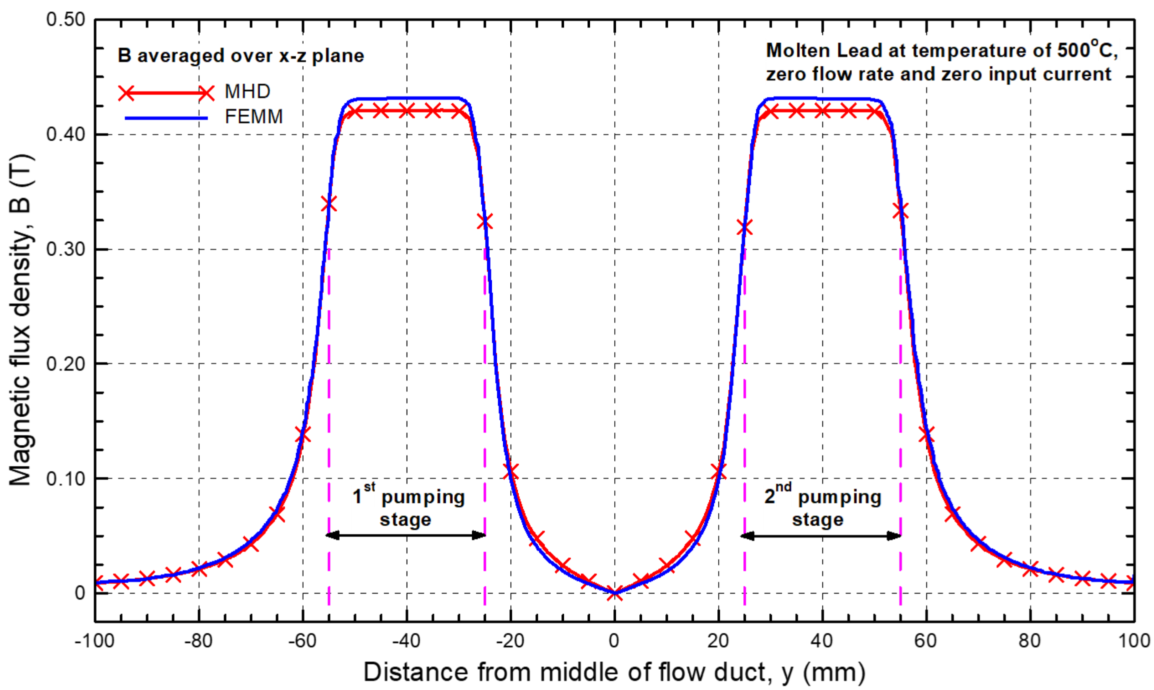

Figure 5-5: Comparison of the calculated magnetic flux density distributions in the present 3-D MHD analyses along the pump flow duct and using the FEMM software at zero flow and zero electric current.

Fig. 5-5 compares the calculated magnetic flux density distribution in the present 3-D MHD analyses along the pump flow duct to those calculated using the FEMM software at zero flow and zero electric current. Unlike the MHD analyses, the 2-D FEMM calculations can only be conducted in the Y-Z plane and assumes a uniform magnetic field distribution across the pump duct (X direction). The results are in general good agreement, however, since the FEMM neglects the decreases in magnetic field distribution across the pump duct in the x-direction (Fig. 5-4a and Fig. 5-5), its predictions are higher than those of the present MHD analyses. The calculated average magnetic flux density using FEMM in each of the two pumping stages are identical and = 0.427T. This value is ~2.4% higher than that determined from the results of MHD numerical analyses of 0.418T.

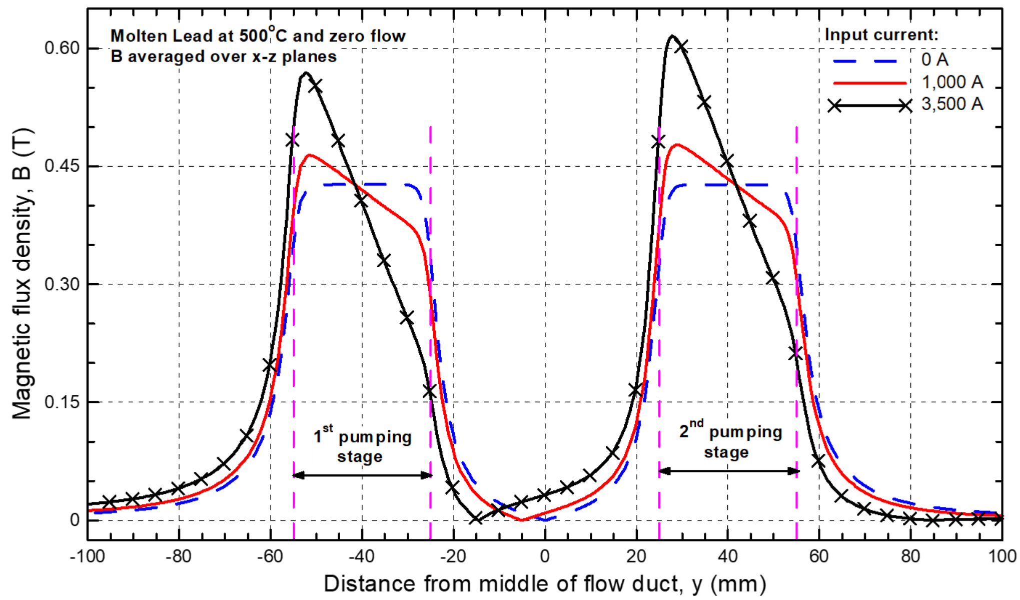

Figure 5-6: Effect of the input electric current on the uniformity of the distribution of the magnetic flux density distribution along the flow direction in the pump duct of molten lead at 500°C.

As indicated in Figs. 5-3 and 5-4, the electrical current to the DC-EMP induces armature magnetic field in the pump duct in the perpendicular direction to that of the electric current, according to the right-hand rule (Baker and Tessier, 1987). The induced magnetic field flux density, which distorts the distribution in the magnetic field in pump duct, is proportional to the magnitude of the electric current. Fig. 5-6 presents the calculated magnetic flux density distribution along the flow direction of molten lead in the dual-stage DC-EMP flow duct at zero flow and different electric currents, namely: 0, 1,000, and 3,500 A. Increasing the electric current increases the non-uniformity of the magnetic flux density in the flow duct in the two pumping stages. The magnetic flux densities increase and decrease at the inlet and exit of the two pumping stages (Fig. 5-6), respectively, of the present DC-EMP.

Similarly, increasing in input electric current increases the fringe magnetic flux density upstream and decreases it downstream regions of the pumping stages (Fig. 5-6). Therefore, the magnetic flux densities in the two pumping stages are neither uniform nor symmetric and the difference in the magnetic flux density distribution in the two pumping stages increases as the electric current increases. For an input current of 1,000A, the peak magnetic flux density in the first and second pumping stages are 0.4642 T and 0.4777 T, respectively, while for an input current of 3,500A, the peak values of the magnetic flux density in the first and second pumping stages are smaller, 0.5696 T and 0.6152 T, respectively (Fig. 5-6).

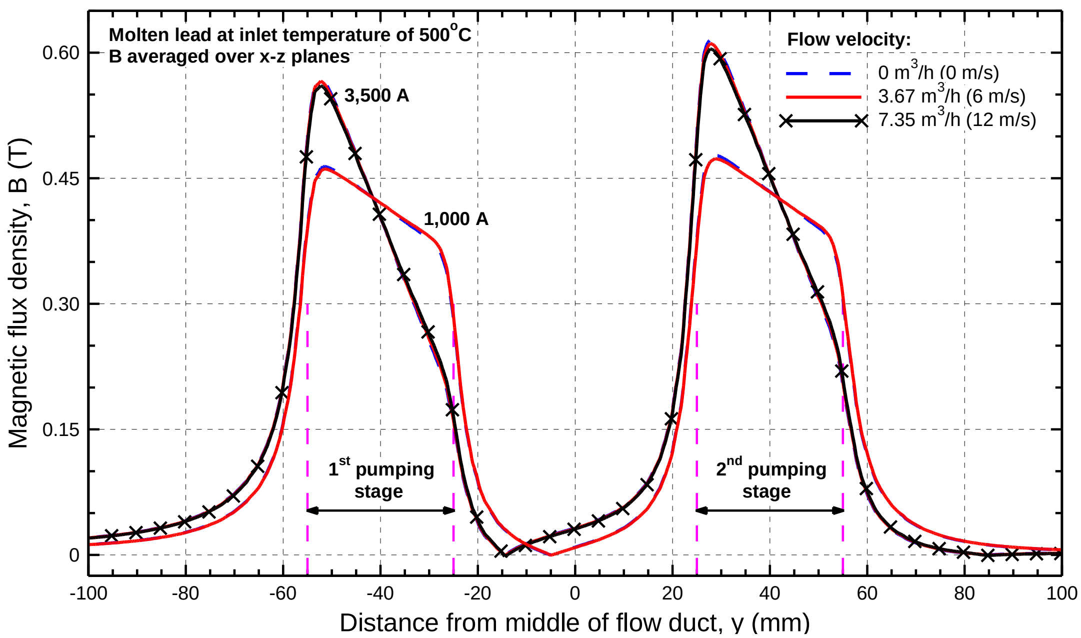

Figure 5-7: Effect of the electrode current on the values and distributions of the calculated magnetic flux density in two-pumping stages of present DC-EMP (Fig. 5-1).

The flow of the working fluid in the presence of the magnetic field provided by the ALNICO-5 permanent magnets in the pump duct generates electrical eddy currents which in turn produce an opposing secondary magnetic field. The latter is negligible when the fluid magnetic Reynold numbers, Re_m, is less than unity. For the present dual-stage DC-EMP the calculated Re_m for molten lead at 500°C (Eq. 5-7) < 0.08. Therefore, the fluid flow will not influence the magnetic field distribution in the pump duct. This is confirmed by comparing the calculated magnetic flux density distributions in the pump duct at different flow rates and input currents (Fig. 5-7). The results in this figure confirm that changing the flow rate of molten lead negligibly affects the value and the distribution of the magnetic flux density in the pump duct. As a result, the magnetic and the flow fields in the present MHD analyses are uncoupled, which reduces the computation time and cost of the numerical analyses without affecting the performance results. The computation time required for converging the analyses results of dual-stage DC-EMP circulating molten lead at flow rate of 3.67 m^3/h decreased by ~18.7%, from 230 to 187 hours, on a machine with 32 cores, 3.69 GHz base speed, and 256 GB of RAM, when the magnetic and the flow fields were uncoupled.

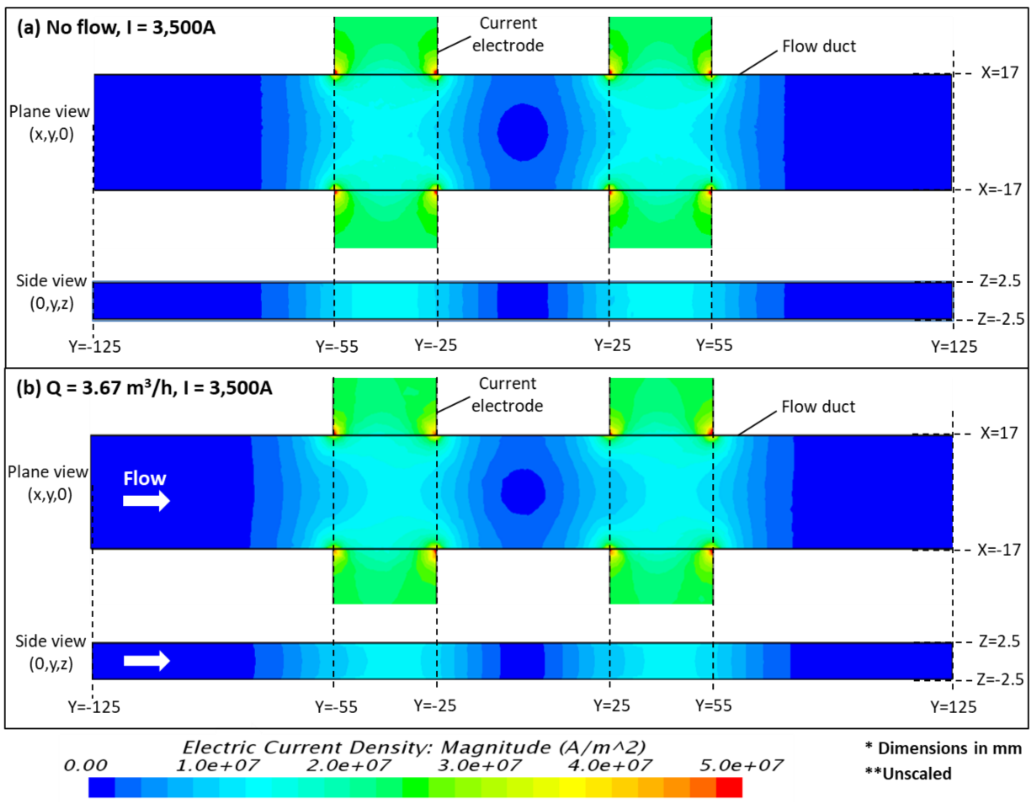

Figure 5-8: Calculated distributions of electric current density in flow duct of the DC-EMP in the present MHD analyses at 3,500A: (a) zero flow, and (b) lead at 3.67 m^3/h.

5.3.2. Electrical Current Field Distribution

The electrical current distribution in the flow duct of the present dual-stage DC-EMP is attributed to two sources, namely: (a) the electrodes electric current, and (b) the induced eddy currents induced by the flowing of the working fluid in the influence of applied magnetic field by the ALNICO permanent magnets. The distribution of the current density in the pump is first calculated at zero flow and validated against that calculated using the FEMM analyses. Fig. 5-8a shows that at zero flow and input electric current of 3,500 A, the current in the two pumping stages splits into three components: through the flowing fluid in the pump duct and the duct walls and in the fringe regions upstream and downstream of the pumping stages.

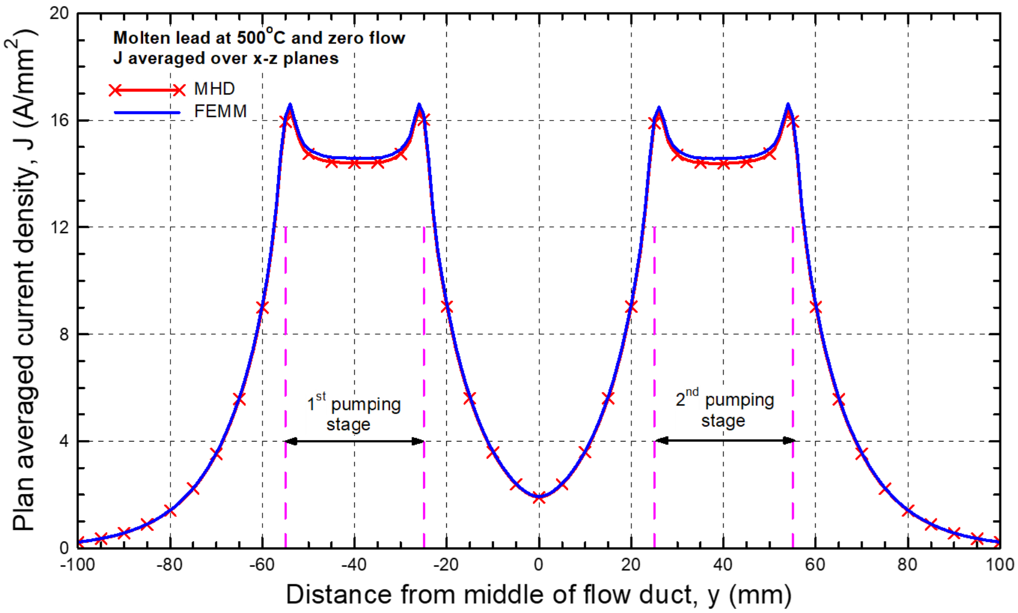

Figure 5-9: Comparison of the calculated electrical current density distributions in the flow duct of the present DC-EMP using MHD and FEMM analyses at zero flow of molten lead at 500^{o}C.

The electrical current density peaks in the pump duct near the current electrodes and gradually decreases upstream and downstream. Similar results are presented in Fig. 5-8b for a molten lead flow rate of 3.67 m^3/h and electrodes current of 3,500 A. The distributions of the electric density in Figs. 5-8a and 5-8b are symmetric in the two pumping stages with a zero value at the center (0,0,0) between the two pumping stages (Fig. 5-9). Fig. 5-9 compares the calculated distributions of the electric current density, averaged in the x-z plane in flow duct in the two pumping stages, in the present MHD analyses at zero molten lead flow to those obtained using the FEMM 2-D analysis in the x-y plane, assuming a uniform magnetic field distribution across the pump duct (z-direction). The results in Fig. 5-9 show good agreement between the two methods, validating the MHD analyses approach used in this work. The calculated average electrical current density using FEMM in each of the two pumping stages of 8.9A/mm^2 is 1.2% higher than that calculated in the present MHD analyses of 8.8A/mm^2 (Fig. 5-9).

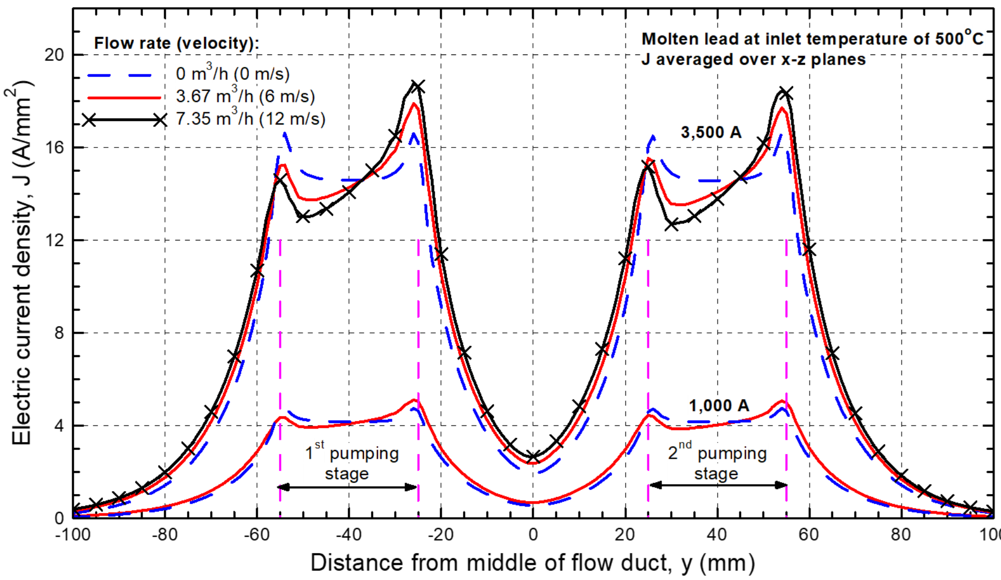

Figure 5-10: Comparison of the effects of the increasing the electrodes electric current and the flow rate of molten lead at 500°C on the calculated electric current density distributions along the flow duct of the present DC-EMP pump.

5.3.2.1. Effect of fluid flow on electrical currents distributions

The working fluid flow in the magnetic field generated by the AlNECO-5 permanent magnets produces opposing eddy electric currents in the perpendicular plane to both the magnetic field and the electrodes electric current. As a result, increasing the flow rates of the working fluid up to 3.67 m^3/h (or flow velocity of 6 m/s), causes the electric current densities at the entrance to decrease and at the exit and in the fringe regions to increase (Figs. 5-8 to 5-10). Fig. 5-10 shows the effect of increasing the flow rate of molten lead at inlet temperature of 500°C and electrodes electric currents of 1,000A and 3,500A, on the calculated average electric current densities over the X-Z plane of the pump duct, with distance along the pump duct. For an electrode current of 3,500A, increasing the molten lead flow rate from 0 to 3.67 m^3/h (6 m/s) decreases the peak electric current density at the entrance of the first pumping stage from 16.5 to 15.2 A/mm^2 and at the entrance of the second pumping stage from the 16.5 to 15.5 A/mm^2. Conversely, the electric current peaks at the exit of the first and second pumping stages increase from 16.5 to 17.9 A/mm^2 and from 16.5 to 17.6 A/mm^2, respectively (Fig. 12).

Further increase of the molten lead flow rate increases the changes in the peak current densities at the entrance and the exit of the two pumping stages of the present DC-EMP designs. The asymmetries of the electric current distributions in the two pumping stages caused by those of the magnetic flux density distributions, which results different magnitudes of the induced eddy electric currents. Results in Fig. 5-10 also show that the electric current densities in fringe regions upstream and downstream of the two pumping stages also increase with increased flow rate of molten in the pump duct. Similar distributions of the electric current density are obtained at different electrode electric currents of 1,000 A and 3,500 A, however, the values for the former are much lower. (Fig. 5-10). The next subsection presents and discusses the calculated performance characteristics of the present DC-EMP design using 3-D MHD analyses for flows of molten lead and liquid sodium at inlet temperature into the pump duct of 500^{o}C.

5.3.3. Pump Performance

This subsection presents and discusses the results of the performance analyses of the present miniature DC-EMP design for molten lead and liquid sodium at inlet temperature of 500^{o}C. These include the spatial distributions in the flow duct of the generated Lorentz force, the flow velocity, the joule heating, the fluid temperature, and the pump characteristics of the pumping pressure versus the flow rate in the pump duct.

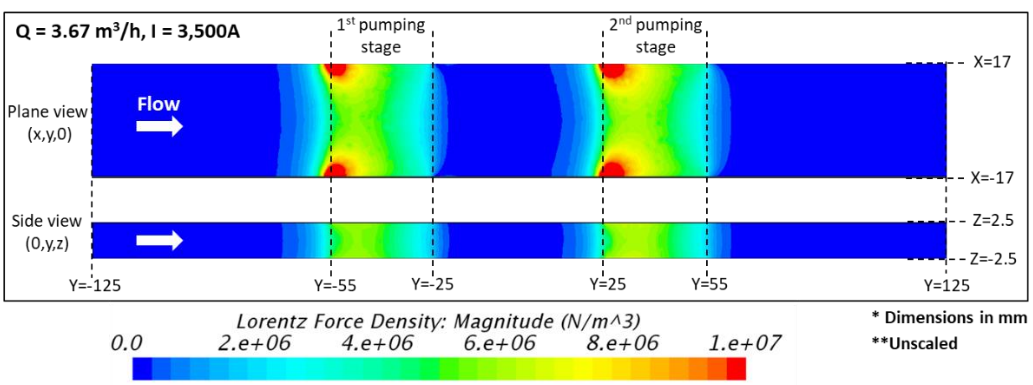

Figure 5-11: Calculated distributions of produced Lorentz force at planes (x,y,0) and (0,y,z) in the flow duct of the present DC-EMP, for electrodes electric current of 3,500A and molten lead flow at 3.67 m^3/h ang inlet temperature of 500^{o}C.

5.3.3.1. Lorentz force distribution

The generated Lorentz from the interaction between the electrical currents and magnetic fields drives the flow of the working fluid in the pump duct (Eq. 5-8) in the perpendicular direction to the electrical currents and magnetic field vectors. As show earlier in Figs. 5-4 and 5-8, the distributions of the magnetic field and the electric current densities in the pump duct are nonuniform and asymmetric, depending on the values of the supplied electrodes electric current and the flow rate of the working fluid. Sequentially, the distribution of the produce Lorentz force in the two pumping stages of the pump duct is nonuniform and asymmetric (Fig 5-11).

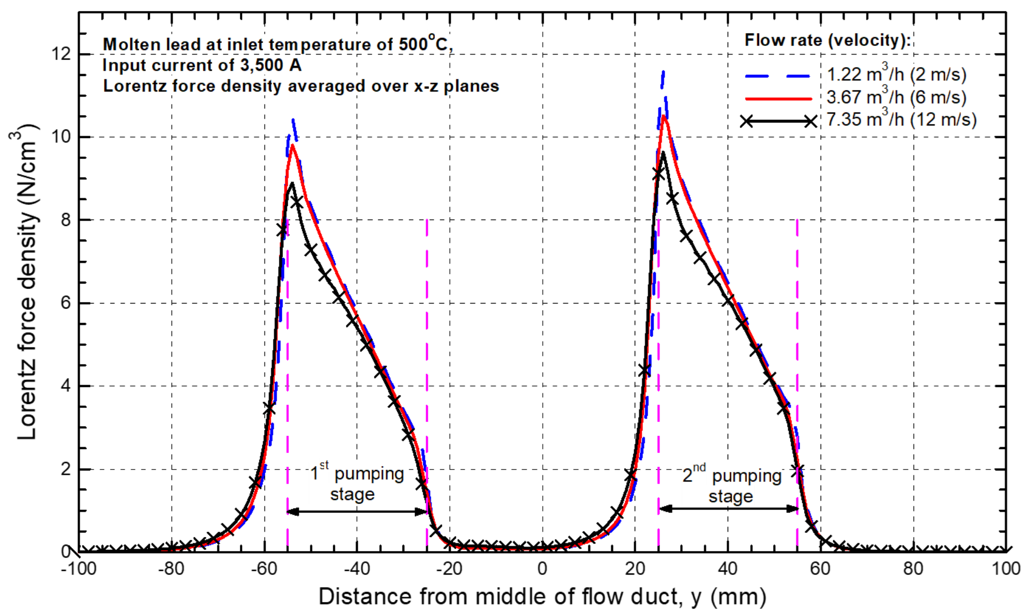

Figure 5-12: Comparison of the calculated distributions of planner averaged Lorentz force density in the flow duct in the two pumping stages of the present DC-EMP at different flow rates of molten lead and electrodes electric current of 3,500 A.

The Lorentz force density peaks at ~10^7 N/m^3 at two locations at the entrance of the two pumping stages, close to the current electrodes (Fig. 5-11). These are because the electric current density peaks near the edges of the current electrodes (Fig. 5-8) and the magnetic flux density peaks at the entrance of the pumping stages (Fig. 5-4b). The Lorentz force density decreases gradually towards the centerline of the flow duct and exit of the two pumping stages. The generated fringe Lorentz forces upstream of the two pumping stages are higher than those generated downstream (Fig. 13), due to the higher magnetic flux densities in the upstream regions (Fig. 6 and Fig. 9). The Lorentz force distribution across the duct height has a parabolic shape that peaks at the center of the flow duct and decease slightly with distance closer to the duct walls (Fig. 13).

The results presented in Fig. 5-12 are of the calculated distributions of the planner averaged Lorentz force along the flow direction in the pump duct in the two pumping stages of the present DC-EMP at different flow rates of molten lead and electrodes electric current of 3,500 A. The planner average Lorentz force peaks in the flow duct at the entrance of the two pumping stages and decreases sharply with distance to exit of the pumping stages. The asymmetric and nonuniform distributions of the Lorentz force in the first and second pumping stages are similar, but the values in the second stage are higher (Fig. 5-12). Since the effect of flow rate on the magnetic flux distribution in the pump duct is negligible (Fig. 5-7), the changes in the generated Lorentz force with increased flow rate is proportional to those of the electric current density in the flow duct (Fig. 5-8).

Increasing the flow rate decreases the generated Lorentz force in the pumping stages and increases it in the upstream and downstream fringe regions (Fig. 5-12). However, the total generated Lorentz force in the pump duct decreases with the increased flow rate. For an electrode input current of 3,500, increase flow rate of molten lead at inlet temperature of 500^{o}C, from 1.22 to 7.35 m^3/h (average flow velocity 2 to 12 m/s) decreases the generated Lorenz force in the first pumping stage from 35.25 N to 30.9 N and in the second pumping stage from 32.17 N to 28.13 N. The corresponding fringe Lorenz forces generated upstream and downstream of first and second pumping stages increase from 3.94 N to 3.97 N and from 3.22 to 3.25 N, respectively. The Lorentz forces generated in the fringe regions amount to 9.6% and 10.9% of the total, with increased molten lead flow rate from 1.22 m^3/h to 7.35 m^3/h (average flow velocity of 2 to 12 m/s), respectively.

5.3.3.2. Flow velocity profile

The present MHD analyses of the flow of working fluid in the pump duct are for uniform inlet velocity and zero pressure at the entrance and exit to the extension length (Fig 5) and non-slip boundary condition at the walls. The developed velocity profile of the working fluid flow in the two pumping stages changes under the influence of the nonuniform and asymmetric distribution of the driving Lorentz force (Fig. 5-11 and Fig. 5-12). As a result, the distribution of flow velocity in the pump duct is nonuniform and asymmetric, like that of the Lorentz force.

Fig. 5-13 shows the calculated velocity profile of molten lead in the flow duct of the dual-stage DC-EMP at Reynolds number of $3x10^5$ or flow rate of 3.67 m^3/h (average inlet velocity of 6 m/s). The profile of the flow velocity in the entrance length of the flow duct does not change until it approaches the first pumping stage where Lorentz forces are present. Since Lorentz forces have higher densities near duct walls (Fig. 5-11), the flow velocity is highest near the duct walls and decreases gradually with distance from the duct walls (Fig. 5-13). Owing to the non-slip condition at the wall, the corresponding flow velocity is zero.

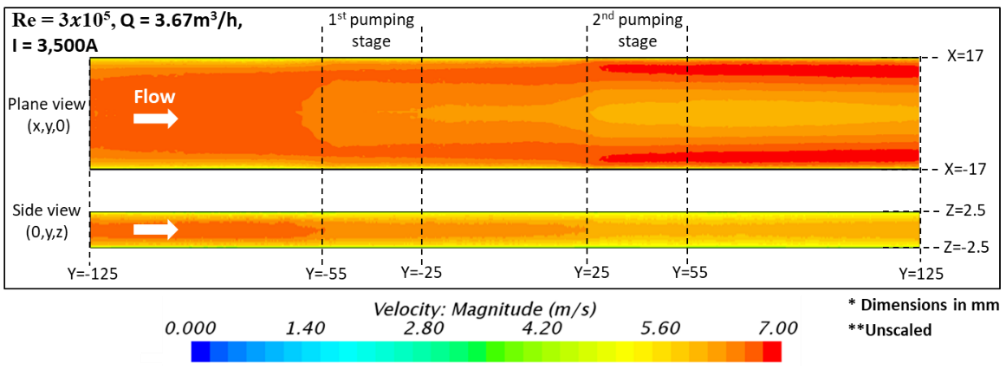

Figure 5-13: Calculated velocity profile at planes (x, y,0) and (0, y, z) in the flow duct of the present DC-EMP of molten lead flowing at 3.67 m^3/h (6 m/s average inlet velocity) for electrodes electric current of 3,500A.

Fig. 5-14 presents the calculated distributions of the molten lead flow velocity at a Reynolds number of $3x10^5$, across the width and height of the pump duct, at different axial locations. At the extension of the flow duct inlet (y = -125mm), there are no Lorentz forces and the developed velocity profile across the duct width is uniform at 6.5m/s, decreasing to at the duct walls (Fig. 5-14a). Upon entering the first pumping stage, the flow velocities increase near duct walls and decrease in the bulk region, owing to nonuniform and asymmetric distribution of the Lorentz forces (Fig. 5-13). The produced M-shape velocity profile in the two pumping stages has two equal peaks near the duct wall. Downstream of the second pumping stage, the two peak velocities increase to 6.87 m/s, and the velocity at the center of the duct drops to 6.0 m/s. In absence of Lorentz force in the exit length of the flow duct, the velocity profile slowly changes back to a developed parabolic profile with the velocity in the bulk region is highest (Fig. 5-14a). Since the generated Lorentz forces in the two pumping stages have parabolic distributions across the flow duct height, the velocity profile has a similar profile (Fig. 5-14b).

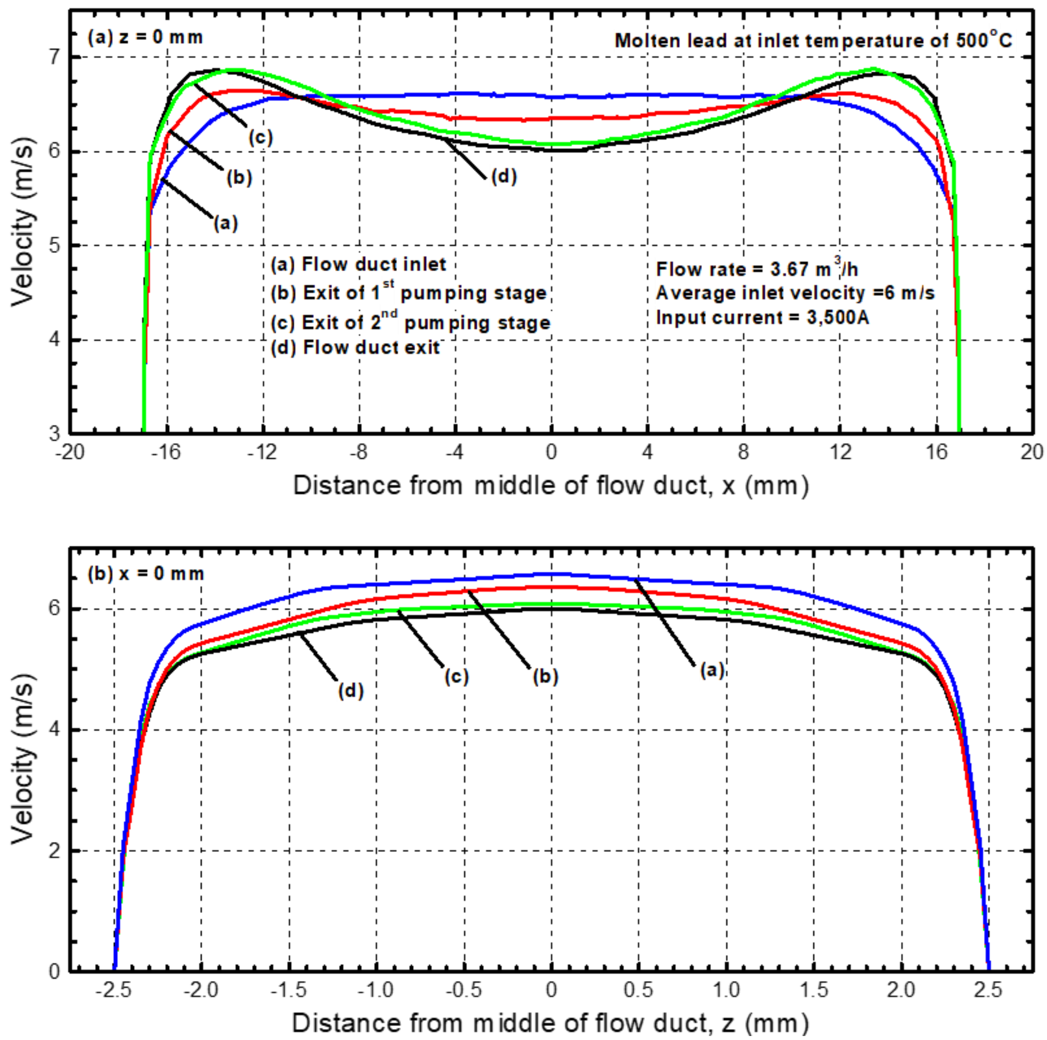

Figure 5-14: Calculated distributions of flow velocity profiles for molten lead at inlet temperature of 500^{o}C, at different locations in flow duct of dual-stage DC-EMP with input electrodes current of 3,500 A.

5.3.3.3. Joule heating and temperature distribution

The electric current passing through the working fluid in the pump duct generates thermal energy by Joule or ohmic heating. The specific ohmic heating rate equals the square of the electric current density multiplied by the electrical resistivity of the working fluid (Eq. 5-11). Fig. 5-15 shows the distribution of the specific ohmic heating rate in the flowing molten lead at 6 m/s in the pump duct, calculated in the present MHD analyses of the DC-EMP (Fig. 5-1). This distribution is like that of the current density (Fig. 5-8b), with peaks of about 500 MW/m^3 near the edges of the electrodes and gradual decreases towards the center of the pump duct and distance upstream and downstream of the two pumping stages.

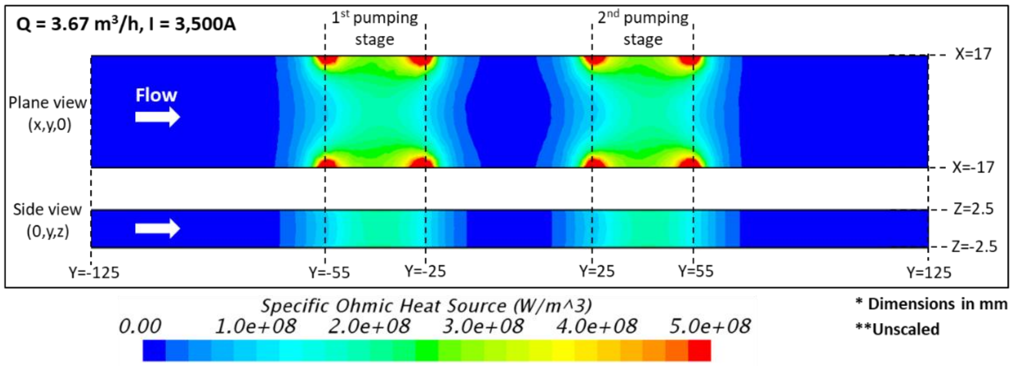

Figure 5-15: Calculated distribution of the specific ohmic heating rate in the flowing molten lead at 3.67 m^3/h (6 m/s) in the pump duct at planes (x,y,0) and (0,y,z)and electrodes electric current of 3,500A.

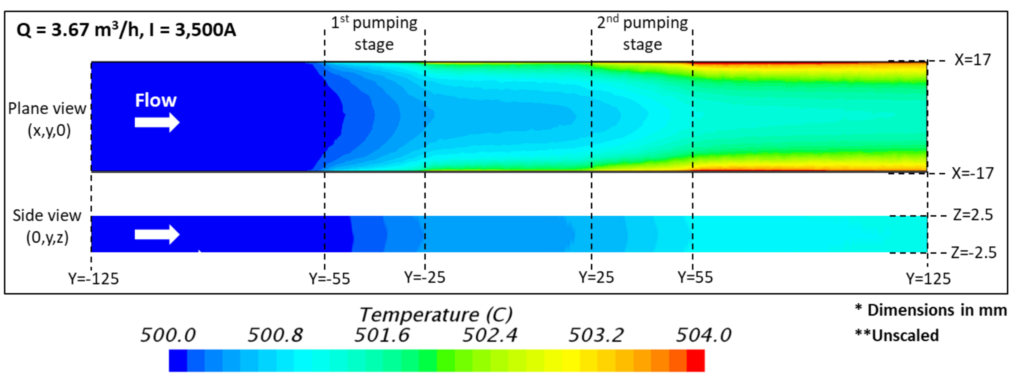

Figure 5-16: Calculated temperature distributions in the flow molten lead flowing at 3.67 m^3/h at planes (x,y,0) and (0,y,z) of the pump duct for electrodes current of 3,500A.

The increase in temperature of the flowing working fluid in the pump duct is proportional to that of the rate of ohmic heating. Fig. 5-16 shows present the temperature distribution of the flowing molten lead in the pump duct. There is no increase in the temperature of the flowing molten lead in the inlet section of the pump duct that extends to the entrance of the first pumping stage. In this and the second pumping stage the ohmic heating rate near the current electrodes increases the temperature of the molten lead near the walls of the pump duct at a higher rate than in the bulk flow. The ohmic heating ceases in the extension of the pump duct beyond the second pumping stage.

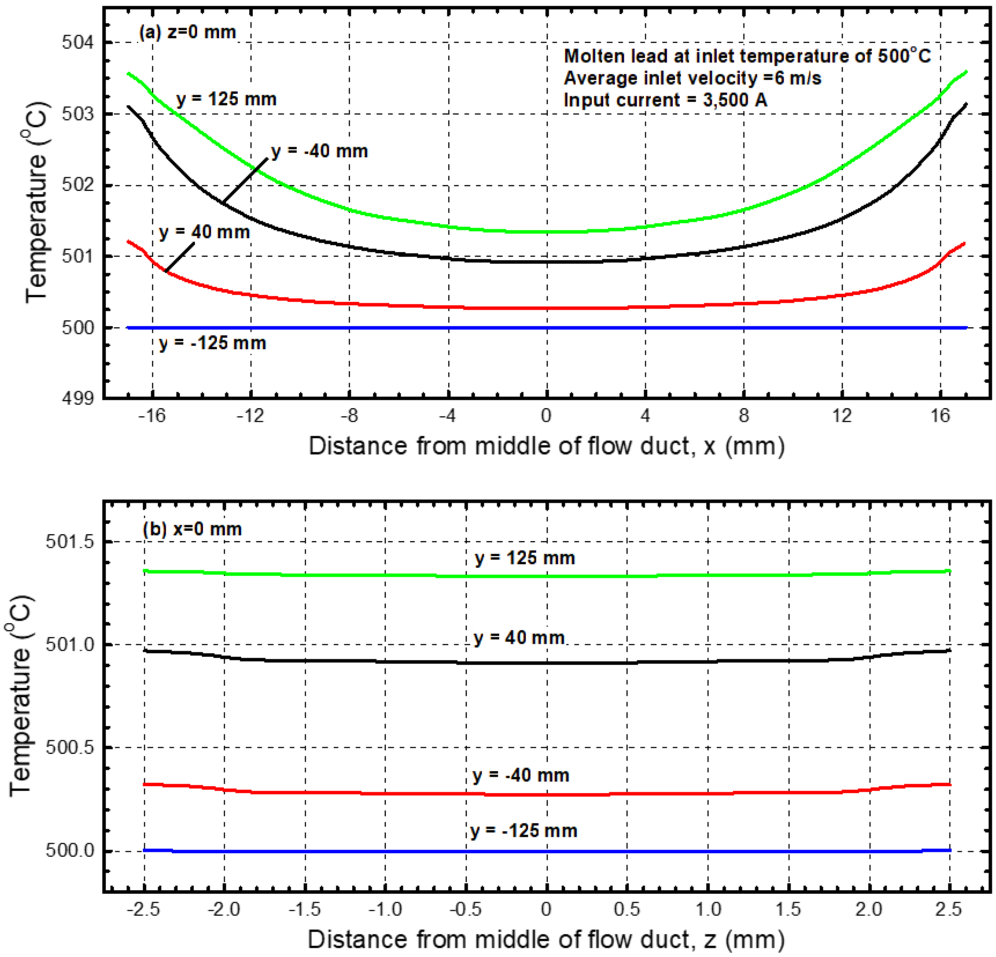

Figure 5-17: Calculated temperature distributions caused by the ohmic heat rate in the flowing molten lead in the duct of the dual-stage DC-EMP at an electrodes current of 3,500 A: (a) across the duct width in x-direction, and (b) across duct height in z-direction.

Fig. 5-17 presents the calculated temperature distributions in the performed MHD analyses at different locations in the duct of the dual-stage DC-EMP due to ohmic heating in the flowing molten lead at electrodes current of 3,500 A. The working fluid enters the pump duct at a uniform temperature of 500^{o}C and its temperature increases due to ohmic heating in the first and second pumping stages (Fig. 5-17). The temperature near duct walls is highest, the temperature across the width of pump duct width (Fig. 5-17a) has a shallow U-shape profile. At the flow duct exit, the temperature of the working fluid increases slightly to 503.6^{o}C near the duct walls in contact with the current electrodes and to 501.3^{o}C in the bulk flow (Fig. 5-17a). The changes in the flowing fluid temperature with height in the pump duct are negligibly small (Fig. 5-17b), since the corresponding electric current density and the ohmic heating rate do not vary much (Fig. 5-16). The increase of the molten lead temperature from 500 to 506.4°C negligibly decreases the physical and electrical properties of the flowing molten (electrical resistivity, density, and dynamic viscosity) by less than 0.1% (Sobolev, 2011).

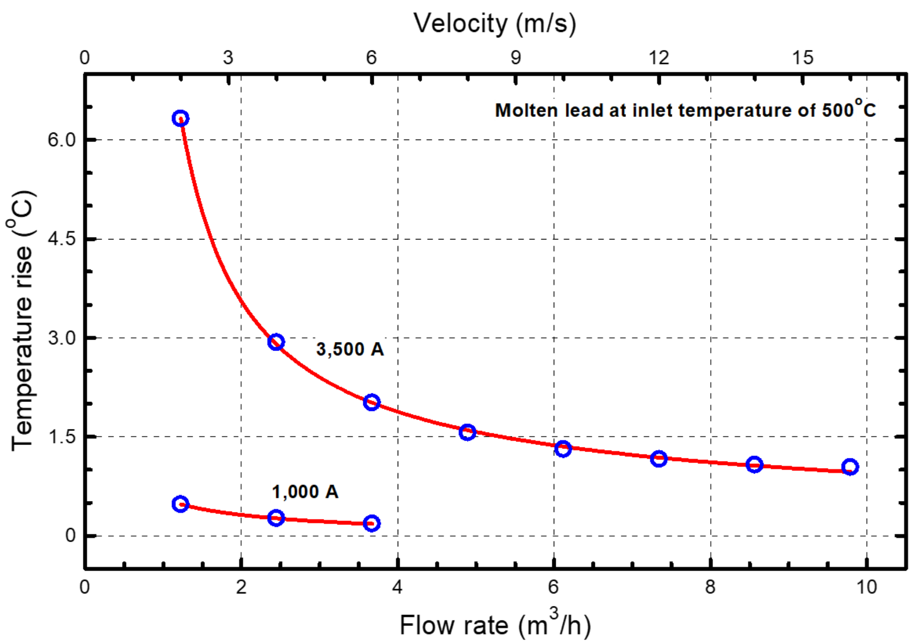

Figure 5-18: Calculated temperature rise due to ohmic heating in flowing molten lead at different rates across the pump duct and for electrodes electric currents of 1,000A and 3,500A.

Fig. 5-18 shows compares the calculated rises of the molten lead temperature due to ohmic heating with increase flow rate in the duct of the dual-stage DC-EMP. The temperatures in Fig. 5-17 are calculated in the MHD numerical analyses at electrodes electric currents of 1,000A and 3,500 A, as the difference between the average temperatures at the inlet and exit of the pump duct. The rise in the temperature across the flow duct due to ohmic heating decreases with increased flow rate of molten lead or decreased electrodes electric current. The largest temperature rises 6.4°C is for electrodes current of 3,500A and low flow rate of 1.22 m^3/h (or average velocity of 2 m/s). Owing to the small effect of ohmic heating on the temperature of the flowing molten lead in the pump duct, the energy balance equation is decoupled from the electromagnetism and fluid flow equations by assuming constant physical electrical properties at the inlet temperature of

500°C. This decreased the computational time for convergence by ~25%, without affecting the calculated values of the performance parameters of the pump.

5.3.3.4. Pump characteristics

This subsection presents the characteristics curve of the present dual-stage DC-EMP using 3-D MHD analyses for molten lead and liquid sodium at entering the pump duct at 500°C. The pump characteristics plot the pumping pressure versus the flow rate (Fig. 5-19a). These characteristics are compared to those calculated using the lumped ECM in Fig. 5-19b to assess the effect of the different assumptions in the ECM on the results. Fig. 5-19a shows the pump characteristics for the dual-stage DC-EMP calculated using ECM for molten lead, entering the pump duct at 500°C, is up to 12% higher than the calculated characteristics using the 3-D MHD numerical analyses (Fig. 5-19b).

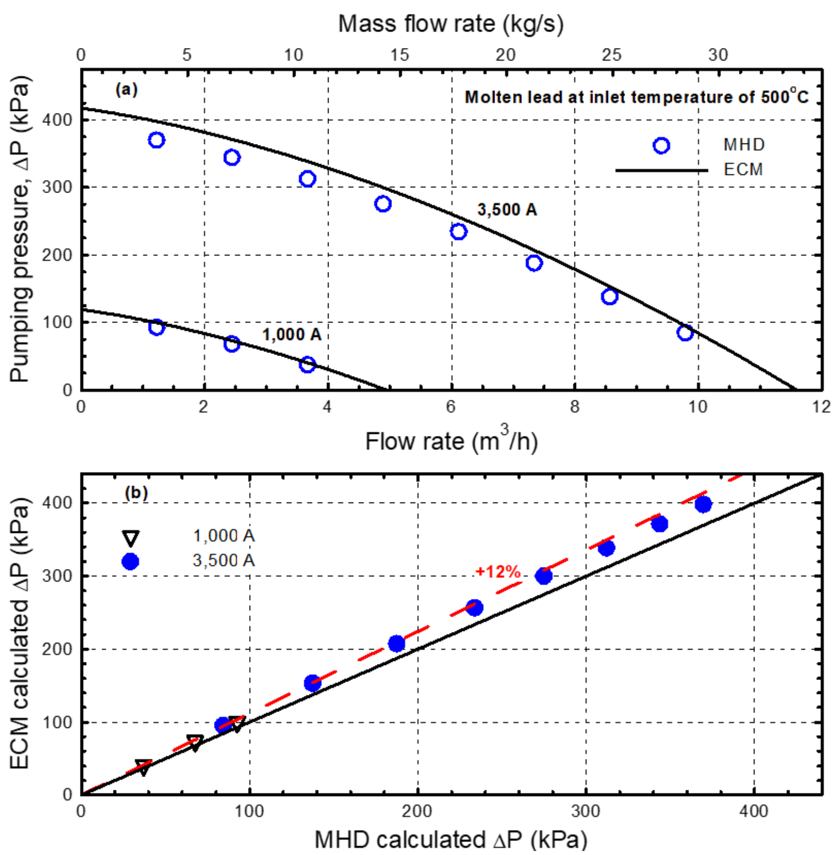

Figure 5-19: Comparison of the calculated characteristics of the present dual-stages DC-EMP, at two values of the electrodes electric current, in the present 3-D MHD analyses and by the lumped ECM for molten lead entering the pump duct at 500°C.

For electric current of 3,500 A, the ECM predicts a static pressure at zero flow of 417 kPa and the highest flow rate of molten lead = 11.6 m^3/h. These performance parameters decrease to 119 kPa and 4.95 m^3/h, respectively, when the electrodes current decreases to 1,000A (Fig. 5-19a). The higher pump characteristics calculated using the ECM is attributed to the simplifying assumptions detailed earlier, specifically those of uniform distributions of the electric current and magnetic flux densities in the pump duct and neglecting the effects of the electrodes current and flow rate on the pumping pressure. The present results of the 3-D MHD numerical analyses have shown that the distributions of the electric current and the magnetic flux densities, and hence that of the generated Lorentz force in the pump duct, are highly nonuniform (Figs. 5-6, 5-9, 5-12).

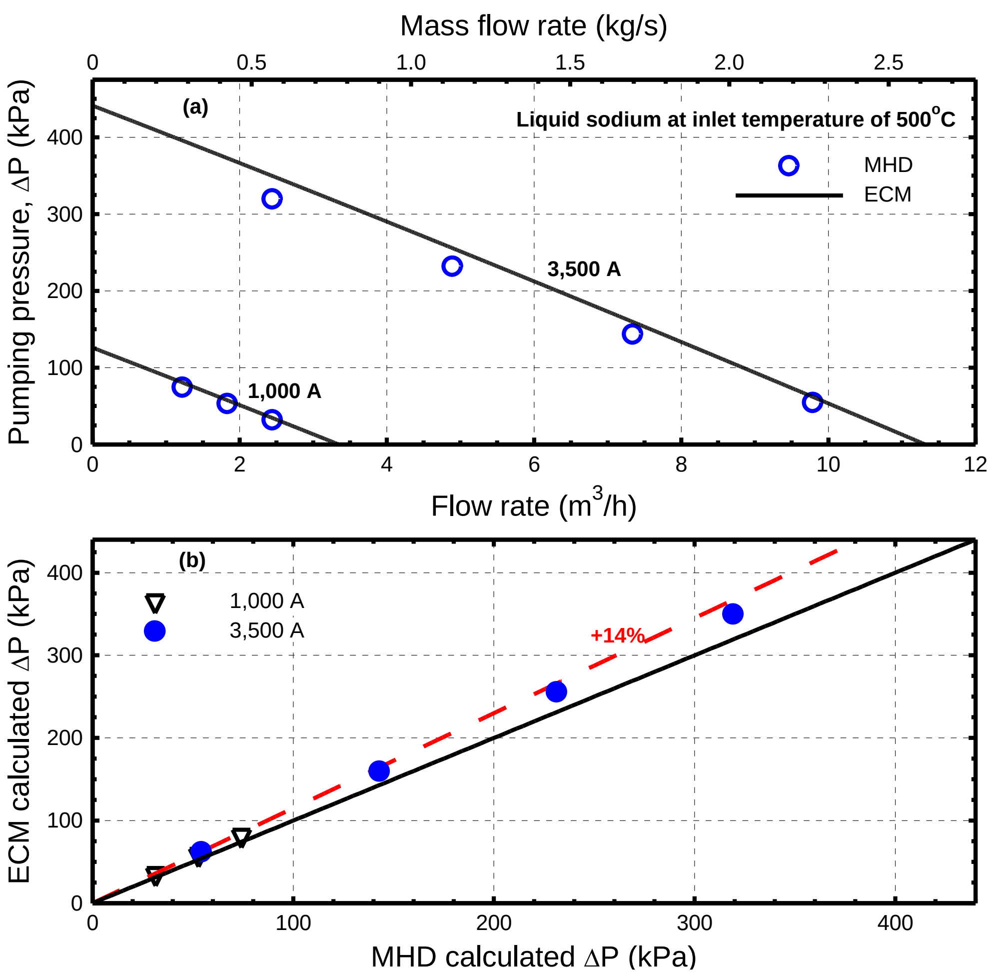

Figure 5-20: Comparison of the calculated characteristics of the present dual-stages DC-EMP, at two values of the electrodes electric current, in the present 3-D MHD analyses and by the lumped ECM for liquid sodium entering the pump duct at 500°C.

These results are consistent with earlier studies showing the ECM overpredicts the DC-EMP characteristics for mercury and alkali liquid metals by more than 12% (Watt et al, 1957; Johnson, 1973; Nashine et al, 2006; Zhang, 2020; Altamimi and El-Genk, 2023a). This is confirmed further for the present dual-stage DC-EMP for liquid sodium entering the pump duct at 500°C (Fig. 5-20). Fig. 5-20b shows that compared to the results of the present 3-D MHD analyses, the ECM overpredicts the pump characteristics by up to 14%, depending on the flow. The results in Figs. 5-19 and 5-20 show that increasing the electrodes electric current from 1,000A to 3,500A increases the pumping pressure and raises the pump characteristics. For an electrode current of 3,500A, the calculated static pressure at zero flow is 441 kPa and the liquid sodium highest flow rate is 11.3 m^3/h. These values decrease to 126 kPa and 3.35 m^3/h, respectively, when the electrodes current decreases to 1,000A (Fig. 5-20a).

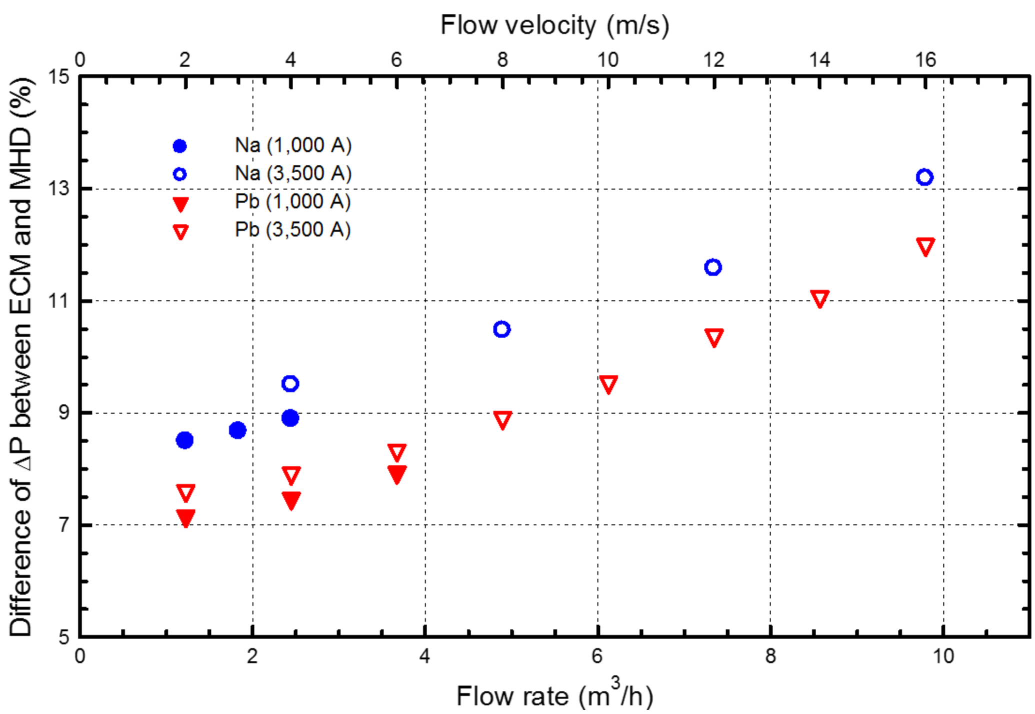

Figure 5-21: Differences in the calculated values of the pumping pressure using ECM and the 3-D MHD analyses for molten lead and liquid sodium at different electrodes currents.

The results in Fig. 4-21 show that, at the same flow rate, the pumping pressures of the present dual-stages DC-EMP for liquid sodium and molten lead, at the same inlet temperature to the pump duct of 500°C, calculated using the ECM are consistently higher than those from the performed MHD analyses. The difference increases with the increased flow rate and the electrodes electric current. For example, an electrodes electric current of 3,500A, increasing the molten lead flow rate in the pump duct from 2.2 to 9.8 m^3/h (average flow velocity of 2 to 12 m/s) increase the difference between the predictions of the ECM and the 3-D MHD analyses of the pumping pressure ~60%, from 7.6% to 12%.

5.4. Summary and Conclusions

In performed the 3-D MHD numerical analyses, although demand large computation time for results conversion, provide insight into the distributions of the electric current, the magnetic flux densities, and the fluid flow, and calculated the characteristics of the present dual-stage DC-EMP. The analytical lumped approach in the ECM, with simplifying assumptions, speed up the calculations but overpredict the pumping pressure. The results showed good general agreement in the shape the calculated pump characteristics using the ECM and the 3-D the MHD numerical analyses, although the pumping pressures of the former are up to 12% and 14% higher for circulating molten lead and liquid sodium, respectively. The difference between the calculated pumping pressures increases with increased of flow rate and electrodes electric current.

The performed 3-D MHD numerical analyses used the capabilities of the finite element capabilities in STAR-CCM+ software to discretize and solve the coupled electromagnetism, fluid flow, and energy balance equations. Mesh refinement analyses using four different arrangements with increased total number of mesh elements (coarse, intermediate, fine, and finer) confirmed that the fine mesh gride is an appropriate choice for considerations of results conversion and shorter computation time. This determination is based on the calculated GCI for the fine mesh grid of 1.5% GCI.

The numerical analyses were first conducted for calculating the uncoupled electrical and magnetic fields in the pump at static conditions for comparison with the FEMM calculations, which were used as input for the ECM analyses. Good agreement was found between the present numerical model and the FEMM results, with FEMM overestimating the calculated average magnetic flux density and electric current density in the pumping stages by 2.4% and 1.2%, respectively.

Results show that owing to the small effect of joule or ohmic heating on the fluid temperature in the pump duct decoupling the energy balance equation speeds up the 3-D MHD calculation with negligible effect of the calculated performance results of the present dual-stage, miniature DC-EMP for both molten lead and liquid sodium. Results also showed that the distributions of the electric current, the magnetic flux densities and the Lorentz force in the pump duct are highly nonuniform. These distributions are strongly influenced by the working fluid flow rate and the electrodes electric current, owing to the eddies induced in the flow duct of the pump and the fringe losses upstream and downstream the two pumping stages. by the electromotive force produced by the fluid flow movement under the magnetic field's influence. Increasing the flow rate decreases the generated Lorenz forces in the two pumping stages and increases the fringe losses. The Lorentz forces generated in the fringe regions increased from 9.6% to 10.9% of the total with increased molten lead flow rate from 1.22 to 7.35 m^3/h.

The results of the performed MHD numerical analyses confirmed that lumped analytical ECM overpredicts the characteristics of the present dual-stage DC-EMP for liquid sodium and molten lead, which increase with increased flow rate and electrodes electric current to up to 12% for molten lead and 14% for liquid sodium. The result of this work confirms that the fast-running ECM are preferable for the initial design optimization of DC-EMP. However, the 3-D MHD analyses could later be used to accurately calculate the pump operation parameters and provide insight into the 3-D distributions of the electric current and magnetic field flux densities as well as the flow field of the working fluid in the pump duct.

The next section describes the analysis methodology used in the present work for evaluating the performance of the developed miniature, submersible ALIP for circulating heavy and alkali metals in both in-pile and out of pile test loops in support of the developments of molten lead and sodium cooled Gen-IV nuclear reactors (Fig. 1-1).

6. ANALYSES METHODOLOGY OF ALIP PERFORMANCE

The second type of electromagnetic pump investigated in this work is the miniature, submersible ALIP. For evaluating the performance of the developed pump design, an ALIP lumped ECM is used. First proposed by Baker and Tessier (1987), ECM has been widely used for analyzing the performance of ALIPs. This model represents the ALIP components using an electric circuit of equivalent values of electrical resistances and reactance. These include the electrical resistances of the winding coils, R_c, the inner wall of the annular flow duct, R_{iw},the outer wall of the annular flow duct, R_{ow}, and the flowing fluid, R_{wf}, in addition to the stator leakage reactance, X_l, and the magnetizing reactance, X_m, (Fig. 6-1). The values of these input parameters are used in the ECM for estimating the induced voltage across the flow annulus, E_A, and the developed pumping pressure, ΔP_p, in the ALIP.

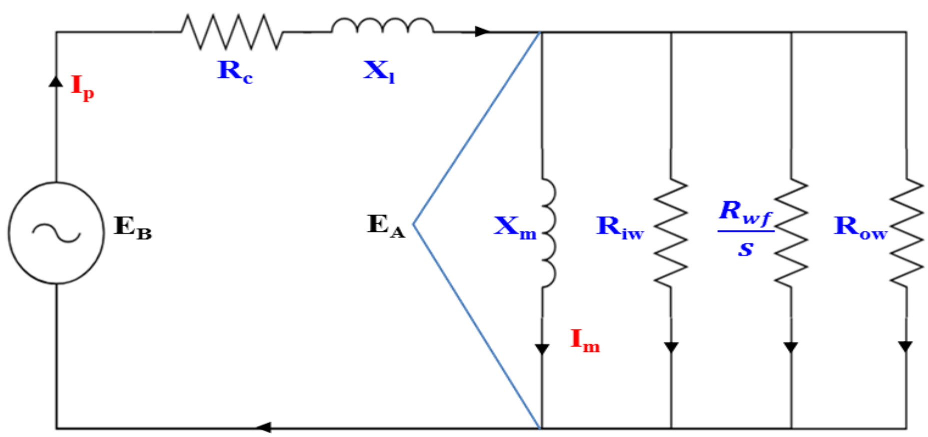

Figure 6-1: Electrical Equivalent Circuit of ALIP.

The ECM of Baker and Tessier (1987) uses equations, based on the basic theory of a tube linear induction motor (Nasar and Boldea, 1976), to obtain the electrical variables in the electromagnetic pumping pressure equation of the ALIP. These equations involve several assumptions, namely: (a) symmetric input power for the three phases; therefore, only one phase is analyzed, and results are applied to the remaining phases; (b) axisymmetric sinusoidal induced magnetic fields and electrical currents distributions in the annular flow duct; (c) continuous magnetic fields in the poles located at the two ends of the pump; (d) uniform flow velocity of fluid in the annular duct; (e) the stator slot leakage reactance is expressed using the tube linear induction motor equation, (f) neglecting the flux leakage outside the stator. The reported predictions of the ALIP characteristics using the ECM proposed by Baker and Tessier (1987) overestimate the experimental measurements for the ALIP designs of Kim and Lee (2011) by $\leq$ 22.3%, Nashine and Rao (2014) by $\leq$ 25%, Kwak and Kim (2019) by $\leq$16%, Sharma et al. (2019) by $\leq$ 13%, and Nashine et al. (2020) by $\leq$ 11%. Nonetheless, owing to the simplicity and the low computational requirements and cost, the ECM has widely been used by researchers for predicting the performance of ALIPs and conducting parametric analyses to support design development.

To improve the predictions accuracy of the ECM proposed by Baker and Tessier (1987), this work derived and used a modified equation, based on the actual geometry of stator, rather than the equation for tube linear induction motor, to determine the slot leakage reactance. The reported experimental data by Sharma et al. (2019) for a low-flow sodium ALIP confirmed the predictions accuracy of the improved ECM, with halved the difference between the model predictions and the reported experimental measurements by Sharma et al. (2019*)* from 11% to 6%. The next subsection presents the governing equations of the improved ECM, followed by that of the validation and performance analyses results of the present miniature, submersible ALIP.

6.1. Equivalent Circuit Model (ECM) for ALIP

The developed pumping pressure, ΔP_p, based on the induced Lorentz force balance along the annular flow duct as a function of mass flow rate of the working fluid is expressed, as (Baker and Tessier, 1987):

$$\Delta P_p = \left(\frac{N_\mathrm{p}-1}{N_\mathrm{p}+1}\right) 3\, \frac{(\mathrm{E}_A)^2\left(Q_{syn}-\frac{\dot{m}}{\rho}\right)}{R_{wf}\,\left(Q_{syn}\right)^2} \tag{6-1}$$

In this expression, N_p is the number of poles in the pump, Q_{syn} is the synchronous working fluid flow rate in (m^3/s), $\dot{m}$ is the working fluid mass flow rate in (kg/s), and ρ is the density of working fluid in (kg/m^3). In Eq. 6-1, the correction factor, $\left(\frac{N_\mathrm{p}-1}{N_\mathrm{p}+1}\right)$, is used to account for the ALIP end-effect caused by generated the Lorentz force in reverse directions from the interaction of the traveling magnetic field and the eddy currents at the inlet and exit regions of the annular flow duct. The induced voltage across the flow annulus, E_A, is calculated as (Fig. 6-1):

$$E_A = \frac{E_B}{\left(\frac{1}{X_m i}+\frac{1}{R_{iw}}+\frac{1}{R_{ow}}+\frac{s}{R_{wf}}\right)(R_c+X_l i)+1}, \quad (6\text{-}2)$$

where E_B is the pump terminal voltage in (V), and s is the slip ratio of working fluid relative to the traveling magnetic field. The expression for calculating the electrical variables in Eq. 6-1and Fig 6-1 are given as, (Baker and Tessier, 1987):

$$X_m = \frac{15.06\times10^{-6} f\, \tau\, (\overline{D_a})\, \left(N_{t,ph} k_p k_d\right)^2}{\delta_{nm} k_{nm} N_\mathrm{p}} \quad (6\text{-}3)$$

$$R_{iw} = \frac{3\rho_w \pi (D_{iw}+\delta_{iw})\left(N_{t,ph} k_p k_d\right)^2}{\delta_{iw}\, \tau\, N_p} \quad (6\text{-}4)$$

$$R_{ow} = \frac{3\rho_w \pi (D_{ow}+\delta_{ow})\left(N_{t,ph} k_p k_d\right)^2}{\delta_{ow}\, \tau\, N_p} \quad (6\text{-}5)$$

$$R_{wf} = \frac{3\rho_{wf} \pi (\overline{D_a})\left(N_{t,ph} k_p k_d\right)^2}{\delta_a\, \tau\, N_p} \quad (6\text{-}6)$$

$$R_c = \frac{\rho_c\, l_\mathrm{t}\, N_{t,\mathrm{c}}\, N_{\mathrm{c,ph}}}{A_c\, N_{w,p}} \quad (6\text{-}7)$$

In these expressions, f is the current frequency in (Hz), τ is the pole pitch in (m), $\overline{D_a}$ is the mean diameter of flow annulus in (m), $N_{t,ph}$ is the number of winding turns of the coil per phase, k_p is the pitch factor, k_d is the winding distribution factor, δ_{nm} is the total non-magnetic gap width in (m), k_{nm} is a multiplier factor for non-magnetic gap width, N_p is the number of the ALIP poles, ρ_w is the electrical resistivity of annular duct walls in (Ω.m), D_{iw} is the inner diameter of the annular flow duct wall in (m), δ_{iw} is the wall thickness of annular flow duct inner wall in (m), D_{ow} is the inner diameter of outer flow duct wall in (m), δ_{ow} is the thickness of annular duct outer wall in (m), ρ_{wf} is the electrical resistivity of working fluid in (Ω.m), δ_a is the width of annular flow channel in (m), ρ_c is the electrical resistivity of winding conductor in (Ω.m), l_t is the average length of the winding turn of the coil in (m), $N_{t,\mathrm{c}}$ is the number of winding turns per coil, $N_{\mathrm{c,ph}}$ is the number of coils per phase in the stator, A_c is the cross-section area of the winding conductor in (m^2), and $N_{w,p}$ is the number of winding wires connected in parallel per phase.

The slot leakage reactance, X_l, which represents the leakage of the primary magnetic flux from its main path to the stator slots, derived in section 6.2.1, given as:

$$X_l = \frac{2\pi^2 f \mu_o N_{t,c}^2 N_{c,ph}}{W_s}\left(\frac{\delta_c D_s + 2\delta_c \delta_{cl}}{3} + \frac{\delta_c^2}{6} + \delta_{cl} D_s\right) \tag{6-8}$$

In this equation, μ_o is the magnetic permeability of free space (H/m), W_s is the stator slot width in (m), δ_c is the coil height in (m), D_s is the stator inner diameter in (m), and δ_{cl} is the slot clearance height in (m). The net pumping pressure, ΔP, of the ALIP equals that generated by the Lorentz force, ΔP_p, given by Eq. (6-1) minus the friction pressure losses, ΔP_{loss}, of the flowing liquid in the pump annular duct, as:

$$\Delta P = \Delta P_p - \Delta P_{loss} \tag{6-9}$$

The friction pressure losses calculated using the Darcy-Weisbach equation (Brown, 2003), expressed as:

$$\Delta P_{loss} = f\ \frac{l}{D_h}\frac{\dot{m}^2}{2\rho A^2} \tag{6-10}$$

In this equation, f is the friction factor, l is the length of annular flow duct in (m), D_h is the equivalent hydraulic diameter of the annular flow duct in (m), and A is the cross-section area of the annular flow duct in (m^2). The empirical correlations of friction factor, f, proposed by Gnielinski (2007) for liquid flow in the annular duct of the ALIP are used in the present analyses. The friction factor for laminar flow (R_e≤2,300), is calculated using the following expression (Gnielinski, 2007) as:

$$\mathrm{f} = \frac{64}{R_e\left(\frac{(1+a^2)\ln(a)+(1-a^2)}{(1-a)^2\ln(a)}\right)} \tag{6-11}$$

In this expression, R_e is the liquid flow Reynold number, and a is the ratio of the inner to outer diameters of the annular flow duct. For turbulent flow (R_e≥7,000), the friction factor, f, is calculated (Gnielinski, 2007), as:

$$\mathrm{f} = \left(1.8\ log\left(R_e\,\frac{(1+a^2)\ln(a)+(1-a^2)}{(1-a)^2\ln(a)}\right) - 1.5\right)^{-2} \tag{6-12}$$

For the transition flow region, 2,300< R_e <7,000, the pressure losses are determined from the linear interpolation of the friction factor values for the laminar and turbulent flows determined from Eqs. 6-11 and 6-12.

The ALIP pumping power, PP, the input electric power, PE, and efficiency, η, are calculated, respectively, as:

$$PP = \Delta P\ Q \tag{6-13}$$

$$PE = \sqrt{3}\ \mathrm{I}_p\ \mathrm{E}_B\ \mathrm{P}_f \tag{6-14}$$

$$\eta = 100\% * \frac{\Delta P\ Q}{\sqrt{3}\ \mathrm{I}_p\ \mathrm{E}_B\ \mathrm{P}_f} \tag{6-15}$$

In these equations, Q is the volumetric flow rate of working fluid in (m^3/s), I_p is the phase current in (A), and P_f, is the pump power factor (Kim and Lee, 2011). The dissipated thermal power during the ALIP operation, PD, to the flowing liquid in the test loop assumed equals the difference between the electrical input power and the generated pumping power, as:

$$PD = PP - PE \tag{6-16}$$

6.1.1. Derived ALIP Slot Leakage Reactance Equation

This section describes the developed equation for calculating the slot leakage reactance, included in the improved ALIP performance analysis ECM detailed earlier. This equation accounts for several effects which have been neglected or overlocked in the methodology described by Baker and Tessier (1987).

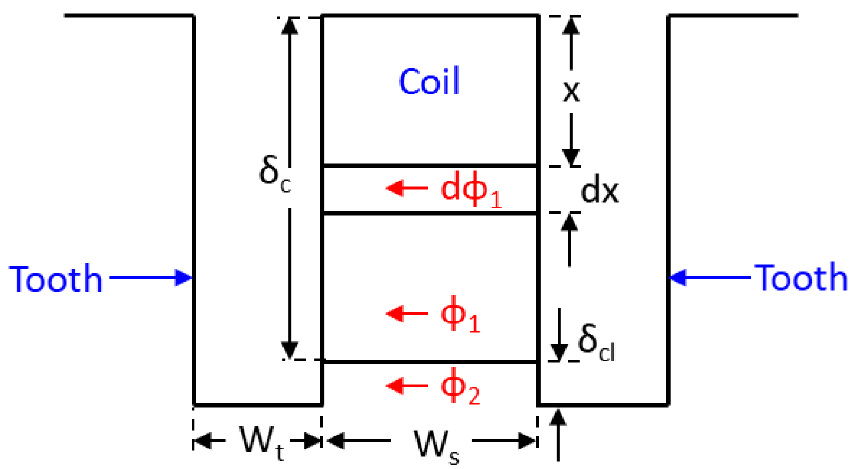

Figure 6-2: Illustration of the leakage magnetic flux in a stator slot

The total leakage magnetic flux in a stator slot consists of two components, the leakage flux passing through the coil, Φ_1, and leakage flux passing through the slot clearance, Φ_2, as shown in Fig. 6-2. Therefore, the leakage inductance consists of two components, L_1 and L_2, and the total leakage reactance is:

$$X_l = 2\,\pi\,f\ (L_1 + L_2)\ N_{c,ph} \tag{6-17}$$

The leakage inductances in the coil, L_1, is expressed as:

$$L_1 = N_{t,c}\ \frac{\phi_1}{I} \tag{6-18}$$

At any strip, dx, the magnetic field, $d\phi_1$, is given as:

$$d\phi_1 = \frac{amp{-}turns}{Reluctance} \tag{6-19}$$

The amp-turns and the reluctance at strip dx, are expressed, respectively, as:

$$amp - turns = IN_{t,c}\ \frac{x}{\delta_c}, \tag{6-20}$$

and,

$$S_{dx} = \frac{Length\ of\ flux\ flow}{\mu_0 * Area\ of\ flux\ flow} = \frac{W_s}{\mu_0\ \pi(D_s+2\delta_{cl}+2\delta_c-2x)dx} \tag{6-21}$$

Therefore, the magnetic flux, $d\phi_1$, at strip dx is calculated as:

$$\phi_1 = \frac{I\ N_{t,c}\ x\ \mu_0\ \pi(D_s+2\delta_{cl}+2\delta_c-2x)dx}{\delta_c\ W_s} \tag{6-22}$$

The leakage inductance at the strip dx, may be expressed as:

$$dL_x = N_{t,c}\ \frac{x}{\delta_c}\frac{d\phi_1}{I} = \frac{{N_{t,c}}^2\ x^2\ \mu_0\ \pi(D_s+2\delta_{cl}+2\delta_c-2x)dx}{{\delta_c}^2\ W_s} \tag{6-23}$$

To calculate L_1, dL_x is integrated along the coil height, d_c, as:

$$L_1 = \int_0^{\delta_c} dL_{l,1} = \frac{{N_{t,c}}^2\mu_0 * \pi}{W_s{\delta_c}^2}\int_0^{\delta_c} x^2.(D_s + 2\delta_{cl} + 2\delta_c - 2x)dx$$

$$= L_1 = \frac{{N_{t,c}}^2\ \mu_0\ \pi}{W_s}\left(\frac{D_8\ \delta_c+2\ \delta_{cl}\ \delta_c}{3} + \frac{{\delta_c}^2}{6}\right), \tag{6-24}$$

For the leakage flux in the slot clearance, ϕ_2, all the coil turns $N_{t,c}$ will contribute at any position, thus:

$$\phi_2 = \frac{\frac{I\ N_{t,c}}{W_s}}{\mu_0\ \pi\ D_s\ \delta_{cl}} = IN_{t,c}\frac{\mu_0\ \pi\ D_s\ \delta_{cl}}{W_s} \tag{6-25}$$

and the Leakage inductance is calculated as:

$$L_2 = N_{t,c}\ \frac{\phi_2}{I} = \frac{{N_{t,c}}^2\ \mu_0\ \pi}{W_s}D_s\ \delta_{cl} \tag{6-26}$$

Substituting Eq. (6-24) and Eq. (6-26) into Eq. (6-17) and multiplying by the number of phases, the total leakage reactance in the slot is given, as:

$$X_l = \frac{2\pi^2 f \mu_o N_{t,c}^2 N_{c,ph}}{W_s}\left(\frac{\delta_c D_s+2\delta_c\delta_{cl}}{3} + \frac{\delta_c^2}{6} + \delta_{cl}D_s\right) \tag{6-27}$$

This equation is included in the improved ECM, detailed in section IV, used to conduct parametric and performance analyses of the present miniature, submersible ALIP design for circulating heavy and alkali liquid metals and fits inside a 2.5-inch standard 5 pipe.

Table 6-1: Reported operation and geometrical parameters of low sodium flow ALIP (Sharma et al., 2019).

Operation parameter	**Value**	**Geometrical parameters**	**Value**
Working fluid	Sodium	Flow annulus width (mm)	1.95
Working fluid Temp. (^oC)	200 - 330	Pole pitch (mm)	132
Coils temperature (^oC)	< 200	Stator tooth width (mm)	10
Terminal voltage (V)	220 - 230	Stator slot width/height (mm)	12/70
Current frequency (Hz)	50	Total air gap (mm)	10.55
Total number of poles	8	Pump length (mm)	1,066
Total number of slots in stator	48	Pump outer diameter (mm)	~254
Turns per coil	58	Depth of back stator (mm)	29

6.2. Validation of ECM for prediction of ALIP performance

The solved equations of the improved ECM used the capabilities of the MATLAB platform (MATLAB, 2022). The physical and thermal properties of different pump components are assumed constant and equal to those evaluated at the inlet temperature for the flowing liquid, neglecting the effect of the increase of the flowing liquid temperature across the annular flow duct temperature of the working fluid across the annular flow duct due Joule heating. The temperature rises for the alkali and heavy liquid metals of interest are small, compared to the inlet temperature of 500^oC in the performed analyses of the present ALIP. The predictions of the improved ECM are compared to the reported experimental measurements by Sharma et al. (2019) for a low sodium flow ALIP for an out-of-pile test loop. They used forced air cooling to maintain the temperature of coils in their ALIP below 200^oC. The performed analysis of the Sharma et al. (2019) ALIP design using the improved ECM developed in this work is for the reported dimensions and design details listed in Table 6-1.

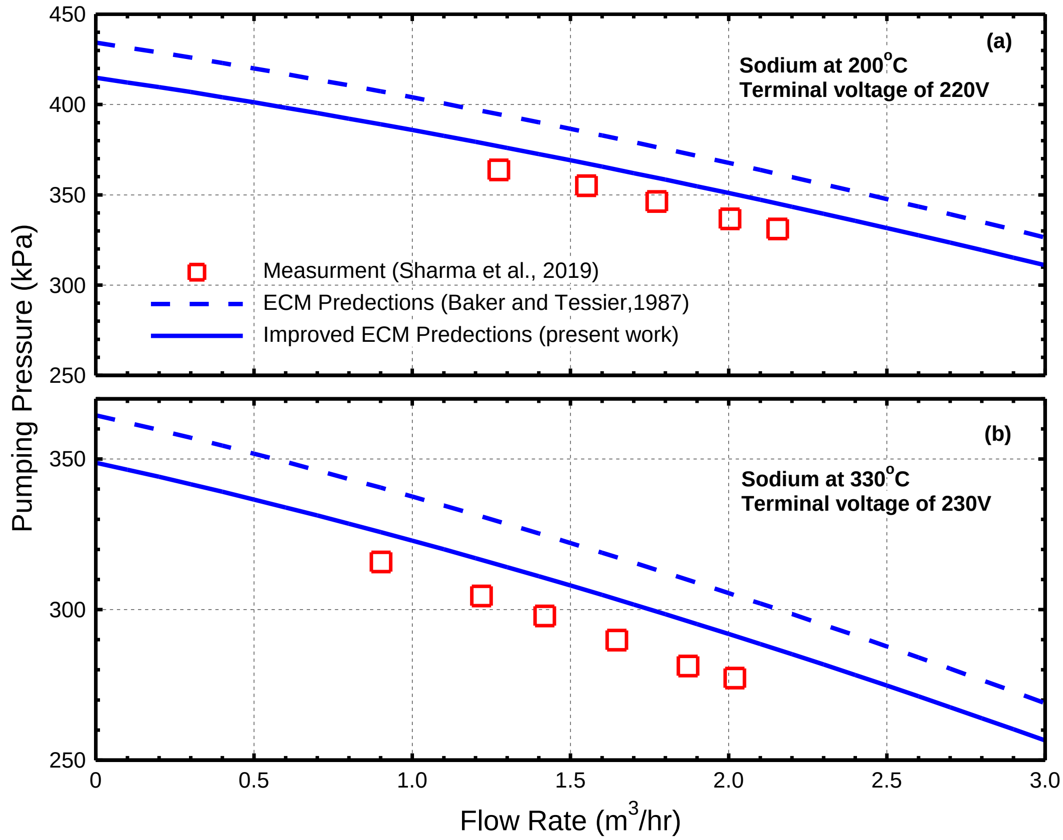

Figure 6-3: Comparison of the predictions of the present improved ECM and the ECM proposed by Baker and Tessier (1987) to the reported experimental results for low-flow sodium ALIP (Sharma et al., 2019).

Two sets of measurements are reported for the low sodium flow ALIP (Sharma et al., 2019), the first is for circulating sodium at 200°C and a terminal voltage of 220 VAC, and the second is for circulating sodium at 330°C and a terminal voltage of 230 VDC. Both the improved ECM developed in this work and that originally proposed by Baker and Tessier (1987) are used to calculate the performance characteristics of the low sodium flow ALIP (Sharma et al., 2019). The obtained results are compared to the reported experimental measurements by Sharma et al. (2019) in Fig. 6-3a and Fig. 6-3b. Both models overpredicted the pumping characteristics at different flow rates, but the predictions of the improved ECM are closer to the reported experimental measurements. For both reported sets of measurements for the low sodium flow ALIP (Sharma et al., 2019), the improved ECM overpredicts the experimentally measured performance data by 6% (Fig. 6-4), while the predictions of the ECM of Baker and Tessier (1987) overpredict the experimental data by~11%. These comparisons confirm the accuracy of the improved ECM, used in the next section to perform parametric analyses of the present miniature submersible ALIP design.

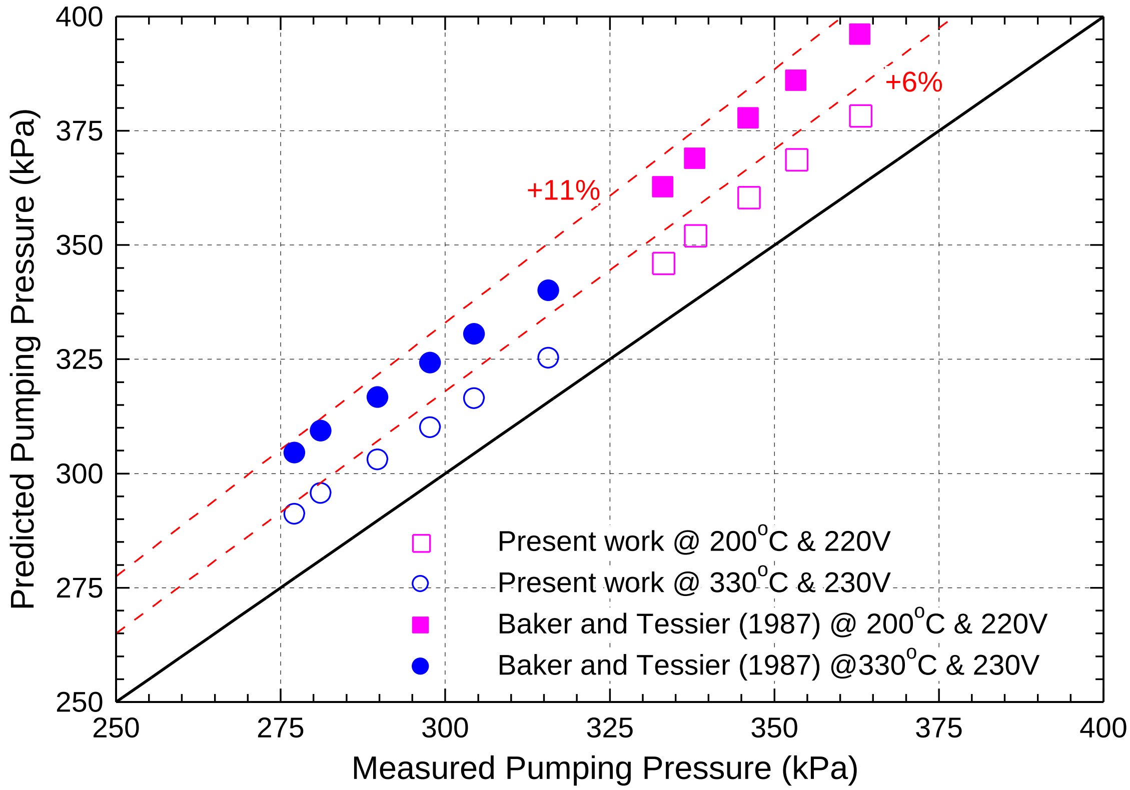

Figure 6-4: Overpredictions of ALIP characteristics using the present improved ECM and the ECM proposed by Baker and Tessier (1987) compared to reported measurements data for low sodium flow ALIP (Sharma et al., 2019).

7. DESIGN AND PERFORMANCE ANALYSES OF MINIATURE, SUBMERSIBLE ALIP

7.1. Introduction

The passive Annular Linear Induction Pumps (ALIPs) with no moving parts have been used for circulating liquid metals in test loops to support the development of advanced terrestrial nuclear reactors and in industrial applications and space nuclear reactor power systems (Baker and Tessier, 1987; Nashine and Rao, 2014; El-Genk et al., 2010; Polzin, 2010; IAEA, 2013; Mignot et al., 2019). The absence of moving parts prolongs the operation lives of these pumps and the sealed structure eliminates fluid leakage and decreases maintenance (Stieglitz and Zeininger, 2005; Kwak and Kim, 2019).

Polzin et al. (2010) have designed and tested a small ALIP for circulating liquid Nak-78 at 125 to 525^{o}C in a test loop for supporting the development of the affordable fission surface power system for potential deployment on the lunar surface. The coils of the ~22 cm diameter pump is cooled by forced convection of helium gas. The measured pump's highest efficiency was ~6% at 120 VAC, 33 Hz, and 125^{o}C. The pump delivered a static pumping pressure of 90 kPa and a runout flow rate of NaK-78 up to 20.5m^3/h. Kim and Lee (2011) have designed and tested a small ALIP for circulating liquid sodium at 150^{o}C in an experimental test loop for supporting the development of a prototype liquid metal reactor. The 30 cm diameter pump used asbestos bands for electrically insulating the ribbon-shaped coils' winding. The fabricated pump developed a pumping pressure of 125kPa at a nominal flow rate of 3.6 m^3/h when operated at a terminal voltage of 227VAC and a current frequency of 60Hz.

Nashine and Rao (2014) have designed and tested an ALIP for circulating liquid sodium at 350 ^{o}C in a steam generator test facility for supporting the development of an Indian prototype Fast Breeder Reactor (FBR). The 59.0 cm diameter pump used external air-forced convection to cool and maintain the temperature of the coils at 100-120^{o}C to avoid melting the electrical insulation and short-circuiting the pump coils. The tested pump at a terminal voltage of 360 VAC and a current frequency of 50 Hz provided a net pumping pressure of 394 kPa at a flow rate of 125 m^3/h and 18% efficiency. Kwak and Kim (2019) have designed and fabricated a medium size ALIP for circulating liquid sodium at 340 ^{o}C in an out-of-pile thermal-hydraulics test loop for supporting the development of a Korean FBR for the generation of 150 MWe. The coils of the ~46 cm diameter pump is cooled by convection of air. When operated at a terminal voltage of 391 VAC at a current frequency of 60Hz the pump delivered a net pumping pressure of 400 kPa at a sodium flow rate of 85 m^3/h and 25% efficiency.

While external cooling of ALIP is readily used in out-of-pile test loops and many industrial applications, for in-pile test loops using submersible ALIPs is desirable and a more practical choice for simplifying of the loop design and avoiding penetrations into the test reactor for circulating an external coolant such as helium. Ota et al. (2004) have designed and tested a large-capacity submersible ALIP for circulating liquid sodium at 452 ^{o}C in the core of the Japanese pool-type FBR. This ALIP used electrically insulating and thermally conductive insulation to transfer the dissipated thermal power by the pump to circulate liquid sodium in the surrounding sodium pool. The insulation comprised of layers of alumina and glass cloth and mica tape. The developed ALIP was 190 cm in diameter and 440 cm long, with a 7.7 cm wide liquid flow annulus for circulating liquid sodium at high flow rates. The pump has been tested for 2,550 hours in an experimental test facility. At a terminal voltage of 1,350 VAC and a current frequency of 20 Hz, the measured pumping pressure was 250 kPa at a nominal sodium flow rate of 9,600 m^3/h and ALIP efficiency of 40%.

Recently, Nashine et al. (2020) have developed a submersible ALIP for draining liquid sodium at temperatures up to 550 ^{o}C from the main vessel of the Indian FBR during an accident. The submersible pump used coils wire with high-temperature inorganic mineral electrical insulation of magnesium oxide, MgO. The dissipated thermal power during pump operation transfers to both the pumped and surrounding sodium. When the 40 cm diameter submersible pump was tested in a sodium pool at a terminal voltage of 150 VAC and a current frequency of 50 Hz, the net pumping pressure of 400 kPa was measured at sodium flow rate of 2.0 m^3/h.

These large-size submersible ALIPs are not suitable for use in small-diameter out-of-pile and in-pile test loops for which miniature submersible ALIPs are needed. Recently, two in-pile test cartridge loops are thought for supporting the development of molten lead and liquid sodium-cooled advanced Generation-IV reactors in the US. These test loops were to be placed in the core of the sodium-cooled Versatile Test Reactor (VTR) for investigating nuclear fuel and materials compatibility and corrosion mechanisms of these heavy and alkali liquid metals under prototypical temperatures and radiation environments (McDuffee et al., 2019; Kim et al., 2022). The US sodium-cooled, 300 MW_{th} VTR is a one-of-a-kind facility for performing large-scale, fast-spectrum neutron irradiation tests at elevated temperatures initially up to 500 ^oC with 316-stainless steel structure and higher temperatures but with FeCrAl steels for compatibility and corrosion investigation with circulating molten lead (Zhang, 2009; Fazio and Balbaud, 2017; El-Genk et al., 2020; Vogt and Proriol, 2021; Roglans-Ribas et al., 2022; Farmer et al., 2022).

The objective of this chapter is to develop a miniature, submersible Annular Linear Induction Pump (ALIP) design with an outer diameter of 66.8 mm and appropriate selections of components materials and dimensions for circulating molten Pb and liquid sodium at temperatures up to 500^{o}C in the VTR test loops to support the development of advanced, Gen-IV nuclear reactors (Table 7-1). The developed ALIP, with high-temperature ceramic insulated coil wires and Hiperco-50 center core and stators, has an outer diameter of 66.8 mm, and fits in a 316 SS, 2.5-inch standard schedule 5 pipe riser of the VTR in-pile test loop with an inner diameter of 68.8 mm and 1.0 mm radial clearance from the pipe wall. Fig. 1-1 presents a schematic of the VTR molten lead in-pile test loop showing the placement of the developed miniature submersible ALIP in the riser tube, downstream of a three fuel rodlets text article in a triangular lattice. To predict the ALIP performance, this work developed and validated an improved Equivalent Circuit Model, and its predictions are compared to those of the widely used ECM introduced by Baker and Tessier (1987) and reported experimental measurements by other investigators for low sodium flow ALIP.

The improved ECM calculated and compared the effects of varying the terminal voltage, current frequency, winding wire diameter, center core length, the width of liquid flow annulus, and working fluid properties (Table 7-1) and temperature on the pump characteristics. The analyses also determined the values of the pumping pressure and flow rate of the different working fluids for maximizing both the pump efficiency and the pumping pressure and calculated the values of the thermal power dissipated by the present

ALIP. This power is removed by the circulating working fluid in the in-pile VTR test loop and rejected to the VTR primary sodium coolant flow along the outer surface of the test cartridge loop.

Table 7-1: Comparison of molten lead, liquid sodium, and liquid Nak-78 properties (Foust, 1978; Sobolev, 2011).

Working fluid	**Melting point (^oC)**	***Thermal conductivity (W/m. k)**	***Dynamic Viscosity (μ Pa. s)**	***Density (kg/m^3)**	***Specific enthalpy (kJ/kg)**	***Specific heat capacity (kJ/m^3. k)**
Pb	327	17.7	1,814	10,452	32	0.144
Na	98	66.4	283	832	517	1.264
NaK-78	-12.6	26.3	192	748	457	0.873

*at 500^{o}C.

7.2. Design layout and material selection

The developed miniature submersible ALIP in the present work, for circulating alkali liquid metals and heavy metal, has an outer diameter of 66.8 mm to fit in the riser tube of the test loop, with 1-mm wide radial clearance (Fig. 1-1). The riser tube is 2.5-inch standard schedule 5 pipe with 68.8 mm inner diameter (Fig. 7-1). This ALIP is mounted in the riser tube downstream of the test article of either a single or multiple nuclear fuel rodlets (Fig. 1-1 and Fig. 7-1). The upper inert gas plenum in the VTR test loop (Fig. 1-1) accommodates the volume changes of the circulating liquid metals with temperature. Typically, cooling the ALIPs maintains the temperature below that recommended for the electrical insulation of the conducting winding coils. This temperature usually ranges from 120^{o}C to 150^{o}C. However, in the present miniature submersible ALIP for operating at higher temperatures up to 500^{o}C, the selected Copper/Nickel winding coils have ceramic insulation (Cables-cpg, 2020). This ceramic insulation withstands a maximum voltage of 150 VAC for continuous operation at up to 1000^{o}C without failure. These ceramic insulated coil wires can also withstand exposure to neutrons and gamma rays without altering the mechanical properties (Cables-cpg, 2020). Because the ceramic insulation, however, limits the minimum bending diameter of the winding coils' wires, a 13AWG coil wire (conductor diameter of ~ 1.83 mm) is selected for the present miniature submersible ALIP design.

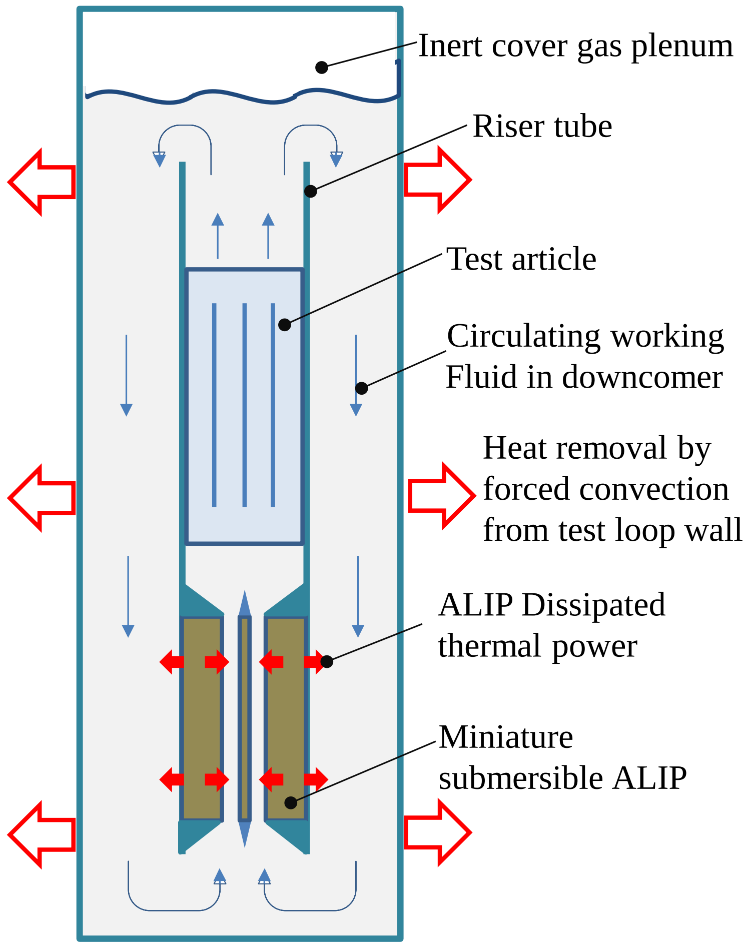

Figure 7-1: A schematic showing placement of miniature, submersible ALIP in the riser tube of an in-pile test loop for circulating molten lead and alkali liquid metals through test article of nuclear fuel rodlets.

Using a small diameter winding coils' wires increases the high electrical resistance and the joule heating rate (or thermal power dissipation) and limits electric current input per phase. To alleviate these limitations and increase the electric current per phase, at the same terminal voltage, the present ALIP design uses a 3-phase delta connection of two parallel coils per phase per pole as shown in Fig. 7-2. In this arrangement, each of the two AC source lines (A, B, and C) are linked together by two parallel wires. Coils of the same phase in the same pole (e.g., coils #1 and 2) are connected in parallel, while coils of the same phase but different poles are connected in series (e.g., coils # 1 and 7). Using two parallel wires halves the total electrical resistance and doubles the electrical current passing through the coils, improving the overall performance of the ALIP.

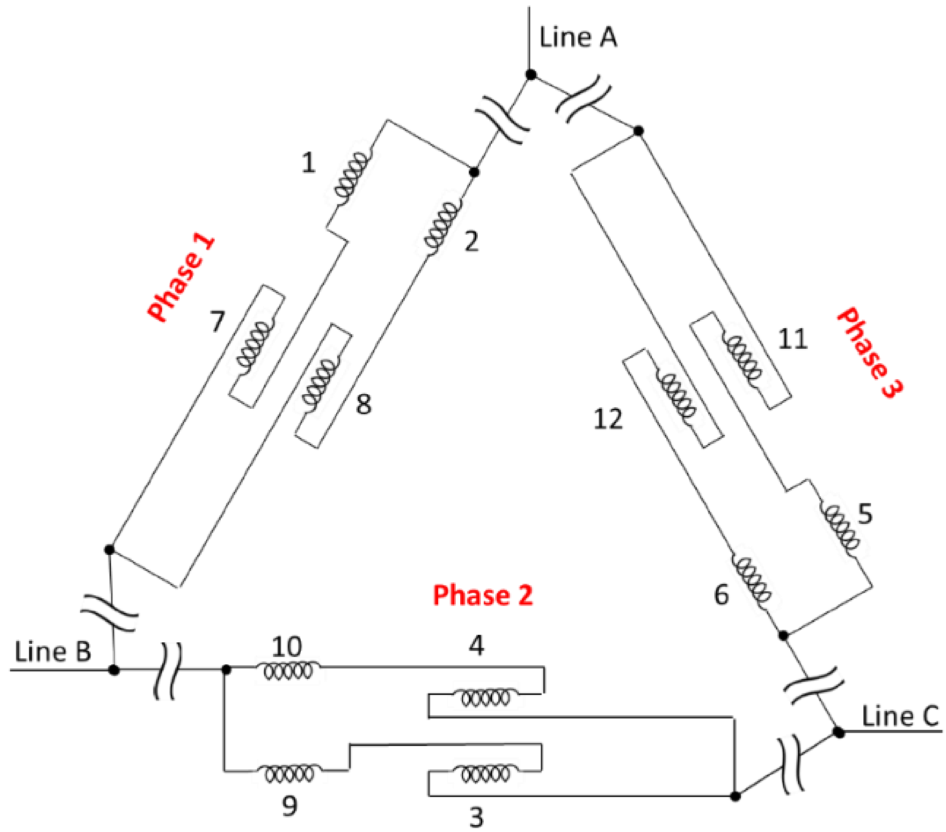

Figure 7-2: A 3-phase wiring configuration of a pole pair in the present ALIP design (Momozaki, 2016).

Other materials for the present ALIP include SS-316 for the walls of the annular flow duct and pump casing, and Hiperco-50 for the center core and outer stator (Fig. 7-3). The non-magnetic SS 316 (Ho and Chu. 1977) avoids disturbing the generated traveling magnetic field in the pump. In addition, its high electrical resistance decreases losses of the induced electrical current outside the liquid flow annulus. The SS-316 is also compatible with alkali metals and with the molten lead up to 500°C. It contains 2-3% molybdenum for enhanced corrosion resistance and improved mechanical strength at elevated temperatures and is one of the most stable stainless-steel types (Watt et al. 1957).

The Hiperco-50 has an attractive magnetic property at elevated temperatures. It has a curie point of ~940°C and one of the highest saturation magnetic field flux densities, B_{sat}, of all soft magnet material ~24.5 kG (Liu et al., 2003; De Groh at al., 2018). The high saturation magnetic flux density helps reduce the size of the stator and inner core, and hence the ALIP outer diameter (Fig. 7-1). By contrast, the widely used silicon steel increases the size of the stator size to ~120% compared to that of the Hiperco-50 for the same magnetic field flux density (Maczieswki, 2019). Furthermore, Hiperco-50 suitable for high radiation exposure has been used in ALIP designs for nuclear power applications (Kilbane and Polzin, 2014).

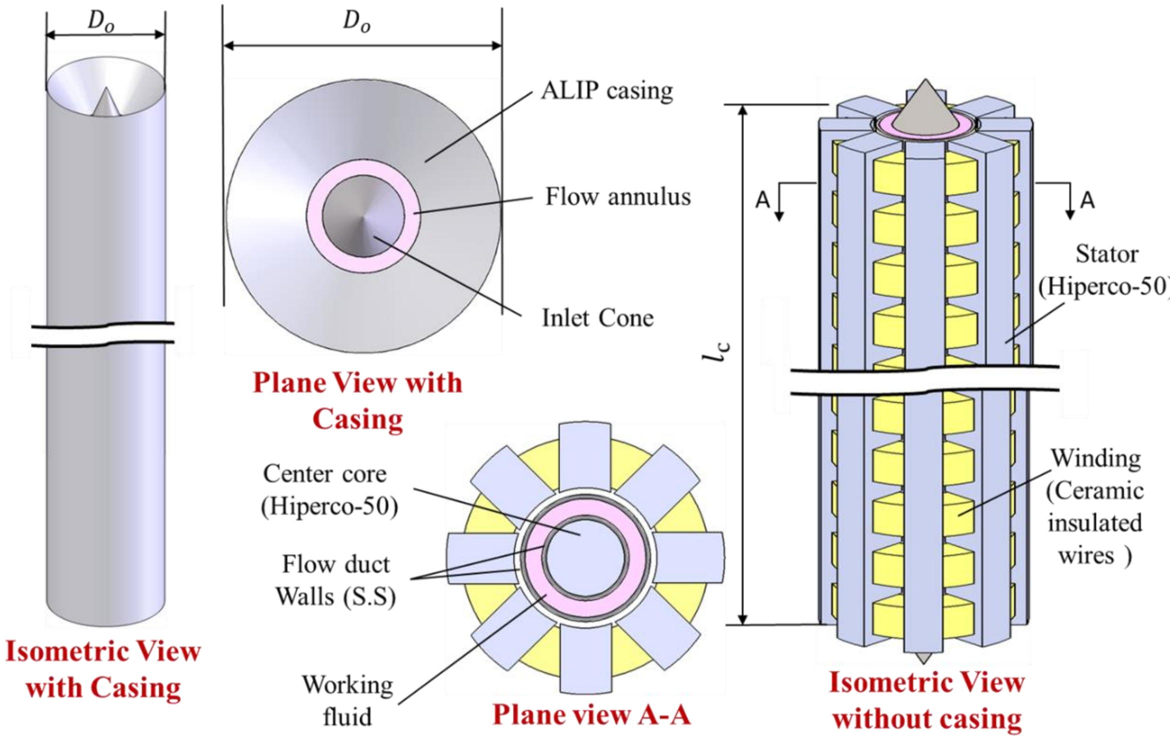

Figure 7-3: Isometric and cross-sectional views of the developed miniature ALIP design of molten lead or sodium at < 500 °C.

Table 7-2 lists the main operational and geometrical parameters of the present miniature, submersible ALIP design (Fig. 7-3). It has six poles per stator, each consists of six coils divided into three phases and operates at commercial current frequency of 60 Hz and an outer diameter center core of 16 mm. This diameter provides sufficient cross-section area for the magnetic field return path without reaching or exceeding the saturation magnetic flux density of the Hiperco-50 during ALIP operation. Similarly, the height of stator back, δ_{sb}, is sufficiently large to pass the generated magnetic field in the stator without reaching the saturation magnetic flux density of Hiperco-50. In the present ALIP, the magnetic flux density passing through the center core and the back stator is selected not to exceed 90% of the saturation flux density for Hiperco-50. The listed outer diameter and total length of the present ALIP design are suitable for out-of-pile and in-pile test loops that support the development of advanced Gen-IV nuclear reactors.

Table 7-2: Operation and geometrical parameters of present miniature ALIP.

Parameter	Value	Parameter	Value
Working fluid	Pb, Na, or Nak-78	*Pumping region length, L_p (mm)	1,000
Operating Temp. (^oC)	500	Center core extension, L_{ex} (mm)	50
*Terminal voltage (V)	150	Pole pitch, τ (mm)	167
*Current Frequency (Hz)	60	Stator slot width, W_s (mm)	17.5
Outer diameter, D_o(mm)	66.8	Stator tooth width, W_t (mm)	10
Number of poles	6	Center core diameter, D_{iw} (mm)	16
Number of coils in the stator	36	Inner duct wall thickness (mm)	1
Coils per phase per pole	2	*Annular channel width, δ_a (mm)	3.9
Number of turns per coil	40	Outer duct wall thickness (mm)	1.5
*Winding wire Dia. (AWG)	13	Coil height, δ_c (mm)	11
Pump total length, L (mm)	1,100	Stator back depth, δ_{sb} (mm)	6

* Analyzed parameters.

7.3. Results and discussions

This section presents and discusses the results of parametric analyses of the present ALIP for molten lead at 500 ^oC. In addition to the operation characteristics of pumping pressure, and pumping power and pump efficiency with increased flow rate of molten lead. Furthermore, performed analyses investigated the effects of the working fluid (Pb, Na, and NaK-78) properties and temperatures on the performance characteristic of the present ALIPs. Using Eqs. (6-9), (6-11) and (6-13), the present ALIP pumping pressure, pumping power and efficiency are calculated for different values of the terminal voltage, electrical current frequency, winding coil diameter, length of the center core, and width of the liquid flow annulus. The values of these variables for the highest pump characteristics for the different liquids are also determined. Other operational and geometrical parameters used in the analyses of the present ALIP are listed in Table 7-2.

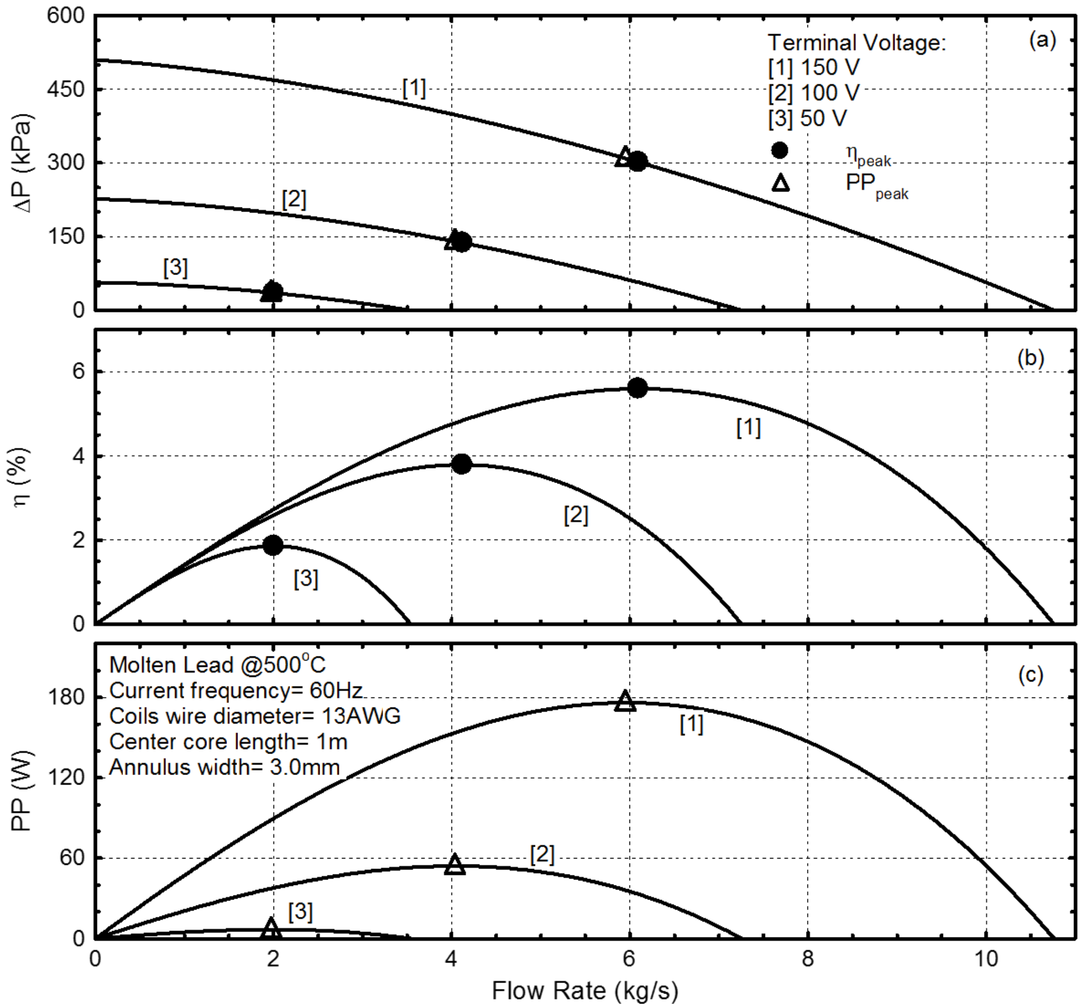

Figure 7-4: Calculated performance of miniature, submersible ALIP for circulating molten lead at 500 °C at different terminal voltages.

7.3.1. Parametric analyses

The ALIP pumping pressure is proportional to the induced voltage in the annular flow duct, E_A, hence, the pump terminal voltage, E_B (Eqs. 6-1 and 6-2). Therefore, the performance characteristics of the ALIP depend on the terminal voltage. Fig. 7-4 compares the calculated performance characteristics of the present ALIP at terminal voltages of 50, 100 and 150 VAC. Increasing the terminal voltage from 50 to 150 VAC increases the pumping pressure at zero flow and the highest flow rate of molten lead from 57 to 510 kPa, and from 3.5 to 10.75 kg/s, respectively. This is in addition to increasing the peak efficiency by 300%, from 1.86% at a pumping pressure of 35 kPa and molten lead flow rate of 2.0 kg/s, to 5.6% at a pumping pressure of 302 kPa and flow rate of 6.1 kg/s (Fig. 7-4b). Also, the peak pumping power increases from 6.8 W at a pumping pressure of 36 kPa and a molten lead flow rate of 2.0 kg/s, to 176 W at a pumping pressure of 309 kPa and a flow rate of 5.95 kg/s (Fig. 7-4c). For the present miniature, submersible ALIP, the terminal voltage is limited to a maximum of 150 VAC by the high-temperature ceramic insulated coil wires.

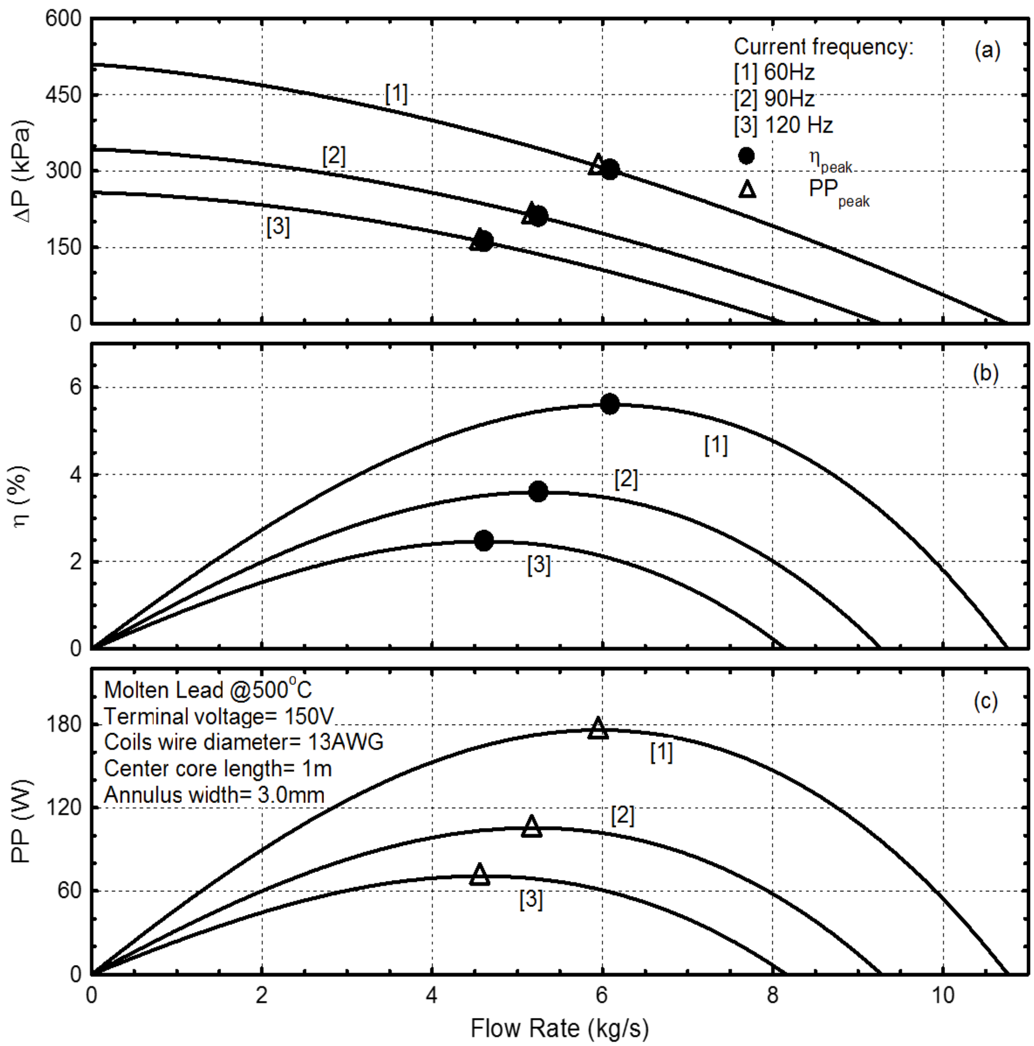

Figure 7-5: Calculated performance of miniature, submersible ALIP for circulating molten lead at 500 °C at different supplied current frequencies.

The generated magnetic field in the stator, and hence the developed pumping pressure is inversely proportional to the frequency of the supplied electrical current to the ALIP coils. Fig. 7-5 compares the calculated performance characteristics of present ALIP for circulating molten lead at electric current frequencies of 60, 90, and 120 Hz. Decreasing the current frequency from 120 to 60 Hz increases the pumping pressure at zero flow and the highest flow rate of molten lead from 257 to 510 kPa, and from 8.1 to 10.75 kg/s, respectively. The corresponding peak efficiency of the ALIP increases 227%, from 2.46% at a pumping pressure of 160 kPa and molten lead flow rate of 4.6 kg/s to 5.6% at a pumping pressure of 302 kPa and flow rate of 6.1 kg/s (Fig. 7-5b). The peak pumping power also increases 245%, from 71 W at a pumping pressure of 162 kPa and flow rate of 4.6k g/s to 176 W at a pumping pressure of 309 kPa and flow rate of 5.95 kg/s (Fig. 7-5c). Though decreasing the current frequency improves the performance of the pump, a frequency of 60 Hz is preferred for the present ALIP to avoid the limitations on the generated magnetic field in the stator back. Decreasing the current frequency below 60 Hz generates a magnetic flux density in the stator back that exceeds the saturation magnetic flux density of Hiperco-50, potentially terminating the pump operation.

The electrical resistance of the winding coils is inversely proportional to the diameter of the wire used (Eq. 6-7). Decreasing the electrical resistance of the winding coils using larger wire diameter increases the electrical currents in the coils, and hence the generated magnetic field and pumping pressure. Fig. 7-6 compares the calculated performance characteristics of present ALIP for circulating molten lead using winding coil wires of 13 and 18AWG with conductor diameters of 1.0 and 1.83 mm, respectively. For the 13 AWG wire, the number of windings turns that fit in one coil equals forty, while for the 18AWG wire it is 135. The increase in wire size from 18 to 13AWG increases the pumping pressure at zero flow and the highest flow rate from 129 to 510 kPa, and from 5.5 to 10.75kg/s, respectively. Similarly, increasing the wire size from 18 to 13AWG increases the pump peak efficiency 250%, from 2.23% at pumping pressure of 80 kPa and molten lead flow rate of 3.1 kg/s to 5.6% at a pumping pressure of 302 kPa and flow rate of 6.1 kg/s (Fig. 7-6b). The peak pumping power also increases 733%, from 24 W at a pumping pressure of 81 kPa and flow rate of 3.1 kg/s to 176 W at a pumping pressure of 309 kPa and flow rate of 5.95 kg/s (Fig. 7-6c). The minimum bending diameter of the high-temperature ceramic insulated coil wires limits the wire size to be used in the present ALIP to a maximum of 13AWG. Larger wires require bending diameters larger than the diameter of the coils in the present ALIP design.

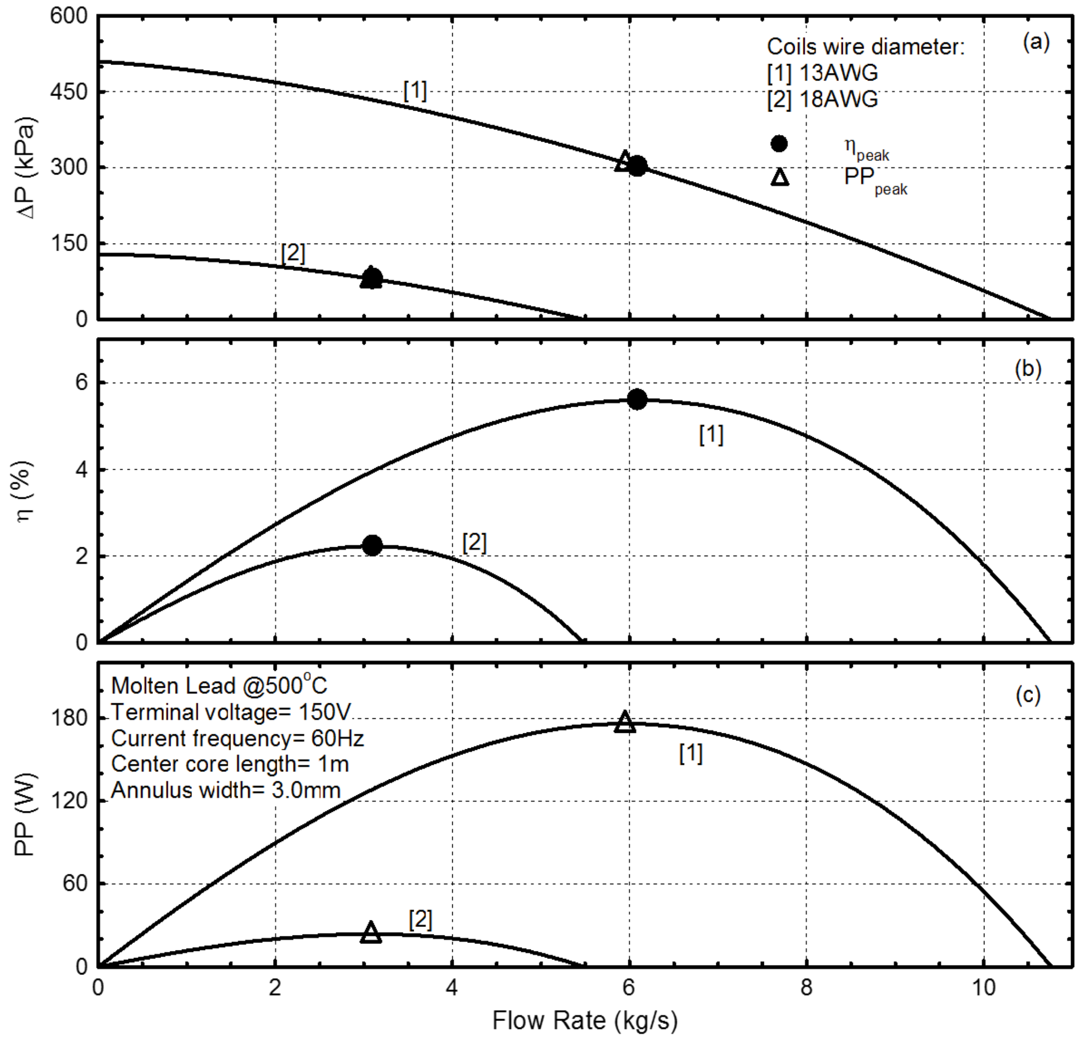

Figure 7-6: Calculated performance of miniature, submersible ALIP for circulating lead at 500 °C using ceramic insulated coil wires.

For constant number of poles, the length of the ALIP center core is proportional to the pole pitch and the induced voltage in the flow annulus. Increasing the center core length increases the developed pumping pressure by the generated Lorentz force in the liquid flow annuls. On the other hand, it also increases the friction pressure losses, which decreases the net pumping pressure for the ALIP. Fig. 7-7 compares the calculated performance characteristics of present ALIP with different center core lengths of 500, 750, and 1,000 mm. Increasing the center core length from 500 to 1000 mm increases the pumping pressure at zero flow and the highest flow rate of molten lead from 147 to 510 kPa, and from 7.35 to 10.75 kg/s, respectively. Compared to the pumping pressure, the increases in the highest flow rate are smaller due to the increase in friction pressure losses for the longer pump.

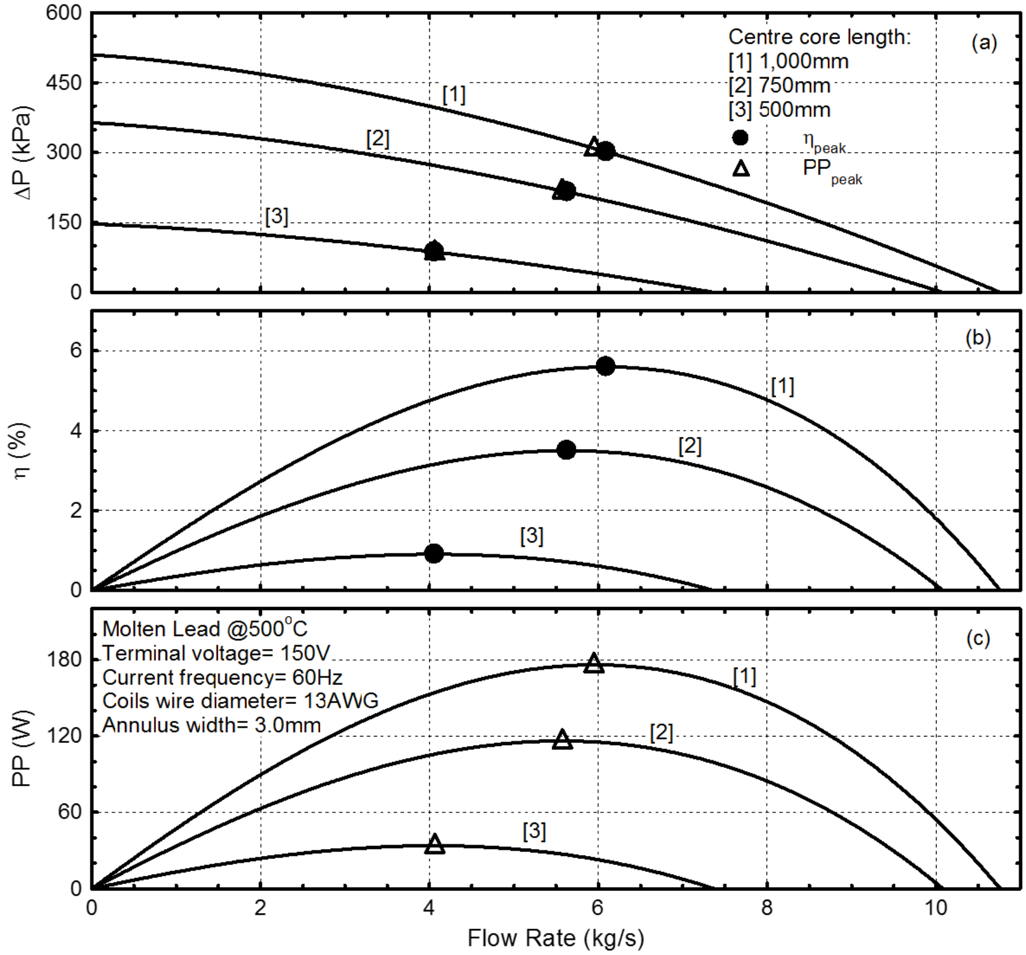

Figure 7-7: Calculated performance of miniature, submersible ALIP for circulating molten lead at 500 °C using different center core lengths.

Increasing the length of the center core from 500 to 1000 mm increases the ALIP peak efficiency 614%, from 0.91% at a pumping pressure of 87 kPa and flow rate of 4.1 kg/s to 5.6% at a pumping pressure of 302 kPa and flow rate of 6.1 kg/s (Fig. 7-7b). The peak pumping power also increases by 718% from 34 W at a pumping pressure of 87k Pa and flow rate of 4.1kg/s, to 176 W at a pumping pressure of 309 kPa and molten lead flow rate of 5.95 kg/s (Fig. 7-7c). In present ALIP, the diameter of the center core is small relative to its length. Therefore, the selected length of center core is 1,000 mm to limit any deformation when operating at temperatures beyond 500°C, potentially failing the ALIP.

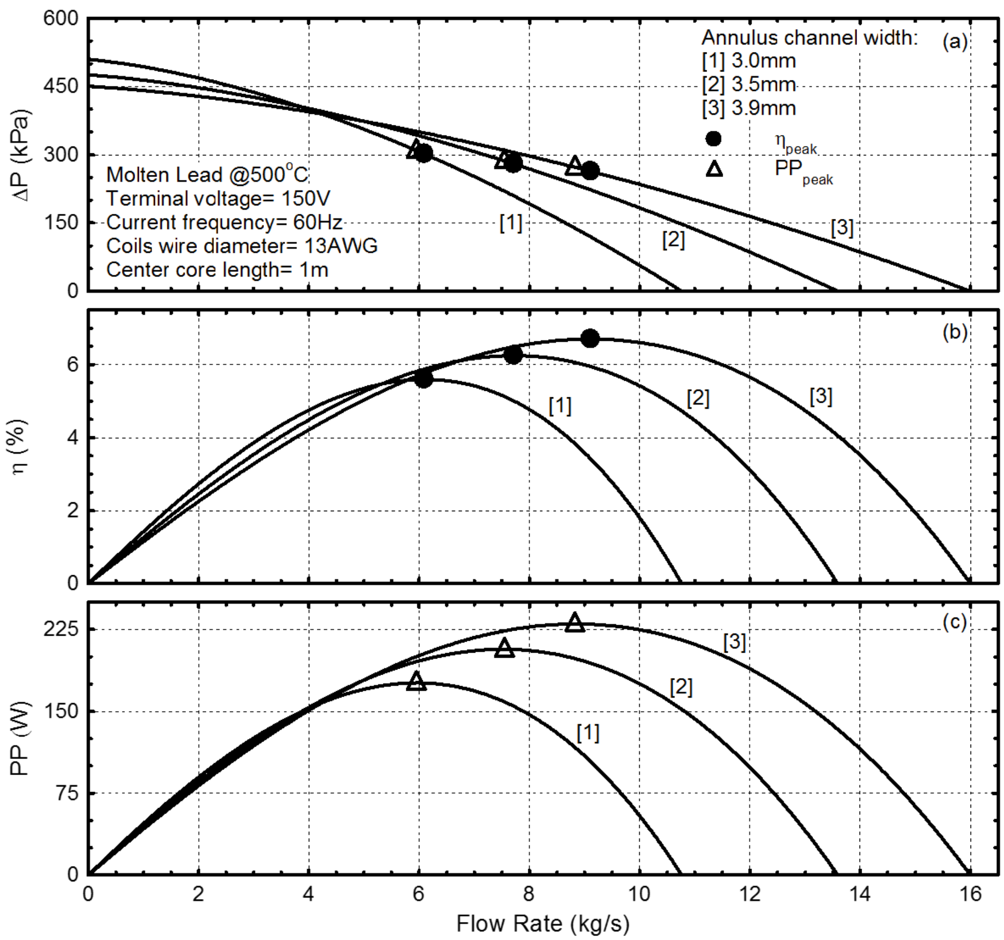

Figure 7-8: Calculated performance of miniature, submersible ALIP for circulating molten lead at 500 °C and with different annular duct width.

The ALIP value of the magnetic circuit inductance is proportional to the cross-sectional area and inversely proportional to the length of the non-magnetic structure of the walls of the annular flow duct. For constant inner and outer duct wall thicknesses, the total length of the air gap is linearly proportional to the width of the annular flow duct. Therefore, increasing the width of the annular flow duct decreases the magnetic flux density in the air gap and the generated Lorentz force in the duct. On the other hand, increasing the width of the annular flow duct decreases the friction pressure losses and increases the net pumping pressure.

Fig. 7-8 compares the calculated performance characteristics of present ALIP with annular flow duct widths of 3.0, 3.5, and 3.9 mm. Increasing the duct width from 3.0 to 3.9 mm decreases the pumping pressure of molten lead at zero flow from 510 to 450 kPa, due to the decrease in the magnetic flux density in the duct. On the other hand, the decreased friction pressure losses in the 3.0 mm wide flow annulus increase in the highest flow rate from 10.75 to 16.0 kg/s. Increasing the flow duct width from 3.0 to 3.9 mm also increases the ALIP peak efficiency for circulating molten lead 83%, from 5.6% at pumping pressure of 30 2kPa and flow rate of 6.1 kg/s to 6.7% at pumping pressure of 263 kPa and flow rate of 9.1 kg/s (Fig. 7-8b). The corresponding peak pumping power increases 131%, from 176 W at pumping pressure of 309 kPa and flow rate of 5.95 kg/s to 230 W at o 272k Pa and 8.83kg/s (Fig. 7-8c). Increasing the width of the annular flow duct beyond 3.9 mm increases the pump outer diameter beyond 66.8 mm and causes the magnetic flux density in the back stator to exceeds the saturation magnetic flux density of Hiperco-50. The smaller annular flow duct width of 3.0 mm is also considered in the present ALIP design. Based on the presented and discussed results of the conducted parametric analyses of present ALIP design, the values of the electrical and geometrical parameters for achieving the highest pump efficiency and the highest pumping pressure are determined. These values are a terminal voltage of 150 VAC, a current frequency of 60 Hz, a winding wire size of 13 AWG, a center core length of 1,000 mm, and an annulus flow duct width of 3.9 mm.

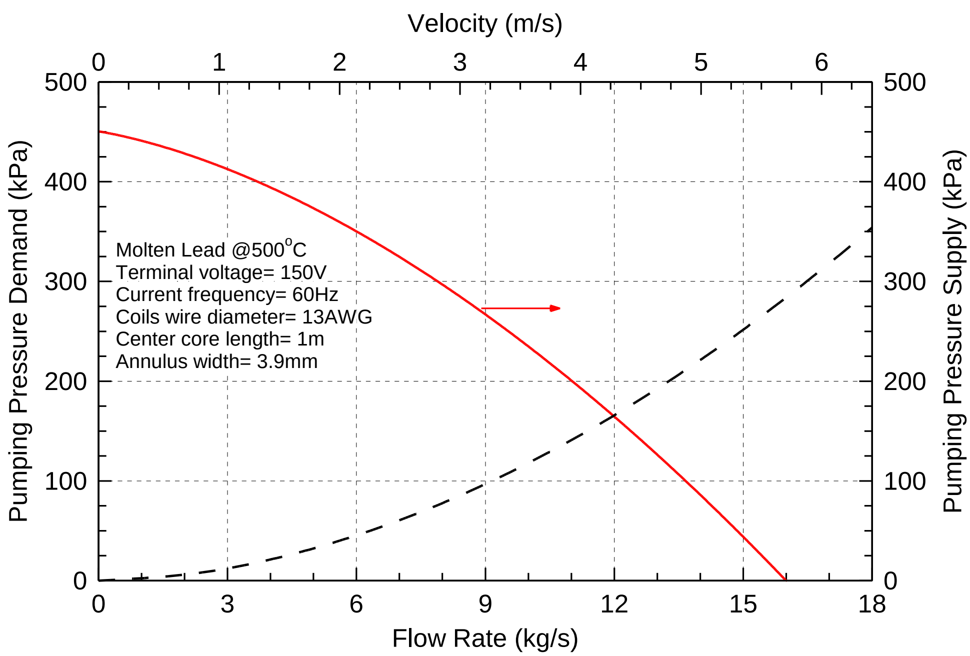

Figure 7-9: Comparison of the calculated supply curve by developed miniature ALIP design and the demand curve for VTR molten lead test loop as function of flow rate.

The calculated supply curves for the present miniature ALIP design and the demand curves for circulating molten Pb at 500°C in the VTR molten lead test loop are presented in Fig. 7-9 (El-Genk et al., 2023). The intersection of the supply and the demand curves indicates a pumping pressure of 164 kPa at a molten lead flow rate of 12.0 kg/s (flow velocity of 4.28 m/s). At these pumping pressure and flow rate, the pump efficiency of 5.68% is 85% of its peak efficiency (El-Genk et al., 2023). Circulating molten lead in the VTR test cartridge at a flow velocity of 4.28 m/s is safe without flow instabilities due to its high density and dynamic viscosity. The following subsection investigates the effects of the liquid properties and temperatures of the operation characteristics of the present ALIP, subject to the electrical and geometrical parameters.

7.3.2. Effects of Fluid Type and Temperatures on ALIP Performance

In addition to molten lead, the developed miniature, submersible ALIP can be used to circulate alkali liquid metals of sodium and NaK-78 alloy for in-pile and out-of-pile test loops at operating temperatures of up to 500^{o}C. This subsection investigates the effects of the circulating liquid properties and temperature on the performance characteristics of the present ALIP. Changing in the temperature changes the working liquid properties of particular interest such the electrical resistivity, dynamic viscosity, and density. In addition, the electrical resistivity of the flow annuls walls and the coil wires, and the magnetic permeability of the stator and center core changes with the temperature. Thus, changing working fluid type and temperatures would affect the ALIP performance in separate ways.

The performance analyses of the present ALIP design using the improved ECM investigated the effects of using molten lead, sodium, and Nak-78 liquids and decreasing the temperature from 500^{o}C to 350^{o}C on the performance characteristics. The presented results are for the pump dimensions listed in Table 7-2 and the selected parameters in the previous subsection, based on the parametric analyses results for achieving the highest pump characteristics for circulating molten lead at 500^{o}C.

Table 7-3 compares the physical properties of molten lead, sodium, and NaK-78 at 500^{o}C and 350^{o}C (Foust, 1978; Sobolev, 2011). Decreasing the temperature from 500 to 350^{o}C decreases the electrical resistivity of molten lead from 1.03 to 0.96 μΩ.m and those for liquid sodium and NaK-78 from 0.32 and 0.67 to 0.23 and 0.55 μΩ.m, respectively. The amount of the decrease in the electrical resistivity increases with decreased temperature increases the induced currents in the annular flow duct and the pumping pressure. Furthermore, the decrease in the electrical resistivity of the winding coils with decreased operation temperature increases the phase current and the generated magnetic field by the coils, and hence, the pumping pressure. On the other hand, decreasing the temperature of the working fluid in the pump flow duct from 500°C to 350°C increases the dynamic viscosity of molten lead from 1,814 to 2,531 µPa.s and those of sodium and Nak-78 from 283 and 192 to 367 and 250 µPa.s, respectively (Table 7-3). The increases in the dynamic viscosity of the working fluid increases the friction pressure losses in the annular flow duct and hence decreases the net pumping pressure and highest flow rate achievable.

Table 7-3: Physical properties of molten lead and liquid sodium at 350 and 500°C (Foust, 1978; Sobolev, 2011).

Working fluid	Temperature (°C)	Electrical resistivity (µΩ.m)	Density (kg/ m³)	Viscosity (Pa. s)
Pb	500	1.03	10,452	1,814
	350	0.96	10,644	2,531
Na	500	0.32	832	283
	350	0.23	868	367
NaK-78	500	0.67	748	192
	350	0.55	783	259

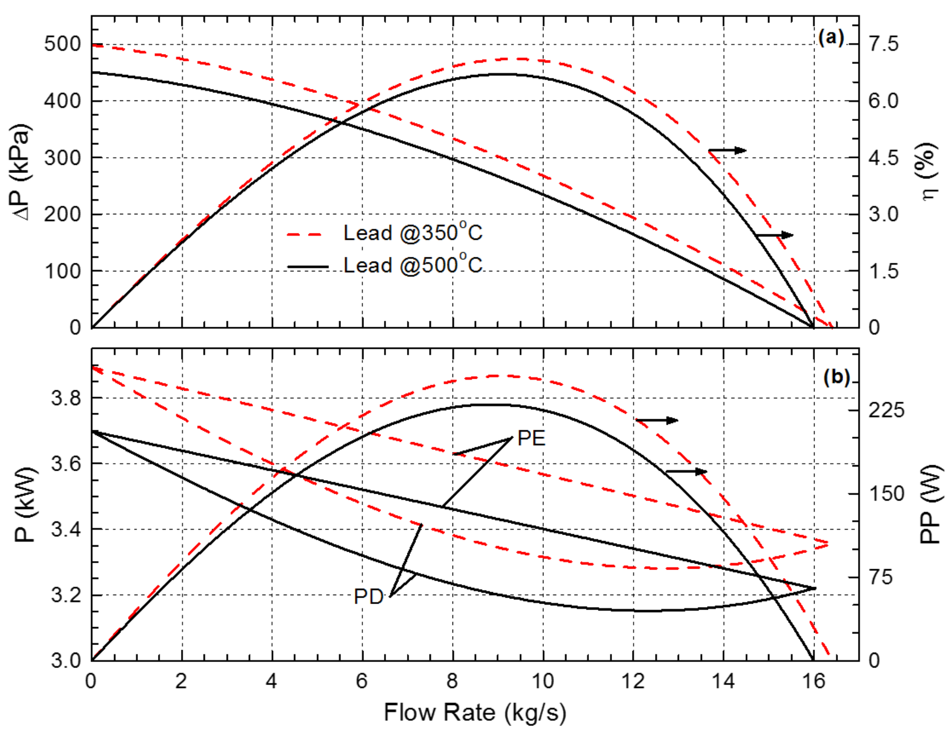

Figure 7-10: Effect of molten lead temperature on the performance of the present miniature, submersible ALIP.

Figs. 7-10 to 7-12 compare the calculated performance characteristics of the present miniature, submersible ALIP for circulating molten lead and alkali metals of sodium and NaK-78, at temperatures of 350°C and 500°C. For the three working fluids, the pumping pressure curves at 350°C are higher than at 500°C (Figs. 7-10a, 7-11a and 7-12a). The higher pumping curves are due to the decreased electrical resistivity with decreased temperature of the working fluid, which increases the induced electrical currents and the magnetic flux density in the pump flow duct.

For the present ALIP design, the used value of phase electric current depends on the type of the working fluid. The used phase currents and the calculated total rates of joule heating for circulating working fluid at 500°C and the calculated peak pump efficiencies for circulating the different working fluids are as follows: 24.9 A and 3.2 kW for molten Pb, 25.5 A and 2.7 kW for Liquid Na and 24.85 A and 2.5 kW Liquid NaK-78. The values of the generated and dissipated thermal power by the present ALIP design, as a function of the working fluid flow rate, are displayed and compared in Figs. 7-10 to 7-12.

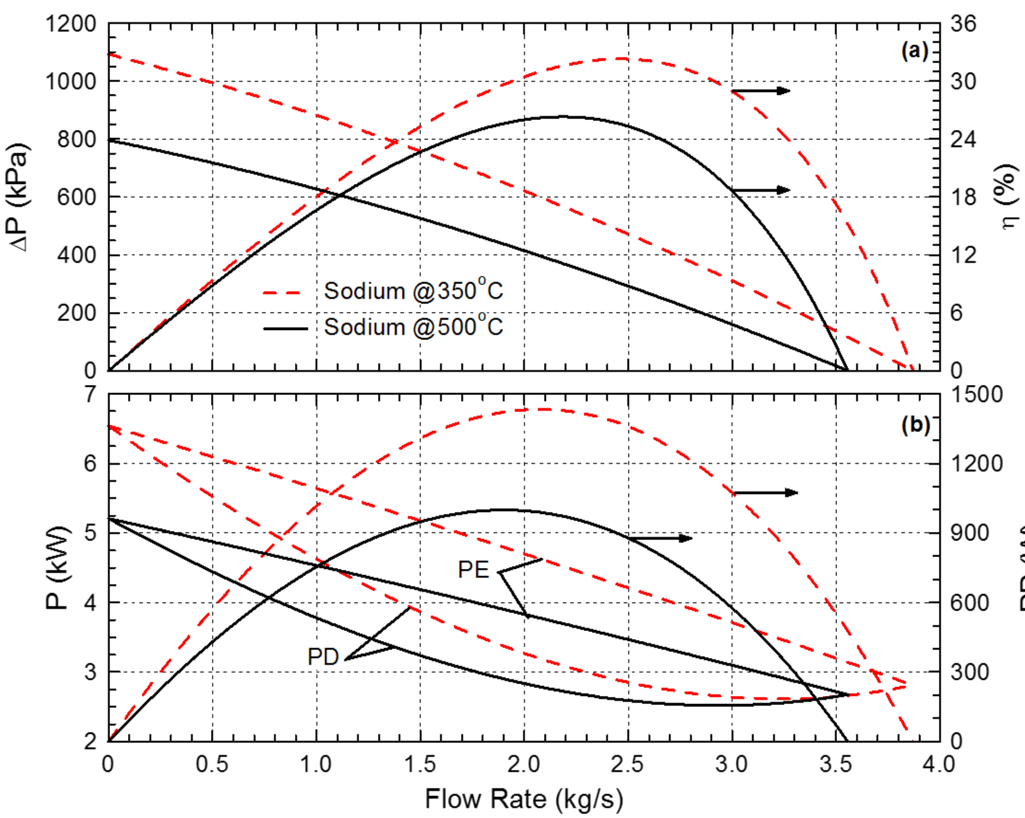

Figure 7-11: Effect of liquid sodium temperature on the performance of developed miniature, submersible ALIP.

Decreasing the molten Pb temperature from 500 to 350°C increases the pumping pressure at zero flow from 450 to 498 kPa and the highest flow rate from 16.0 kg/s (flow velocity of 5.7 m/s) to 16.4 kg/s (flow velocity 5.8 m/s). For circulating liquid sodium, the pumping pressures at zero flow are much higher than for molten Pb. They increase from 796 to 1,092 kPa, and the highest flow rate increases from 3.55 kg/s (flow velocity of 16.6 m/s) to 3.87 kg/s (flow velocity of 15.9 m/s). For circulating liquid NaK-78, the pumping pressures at zero flow increases from 652 kPa to 818 kPa, and the highest flow rates increase from 3.15 kg/s (flow velocity of 16.0 m/s) to 3.38 kg/s (flow velocity of 15.7 m/s) with decreased temperature from 500°C to 350°C.

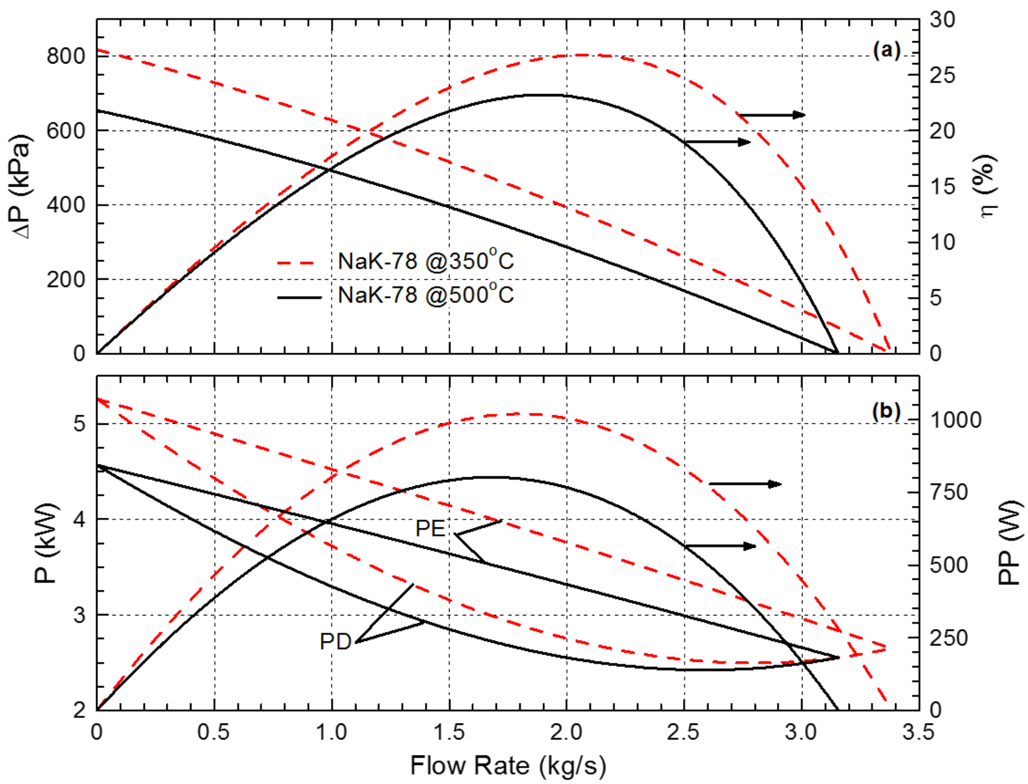

Figure 7-12: Effect of liquid NaK-78 temperature on the performance of the present miniature, submersible ALIP.

The decreases in the electrical resistivities of sodium and NaK-78 with decreased temperature are much larger than for molten Lead, and the differences in the pumping pressure curves are also larger. As the flow rate increases, the difference between the calculated pumping pressures at 350 °C and 500°C decreases for all three working fluids investigated (Figs. 7-10a, 7-11a and 7-12a). This is caused by the larger increases in the friction pressure losses at 350°C compared to those at 500°C.

At the same operation temperature, the present submersible ALIP for circulating liquid sodium produces the highest pumping pressure at zero flow rate because sodium has the lowest electrical resistances compared to those for NaK-78 and molten lead. The latter has the lowest pumping pressure at zero flow. On the other hand, the pumping pressure curves of circulating the liquid sodium and NaK-78 decrease faster than for molten lead with increased flow rate to much lower values of the highest flow rates. These are because the densities of sodium and NaK-78 are only 12-14% of that of molten lead (Table 7-3).

Decreasing temperature from 500 to 350°C negligibly affects the present ALIP efficiency for circulating molten lead, compared to sodium and NaK-78 (Figs. 7-10a, 7-11a and 7-12a). The peak efficiency for circulating molten lead increases with increased temperature from 6.7% to 7.1%, while for liquid sodium and NaK-78 the ALIP efficiencies are much higher and increase from 26.3% and 23.0% to 32.3% and 26.8%, respectively. Similarly, the peak pumping power of molten lead increases from 230 W to 255W compared to 999 W and 760 W to 1,433 and 1,830 W for circulating liquid sodium and NaK-78, respectively (Figs. 7-10b, 7-11b and 7-12b).

The thermal power dissipated by the present ALIP for circulating molten lead in the ATR in-pile test loop, Fig. 1-1, when operating at the peak pump efficiency is 3.2 kW. This thermal power is higher than those for circulating liquid sodium and NaK-78 of 2.7 kW and 2.5 kW, respectively (Figs. 7-10b, 7-11b and 7-12b). The thermal power produced by the Joule heating in the pump coils is conducted by the circulating working fluid in the test loop (Pb, Na or NaK-78) and rejected into the primary Na coolant of the VTR (36). The phase current passing through the winding coils at the peak efficiency of the present ALIP design is the highest for circulating liquid sodium (25.5A), compared to 24.85A and 24.9A for circulating liquid NaK-78 and molten lead, respectively.

Depending on the type of the working fluid, decreasing the temperature increases the pumping pressure, the highest flow rate, the ALIP efficiency, and the peak pumping power. At the same temperature, the circulating liquid sodium and NaK-78 using the present ALIP experience higher pumping pressures at zero flow, than molten lead. However, the pumping characteristic curves decrease faster to smaller values of the highest flow rates than for molten lead. The ALIP efficiency and pumping power curves for circulating molten lead at 350°C and 500°C are close, and the calculated differences are much smaller than for circulating liquid sodium and NaK-78 with increased temperatures. Increasing temperature decreases the ALIP efficiency and pumping power and increases the dissipated thermal power due to the changes in physical properties, particularly the increased electrical resistivity.

7.4. Summary and Conclusions

This chapter developed a miniature, submersible ALIP for circulating molten lead and alkali liquid metals of sodium and NaK-78 at temperatures up to 500°C in test loops supporting materials selection and fuel development for advanced Gen-IV nuclear reactors. The present 66.8 mm diameter ALIP design employs high-temperature ceramic insulated wires for the winding coils and Hiperco-50 for the center core and the stator to maximize the magnetic flux density in the non-magnetic gap without exceeding the saturation flux density in the back stator and center core. The performance characteristics of the present ALIP design are calculated using an improved ECM developed in the present work. It incorporates an equation for calculating the leakage reactance in the stator slot based on the actual geometry of the ALIP, rather than that of a linear induction motor as in the ECM originally proposed by Baker and Tessier (1987) and widely used in the literature. The better predictions of the improved ECM are confirmed based on the comparison to the reported experimental measurements by other investigators for low liquid sodium flow ALIP at 200°C and 330°C. The improved ECM overpredicts the ALIP characteristics by ~ 6%, compared to 11% to 25% using the ECM by Baker and Tessier (1987).

Parametric performance analyses of the present miniature, submersible ALIP investigated the effects of varying the terminal voltage, the electrical current frequency, the diameter of the ceramic insulated wires in the winding coils, the length of the center core, the width of the liquid flow annulus and the properties of the working fluid on the pump characteristics, the pumping power, the pump efficiency, and the dissipated thermal power with increased flow rate. Based on the analyses results of the performance of the present ALIP design, the selected values of the electrical and geometrical parameters for achieving the highest pump efficiency and pumping pressure are terminal voltage of 150

VAC, current frequency of 60 Hz, winding wire size of 13 AWG, 1,000 mm long center core, and an annulus flow duct width of 3.9 mm.

Results show that the pumping power and efficiency for circulating molten lead using the present ALIP is much lower than for circulating both sodium and Nak-78, but the dissipated thermal power is higher, increasing the cooling requirements. For circulating molten lead at 500^{o}C the present ALIP has a peak pump efficiency of 6.7% at a flow rate of 9.5 kg/s and pumping pressure of 263 kPa, which are significantly lower than those for circulating liquid sodium and Nak-78. For circulating liquid sodium and Nak-78 at same temperature of 500^{o}C, the present ALIP has peak efficiencies of 26.3% and 23% occurring at flow rates of 2.2 kg/s and 1.9 kg/s and pumping pressures of 364 kPa and 310 kPa, respectively. Furthermore, cooling requirement of the present ALIP design for circulating molten lead of 3.2 kW, is higher than those for circulating liquid sodium and liquid NaK-78 of 2.7 and 2.5 kW, respectively. Decreasing the working fluid temperature increases the pumping pressure and efficiency and the pumping power for the three working fluids investigated at varying magnitudes, depending on the decreases in their electrical resistivities.

The present ALIP design and performance are suitable for uses in out-of-pile and in-pile test loops to support current and future developments of Gen-IV advanced molten lead cooled reactors and sodium fast reactor for terrestrial power generations and the development of nuclear reactor power systems employing Nak-78 working fluid for space exploration and planetary surface power. For these applications, Nak-78 alloy with a low freezing temperature of -12^{o}C, has been and still an attractive choice for cooling the nuclear reactor and transporting waste heat from the energy conversion subsystem to heat pipe radiators to be radiatively rejected into space.

8. SUMMARY AND CONCLUSIONS

The presented and discussed research results are for developing designs and performing analyses of miniature, submersible electromagnetic pumps for circulating molten lead and sodium in in-pile and out-of-pile test loops for supporting the development of Gen-IV, liquid metals cooled, fast nuclear reactors. The two electromagnetic pumps investigated are: (a) The Direct Current-ElectroMagnetic Pump (DC-EMP) and (b) The alternating Linear Induction Pump (ALIP). These 66.8 mm diameter pumps that fit inside a 2.5-inch standard tube of the test loop riser, with an inner diameter of 68.8 mm, are designed to operate at inlet temperatures up to 500^{o}C. The generated thermal powers due ohmic heating in the flow duct by these pumps are convectively removed by the circulating work fluid to the downcomer of the test loop that is externally cooled.

The DC-EMP design with a pair of Alnico-5 permanent magnets with Hiperco-50 pole pieces, for focusing the magnetic field lines in a rectangular 316SS flow duct, has dual pumping stages for enhanced performance. This is accomplished by mounting the two Alnico-5 permanent magnets, along the rectangular flow duct, and with opposite magnetizing directions in the two pumping stages. The supplied electrical currents to the pump electrodes in the two pumping stages flow in the perpendicular directions to those of the magnetic field lines and the flow of the working fluid. The electric currents in the two pumping stages flow in opposite directions so that the Lorentz forces in the two pumping stages act in the same flow direction.

The developed ALIP design utilizes high-temperature, ceramic insulated Copper wires for the winding coils, and Hiperco-50 for the center core and the stator to strengthen the magnetic field flux density in the narrow annular flow duct without exceeding their saturation flux density. The 3-phase alternating current in the coils, two per pole, are Delta connected in parallel to increase the electric current per phase for generating a moving magnetic field through the annular flow duct.

The analytical and lumped, electrical Equivalent Circuit Model (ECM) predicted the performance of both the DC-EMP and the ALIP for molten lead and liquid sodium working fluids at inlet temperatures $\leq$ 500^{o}C. These models with several simplifying assumptions are fast running with modest computation hardware requirements. That for the DC-EMP neglects the effects on the pump performance of the changes in the values and distributions of the effective electric current and magnetic flux density in the flow duct as function of the flow rate. Instead, it uses the distributions calculated by the FEMM software at zero flow. The ECM for DC-EMPs also assumes isothermal flow of the working fluid at the inlet temperature, thus neglecting the effect of ohmic heating on the working fluid temperature in the pump duct. It predicts the pump characteristics, of the pumping pressure versus the flow, for molten lead and liquid sodium and provides estimates of the pump efficiency and the rate of ohmic heating due to the flow of electric current in the liquid in the pump duct. Therefore, the ECM for the DC-EMPs does not provide details of the actual flow field and the distributions of electric current and the magnetic field flux density in the pump duct.

For the present DC-EMP design, the ECM on MATLAB platform is linked to the two-dimensional FEMM software that calculates the effective electrical currents and magnetic flux distributions in the pump duct at zero flow. The FEMM software results are validated using reported experimental data in the literature for a mercury DC-EMP and water thruster, at zero flow. The FEMM predictions of the effective magnetic flux and electrical current densities are in excellent agreement with reported experimental measurements within ~1%. The fast-running ECM has been shown by other investigators and in this work to overpredict the characteristics of the DC-EMP for different fluids by ~10-25%. Present results of the present DC-EMP using the ECM for molten lead at inlet temperature of 500°C, indicate a peak pump efficiency of 11.3% at a flow rate of 5.75 m^3/h (16.2 kg/s), pumping pressure of 282 kPa, and dissipated thermal power of 3.2 kW. For liquid sodium at the same inlet temperature, the calculated pump peak efficiency is much higher, ~ 36.5% and occurs at a flow rate of 3.95 m^3/h (0.9 kg/s), pumping pressure of 379 kPa and dissipated thermal power of 4.1 kW.

The improved ECM model used in this work for predicting the performance characteristics of the present ALIP design is more accurate than the widely used model originally proposed by Baker and Tessier. The improved model incorporates accurate leakage reactance expressions for the stator geometry. Comparison of this model predictions to the reported experimental data by other investigators for low-flow sodium, small ALIP confirmed its accuracy. The predicted ALIP characteristics are < 6% higher than the reported experimental measurements, compared to ~11% using the ECM by Baker and Tessier. The present ALIP analyses investigated the effect of changing various design and operation parameters on the pump. These include the inlet temperatures of the molten lead and liquid sodium working fluids, the electrodes electric current, the diameter of the ceramic insulated wires in the winding coils, the length of the center core, the width of the flow annulus, the terminal voltage, and the alternative current frequency.

The predicted efficiency of the developed miniature, submersible ALIP design for molten lead at inlet temperature of 500^{o}C is lower than for the DC-EMP. The ALIP peak efficiency is only ~ 6.7% and occurs at a flow rate of 3.37 m^3/h (9.5 kg/s), pumping pressure of 263 kPa, and dissipated thermal power of 3.2 kW. For circulating liquid sodium at the same temperature, ALIP peak efficiency increases to 26.3% and occurs at a flow rate of 9.66 m^3/h (2.2 kg/s), pumping pressure of 364 kPa, and dissipated thermal power of 2.7 kW. Furthermore, decreasing the temperature raises the pump characteristics, efficiency and the pumping power for molten lead and liquid sodium by varying magnitudes, commensurate with the decreases in their electrical resistivities.

To accurately calculate the performance and operation characteristics of the present dual stages, DC-EMP design, this work also performed 3-D magnetohydrodynamic numerical analyses. These analyses also provide useful details of the distributions of the flow, electrode electric current, the magnetic field flux density, and the Lorentz force density in the flow duct as functions of the flow rate, electrode current, and working fluid properties and temperatures. The results quantify the effect of the simplifying assumption in the ECM on the calculated pump characteristics and operation parameters.

The performed 3-D MHD numerical analyses of the present dual-stages DC-EMP design used the capabilities in Star-CCM+ commercial software to solve the coupled electromagnetism, and momentum and energy balance equations. Results include the pump characteristics and 3-D distributions of the fluid flow, electric current, the magnetic flux density, and Lorentz force density in the pump flow duct. The Grid Convergence Index (GCI) criterion confirmed the adequacy of the employed numerical mesh refinement and the results conversion.

The performed 3-D MHD analyses of the present 66.8 mm diameter, dual pumping stages DC-EMP investigated the effects of varying the flow duct dimensions, the length of the current electrodes, the thickness of the ALNICO-5 permanent magnets, and the separation distance between the two pumping stages on the operation parameters. These are the pump characteristics of the pumping pressure versus flow rate, and the pump efficiency and the dissipated thermal power as functions of the input electrode current and the flow rate of molten lead and liquid sodium.

Results of the 3-D MHD numerical analyses demonstrated the strong dependence of the spatial distribution of the magnetic field flux density in the pump duct on the value and the distribution of the electric current, but negligible effect of joule or ohmic heating on fluid temperature and the pump characteristics. The highest densities of the Lorentz force occur at the entrance of the two pumping stages, with approximately 10.0% of the total force occurring in the fringe regions upstream and downstream of pumping stages. The calculated MHD pump characteristics are in general agreement with, but consistently lower than the lumped ECM predictions. The differences increase with increased flow rate and input electric current, up to 12% and 14% for molten lead and liquid sodium, respectively. In summary, the original contribution of the conducted research in this Dissertation are:

1. Developed designs of 66.8 mm diameter, submersible dual stages DC-EMP and ALIP for molten lead and sodium at temperatures up to 500^{o}C. These designs are particularly suited for In-pile and out-of-pile test loops that support the development of Gen-IV liquid metals cooled fast nuclear reactors. These pumps can also be used in other nuclear and industrial applications.
2. Linked the ECM of the DC-EMP to FEMM software on the MATLAB platform to estimate the pump characteristics and operation parameters as function of flow rate, and temperature of molten lead and sodium working fluids.
3. Developed an improved and more accurate ECM for predicting the performance of the present miniature ALIP design and confirmed its accuracy by comparing predictions to experimental measurements reported by other investigators.
4. Linked the ECM for the DC-EMP to the FEMM software on the MATLAB platform to speed up the calculations and obtain estimates of the pump characteristics and operation diameters. Compared results to experimental measurements reported by other investigators confirmed the overestimates the pump performance due to the simplifying assumption in the ECM.

5. Performed 3-D MHD numerical analyses using the capabilities in the Star-CCM+ commercial code to gain insights into the pump operation parameters and the spatial distributions of the flow, the electric current density, the magnetic field flux density, the Lorentz force density in the pump duct and the fringe regions upstream and downstream of the two pumping stages. Results confirmed the effect of the simplifying assumption in the ECM on overestimating the characteristics and operation parameters of the dual-stage DC-EMP.

.

9. FUTURE WORK

Suggestions for future research include investigating the use of the developed miniature DC-EMP and ALIP designs for molten salt test loops. Though the performance of the pumps is expected to by lower for circulating molten salt than for molten lead and sodium, because of the lower electrical conductivity of the former, it may have the potential to satisfy the pumping pressure and flow rater requirements of the test loops. Nonetheless, special attention should be given to selection of the structure materials that are compatible with molten salts, and which would affect the pumps' performance and longevity.

Suggestions for future research also include conducting 3-D MHD numerical analyses of ALIP to further evaluate the impact of different simplifying assumptions of the ECM on the accuracy of predicting the pump performance, and to gain insight into the undergoing physics and the spatial distributions of various operation parameters. Thes include the distributions of the moving magnetic field flux density, the fluid flow, and the Lorentz force density in the narrow annular flow duct of the ALIP.

Furthermore, explore new structure materials for improving the performance of the present designs of the miniature DC-EMP and ALIP for a wide range of fluids at temperatures up to 700^{o}C. Examples are molten lead, liquid sodium, molten lead-bismuth Eutectic (LBE), gallium, aluminum, sodium-potassium alloys, and lithium. Also explore using liquid metal heat pipe for cooling the DC-EMP and ALIP by transporting and dissipating the generated ohmic heating power to an ultimate heat sink.

REFERENCES

Abderrahim, H.A., Baeten, P., De Bruyn, D. and Fernandez, R., 2012. MYRRHA–A multi-purpose fast spectrum research reactor. Energy conversion and management, 63, pp.4-10.

Abhari, F., Jaafar, H., and Yunus, N., 2012. A comprehensive study of micropumps technologies. Int. J. Electrochem. Sci, 7(10), pp.9765-9780.

Abram, T., and Ion, S., 2008. Generation-IV nuclear power: A review of the state of the science. Energy Policy, 36(12), pp.4323-4330.

Aizawa, R., Suzuki, T., Laffont, G., and Rey, F., 2014. Large electro-magnetic pump design for application in the ASTRID sodium-cooled fast reactor. In International Conference on Nuclear Engineering (45936-V003T05A008). American Society of Mechanical Engineers.

Alemberti, A., Smirnov, V., Smith, C., and Takahashi, M., 2014. Overview of lead-cooled fast reactor activities. Progress in Nuclear Energy, 77, pp.300-307.

Al-Habahbeh, O., Al-Saqqa, M., Safi, M., and Khater, T., 2016. Review of magnetohydrodynamic pump applications. Alexandria Engineering Journal, 55(2), pp.1347-1358.

Alfredo, P., Alberto, P., and Fausto, P., 2019. A review of the application performances of concentrated solar power systems, Applied Energy 255, 113893. https://doi.org/10.1016/j.apenergy.2019.113893

Allen, T., Busby, J., Meyer, M., and Petti, D., 2010. Materials challenges for nuclear systems. Materials today, 13(12), pp.14-23.

Allen, T., and Crawford, D., 2007. Lead-cooled fast reactor systems and the fuels and materials challenges. Science and Technology of Nuclear Installations, 2007.

Altamimi, R., and El Genk, M., 2022. Miniature DC Electromagnetic Pumps of Heavy and Alkali Liquid Metals at up to 500°C for Nuclear and Industrial Applications. U'S patent disclosure application No. 63/420,062, filed Oct 27, 2022.

Altamimi, R., and El-Genk, M. S., 2023 a. Equivalent Circuit Model for Predicting the Performance Characteristics of Direct Current-Electromagnetic Pumps. J Material Sci. Eng. 12 (2023):629.

Altamimi, R., and El-Genk, M. S., 2023 b. Miniature DC electromagnetic pumps of molten lead and sodium to support development of Gen-IV nuclear reactors. Nuclear Engineering and Design 410, 112376

Aoki, L.P., Schulz, H.E., and Maunsell, M.G., 2013. An MHD study of the behavior of an electrolyte solution using 3-D numerical simulation and experimental results. In proceedings of the COMSOL conference, Boston, MA. October 17–18, 2013.

Aoto, K., Dufour, P., Hongyi, Y., Glatz, J.P., Kim, Y.I., Ashurko, Y., Hill, R. and Uto, N., 2014. A summary of sodium-cooled fast reactor development. Progress in Nuclear Energy, 77, 247-265.

Arnold Magnetic Technology, 2003. Cast Alnico Permanent Magnets, Report No. 613-00-125, Rev. C.

Ashurko, Y.M., Gulevich, A.V., Klinov, D.A., Vasil'Ev, B.A., Vasyaev, A.V., Marova, E.V. and Shepelev, S.F., 2019. Gen-IV Reactor Systems Criteria Implementation in BN-1200. Atomic Energy, 125, 351-358.

Baker, R.S. and Tessier, M.J., 1987. Handbook of Electromagnetic Pump Technology, Elsevier Science Publishing, New York.

Balderrama, S., Sabharwall, P. and Wachs, D., 2018. Versatile Test Reactor for Advanced Reactor Testing. Transactions of the American Nuclear Society, 119, 942-945.

Baltzis, K.B., 2008. The FEMM Package: A Simple, Fast, and Accurate Open-Source Electromagnetic Tool in Science and Engineering. Journal of Engineering Science & Technology Review 1, 83-89.

Barnes, A.H., 1953. Direct Current Electromagnetic Pumps. Nucleonics 11 (1), 16-21.

Blake, L.R., 1957. Conduction and Induction Pumps for Liquid Metals, Proceedings of the IEE Part A: Power Engineering 104 (13), 49-67.

Bragg-Sitton, S.M., 2022. Next Generation Nuclear Energy: Advanced Reactors and Integrated Energy Systems. Report No. INL/MIS-22-66708-Rev000. Idaho National Laboratory, Idaho Falls, ID.

Brown, G. 2003. The history of the Darcy-Weisbach equation for pipe flow resistance, Environmental and water resources history, 34-43.

Buckthorpe, D., 2017. Introduction to Generation IV nuclear reactors. In Structural Materials for Generation IV Nuclear Reactors (pp. 1-22). Woodhead Publishing.

Cables-cpg, 2020, “Cerafil500 - very high temperature ceramic insulated wire,” data sheet - www.cables- cgp.com/products/cerafil-cerafil500

Casella, A.M., 2022. Natrium Demonstration Reactor Support-CRADA 559. Report No. PNNL-33749. Pacific Northwest National Laboratory, Richland, WA.

Choi, H., Schleicher, R.W., Shapovalov, K., Ellis, C. and Bolin, J., 2021. Feasibility study of a gas cartridge loop for the versatile test reactor. Nuclear Engineering and Design, 377, p.111111.

Crawford, D.C., Porter, D.L., Hayes, S.L., Meyer, M.K., Petti, D.A. and Pasamehmetoglu, K., 2007. An approach to fuel development and qualification. Journal of Nuclear Materials, 371(1-3), 232-242.

Daoud, A. and Kandev, N., 2008, November. Magneto-hydrodynamic numerical study of DC electromagnetic pump for liquid metal. In proceedings of the COMSOL conference, Hannover, Germany. November 5-7, 2008

Davidson, P.A., 2002. An introduction to magnetohydrodynamics, Cambridge University Press. Cambridge, UK.

Davis, K.A., 1966. SNAP-10A Thermoelectric Pump. Final Report (No. NAA-SR-11879). Atomics International, Canoga Park, California.

De Groh III, H.C., Geng, S.M., Niedra, J.M. and Hofer, R.R., 2018. Magnetic Properties of Fe-49Co-2V alloy and pure Fe at Room and Elevated Temperatures. NASA Technical Memorandum, NASA/TM-2018-219872, Glenn Research Center Cleveland, Ohio

Demuth, S.F., 2003. SP100 space reactor design. Progress in Nuclear Energy 42, 323-359. https://doi.org/10.1016/S0149-1970(03)90003-5

Deng, X.F., Hou, J.B., Cheng, L. and Tian, R.N., 2013. Research on mechanism of overland flow losses of direct-current conduction electromagnetic pump for casting. In Applied Mechanics and Materials. 401, 250-253.

Deng, Y., Jiang, Y. and Liu, J., 2021. Liquid metal technology in solar power generation-basics and applications. Solar Energy Materials and Solar Cells, 222, 110925.

Driscoll, M.J. and Hejzlar, P., 2005. Reactor physics challenges in Gen-IV reactor design. Nuclear Engineering and Technology, 37(1), 1-10.

Eldrup, M. and Singh, B.N., 1998. Influence of Composition, Heat Treatment and Neutron Irradiation on The Electrical Conductivity of Copper Alloys. Journal of nuclear materials, 258, 1022-1027

El-Genk, M.S., 2009. Deployment history and design considerations for space reactor power systems. Acta Astronautica, 64(9-10), 833-849.

El-Genk, M.S., Buksa, J.J., and Seo, J.T., 1987. A Self Induced Thermoelectric Electromagnetic Pump Model for SP-100 Systems. Space Nuclear Power Systems 1987, CONF-860102, edited by M. S. El-Genk and M. D. Hoover, Orbit, Malabar, FL, 1987, 161-172.

El-Genk, M.S. and Paramonov, D.V., 1994. An Integrated Model of the TOPAZ-II Electromagnetic Pump. Journal of Nuclear Technology 108, 171-180. https://doi.org/10.13182/NT94-A35028

El-Genk, M.S., and Rider, W.J., 1990. Reliability and vulnerability studies of the SP-100 dual-loop thermoelectric-electromagnetic pump. Journal of Propulsion and Power, 6(3), 305-314.

El-Genk, M.S., Schriener, T., Altamimi, R. and Hahn, A., 2020. Design Optimization and Performance of Pumping Options for VTR Extended Length Test Assembly for Lead Coolant (ELTA-LC). Technical Report No. UNM-ISNPS-5-2020, Institute for Space and Nuclear Power Studies, University of New Mexico, Albuquerque, New Mexico.

El-Genk, M.S., Schriener, T.M., Altamimi, R. and Hahn, A., 2023. Pumping Options for Versatile Test Reactor Molten Lead In-Pile Test Cartridge. Nuclear Science and Engineering, 197, 1-28.

El-Genk, M.S., Tournier, J.M.P. and Gallo, B.M., 2010. Dynamic simulation of a space reactor system with closed Brayton cycle loops. Journal of propulsion and power, 26(3), 394-406.

El-Wakil, M.M., 1978. Nuclear Heat Transport. American Nuclear Society, La Grange Park, Illinois.

Engelen, J., Abderrahim, H.A., Baeten, P., De Bruyn, D. and Leysen, P., 2015. MYRRHA: Preliminary front-end engineering design. International Journal of Hydrogen Energy, 40(44), 15137-15147.

Farmer, M.T., Weathered, M., Lisowski, D., Bremer, N., Kilsdonk, D., Stack, T., Tomlin, C., Plucker, C., Moreno, E., Kong, R. and Quan, Z., 2022. Development of a Sodium Fast Reactor Cartridge Loop Testing Capability for the Versatile Test Reactor. Nuclear Science and Engineering, 196, 1-17.

Fazio, C. and Balbaud, F., 2017. Corrosion phenomena induced by liquid metals in Generation IV reactors. In Structural Materials for Generation IV Nuclear Reactors; Yvon, P., Ed.; Elsevier: Amsterdam, The Netherlands, Chapter 2; 23–74.

Ferroni, P., Stansbury, C., Liao, J., Utley, D., Levinsky, A., Gustavsson, E., Wright, R., Lee, S.J., Banyay, G., Franceschini, F. and Chrzanowski, J., 2019. The Westinghouse lead fast reactor. In Proceedings of International Congress on Advances in Nuclear Power Plants (ICAPP-19), Juan-les-pins, France. May 12–15, 2019

Foust, O. J., 1978. Sodium-NaK Engineering Handbook Volume I: Sodium Chemistry and Physical Properties. Liquid Metal Engineering Center, Gordon and Breach, New York.

Gnielinski, V., 2007. Berechnung des Druckverlustes in glatten konzentrischen Ringspalten bei ausgebildeter laminarer und turbulenter isothermer Strömung. Chemie Ingenieur Technik, 79(1-2), 91-95.

Gougar, H. D., Bari, R. A., Kim, T. K., Sowinski, T. E. and Worrall, A., 2015. Assessment of the Technical Maturity of Generation IV Concepts for Test or Demonstration Reactor Applications. Technical Report INL/EXIT-15-36427, Revision 2, Idaho National Laboratory, Idaho Fall, ID, USA, October 2015.

Gutierrez, A.U. and Heckathorm, C.E., 1965. Electromagnetic Pumps for Liquid Metals. Naval Postgraduate School, Monterey, California.

Hasan, M.I., Ali, A.J.F. and Tufah, R.S., 2017. Numerical study of the effect of channel geometry on the performance of Magnetohydrodynamic micro pump. Engineering science and technology, an international journal, 20(3), 982-989.

Haskins, D.A. and El-Genk, M.S., 2016. CFD Analyses and Correlation of Pressure Losses on the Shell-Side of Concentric, Helically-Coiled Tubes Heat Exchanger. J. Nuclear Engineering & Design, 305, 531-546.

Heck, C., 2013. Magnetic Materials and their Applications. Elsevier, Netherlands.

Heidet, F. and Roglans-Ribas, J., 2022. Versatile Test Reactor Conceptual Core Design. Nuclear Science and Engineering, 196(sup1), 23-37.

Heinzel, A., Hering, W., Konys, J., Marocco, L., Litfin, K., Müller, G., Pacio, J., Schroer, C., Stieglitz, R., Stoppel, L. and Weisenburger, A., 2017. Liquid metals as efficient high-temperature heat-transport fluids. Energy Technology, 5(7),.1026-1036.

Hejzlar, P., Pope, M.J., Williams, W.C. and Driscoll, M.J., 2005. Gas cooled fast reactor for generation IV service. Progress in Nuclear Energy, 47(1-4), 271-282.

Ho, C.Y. and Chu, T.K., 1977. Electrical Resistivity and Thermal Conductivity of Nine Selected AISI Stainless Steels, CINDAS Report 45, Washington.

Ho, M., Obbard, E., Burr, P.A. and Yeoh, G., 2019. A review on the development of nuclear power reactors. Energy Procedia, 160, 459-466.

Homsy, A., Koster, S., Eijkel, J.C.T., Berg, A.V., Lucklum, F., Verpoorte, E. and Rooij N.F., 2005. A high current density DC magnetohydrodinamic (MHD) micropump. Lab on a Chip 5, 466–471. https://doi.org/10.1039/b417892k

Hughes, M., Pericleous, K. and Cross, M., 1995. The Numerical modelling of DC electromagnetic pump and brake flow. Applied mathematical modelling 19(12), 713-723.

IAEA, 2008. Liquid Metal Cooled Reactors: Experience in Design and Operation. Report IAEA-TECDOC-1569, International Atomic Energy Agency, Vienna, Austria.

IAEA. 2012. Structural Materials for Liquid Metal Cooled Fast Reactor Fuel Assemblies Operation Behaviour. Nuclear Energy Services No. NF-T.4.3. International Atomic Energy Agency, Vienna, Austria.

IAEA, 2013. In-Pile Testing and Instrumentation for Development of Generation-IV Fuels and Materials. Proceedings of a Technical Meeting. Report IAEA-TECDOC-CD-1726, International Atomic Energy Agency, Vienna, Austria.

IAEA, 2020. Advances in Small Modular Reactor Technology Developments. A Supplement to: IAEA Advanced Reactors Information System (ARIS). International Atomic Energy Agency, Vienna, Austria.

Ito, K., Takahashi, T., Fujino, T. and Ishikawa, M., 2014. Influences of channel size and operating conditions on fluid behavior in a MHD micro pump for micro total analysis system. Journal of International Council on Electrical Engineering, 4(3), 220-226.

Jayaraman, T.V., 2015. Effect of Processing of HIPERCO® 50 Alloy Laminates on their Magnetic Properties. Journal of Electronic Materials, 44(11), 4379-4386.

Ji, C., Xie, B., Guo, X., Han, W., Hao, Y., Chen, J., Huang, S., Wang, K., Wei, H. and Liang, Y., 2021. A Sodium-Cooled Fast Reactor Simulation System and its Application in Teaching Research Based on VPOWER Platform. In International Conference on Nuclear Engineering (ICONE-28), Virtual meeting, August 4 – 6, 2021.

Johnson, J.L., 1973. Space Nuclear System Thermoelectric NaK Pump Development: Summary Report. Atomics International Division, California. Report No. NASA-CR-121231.

Kadak, A.C., 2016. The status of the US high-temperature gas reactors. Engineering, 2(1), 119-123.

Kale, R.D., 2020. India's fast reactor programme–A review and critical assessment. Progress in Nuclear Energy, 122, 103265.

Kamide, H., Rodriguez, G., Guiberteau, P., Kawasaki, N., Hatala, B., Alemberti, A., Bourg, S., Huang, Y., Serre, F., Fuetterer, M.A. and Shropshire, D., 2021. Generation IV International Forum-GIF. Report No. INIS-FR--21-0718.

Kandev, N., 2012. Numerical Study of a DC Electromagnetic Liquid Metal Pump: Limits of the Model. In Proceeding of the COMSOL conference, Boston, MA. October 3–5, 2012.

Kelly, J.E., 2014. Generation IV International Forum: A decade of progress through international cooperation. Progress in Nuclear Energy, 77, 240-246.

Kilbane, J. and Polzin, K.A., 2014. Multiphysics Modelling of an Annular Linear Induction Pump with Applications to Space Nuclear Power Systems (No. M-1377).

Kim, D., Hong, J. and Lee, T., 2014. Design Of DC Conduction Pump for PGSFR Active Decay Heat Removal System, in: Transactions of the Korean Nuclear Society Spring Meeting, Jeju, Korea, May 29-30, 2014.

Kim, H.R., and Lee, Y.B., 2011. A design and characteristic experiment of the small annular linear induction electromagnetic pump. Annals of Nuclear Energy, 38(5), 1046-1052.

Kim, S.J., Woloshun, K., Richard, J., Galloway, J., Unal, C., Arndt, J., Ickes, M., Ferroni, P., Wright, R., Anderoglu, O. and Cakez, C., 2022. Development of Conceptual Lead Cartridge Design to Perform Irradiation Experiments in VTR. Nuclear Science and Engineering, 196(sup1), 165-182.

Kwak, J.S. and Kim, H.R., 2019. Performance analysis of magnetohydrodynamic pump for sodium-cooled fast reactor thermal hydraulic experiment. Annals of Nuclear Energy, 132, 191–198

Lee, G.H. and Kim, H.R., 2017. Design Analysis of DC Electromagnetic Pump for Liquid Sodium–CO2 Reaction Experimental Characterization. Annals of Nuclear Energy 109, 490–497. http://dx.doi.org/10.1016/j.anucene.2017.05.054

Lee, G.H. and Kim, H.R., 2018. Numerical Analysis of The Electromagnetic Force for Design Optimization of a Rectangular Direct Current Electromagnetic Pump, Nuclear Engineering and Technology, 50, 869-876.

Lee, G.H. and Kim, H.R., 2019. Mathematical approach for optimization of magnetohydrodynamic circulation system. Nuclear Engineering and Technology, 51(3), 654-664.

Li, Y.H., Zeng, C.H. and Chen, Y.J., 2021. Enhancement for magnetic field strength of a magnetohydrodynamic thruster consisting of permanent magnets. AIP Advances, 11(1), 015008.

Liao, J., Ferroni, P., Wright, R.F., Bachrach, U., Scobel, J.H., Sofu, T., Tentner, A.M., Lee, S.J., Epstein, M., Frignani, M. and Tarantino, M., 2021. Development of phenomena identification and ranking table for Westinghouse lead fast reactor's safety. Progress in Nuclear Energy, 131, 103577.

Liu, S., Bauser, S., Turgut, Z., Coate, J. and Fingers, R.T., 2003. Fe–Co–V alloy with improved magnetic properties and high-temperature creep resistance. Journal of applied physics, 93(10), 7118-7120.

Locatelli, G., Mancini, M. and Todeschini, N., 2013. Generation IV Nuclear Reactors: Current Status and Future Prospects. Energy Policy 61, 1503–1520.

Macziewski, C., 2019. Determination of the structure-processing-properties relationship of Fe-6.5 wt% Si. Doctoral dissertation, Iowa State University (ISU), Ames, Iowa.

Markusic, T.E., Polzin, K.A. and Dehoyos, A., 2005. Electromagnetic Pumps for Conductive-Propellant Feed Systems. Proceeding of 29th International Electric Propulsion Conference, Princeton, New Jersey. Paper No. IEPC-2005-295.

Maroufian, S.S. and Pillay, P., 2019. Design and Analysis of a Novel PM-Assisted Synchronous Reluctance Machine Topology with Alnico Magnets. IEEE Transactions on Industry Applications, 55(5), 4733-4742.

MATLAB, 2022. The MathWorks Inc. Natick, Massachusetts, United States.

McAdams, W. H., 1954. Heat Transmission. 3rd ed. McGraw-Hill, New York, USA.

McDuffee, J., Christensen, R., Eichel, D., Simpson, M., Phongikaroon, S., Sun, X., Baird, J., Burak, A., Chapel, S., Choi, J. and Gorton, J., 2022. Design and Control of a Fuelled Molten Salt Cartridge Experiment for the Versatile Test Reactor. Nuclear Science and Engineering, 196(sup1), pp.234-259.

McDuffee, J., Felde, D., Weaver, K.D., Farmer, M., Subharwall, P., Howard, R.H. and Mulligan, P.L., 2019. Flow Test Plan to Support the Development of Cartridge Loops in the Versatile Test Reactor. Transactions of the American Nuclear Society, Vol. 121, Washington, D.C., November 17–21, 2019

Meeker, D., 2015. Finite Element Method Magnetics, Version 4.2 User Manual. Online technical report, October 2015. (http://www.femm.info/wiki/Documentationn)

Meunier, G., 2010. The Finite Element Method for Electromagnetic Modeling; ISTE, Wiley: Hoboken, NJ, USA,

Mignot, G., Briggs, S., Torres, C.T., Young, G., Brittan, A., Teeter, L., Wojcik, A., Waitt, M. and Tucker, J.D., 2019. In-Situ mechanical and corrosion testing for versatile test reactor application. Transactions of American Nuclear Society, Vol. 121, 1411-1414. ANS, IL.

Mom Ozaki, Y., 2016. A model of annular linear induction pumps. Report No. ANL-16/20. Argonne National Laboratory (AN), Argonne, IL.

Mundt, J.F., Truscello, V.C. and Marriott, A.T., 1994. SP-100 Power Program. In AIP Conference Proceedings. 301, 143-155, American Institute of Physics.

Moskowitz, L. R., 1995. Permanent Magnet Design and Application Handbook, Krieger, Melbourne, FL.

Murty, KAL. and Charit, I., 2008. Structural materials for Gen-IV nuclear reactors: Challenges and opportunities. Journal of Nuclear Materials, 383(1-2), 189-195.

Nasar, S. and Bolder, I., 1976. Linear Motion Electric Machines, John Wiley & Sons, New York.

Nashie, B.K., Dash, S.K., Guru Murthy, K., Rajan, M. and Vaidyanathan, G., 2006, January. Design and testing of DC conduction pump for sodium cooled fast reactor. In International Conference on Nuclear Engineering, 42444, 357-362.

Nashie, B.K., Dash, S.K., Guru Murthy, K., Kale, U., Sharma, V.D., Prabhakar, R., Rajan, M. and Vaidyanathan, G., 2007. Performance testing of indigenously developed DC conduction pump for sodium cooled fast reactor. Indian Journal of Engineering & Materials Sciences, 14, 209-214.

Nashie B. and Rao, B., 2014. Design, in-sodium testing and performance evaluation of annular linear induction pump for a sodium cooled fast reactor. Annals of Nuclear Energy 73, 527–536

Nashie, B.K., Sharma, P., Venkatesan, N., Kumar, S.K., Chandramouli, S., Prasad, R.R., Vijayakumar, G. and Selvaraj, P., 2020. Design, development, and testing of a sodium submersible Annular Linear Induction Pump for application in sodium cooled fast reactor. Annals of Nuclear Energy, 145, 107494.

Nobuyuki, U., Izumi, K., Akio, M., Shigeo, K., Tsugio, Y., and Shigeki, M., 2005. Sodium cooled small fast long-life reactor “4S”. Progress in Nuclear Energy (47), 222-230.

O'Grady, D.J., Keckler, C. and Fanning, T., 2021. Status of EM Pump Modeling Capability for VTR. Report No. ANL-VTR-87, Rev. 1. Argonne National Laboratory (ANL), Argonne, IL, US.

Ohshima, H. and Kubo, S., 2016. Sodium-cooled fast reactor. In Handbook of Generation IV Nuclear Reactors (pp. 97-118). Woodhead Publishing.

Orlov, A.I. and Gabaraev, B.A., 2023. Heavy liquid metal cooled fast reactors: peculiarities and development status of the major projects. Nuclear Energy and Technology, 9(1),1-18.

Ota, H., Katsuki, K., Funato, M., Taguchi, J., Fanning, A.W., Doi, Y., Nibe, N., Ueta, M. and Inagaki, T., 2004. Development of 160 m^3/min large capacity sodium-immersed self-cooled electromagnetic pump. Journal of nuclear science and technology, 41(4), 511-523.

Pasamehmetoglu, K., 2019. Versatile Test Reactor Overview. Proceedings of Advanced Reactors Summit VI, San Diego, California. January 29-31, 2019.

Perlow, M., 1964. SNAP 10A thermoelectric pump development. Atomics International Report No. NAA-SR-9486, Ca, US.

Pioro, I., 2022. Handbook of Generation IV Nuclear Reactors: A Guidebook. Woodhead Publishing.

Polzin, K. and Godfroy, T., 2008. Flow Components in A Nak Test Loop Designed to Simulate Conditions in A Nuclear Surface Power Reactor. Space Technology and Applications International Forum (STAIF-2008), Editor, M. S. El-Genk, American Institute of Physics, 969, 423-429.

Polzin, K., Schoenfeld, M., Pearson, J.B., Webster, K., Godfroy, T., Adkins, H., Werner, J. and Bossard, J., 2010. Performance of an annular linear induction pump with applications to space nuclear power systems. In 46th AIAA/ASME/SAE/ASEE Joint Propulsion Conference & Exhibit, paper AIAA 2010-6600, Nashville, TN

Quan, Z., Kong, R., Dix, A., Kim, S., Ishii, M., and Farmer, M.T., 2020, November. CFD Simulations of the Sodium Cartridge Loop of the Versatile Test Reactor. In Transactions of the American Nuclear Society, Vol. 123, ANS Virtual Winter Meeting, November 16-19, 2020.

Rahman, M.M., Dongxu, J., Jahan, N., Salvatores, M. and Zhao, J., 2020. Design concepts of supercritical water-cooled reactor (SCWR) and nuclear marine vessel: A review. Progress in Nuclear Energy, 124, 103320.

Rajan, K.K., 2021, February. A study on sodium-the fast breeder reactor coolant. In IOP Conference Series: Materials Science and Engineering, 1045, 012013. Hainan Province, China. November 12-14, 2021.

Rehman, S.U., Jiang, Q., Ge, Q., Lei, W., Zhang, L., Zeng, Q., Ul Haq, A., Liu, R. and Zhong, Z., 2018. Microstructure and magnetic properties of alnico permanent magnetic alloys with Zr-B additives. Magnetism and Magnetic Materials, 451, 243-247.

Renault, C., Hron, R., Konings, D. and Holcomb, D., 2009. The Molten Salt Reactor in Generation IV: Overview and Perspectives, GIF Symposium proceeding, Paris, France. 9-10 Sep 2009.

Roache, P.J., 1994. Perspective: a method for uniform reporting of grid refinement studies. J. Fluids Eng. 116, 405–413.

Roelofs, F., 2019. Introduction to liquid metal cooled reactors. In Thermal Hydraulics Aspects of Liquid Metal Cooled Nuclear Reactors. Woodhead Publishing, Sawston, United Kingdom

Roelofs, F., Zwijsen, K., Uitslag-Doolaard, H., Alcaro, F., Stempniewicz, M. and Wallenius, J., 2021. Validation of Thermal Hydraulic Design Support and Safety Methodology and Application Sealer. Report No. IAEA-TECDOC--1972. International Atomic Energy Agency, Vienna, Austria.

Roglans-Ribas, J., Pasamehmetoglu, K., and O'Connor, J., 2022. The Versatile Test Reactor Project: Mission, Requirements, and Description, Nuclear Science and Engineering, DOI: 10.1080/00295639.2022.2035183

Sabharwall, P., Bragg-Sitton, S.M. and Stoots, C., 2013. Challenges in the development of high temperature reactors. Energy conversion and management, 74, 574-581.

Saha, C., 2011. Modelling Theory and Applications of The Electromagnetic Vibrational Generator. In Sustainable Energy Harvesting Technologies: Past, Present, and Future. 55-108. Nottingham, UK.

Schulenberg, T., Leung, L.K. and Oka, Y., 2014. Review of R&D for supercritical water cooled reactors. Progress in Nuclear Energy, 77, 282-299.

Serp, J., Allibert, M., Beneš, O., Delpech, S., Feynberg, O., Ghetta, V., Heuer, D., Holcomb, D., Ignatiev, V., Kloosterman, J.L. and Luzzi, L., 2014. The molten salt reactor (MSR) in generation IV: overview and perspectives. Progress in Nuclear Energy, 77, 308-319.

Shadrin, A.Y., Dvoeglazov, K.N., Kascheyev, V.A., Vidanov, V.L., Volk, V.I., Veselov, S.N., Zilberman, B.Y. and Ryabkov, D.V., 2016. Hydrometallurgical reprocessing of BREST-OD-300 mixed uranium-plutonium nuclear fuel. Procedia Chemistry, 21, 148-155.

Sharma, P., Krishnakumar, S., Chandramouli, S., Nashine, B.K. and Mani, A., 2019. Performance evaluation of a low flow rate Annular Linear Induction Pump. Annals of Nuclear Energy, 132, 299-310.

Siemens, P.L.M., 2018. SIMCENTER, STAR CCM+, User Guide. version 13.06.

Sobolev, V., 2011. Database of ThermoPhysical Properties of Liquid Metal Coolants for GEN-IV. 2nd ed. Open Report of the Belgian Nuclear Research Centre; BLG-1069.

SolidWorks Corporation, 2016, SolidWorks 2016 User Guide. Waltham, Massachusetts.

Spencer, B.W., Marchaterre, J.F., Anderson, R.P., Armstrong, D.R., Baker, L., Cho, D.H., Gabor, J.D., Pedersen, D.R., Sienicki, J.J. and Stein, R.P., 1987. Status of Argonne National Laboratory out-of-pile investigations of severe accident phenomena for liquid metal reactors. In Science and technology of fast reactor safety,1-231, Thomas Telford Publishing.

Stainsby R., Peers K., Mitchell C., Poette C., Mikityuk K., and Somers J., 2011. Gas cooled fast reactor research in Europe. Nuclear Engineering and Design, 241, 3481– 3489.

Stieglitz, R. and Zeininger, J., 2005. A 2D model to design MHD induction pumps. In The 15th Riga and 6th Pamir Conference on Fundamental and Applied MHD, Latvia, 35-49.

Sun, P., Zhang, H., Jiang, F.C. and He, Z., 2021. Self-driven liquid metal cooling connector for direct current high power charging to electric vehicle. Etransportation, 10, 100132.

Takahashi, M., Igashira, M., Obara, T., Sekimoto, H., Kikuchi, K., Aoto, K. and Kitano, T., 2002, January. Studies on materials for heavy-liquid-metal-cooled reactors in Japan. In International Conference on Nuclear Engineering, 35960, 549-559.

Umans, A., Railey, K. and Wise, D., 2013. Gallium conduction pump design and analysis. Proceedings of ASME 2013 International Mechanical Engineering Congress and Exposition, San Diego, California, November 15–21, 2013.

Van Tichelen, K., Kennedy, G., Mirelli, F., Marino, A., Toti, A., Rozzia, D., Cascioli, E., Keijers, S. and Planquart, P., 2020. Advanced liquid-metal thermal-hydraulic research for MYRRHA. Nuclear Technology, 206(2),150-163.

Vogt, J.-B. and Proriol, I. 2021. A review of Surface Modifications for Corrosion Mitigation of Steels in Lead and LBE, Coating, 11(1), 53.

Wallenius, J. and Bortot, S., 2014. SEALER: a very small lead cooled fast reactor for commercial energy production in off-grid communities. 3rd International technical meeting on small reactors. In 3rd International technical meeting on small reactors, Ontario, Canada. November 5-7, 2014.

Wallenius, J., Qvist, S., Mickus, I., Bortot, S., Szakalos, P. and Ejenstam, J., 2017. Design of SEALER, a very small lead-cooled reactor for commercial power production in off-grid applications. Nuclear Engineering and Design, 338, 23-33.

Wang, P.J., Chang, C.Y. and Chang, M.L., 2004. Simulation of two-dimensional fully developed laminar flow for a magneto-hydrodynamic (MHD) pump. Biosensors and bioelectronics, 20(1), 115-121.

Watt, D.A., 1959. The Design of Electromagnetic Pumps for Liquid Metals, Proceedings of the IEE Part A: Power Engineering 106 (26), 94-103.

Watt, D., O'connor, R. and Holland, E., 1957. Tests on an Experimental D.C. Pump for Liquid Metals. Atomic Energy Research Establishment, Harwell, UK. Report No. R/R 2274.

Wright, W.E., 1985. Accomplishments and plans of SP-100 program. In Space nuclear power systems 1984; Proceedings of the First Symposium, Albuquerque, NM, January 11-13, 1984.

Wydler, P., 2005. Liquid metal cooled reactors. Chimia, 59(12), 970-970.

Yvon, P. and Carré, F., 2009. Structural materials challenges for advanced reactor systems. Journal of nuclear materials, 385(2), 217-222.

Zaharescu, T., Nemes, E., Rapa, M. and Grosu, E., 2006. Radiation Modification of Functional Properties in PVC/Mica Electrical Insulation. Polymer Bulletin, 57(1), 83-90

Zhang, J., 2009. A review of steel corrosion by liquid lead and lead–bismuth. Corrosion Science, 51(6), 1207-1227.

Zhang, X., Zhou, Y. and Liu, J., 2020. A novel layered stack electromagnetic pump towards circulating metal fluid: Design, fabrication, and test. Applied Thermal Engineering 179, 115610. https://doi.org/10.1016/j.applthermaleng.2020.115610

Zhang, Z., Wu, Z., Wang, D. and Tong, J., 2019. Development strategy of high temperature gas cooled reactor in China. Strategic Study of Chinese Academy of Engineering, 21(1), 12-19.

APPENDIX A: LIST OF RELEVANT PUBLICATIONS

Journal papers:

- Altamimi, R., El Genk, M.S., 2023. Miniature DC electromagnetic pumps of molten lead and sodium to support development of Gen-IV nuclear reactors. Nuclear Engineering and Design 410, 112376
- Altamimi, R., El Genk, M.S., 2023 Equivalent Circuit Model for Predicting the Performance Characteristics of DC Electromagnetic Pumps. J Material Sci Eng (12) 629
- El-Genk, M.S., Schriener, T.M., Altamimi, R. and Hahn, A., 2023. Pumping Options for Versatile Test Reactor Molten Lead In-Pile Test Cartridge. Nuclear Science and Engineering, pp.1-28
- Altamimi, R., El Genk, M., 2023. Miniature, Submersible Annular Linear Induction Pump of Heavy and Alkali Liquid Metals in Test Loops for Advanced Reactors. Nuclear Science and Engineering (Under review).
- Altamimi, R., El Genk, M.S., 2023. Magnetohydrodynamic Analyses of a Miniature Dual-Stage Electromagnetic Pump for Lead and Sodium In-pile Test Loops. Nuclear Science and Engineering (Under review).

Patent Disclosures:

- Altamimi, R., and El Genk, M., 2022. Miniature DC Electromagnetic Pumps of Heavy and Alkali Liquid Metals at up to 500^{o}C for Nuclear and Industrial Applications. U.S patent disclosure application No. 63/420,062, filed Oct 27, 2022.

Technical reports:

- El-Genk, M.S., Schriener, T., Altamimi, R., Hahn, A., 2020. Design Optimization and Performance of Pumping Options for VTR Extended Length Test Assembly for Lead Coolant (ELTA-LC). Institute for Space and Nuclear Power Studies, Albuquerque, New Mexico. Technical Report No. UNM-ISNPS-5-2020.